Universidad de Valladolid

Escuela de Doctorado Universidad de Valladolid

PROGRAMA DE DOCTORADO EN FÍSICA

TESIS DOCTORAL:

Interaction Between Coherent Light and Axially Heterostructured Semiconductor Nanowires

Presentada por Jose Luis Pura Ruiz para optar al grado de Doctor por la Universidad de Valladolid

Dirigida por:
Juan Jiménez López
y
Jorge Souto Bartolomé

Agradecimientos

Quiero empezar estos agradecimientos por mis directores de tesis: Juan Jiménez y Jorge Souto. Podría empezar diciendo todo lo que he aprendido de ellos en estos años, toda la física, la manera de abordar los problemas, los conocimientos sobre los equipos del laboratorio, sobre las técnicas de medida... Sin embargo, quiero hacer hincapié en algo, en mi opinión, mucho más valioso. Su cercanía. He tenido la suerte de tener dos directores con una disponibilidad prácticamente absoluta. Jorge sentado a mi lado en el despacho, escuchando incansablemente y día tras día mis desvaríos, y no solo eso, sino contestando siempre mis dudas, ya fueran de física, inglés o de cualquier otra cosa. Juan, en cambio, siempre ha sido más prudente y consiguió alejarse unos metros más de mi. Aunque eso no evitaba que en cualquier momento a lo largo del día un servidor apareciese por su despacho con alguna cuestión que él resolvía instantáneamente. Mil gracias a ambos por todo lo que me habéis enseñado y por vuestra dedicación.

Me gustaría continuar con el resto de compañeros del laboratorio, los que aguantan mis bobadas diarias y los fieles compañeros de café: Alfredo, por tus clases particulares de SEM y las mil charlas científicas y otras mil que no lo han sido tanto, pero siempre enriquecedoras; Carmelo, por tus consejos y risas; Ángel, por tu infinita ayuda en el laboratorio y por ser mucho más que un compañero de trabajo; y por supuesto a todos los demás que hacéis que el grupo siga funcionando: Óscar, Miguel Ángel, Manu, Marta, Shabnam, y sin olvidar a los que pasaron por aquí: Luis, Sofía, José María, Miguel, Dani, Vincenzo, Blas... Con buena gente y risas el trabajo no es trabajo.

Quiero agradecer también con estas palabras a mis amigos, a todos aquellos que, estemos más cerca o más lejos, siguen pensando que lo somos. Con especial mención a los compañeros de clase, Los Frikifísicos, que cinco años después de terminar la carrera seguimos encontrando tiempo para juntarnos. La gente del teatro, Los Mirmidones. ¡Oh, Zeus, qué haría yo sin ellos! A mis incondicionales del WhatsApp, Edu y Tolosa, gracias por darme cinco minutos de esparcimiento al día los 365 días del año y por ayudar siempre con cualquier cuestión de física. Y para terminar, no puedo dejar de mencionar a Álvaro, toda la vida ahí, siempre, incluso formando parte de este trabajo, gracias hermano.

A mi familia, todos los que me apoyan y se alegran siempre de mis logros. Todos aquellos que os sintáis así sois mi familia. En especial quiero agradecer a mis padres y a mi hermano, porque por ser ellos como son, yo soy como soy. Gracias por vuestro apoyo, por sentiros orgullosos de mi y por quererme así.

Y para terminar quiero agradecer a esa chica que empezó la tesis conmigo como mi novia, y en el camino se ha convertido en mi mujer. Gracias por estar ahí, gracias por ser mi apoyo y sobre todo mi referente. Porque además de apoyarme durante este tiempo como pareja tengo que agradecer el haber tenido a una extraordinaria científica en el camino. Me has enseñado (entre otros mil millones de cosas) algo que yo antes creía imposible, que realmente se pueden organizar datos científicos para que otra persona pueda leerlos y entenderlos. Me has enseñado lo que es trabajar duro y has llenado de colores mis gráficas y mi vida. Por todo esto y mucho más, gracias. Una tesis se hace mucho más llevadera con esa sonrisa al lado.

Physics isn't the most important thing. Love is.
- Richard Feynman -

Financiación

Quiero agradecer la financión recibida para la realización de esta tesis a través de diversas instituciones. En primer lugar al **Ministerio de Educación, Cultura y Deporte** por su financiación a través del programa de Formación del Profesorado Universitario (**FPU14/00916**). También a la financiación recibida por el grupo que ha permitido llevar a cabo esta investigación:

- Nanohilos semiconductores para aplicaciones fotovoltaicas y de conversión termoeléctrica **Junta de Castilla y León: VA293U13**
- Desarrollo de sistemas de imagen por electroluminiscencia para la inspección y mantenimiento de plantas solares **Junta de Castilla y León: VA283P18**
- Caracterización óptica de obleas y células tandem de silicio de bajo coste para aplicaciones fotovoltaicas y de conversión termoeléctrica **MINECO (Spanish Government): ENE2014-56069-C4-4-R**
- Diseño y desarrollo de un sistema de imagen por fotoluminiscencia para calificación de obleas y células solares de silicio multicristalino **Junta de Castilla y León: VA081U16**
- Caracterización Eléctrica y lumínica de sustratos y células solares para la fabricación de módulos bifaciales de silicio solar **MINECO (Spanish Government): ENE2017-89561-C4-3-R**

Funding

Financial support from different institutions is gratefully acknowledged. First, the funding received by **Ministerio de Educación, Cultura y Deporte** from the Spanish Government through the program Formación del Profesorado Universitario (**FPU14/00916**). The funding received by the group that allowed this investigation is also appreciated:

- Nanohilos semiconductores para aplicaciones fotovoltaicas y de conversión termoeléctrica **Junta de Castilla y León: VA293U13**
- Desarrollo de sistemas de imagen por electroluminiscencia para la inspección y mantenimiento de plantas solares **Junta de Castilla y León: VA283P18**
- Caracterización óptica de obleas y células tandem de silicio de bajo coste para aplicaciones fotovoltaicas y de conversión termoeléctrica **MINECO (Spanish Government): ENE2014-56069-C4-4-R**
- Diseño y desarrollo de un sistema de imagen por fotoluminiscencia para calificación de obleas y células solares de silicio multicristalino **Junta de Castilla y León: VA081U16**
- Caracterización Eléctrica y lumínica de sustratos y células solares para la fabricación de módulos bifaciales de silicio solar **MINECO (Spanish Government): ENE2017-89561-C4-3-R**

Contents

List of Figures

List of Tables

Chapter 0

Dime cómo se ve el mundo
con esos ojos...

Resumen en Español

Tanto el mundo macroscópico como el mundo de los átomos han sido estudiados por la física a lo largo de la historia. El primero de ellos, el mundo que podemos observar con nuestros ojos, ha despertado nuestro interés desde los inicios de la humanidad, incluso cuando la ”Física” aún no existía como la disciplina que conocemos hoy en día. Al principio, el trabajo de entender el mundo recaía sobre los filósofos, que siglos después fueron llamados ”filósofos de la naturaleza”. Ellos estudiaban el mundo que nos rodea y las leyes que lo gobiernan. En cambio, el mundo a escala atómica sólo ha sido estudiado durante poco más de un siglo. Sin embargo, en este corto periodo de tiempo, tanto la ciencia como la tecnología han avanzado a un ritmo nunca antes visto en la historia de la humanidad. Independientemente de las diferencias evidentes entre estos dos mundos se podría decir que (casi) todos los fenómenos básicos que ocurren en estas dos escalas se pueden entender desde un punto de vista físico: ya sea con la ayuda de fuerzas, energías o la termodinámica en el caso del mundo macroscópico, o bien utilizando estados propios, hamiltonianos y operadores para el mundo cuántico. El aspecto fundamental en ambos casos es que la física provee un marco de trabajo bien definido sobre el que proponer hipótesis y obtener conclusiones. Sin embargo, para bien o para mal, la naturaleza no es tan ”simple” cuando la estudiamos en un nivel intermedio entre estos dos.

El mundo ”nano” se define como aquel con al menos una dimensión en el rango entre 1 y 100 nanómetros; sin embargo, esta frontera no se debe tomar como exacta e inamovible, sino como un orden de magnitud en el que comienzan a aparecer efectos físicos nuevos. La nanociencia se encarga del estudio de aquellas situaciones en las que hay demasiados átomos para resolver los problemas utilizando directamente la mecánica cuántica, pero no hay suficientes para considerar el sistema como macroscópico. El concepto de nanocien-

cia engloba gran cantidad de campos del conocimiento como la física, química, biología, ingeniería de materiales, ciencia de superficies, etc. Asimismo, sus posibles aplicaciones son tan diversas como los campos que la componen: desde aplicaciones en dispositivos, como láseres [1], transistores [2], baterías [3] o células solares [4], pasando por sensores químicos y soluciones para la contaminación del agua y del aire [5], o aplicaciones médicas y biológicas, como administración de fármacos o tratamientos contra el cáncer [6]. La gran mayoría de estas aplicaciones no se apoyan únicamente en una de las disciplinas científicas mencionadas anteriormente, sino que necesitan de la cooperación de varias ramas distintas, lo que hace de la nanotecnología un campo de investigación enormemente interdisciplinario.

Los nanohilos semiconductores son sistemas nanométricos cuasi-unidimensionales (1D). Se caracterizan por su reducida dimensión radial, presentando diámetros que van desde unos pocos nanómetros hasta algunos cientos. Como consecuencia de su baja dimensionalidad presentan efectos de confinamiento cuando su diámetro es comparable a las longitudes características de distintos procesos físicos. Por ejemplo, cuando el diámetro de un nanohilo es menor que la longitud de onda de la radiación incidente, el confinamiento del campo electromagnético produce resonancias muy interesantes en los procesos de absorción y dispersión de la luz[7–9]. Estas resonancias se han detectado en distintos experimentos ópticos: generación de segundo armónico, dispersión Raman, extinción de luz, etc. Análogamente, se pueden observar efectos similares en muchas otras interacciones físicas, como el confinamiento de fonones cuando el diámetro del nanohilo es menor que su recorrido libre medio [10, 11]; confinamiento de excitones, observable en medidas de fotoluminiscencia en nanohilos [12], pero también en otros sistemas nanoestructurados como puntos cuánticos [13, 14] o pozos cuánticos [15]. Su baja dimensionalidad proporciona además otra ventaja: la posibilidad de crecer nanohilos sin dislocaciones ni otros defectos estructurales. Esta propiedad es especialmente interesante cuando se trabaja con heterouniones, ya que en dispositivos convencionales la diferencia de parámetros de red de los distintos materiales que componen la heterounión produce numerosos problemas durante el crecimiento epitaxial, así como una baja calidad cristalina de los materiales resultantes [16–18]. El tamaño reducido de los nanohilos permite la combinación de materiales con parámetros de red muy distintos, previniendo la formación de defectos durante el crecimiento, como pueden ser dislocaciones o defectos de apilamiento, y mejorando notablemente la calidad cristalina de los materiales apilados [19, 20].

Entre el elevado número de semiconductores que existen podemos encontrar dos grupos que atraen la mayor parte de la atención: los semiconductores del grupo IV y los semiconductores de tipo III-V. Entre los semiconductores del grupo IV encontramos el silicio, el germanio y sus aleaciones, todos ellos compatibles con la tecnología CMOS (semiconductor complementario de óxido metálico). Su producción y propiedades han sido ampliamente estudiadas, y ambos presentan bajos valores del gap, lo que les hace

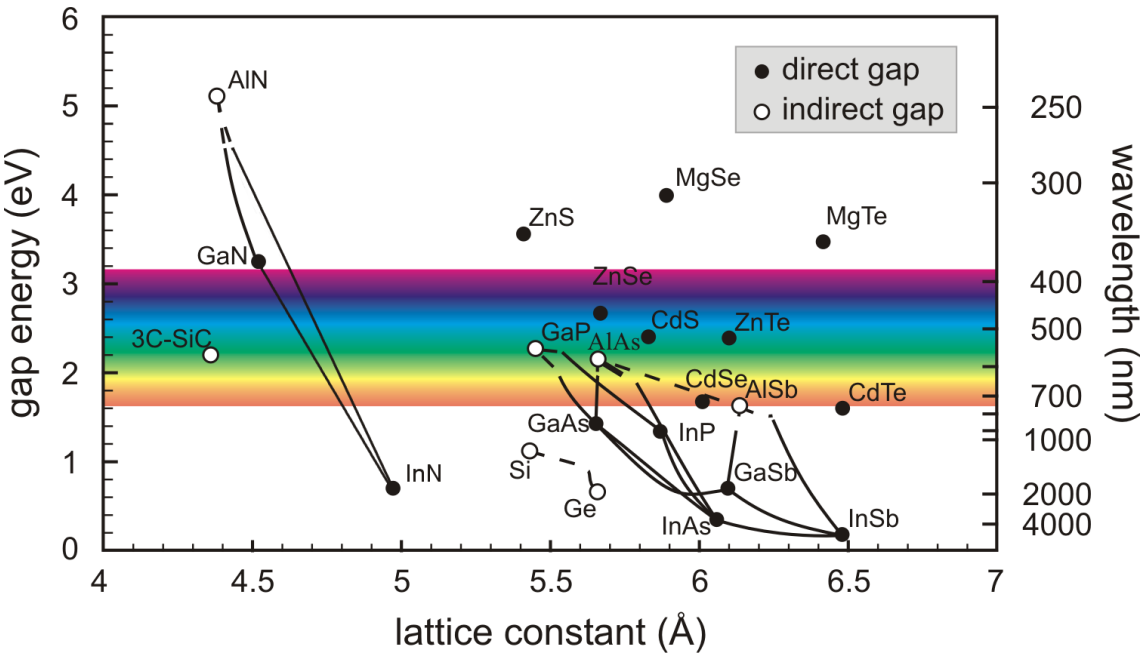

Figura 0.1: Resumen de los valores del gap de los semiconductores más importantes en función de su parámetro de red, así como la naturaleza del gap (directo/indirecto).

especialmente interesantes para aplicaciones fotovoltaicas. Su principal desventaja es la baja movilidad de los portadores y la ausencia de gap directo, lo que impide su utilización en dispositivos emisores de luz. Los semiconductores del grupo III-V, como GaAs, InAs, InP, InGaAs, etc, presentan en general movilidades de portadores mucho más altas que los del grupo IV. Típicamente presentan gap directo y en muchos casos la energía del gap se encuentra en el espectro visible o el infrarrojo cercano. Esto hace que sean una opción común para el desarrollo de emisores de luz como LEDs o láseres, también células solares de alta eficiencia y gran variedad de dispositivos opto-electrónicos. Otra ventaja de los semiconductores de este grupo es la posibilidad de fabricar compuestos ternarios y cuaternarios, como por ejemplo $In_xGa_{(1-x)}As$ o $Al_xGa_yIn_{(1-x-y)}P$, cuyas propiedades, como el gap o el índice de refracción, se pueden variar de manera continua en función de la composición [21]. La figura 0.1 muestra los valores del gap, así como su naturaleza (directo/indirecto), de los semiconductores más estudiados en función de su parámetro de red.

La diferencia principal entre estos dos grupos de semiconductores es su diferente naturaleza polar: los semiconductores del grupo IV no son polares, mientras que los del grupo III-V si lo son. Como consecuencia, materiales que correspondan a diferentes grupos serán completamente inmiscibles lo que hace especialmente complicado fabricar heteroestructuras mixtas. Sin embargo, cuando este tipo de heteroestructuras se fabrican a lo

largo de un nanohilo la diferencia de parámetros de red se acomoda elásticamente como resultado de la alta relación superficie/volumen. Esto hace que los defectos que aparecerían en la misma heteroestructura en un material volúmico se vean ampliamente reducidos en los nanohilos. De este modo, es posible sintetizar más fácilmente heteroestructuras ïmposibles" entre estos dos tipos de materiales, permitiendo combinar las ventajas de ambos en un sólo dispositivo.

El primer paso para entender y controlar las propiedades de los nanohilos es su caracterización. Inicialmente, el proceso de caracterización se realizaba sobre grupos de nanohilos. La razón principal para utilizar esta metodología es la disposición de los nanohilos después de su crecimiento. Estos se suelen encontrar depositados sobre el sustrato de crecimiento en una densidad relativamente alta, muchas veces formando madejas o ramilletes. De esta manera, cualquier método de medida macroscópico (y de hecho la mayoría de los microscópicos) analizarán simultáneamente un gran número de nanohilos. La ventaja de este enfoque es la gran cantidad de materia analizada en una sola medida, obteniendo mejores señales de medida. Sin embargo, la principal desventaja es que cualquier magnitud física medida será un promedio de las medidas sobre ese conjunto de nanohilos, y uno de los distintivos de las nanoestructuras es la dependencia de sus propiedades con el tamaño.

En el caso de la caracterización de las propiedades ópticas esto adquiere especial relevancia. Como se ha mencionado anteriormente, la respuesta de los nanohilos a la luz coherente depende críticamente de la relación entre la longitud de onda de la luz y el diámetro del nanohilo. La presencia de nanohilos con distintos diámetros en la misma medida hace que se detecte una gran variedad de respuestas distintas simultáneamente, haciendo imposible determinar la dependencia exacta de la magnitud medida con las propiedades de cada nanohilo. La medición sobre nanohilos aislados permite controlar cuidadosamente las características de cada nanohilo estudiado. De esta manera, es posible establecer una relación entre la respuesta del nanohilo y sus propiedad específicas (composición, diámetro, longitud, estructura, etc). La principal desventaja del estudio de nanohilos individuales es el pequeño volumen de muestra disponible, lo que resulta, a priori, en bajas intensidades de medida. Como se verá a lo largo de esta tesis, las resonancias de los nanohilos semiconductores permiten obtener señales de medida suficientes para su estudio individualizado.

Como ejemplo de la reducida cantidad de material con la que se trabaja supongamos un nanohilo de 100 nm de diámetro iluminado por un haz láser de 1 µm. El volumen de material iluminado será aproximadamente $V = L\pi r^2 = 1000\pi 50^2\ nm^3 \simeq 8\times10^6\,\mathrm{nm}^3 = 8\times10^{-15}\,\mathrm{cm}^3$. Si consideramos la densidad del Si $\rho = 2.33\,\mathrm{g\,cm}^{-3}$ obtenemos una masa del orden de 18 pg, una cantidad de materia extraordinariamente pequeña.

0.1 Aplicaciones

Todas las propiedades únicas de los nanohilos semiconductores los convierten en candidatos muy prometedores para ser los componentes fundamentales de los nanodispositivos del futuro. Sus aplicaciones comprenden gran variedad de dispositivos opto-electrónicos como células solares, sensores, transistores, emisores de luz o células termoeléctricas. Todas estas aplicaciones tienen un denominador común: la necesidad de trabajar con heterouniones de distintos materiales.

Células Solares

Los nanohilos semiconductores han sido estudiados extensivamente por sus interesantes aplicaciones en células fotovoltaicas [22–25]. En concreto, los nanohilos semiconductores del grupo III-V han despertado mucho interés en los últimos años, como nanohilos de GaAs [26], InAs [27], o InP [28], con los que se han conseguido células solares con eficiencias de hasta el 13.8 %. Por otra parte, las células solares basadas en nanohilos de Si son sumamente interesantes, principalmente por su compatibilidad con la actual tecnología CMOS y, como consecuencia, la relativa facilidad para su integración en microchips [4, 29].

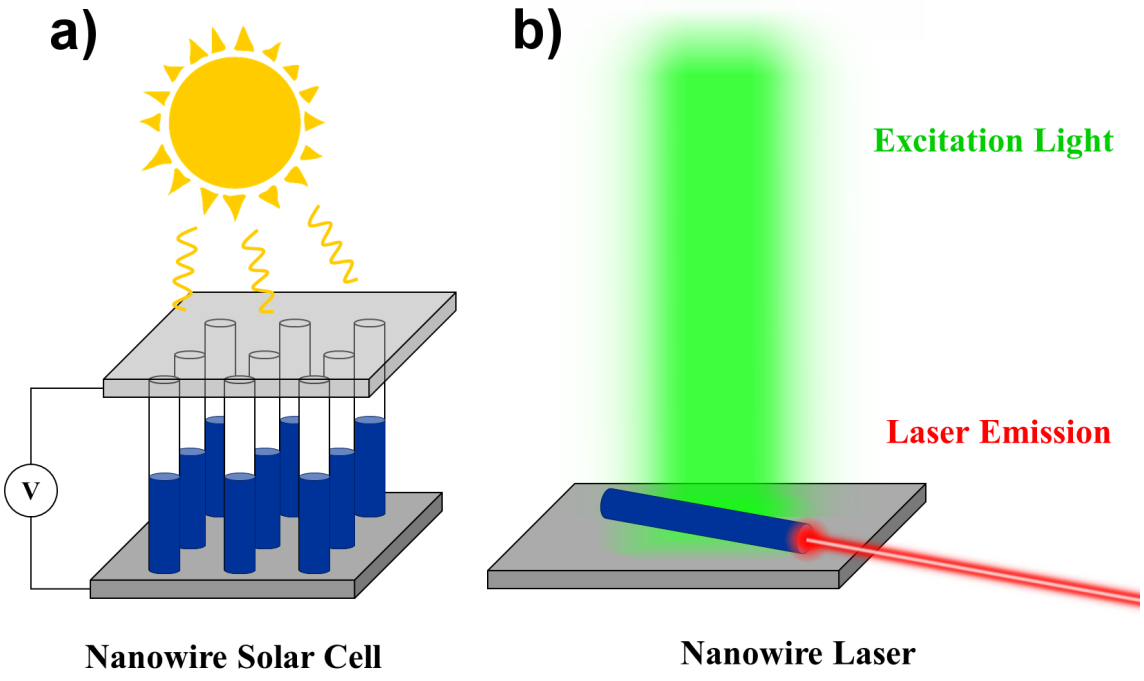

Figura 0.2: Ejemplos de aplicaciones de nanohilos. a) Esquema de una célula solar basada en nanohilos con unión axial. b) Esquema de un láser basado en nanohilos. El nanohilo actúa como una cavidad resonante produciendo luz coherente al ser bombeado con una fuente externa.

Transistores

Los transistores de efecto de campo basados en nanohilos (NWFETs) son una opción muy prometedora para abordar el proceso de escalado de los dispositivos basados en la tecnología CMOS. El principal problema a la hora de escalar un transistor es la reducción de las dimensiones del canal. En un NWFET el canal es reemplazado por un nanohilo semiconductor, obteniendo así sus ventajas: la posibilidad de controlar cuidadosamente las dimensiones (diámetro), la reproducibilidad y la alta calidad cristalina tanto del nanohilo como de su superficie. Se han proporcionado distintos enfoques a este tipo de dispositivos en la literatura [2, 30, 31], basándose tanto en nanohilos homogéneos como heteroestructurados.

Emisores de Luz

Los nanohilos semiconductores también se pueden utilizar como fuentes de luz, por ejemplo láseres o LEDs [32–36], pero también en dispositivos más complejos como fuentes emisoras de un solo fotón [37]. De cara a las aplicaciones láser resultan más interesantes los nanohilos del grupo III-V ya que presentan gap directo, así como mayores movilidades de portadores, como ya se ha mencionado. Por otra parte, la posibilidad de fabricar heterouniones así como poder controlar el dopado de los materiales facilita el control del gap y, por tanto, las propiedades de emisión de luz del dispositivo final. Al mismo tiempo, la dimensión reducida de los nanohilos hace que se comporten como guías de ondas (incluso para diámetros menores que la longitud de onda de la luz), permitiendo confinar y transportar la luz generada en su interior de acuerdo con las necesidades del dispositivo final.

Generadores Termoeléctricos

Las células de conversión termoeléctrica aprovechan el efecto Seebeck para obtener energía eléctrica a partir de un gradiente de temperatura. Su eficiencia depende de la *figura de mérito termoeléctrica*: $ZT = S^2T/\rho\kappa$, donde S es el coeficiente Seebeck del material, T es la temperatura, ρ la resistividad eléctrica y κ la conductividad térmica. Maximizar ZT significa en la práctica optimizar la eficiencia del dispositivo final. Para hacer esto ρ y κ deben ser lo más pequeñas posible de manera simultánea. En materiales volúmicos, las conductividades eléctrica y térmica están relacionadas, por tanto cuando se intenta reducir κ, ρ aumenta, y viceversa. En cambio, los nanohilos semiconductores permiten desacoplar las contribuciones de electrones y fonones en las conductividades, de esta manera, la conductividad térmica se puede reducir cambiando las condiciones de dispersión de los fonones sin modificar significativamente las propiedades eléctricas del material [38–41]. Esta estrategia permite sobrepasar las limitaciones de los materiales volúmicos en cuanto a conversión termoeléctrica.

Sensores

Los nanohilos semiconductores también se utilizan como sensores de luz [42, 43] y sensores químicos [44, 45]. El fenómeno físico utilizado en ambos casos es similar: en los sensores químicos debido a la interacción de ciertas moléculas con la superficie del nanohilo se modifican sus propiedades electrónicas y por tanto cambiará la corriente que lo atraviesa al aplicar un voltaje; en los sensores de luz es la radiación de una cierta longitud de onda la que cambia las propiedades del nanohilo. Como consecuencia, la detección tanto química como luminosa se realiza a través de la diferencia en la conductividad del nanohilo cuando estos factores están o no presentes. Se ha demostrado experimentalmente que este tipo de medidas pueden ser muy sensibles en las condiciones apropiadas.

0.2 Contexto de la Tesis

Esta tesis se ha desarrollado en el Grupo de Semiconductores (GdS) Optronlab del Departamento de Física de la Materia Condensada de la Universidad de Valladolid. El grupo Optronlab se centra en la caracterización de las propiedades ópticas y electrónicas de materiales semiconductores. El grupo tiene 3 ramas de investigación principales: Caracterización de Semiconductores Nanoestructurados, Transporte Térmico en Nanoescala y Caracterización de Materiales Fotovoltaicos. Este trabajo se enmarca en la primera rama, Caracterización de Semiconductores Nanoestructurados, ya que se centra en la investigación de sistemas nanoestructurados como son los nanohilos. En trabajos anteriores el grupo ha estudiado las propiedades térmicas de nanohilos de Si y SiGe, utilizando Espectroscopía μ-Raman y simulaciones de elementos finitos [46]. Esta tesis extiende esta metodología en la que se combinan medidas experimentales con simulaciones para estudiar las propiedades ópticas de nanohilos semiconductores con heterouniones axiales. Paralelamente se ha trabajado también en la segunda rama, Transporte Térmico en Nanoescala. La metodología desarrollada para el estudio del campo electromagnético en nanohilos se ha aplicado a la estructura de pozo cuántico en láseres de diodo de alta potencia. Esto permite estudiar tanto la generación y propagación de puntos locales de calentamiento en estos dispositivos, como el efecto de estos puntos sobre el campo electromagnético del propio láser y su eventual degradación.

0.3 Objetivos

Como ya se ha mencionado las heteroestructuras son elementos básicos de la mayoría de los dispositivos. El objetivo de esta tesis es estudiar las propiedades ópticas de nanohilos con heteroestructuras axiales, y, al mismo tiempo, proporcionar un marco teórico desde el que entender mejor la interacción luz-materia en este tipo de sistemas. Para alcanzar este objetivo el problema se abordará desde dos puntos de vista que se complementan mutuamente: medidas experimentales de la respuesta óptica de nanohilos con heterouniones axiales, y, simultáneamente, simulaciones teóricas de la interacción luz-nanohilo que reproduzcan los resultados experimentales.

El **análisis experimental** se centrará en la dispersión μ-Raman. Los nanohilos se analizan de manera individual registrando los espectros Raman en distintas condiciones de iluminación. Como se explicará más adelante, la espectroscopía Raman es extremadamente sensible a la estructura de los materiales (composición, dopado, presencia de defectos, etc). Esto permite detectar señales claramente distinguibles de los diferentes materiales que componen el nanohilo heteroestructurado. Asimismo, la señal Raman es proporcional a la intensidad de la luz incidente (i.e. $|E|^2$), por lo tanto, los espectros Raman nos proporcionarán información sobre la intensidad del campo electromagnético en los diferentes materiales del nanohilo, lo que equivale a una medida indirecta de la distribución del campo electromagnético tanto en el interior del nanohilo como en sus alrededores.

El **análisis teórico** se llevará a cabo resolviendo las ecuaciones de Maxwell para el sistema formado por el haz láser, el nanohilo y su entorno. Para ello, las ecuaciones de Maxwell se resuelven de forma numérica por el método de elementos finitos. El análisis del campo electromagnético resultante nos proporciona el marco teórico que buscamos para entender la interacción entre el nanohilo y el campo electromagnético incidente, y al mismo tiempo comprender los nuevos efectos que aparecen en los sistemas nanoestructurados.

0.4 Estructura de la Tesis

Esta tesis se ha escrito como un compendio de publicaciones. Los resultados obtenidos se encuentran publicados en siete artículos científicos recogidos en la Tabla 0.1 de la siguiente sección. Asimismo, esta tesis cumple los requisitos para ser acreditada con **Mención Internacional**.

La tesis está organizada en 8 Capítulos y un apéndice. Los Capítulos 1 a 3 contienen la información básica para entender los resultados presentados.

Capítulo 1 - Introducción. El primer capítulo comienza con un resumen general del tema principal de la tesis. Se explican la relevancia y aplicaciones de los nanohilos semiconductores, la importancia de las heterouniones y su estudio, así como los objetivos y la metodología de la tesis.

Capítulo 2 - Estado del Arte. El segundo capítulo se dedica al Estado del Arte. Se centra en la teoría de la dispersión μ-Raman y su uso como herramienta para la medida local del campo electromagnético. En este capítulo también se presentan las ecuaciones de Maxwell y su solución a través del método de elementos finitos y la transformada de Fourier como herramienta clave para el estudio del campo electromagnético inducido en el interior de los nanohilos.

Capítulo 3 - Métodos Experimentales y Preparación de las Muestras. En este capítulo se hace hincapié en la metodología de preparación de las muestras y realización de las medidas Raman. Por otra parte, se proporcionan y analizan los espectros Raman de referencia de todos los materiales estudiados.

Los Capítulos 4 a 7 contienen los resultados principales de la tesis. Cada uno de ellos se centra en temas independientes exceptuando el capítulo 7, en el que se ahonda en el estudio de la interacción electromagnética de cara a entender mejor los resultados de los capítulos 4 y 6.

Capítulo 4 - Nanohilos heteroestructurados de Si/SiGe. En el Capítulo 4 se presenta la mayoría de los resultados de la tesis. El capítulo está dedicado al estudio de nanohilos con heterouniones axiales de Si/SiGe. El efecto de amplificación de la señal Raman se descubrió por primera vez en estos nanohilos, por este motivo han sido extensivamente estudiados. En este capítulo se correlaciona la amplificación detectada experimentalmente con los resultados de las simulaciones de elementos finitos.

Capítulo 5 - Nanohilos heteroestructurados de Si/III-V. El objetivo principal de este capítulo es verificar que el efecto de amplificación del campo electromagnético no es propio del material del nanohilo, sino que es consecuencia directa de la discontinuidad que tiene lugar en la heterounión. Como resultado de la inmiscibilidad del Si (no polar) con los materiales del grupo III-V (polares) la heterounión entre estos materiales es totalmente abrupta a nivel atómico, y, en este caso, no hay un volumen asociado a la heterounión. A pesar de las diferencias entre estos nanohilos y los del grupo IV se detecta un efecto de

amplificación análogo en el material cercano a la heterounión. Esto respalda la explicación de la amplificación y localización del campo electromagnético como consecuencia de la heterounión.

Capítulo 6 - Modelo de Crecimiento de Nanohilos Heteroestructurados. En este capítulo se analizan los modelos de crecimiento de nanohilos. En primer lugar se presentan los métodos y modelos existentes. A continuación se presenta un nuevo modelo para el crecimiento de nanohilos de SiGe y un estudio de su repercusión en la fabricación de heterouniones axiales de Si/SiGe. Este modelo permite controlar la composición de crecimiento de los nanohilos y la extensión de las transiciones entre distintos materiales modificando parámetros de crecimiento como la temperatura o las presiones parciales de los gases precursores.

Capítulo 7 - Estudio teórico del efecto de amplificación electromagnética. El objetivo de este capítulo es profundizar en el estudio de la interacción luz-nanohilo heteroestructurado. Las distribuciones del campo electromagnético estudiadas en capítulos anteriores se analizan utilizando la Transformada de Fourier. Esta herramienta matemática permite determinar el efecto de la heterounión sobre el campo electromagnético y su repercusión en el aumento de la señal Raman.

Capítulo 8 - Conclusiones. El último capítulo contiene una recapitulación de los resultados obtenidos y una evaluación del grado de consecución de los objetivos iniciales. Finalmente se proponen unas perspectivas de trabajo futuro de cara a continuar el estudio de los nanohilos heteroestructurados.

Apéndice A - Degradación Óptica Catastrófica de láseres de diodo de alta potencia. Este apéndice es un compendio del trabajo desarrollado sobre la Degradación Óptica Catastrófica (COD) de láseres de diodo de alta potencia. Aunque no es el tema principal de la tesis, el modelo desarrollado para el estudio de la interacción luz/nanohilo se ha utilizado para el estudio de la distribución de la radiación electromagnética en el interior de estos láseres. Es importante notar que la idea subyacente en ambos casos es esencialmente la misma. Los láseres de diodo son también sistemas heteroestructurados en los que la zona activa, el pozo cuántico, es un material bidimensional. Como consecuencia, la interacción luz/pozo cuántico tiene lugar en una heteroestructura en condiciones de confinamiento, lo que lleva a un comportamiento no trivial del campo electromagnético. El apéndice se centra en estudiar el efecto que tiene una pequeña región degradada sobre la distribución de la luz láser en el pozo cuántico y su posible repercusión en la degradación del dispositivo.

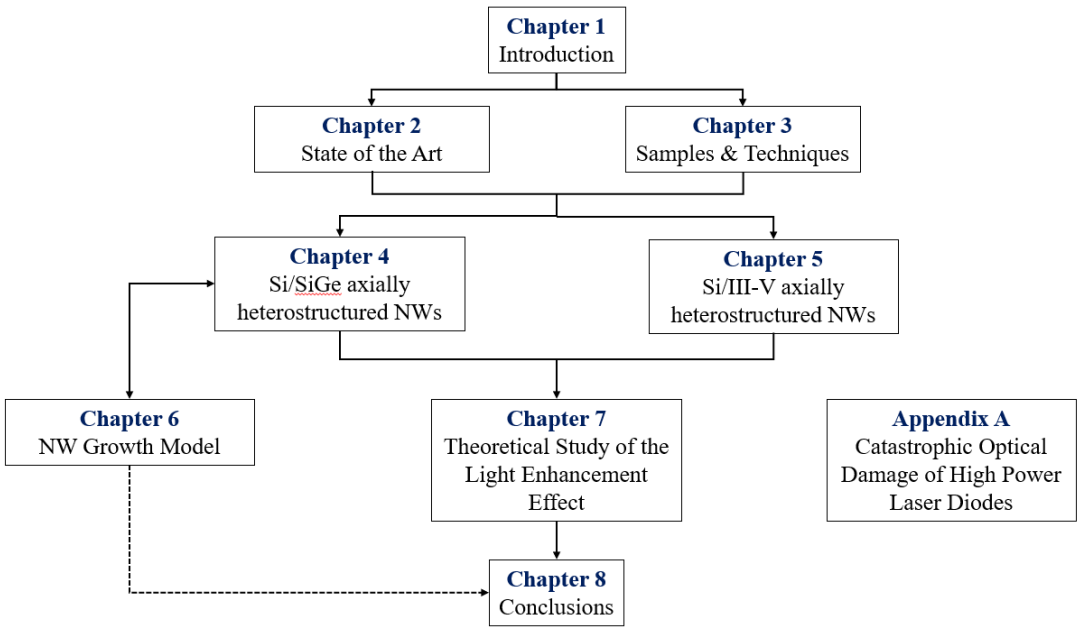

Figura 0.3: Diagrama con la distribución de capítulos de esta tesis.

0.5 Conclusiones

A lo largo de esta tesis se han estudiado las propiedades ópticas de nanohilos con heterouniones axiales. Para ello se ha utilizado la espectroscopía μ-Raman, que permite realizar medidas indirectas del campo electromagnético inducido en este tipo de nanohilos.

En el **capítulo 4** se estudian nanohilos basados en Si y SiGe. Las medidas Raman demuestran la presencia de una amplificación de la señal Raman cuando se ilumina la región de la heterounión. Paralelamente se ha diseñado un modelo que resuelve las ecuaciones de Maxwell por el método de elementos finitos (FEM), de esta manera se puede calcular el espectro Raman esperado de estos nanohilos. Las simulaciones muestran una concentración y un aumento del campo electromagnético cuando la heterounión es iluminada, en excelente correlación con las medidas experimentales y el efecto de amplificación Raman.

En el **capítulo 5** se ha repetido el estudio utilizando nanohilos con heterouniones axiales de Si/III-V. El objetivo es detectar una amplificación de la señal Raman similar a la de los nanohilos de Si/SiGe en la zona de la heterounión. De los tres tipos de semiconductores III-V estudiados se detectó el efecto en dos de ellos: InAs e InGaAs, demostrando que el efecto de amplificación en la heterounión no se debe al material concreto del que están formado los nanohilos, sino que está causado por el cambio de las propiedades ópticas que

tiene lugar en la heterounión. Los últimos nanohilosestudiados, con GaAs, no mostraban segmentos completos de GaAs por lo que no se pudo detectar dicho efecto.

El **capítulo 6** contiene un análisis del crecimiento de nanohilos de SiGe/Si con heterouniones axiales. En el capítulo 4 se había observado cómo la anchura de la heterounión es muy importante de cara al efecto de amplificación y cómo los resultados experimentales no concuerdan con los modelos existentes. Por ello se ha desarrollado un nuevo modelo que permite estimar el crecimiento de las heterouniones y sus características. Esto permite estudiar la extensión axial de las distintas heterouniones, dependiendo de las condiciones de crecimiento, así como calcular los resultados esperados antes de realizar un proceso de crecimiento. Este análisis ha permitido establecer un mapa de composición con el que se puede calcular la concentración de Ge de la fase sólida una vez conocida las concentraciones de Si y Ge en el catalizador metálico. El análisis muestra un buen acuerdo con las medidas realizadas en el capítulo 4 así como con otros trabajos experimentales.

Finalmente, en el **capítulo 7** se presenta un estudio más detallado del campo electromagnético inducido en los nanohilos heteroestructurados de cara a entender el efecto de amplificación observado. Se ha utilizado la transformada de Fourier para obtener las componentes principales del campo electromagnético inducido en nanohilos homogéneos de Si y heteroestructurados de SiGe/Si. Este estudio muestra la aparición de una nueva componente del campo electromagnético en los nanohilos heteroestructurados que no está presente en los nanohilos homogéneos. Esta componente da cuenta del papel de la heterounión, cuyo efecto es el aumento de la intensidad del campo de excitación en la región de la heterounión.

Como resumen, el estudio de la interacción de la luz con nanohilos con heterouniones axiales nos ha permitido entender mejor este tipo de interacciones complejas. Comprender y controlar estos efectos de amplificación es el primer paso para la aplicación de nanohilos heteroestructurados en nanodispositivos optoelectrónicos de nueva generación.

0.6 Publicaciones, Congresos, Estancias y Participación en Proyectos

	Referencia	Capítulo
1	J. L. Pura, J. Anaya, J. Souto, A. C. Prieto, A. Rodríguez, T. Rodríguez and J. Jiménez. Local electric field enhancement at the heterojunction of Si/SiGe axially heterostructured nanowires under laser illumination. *Nanotechnology* **27**, 455709 (7pp), 2016	4
2	J. L. Pura, J. Anaya, J. Souto, A. C. Prieto, A. Rodríguez, T. Rodríguez, P. Periwal, T. Baron and J. Jiménez. Electromagnetic field enhancement effects in group IV semiconductor nanowires. A Raman spectroscopy approach. *J. Appl. Phys.* **123**, 114302, 2018	4
3	J. L. Pura, J. Souto, P. Periwal, T. Baron and J. Jiménez. Electromagnetic Field Enhancement on Axially Heterostructured NWs: The Role of the Heterojunctions. *J. Electron. Mater.* 2018	4
4	J. L. Pura, J. Anaya and J. Jiménez. About the Interaction Between a Laser Beam and Group IV Nanowires: A Study of the Electromagnetic Field Enhancement in Homogeneous and Heterostructured Nanowires. *Phys. Status Solidi A* **215**, 1800336, 2018	4
5	J. L. Pura, P. Periwal, T. Baron and J. Jiménez. Growth dynamics of SiGe nanowires by the vapour-liquid-solid method and its impact on SiGe/Si axial heterojunction abruptness. *Nanotechnology* **29**, 355602 (9pp), 2018	6
6	J. L. Pura, A. J. Magdaleno, D. Muñoz-Segovia, M. Glaser, A. Lugstein and J. Jiménez. Electromagnetic enhancement effect on the atomically abrupt heterojunction of Si/InAs heterostructured nanowires. *J. Appl. Phys.* **125**, 064303, 2019	5
7	J. L. Pura, J. Jiménez. Fourier Transform Study of the Complex Electric Field Induced on Axially Heterostructured NWs. *Submitted*	7

Tabla 0.1: Recopilación de los artículos incluidos en la tesis

	Referencia
1	J.Souto, J.L.Pura, M.Rodríguez, J.Anaya, A.Torres, J.Jiménez. Mechanisms driving the catastrophic optical damage in high power laser diodes. *Proc. of SPIE* **9348**, 93480O (7pp), 2015
2	J.Souto, J.L.Pura, A.Torres, J.Jiménez, M. Bettiati, F.J. Laruelle. Sequential Description of the Catastrophic Optical Damage of High Power Laser Diodes. *Proc. of SPIE* **9733**, 973306 (6pp), 2016
3	J.Souto, J.L.Pura, J.Jiménez. About the physical meaning of the critical temperature for catastrophic optical damage in high power laser diodes. *Laser Phys. Lett.* **13**, 025005 (6pp), 2016
4	J.Souto, J.L.Pura, J.Jiménez. Catastrophic optical damage of high power InGaAs/AlGaAs laser diodes. *Microelectron. Reliab.* **64**, 627-630, 2016
5	J. Souto, J.L.Pura, A. Torres, J.Jiménez. Thermomechanical degradation of single and multiple quantum well AlGaAs/GaAs laser diodes. *Microelectron. Reliab.* **76-77**, 588591, 2017
6	J.Souto, J.L.Pura, A.Torres, J.Jiménez. About the impact of the materials properties in the catastrophic degradation of high power GaAs based laser diodes. *Proc. of SPIE* **10086**, 100860P (6pp), 2017
7	J.Souto, J.L.Pura, J.Jiménez. Nanoscale effects on the thermal and mechanical properties of AlGaAs/GaAs quantum well laser diodes: influence on the catastrophic optical damage. *J. Phys. D: Appl. Phys.* **50**, 235101, 2017
8	J.Souto, J.L.Pura, J.Jiménez. Thermal and mechanical issues of high-power laser diode degradation. *MRS Commun.* **8 (3)**, 995-999, 2018
9	J.Souto, J.L.Pura, J.Jiménez. Thermomechanical Issues of High Power Laser Diode Catastrophic Optical Degradation. *J. Phys. D: Appl. Phys.*, **52** 343002, 2019 (Topical Review)
10	J. Souto, J. L. Pura, A. Torres, and J. Jimenéz. A comparative analysis of the catastrophic degradation of AlGaAs/GaAs and AlGaAs/InGaAs laser diodes: role of the strained QWs. *Proc. SPIE* **10900** , 2019
11	J. Martín-de León, J. L. Pura, V. Bernardo, M. Á. Rodríguez-Pérez. Transparent nanocellular PMMA: Characterization and modeling of the optical properties. *Polymer* **170**, 16-23 , 2019

Tabla 0.2: Recopilación de los artículos escritos durante la tesis que no están relacionados con el tema principal.

	Congreso	Contribución
1	J.L.Pura, J.Jiménez. Thermal Transport in Nanostructures. *XVI Escuela Nacional de Materiales Moleculares* Santa Pola (Spain), February 1-6 2015	Oral
2	J.L.Pura, J.Jiménez. Enhanced Raman Scattering in Semiconductor Nanowires. *VIII European School on Molecular Nanoscience* Paris (France) October 25-29 2015	Oral
3	J.L.Pura, J.Jiménez. Enhanced Raman Signal at the Heterojunction Region of Si/SiGe Axially Heterostructured Nanowires. *EXMATEC 2016* Aveiro (Portugal) June 6-10 2016	Oral
4	J.L.Pura, J.Anaya, J.Souto, A.C.Prieto, A.Rodríguez, T.Rodríguez, T.Baron, J.Jiménez. Enhanced Raman signal at the heterojunction region of SiGe/Si axially heterostructured nanowires. *MRS Fall Meeting & Exhibit 2016* Boston (USA) November 27 - December 2 2016	Oral
5	J.L.Pura, J.Jiménez. Raman Enhancement on Si/SiGe Axially Heterostructured NWs. *SENM 2017* June 26-29 2017	Oral
6	J. L. Pura, J. Souto, P. Periwal, T. Baron, J. Jiménez. Electromagnetic Field Enhancement on axially heterostructured NWs: the role of the heterojunctions. *DRIP 2017* Valladolid (Spain) October 8 - 12 2017	Oral
7	J. L. Pura, M. Glaser, A. J. Magdaleno, A. C. Prieto, S. Rodríguez-Conde, A. Lugstein, J. Jiménez. Local electromagnetic field enhancement on Si/InAs axially heterostructured NWs. *DRIP 2017* Valladolid (Spain) October 8 - 12 2017	Poster
8	J. L. Pura, P. Periwal, T. Baron, J. Jiménez. Light absorption in axially heterostructured semiconductor NWs. *MRS Fall Meeting & Exhibit 2017* Boston (USA) November 26 - December 1 2017	Poster

Tabla 0.3: Recopilación de las contribuciones en congresos directamente relacionadas con la tesis.

	Congreso	Contribución
1	J.Souto, J.L.Pura, M.Rodríguez, J.Anaya, A.Torres, J. Jiménez. Mechanisms driving the catastrophic optical damage in high power laser diodes. *Photonic West 2015* San Francisco (USA), February 7-12 2015	Oral
2	J.Souto, J.L.Pura, A.Torres, J. Jiménez, M..Bettiati, F.J. Laruelle. Sequential Description of the Catastrophic Optical Damage of High Power Laser Diodes. *Photonic West 2016* San Francisco (USA), January 28 - February 2 2016	Oral
3	J.Souto, J.L.Pura, A.Torres, J.Jiménez. Role of the Mechanical Strength of Quantum Wells in the Catastrophic Optical Damage of High Power Laser Diodes. *ESREF 2016* Halle (Germany) September 19-22 2016	Oral
4	J.Souto, J.L.Pura, A. Torres, J.Jiménez. About the impact of the materials properties in the catastrophic degradation of high power GaAs based laser diodes. *Photonic West 2017* San Francisco (USA) January 28 - February 2 2017	Oral
5	J. Souto, J. L. Pura, A. Torres, J. Jiménez. Thermomechanical model for the degradation of AlGaAs and InGaAs laser diodes: correlation with cathodoluminescence measurements. *DRIP 2017* Valladolid (Spain) October 8 - 12 2017	Poster
6	J.Souto, J.L.Pura, J.Jiménez. Materials issues for the catastrophic degradation of high power laser diodes. (Invited Talk) *2017 IEEE High Power Diode Lasers & Systems Conference* Coventry (UK) October 12 - 13 2017	Oral
7	J.Souto, J.L.Pura, J.Jiménez. Thermal and Mechanical Issues of High Power Laser Diode Degradation. (Invited Talk) *MRS Spring Meeting & Exhibit 2018* Phoenix (USA) April 2 - 6 2018	Oral
8	J. L. Pura. High School Excellence Projects: A Way to Introduce High School Students to University Research. *Edulearn 2018* Palma de Mallorca (Spain) July 2 - 4 2018	Virtual P.
9	J.Souto, J.L.Pura, A. Torres, J.Jiménez. A comparative analysis of the catastrophic degradation of AlGaAs/GaAs and AlGaAs/InGaAs laser diodes: role of the strained QWs. *Photonic West 2019* San Francisco (USA) February 2 - 7 2019	Oral

Tabla 0.4: Recopilación de otras presentaciones en congresos durante la tesis.

Estancias en Centros de Investigación
Un mes en el departamento de Física Aplicada de la Universidad de Málaga (España), Junio 2017
Tema: Elaboración de contactos de Pt en nanohilos heteroestructurados de Si/SiGe y Si/InAs para su caracterización eléctrica y electro-óptica
Tres meses en el Cambridge Graphene Centre de la Universidad de Cambridge (UK), Septeembre - Noviembre 2018
Tema: Estudio de las propiedades ópticas de nanohilos heteroestructurados depositados sobre grafeno & Exfoliación y Caracterización de capas delgadas de GeSe

Tabla 0.5: Estancias en otros centros de investigación.

	Participación en Proyectos
1	Nanohilos semiconductores para aplicaciones fotovoltaicas y de conversión termoeléctrica **Junta de Castilla y León: VA293U13**
2	Desarrollo de sistemas de imagen por electroluminiscencia para la inspección y mantenimiento de plantas solares **Junta de Castilla y León: VA283P18**
3	Caracterización óptica de obleas y células tandem de silicio de bajo coste para aplicaciones fotovoltaicas y de conversión termoeléctrica **MINECO (Spanish Government): ENE2014-56069-C4-4-R**
4	Diseño y desarrollo de un sistema de imagen por fotoluminiscencia para calificación de obleas y células solares de silicio multicristalino **Junta de Castilla y León: VA081U16**
5	Caracterización Eléctrica y lumínica de sustratos y células solares para la fabricación de módulos bifaciales de silicio solar **MINECO (Spanish Government): ENE2017-89561-C4-3-R**

Tabla 0.6: Participación en proyectos de investigación durante la tesis.

Bibliografía

[1] A. B. Greytak, C. J. Barrelet, Y. Li, C. M. Lieber. Semiconductor nanowire laser and nanowire waveguide electro-optic modulators. *Applied Physics Letters*, **87** (15), 1–3 (2005). doi:10.1063/1.2089157

[2] W. Lu, P. Xie, C. M. Lieber. Nanowire transistor performance limits and applications. *IEEE Transactions on Electron Devices*, **55** (11), 2859–2876 (2008). doi:10.1109/TED.2008.2005158

[3] C. K. Chan, H. Peng, G. Liu, K. McIlwrath, X. F. Zhang, R. A. Huggins, Y. Cui. High-performance lithium battery anodes using silicon nanowires. *Nature Nanotechnology*, **3** (1), 31–35 (2007). doi:10.1038/nnano.2007.411

[4] B. Tian, X. Zheng, T. J. Kempa, Y. Fang, N. Yu, G. Yu, J. Huang, C. M. Lieber. Coaxial silicon nanowires as solar cells and nanoelectronic power sources. *Nature*, **449** (18), 885–889 (2007). doi:10.1038/nature06181

[5] X. Qu, P. J. J. Alvarez, Q. Li. Applications of nanotechnology in water and wastewater treatment. *Water Research*, **47** (12), 3931–3946 (2013). doi:10.1016/j.watres.2012.09.058

[6] M. Ferrari. Cancer nanotechnology: Opportunities and challenges. *Nature Reviews Cancer*, **5** (3), 161–171 (2005). doi:10.1038/nrc1566

[7] R. Rurali. Colloquium: Structural, electronic, and transport properties of silicon nanowires. *Reviews of Modern Physics*, **82** (1), 427–449 (2010). doi:10.1103/RevModPhys.82.427

[8] H. Kallel, A. Arbouet, G. Benassayag, A. Chehaidar, A. Potié, B. Salem, T. Baron, V. Paillard. Tunable enhancement of light absorption and scattering in Si 1-xGe x nanowires. *Physical Review B - Condensed Matter and Materials Physics*, **86** (8) (2012). doi:10.1103/PhysRevB.86.085318

[9] L. Cao, J. S. Park, P. Fan, B. Clemens, M. L. Brongersma. Resonant germanium nanoantenna photodetectors. *Nano Letters*, **10** (4), 1229–1233 (2010). doi:10.1021/nl9037278

[10] Z. V. Popovic, M. Cardona. Phonons in GaAs/AlAs superlattices grown along the [111] direction. *Physical Review B*, **41** (9), 5904–5913 (1990)

[11] K. W. Adu, H. R. Gutiérrez, U. J. Kim, G. U. Sumanasekera, P. C. Eklund. Confined Phonons in Si Nanowires. *Nano Letters*, **5** (3), 409–414 (2005). doi:10.1021/nl0486259

[12] R. Rinaldi, R. Cingolani, M. Lepore, M. Ferrara, I. M. Catalano, F. Rossi, L. Rota, E. Molinari, P. Lugli, U. Marti, D. Martin, F. Morier-Gemoud, P. Ruterana, F. K. Reinhart. Exciton Binding Energy in GaAs V-Shaped Quantum Wires. *Phys. Rev. Lett.*, **73** (21), 2899–2902 (1994)

[13] E. J. H. Lee, J. A. Varela, C. Ribeiro, E. R. Leite, E. Longo, T. R. Giraldi. Photoluminescence in quantum-confined SnO2 nanocrystals: Evidence of free exciton decay. *Applied Physics Letters*, **84** (10), 1745–1747 (2004). doi:10.1063/1.1655693

[14] P. Ramvall, S. Tanaka, S. Nomura, P. Riblet, Y. Aoyagi. Observation of confinement-dependent exciton binding energy of GaN quantum dots. *Applied Physics Letters*, **73** (8), 1104–1106 (1998). doi:10.1063/1.122098

[15] F. F. So, S. R. Forrest. Evidence for Exciton Confinement in Crystalline Organic Multiple Quantum Wells. *Phys. Rev. Lett.*, **66** (20), 2649–2652 (1991). doi:10.1038/2071238d0

[16] V. I. Vdovin, M. G. Mil'vidskii, T. G. Yugova, K. L. Lyutovich, S. M. Saidov. Effect of alloy composition on defect formation in GexSi(1-x)/Si heterostructures obtained by molecular beam epitaxy. *Journal of Crystal Growth*, **141**, 109–118 (1994)

[17] J. Narayan, K. Dovidenko, A. K. Sharma, S. Oktyabrsky. Defects and interfaces in epitaxial ZnO/α-Al2O3and AlN/ZnO/α-Al2O3heterostructures. *Journal of Applied Physics*, **84** (5), 2597–2601 (1998). doi:10.1063/1.368440

[18] V. Narayanan, K. Lorenz, W. Kim, S. Mahajan. Origins of threading dislocations in GaN epitaxial layers grown on sapphire by metalorganic chemical vapor deposition. *Applied Physics Letters*, **78** (11), 1544–1546 (2001). doi:10.1063/1.1352699

[19] M. J. Tambe, S. K. Lim, M. J. Smith, L. F. Allard, S. Gradečak. Realization of defect-free epitaxial core-shell GaAs/AlGaAs nanowire heterostructures. *Applied Physics Letters*, **93** (15), 2013–2016 (2008). doi:10.1063/1.3002299

[20] D. Ercolani, F. Rossi, A. Li, G. Salviati, V. Grillo, L. Sorba, F. Beltram, D. Ercolani, S. Roddaro, F. Rossi. InAs/InSb nanowire heterostructures grown by chemical beam epitaxy. *Nanotechnology*, **20** (50), 505605 (2009). doi:10.1088/0957-4484/20/50/505605

[21] X. Zhuang, C. Z. Ning, A. Pan. Composition and Bandgap-Graded Semiconductor Alloy Nanowires. *Advanced Materials*, **24** (1), 13–33 (2012). doi:10.1002/adma.201103191

[22] G. Otnes, M. T. Borgström. Towards high efficiency nanowire solar cells. *Nano Today*, **12**, 31–45 (2017). doi:10.1016/j.nantod.2016.10.007

[23] N. Anttu, H. Q. Xu. Efficient light management in vertical nanowire arrays for photovoltaics. *Optics Express*, **21** (S3), A558 (2013). doi:10.1364/OE.21.00A558

[24] E. Garnett, P. Yang. Light Trapping in Silicon Nanowire Solar Cells. *Nano Letters*, **10** (3), 1082–1087 (2010). doi:10.1021/nl100161z

[25] A. Nowzari, M. Heurlin, V. Jain, K. Storm, A. Hosseinnia, N. Anttu, M. T. Borgström, H. Pettersson, L. Samuelson. A Comparative Study of Absorption in Vertically and Laterally Oriented InP Core-Shell Nanowire Photovoltaic Devices. *Nano Letters*, **15** (3), 1809–1814 (2015). doi:10.1021/nl504559g

[26] G. Mariani, A. C. Scofield, C. H. Hung, D. L. Huffaker. GaAs nanopillar-array solar cells employing in situ surface passivation. *Nature Communications*, **4**, 1497 (2013). doi:10.1038/ncomms2509

[27] W. Wei, X.-y. Bao, C. Soci, Y. Ding, Z.-l. Wang, D. Wang. Direct Heteroepitaxy of Vertical InAs Nanowire Array on Si (111) Substrates for Broadband Photovoltaics and Photodetection. *Nano Letters*, **9** (8), 2926–2934 (2009)

[28] J. Wallentin, N. Anttu, D. Asoli, M. Huffman, I. Åberg, M. H. Magnusson, G. Siefer, P. Fuss-Kailuweit, F. Dimroth, B. Witzigmann, H. Q. Xu, L. Samuelson, K. Deppert, M. T. Borgström. InP Nanowire Array Solar Cells Achieving 13.8 % Efficiency by Exceeding the Ray Optics Limit. *Science*, **339** (6123), 1057–1060 (2013). doi:10.1126/science.1230969

[29] L. Tsakalakos, J. Balch, J. Fronheiser, B. A. Korevaar. Silicon nanowire solar cells. *Applied Physics Letters*, **91**, 233117 (2007). doi:10.1007/978-3-319-69703-1_10

[30] T. Bryllert, L. E. Wernersson, L. E. Fröberg, L. Samuelson. Vertical high-mobility wrap-gated InAs nanowire transistor. *IEEE Electron Device Letters*, **27** (5), 323–325 (2006). doi:10.1109/LED.2006.873371

[31] K. Tomioka, M. Yoshimura, T. Fukui. A III-V nanowire channel on silicon for high-performance vertical transistors. *Nature*, **488** (7410), 189–192 (2012). doi:10.1038/nature11293

[32] F. Qian, Y. Li, S. Gradečak, H. G. Park, Y. Dong, Y. Ding, Z. L. Wang, C. M. Lieber. Multi-quantum-well nanowire heterostructures for wavelength-controlled lasers. *Nature Materials*, **7** (9), 701–706 (2008). doi:10.1038/nmat2253

[33] Y. J. Lu, C. Y. Wang, J. Kim, H. Y. Chen, M. Y. Lu, Y. C. Chen, W. H. Chang, L. J. Chen, M. I. Stockman, C. K. Shih, S. Gwo. All-color plasmonic nanolasers with ultralow thresholds: Autotuning mechanism for single-mode lasing. *Nano Letters*, **14** (8), 4381–4388 (2014). doi:10.1021/nl501273u

[34] Y. Zhang, J. Wu, M. Aagesen, H. Liu. III-V nanowires and nanowire optoelectronic devices. *Journal of Physics D: Applied Physics*, **48** (46), 463001 (29pp) (2015). doi:10.1088/0022-3727/48/46/463001

[35] H. Kim, W. J. Lee, A. C. Farrell, J. S. Morales, P. Senanayake, S. V. Prikhodko, T. J. Ochalski, D. L. Huffaker. Monolithic InGaAs Nanowire Array Lasers on Silicon-on-Insulator Operating at Room Temperature. *Nano Letters*, **17** (6), 3465–3470 (2017). doi:10.1021/acs.nanolett.7b00384

[36] F. Lu, I. Bhattacharya, H. Sun, T.-T. D. Tran, K. W. Ng, G. N. Malheiros-Silveira, C. Chang-Hasnain. Nanopillar quantum well lasers directly grown on silicon and emitting at silicon-transparent wavelengths. *Optica*, **4** (7), 717 (2017). doi:10.1364/OPTICA.4.000717

[37] T. M. Babinec, B. J. M. Hausmann, M. Khan, Y. Zhang, J. R. Maze, P. R. Hemmer, M. Lončar. A diamond nanowire single-photon source. *Nature Nanotechnology*, **5** (3), 195–199 (2010). doi:10.1038/nnano.2010.6

[38] A. I. Hochbaum, R. Chen, R. D. Delgado, W. Liang, E. C. Garnett, M. Najarian, A. Majumdar, P. Yang. Enhanced thermoelectric performance of rough silicon nanowires. *Nature*, **451** (7175), 163–167 (2008). doi:10.1038/nature06381

[39] N. Mingo. Thermoelectric figure of merit of II-VI semiconductor nanowires. *Applied Physics Letters*, **85** (24), 5986–5988 (2004). doi:10.1063/1.1829391

[40] L. Shi, D. Yao, G. Zhang, B. Li. Large thermoelectric figure of merit in Si1-x Gex nanowires. *Applied Physics Letters*, **96** (17), 1–4 (2010). doi:10.1063/1.3421543

[41] R. Kim, S. Datta, M. S. Lundstrom. Influence of dimensionality on thermoelectric device performance. *Journal of Applied Physics*, **105** (3) (2009). doi:10.1063/1.3074347

[42] H. Kind, H. Yan, B. Messer, M. Law, P. Yang. Nanowire Ultraviolet Photodetectors and Optical Switches. *Advanced Materials*, **14** (2), 158–160 (2002). doi:10.1002/1521-4095(20020116)14:2<158::aid-adma158>3.0.co;2-w

[43] T. Zhai, X. Fang, M. Liao, X. Xu, L. Li, B. Liu, Y. Koide. Fabrication of High-Quality In2Se3 Nanowire Arrays toward High-Performance Visible-Light Photodetectors. *ACS Nano*, **4** (3), 1596–1602 (2010). doi:10.1021/nn9012466

[44] Y. Hu, J. Zhou, P.-H. Yeh, Z. Li, T.-Y. Wei, Z. L. Wang. Supersensitive, Fast-Response Nanowire Sensors by Using Schottky Contacts. *Advanced Materials*, **22** (30), 3327–3332 (2010). doi:10.1002/adma.201000278

[45] A. Kolmakov, Y. Zhang, G. Cheng, M. Moskovits. Detection of CO and O2 using tin oxide nanowire sensors. *Advanced Materials*, **15** (12), 997–1000 (2003). doi:10.1002/adma.200304889

[46] J. Anaya Calvo. *Transporte térmico y caracterización Raman de Nanohilos Semiconductores de Silicio-Germanio*. Dissertation, Universidad de Valladolid (2013). doi:10.35376/10324/4451

Chapter 1

Embrace your dreams...
- Zack Fair -

Introduction

Both the macroscopic and the atomic worlds have been extensively studied by physics. The first one, which is the world that can be seen by the naked eye, has awakened our interest from the very beginning of humankind, even when the discipline of ”Physics” as it is known nowadays was not established yet. In the beginning, this work was performed by philosophers, who several centuries later started to be called ”philosophers of nature”. They kept on studying the world surrounding us and the laws that govern it. The atomic world, on the other hand, has only been explored for a little more than a century. However, in this short period of time, science and technology advanced at rates never experienced before. Regardless of the evident differences and limitations between these two worlds, it could be said that (almost all) the basic phenomena occurring at these two scales can be explained from a physical point of view: maybe with the use of forces, energies and thermodynamics, in the case of the macroscopic world, or maybe with the use of eigenstates, hamiltonians and operators for the quantum world. The critical point is that in both cases, physics has a well-defined framework to propose a hypothesis and obtain conclusions. However, for better or worse, nature is not so ”simple” when the intermediate level is being studied.

The nanoscale world is defined as that with at least one dimension in the range between 1 to 100 nanometres; however, the frontier should not be taken as an exact and immovable value, but as an order of magnitude on which interesting new effects start to appear. As a result, nanoscience involves the study of those situations in which there are too many atoms to solve the problem by using quantum mechanics, but there are still not enough of them to consider the system as continuous (macroscopic). The concept of nanoscience includes many scientific fields such as physics, chemistry, biology, materials

engineering, or surface sciences. As a result, the applications are as diverse as the different fields involved. They range from physics of devices, e.g., lasers [1], transistors [2], batteries [3] or solar cells [4], going through chemical sensors and solutions to air and water pollution [5], and finishing with medical and biological applications, like drug delivery or cancer treatments [6]. Moreover, most of these applications do not rely only on one of the disciplines that have been mentioned, but the cooperation of several approaches is usually necessary, making nanotechnology a highly interdisciplinary research field.

Semiconductor nanowires (NWs) are quasi-1D systems. They are characterized by their reduced radial dimension, with diameters ranging from a few nanometres to several hundred. As a result of their small radial size, they present unique confinement effects when their diameter is comparable to the relevant lengths of the involved physical processes. For example, when the NW diameter is smaller than the incident light wavelength, the confinement of the electromagnetic field inside the NW leads to very interesting scattering and absorption resonances [7–9]. This has been detected in a wide variety of optical experiments, like second harmonic generation, Raman Scattering, or light extinction. However, analogous behaviours can also be observed in many other physical interactions like phonon confinement, when the diameter is smaller than the phonon mean free path [10, 11]; or exciton confinement effects on the photoluminescence of NWs [12], quantum dots [13, 14] or quantum wells [15]. Their reduced dimension comes with another advantage: the possibility of growing NWs free of dislocations or other structural defects. This is especially important when working with heterojunctions since the lattice mismatch between the different materials typically results in many problems during epitaxial growth and a faulty crystalline quality of the resulting materials [16–18]. The NW dimensionality allows for the combination of highly lattice-mismatched materials, preventing the formation of growth defects like dislocations or stacking faults, thus highly improving the crystalline quality [19, 20].

Among all the types of semiconductors, there are two groups that attract the majority of the research interest: groups IV and III-V semiconductors. Group IV semiconductors, like Si, Ge, and its alloys are compatible with the current CMOS (complementary metal-oxide-semiconductor) technology. Their manufacture and properties are very well known, and they have low bandgaps, which makes them suitable for photovoltaics. The main drawback is their low carrier mobility, and the indirect bandgap hinders its possible use as efficient light emitters. III-V semiconductors, like GaAs, InAs, InP, or InGaAs, present much higher carrier mobilities than their group IV counterparts. Typically, they have a direct bandgap, and in most cases their emission lies in the visible range or near infrared, being a common choice for the manufacture of light emitting diodes (LEDs), lasers, high-efficiency solar cells and a great variety of optoelectronic devices. Another advantage of this group is the feasibility of growing ternary and quaternary alloys, e.g., $In_xGa_{(1-x)}As$ or $Al_xGa_yIn_{(1-x-y)}P$, whose properties, like bandgap or refractive index, can be varied

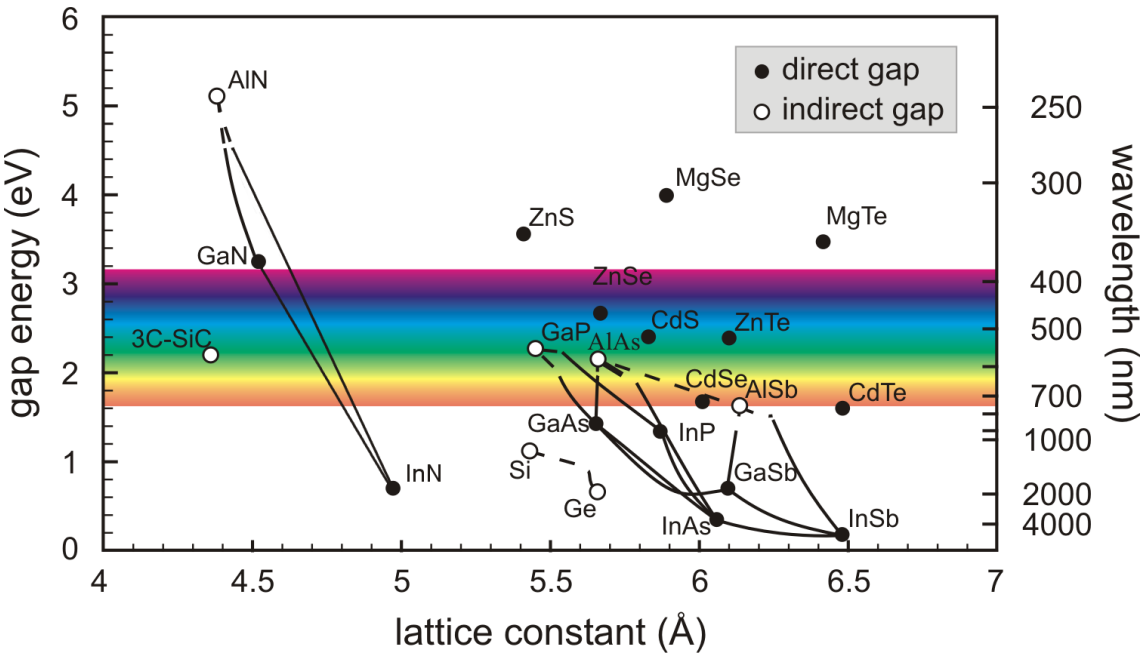

Figure 1.1: Summary of the band gaps of the most important semiconductors as a function of their lattice constant, as well as the band gap character (direct/indirect).

continuously as a function of its composition [21]. Figure 1.1 summarizes the band gap value and character (direct/indirect) of the most studied semiconductors as a function of their lattice parameter.

The most crucial difference between these two groups of semiconductors is their different polar nature. Group IV semiconductors are non-polar, while III-V semiconductors are polar. As a result, they cannot be mixed, and achieving a high-quality heterostructure between these materials is highly challenging. Nevertheless, when these materials are grown in the form of NWs, the lattice can be elastically accommodated as a result of the large surface/bulk ratio, and the defects that would appear in a bulk material are highly suppressed in the NW. This allows to synthesizing heterostructured NWs of these two groups combined, joining the advantages of both materials in a single device.

The NWs characterization is the first step to understand and control their properties. The earliest characterizations were done on ensembles of NWs. The main reason for using this procedure is the distribution of the NWs after their growth. The NWs are lying on the growth substrate, and they present a relatively high density, forming bundles of NWs. This means that the probe of any kind of macroscopic characterization technique (and in fact most of the microscopic ones) will sample a certain number of NWs. The advantage of this approach is the high number of NWs that is measured at a time, which results in better signals. However, the main disadvantage is that any physical magnitude that would be measured will be an average over the NW population.

In the case of characterization of optical properties, this will be an essential point. As it has been mentioned before, the response of the NW to coherent light critically depends on both the light wavelength and NW diameter. The presence of different diameters in the same measurement will result in the combined detection of a diversity of responses, making it impossible to ascertain the exact dependence of the measured magnitude with the NW properties.

Measuring isolated NWs allows controlling the characteristics of each studied NW carefully. As a result, the relation between the NW response and its specific properties (like composition, diameter, length, or environment) can be accurately established. The major drawback of measuring single NWs is their reduced material volume, and the, a priori, subsequent low measurement signal. Having such small amounts of the material makes the acquisition of a proper experimental measurement a true challenge. However, as will be shown throughout the thesis, the NW resonances can be used to substantially improve these sensitive measurements. As an example, let us consider a Si NW with a diameter of 100 nm illuminated by a 1 μm laser spot. The sampling volume would be roughly $V = L\pi r^2 = 1000\pi 50^2\ nm^3\ 8 \times 10^6\,\mathrm{nm}^3 = 8 \times 10^{-15}\,\mathrm{cm}^3$, and considering the density of Si, $\rho = 2.33\,\mathrm{g\,cm}^{-3}$, the mass probed by the laser beam will be of the order of 18 pg, which is extraordinary low.

1.1 Applications

All these unique properties make of semiconductor NWs promising candidates to be the building blocks of future nanodevices. Their applications comprise a great variety of optoelectronic devices like solar cells, sensors, transistors, light sources, or thermoelectric cells. All the cited applications have a common factor, which is the requirement of heterojunctions between different materials.

Solar Cells

Semiconductor NWs have been extensively studied for their applications on photovoltaics [22–25]. As a matter of fact, a great deal of attention is being paid to III-V semiconductor NWs like GaAs [26], InAs [27], or InP [28], with which efficiencies up to 13.8 % have been achieved. On the other hand, Si-based NW solar cells are very interesting because of their compatibility with the current CMOS technology and the subsequent easiness for on-chip integration of this kind of devices [4, 29]. The presence of absorption resonances, as well as the antenna effect for semiconductor NWs, could improve the photon harvesting capabilities of advanced NW-based solar cells.

Transistors

NW based field effect transistors (NWFETs) are a promising option for the development of new routes to approach the down-scaling of current CMOS devices. The main

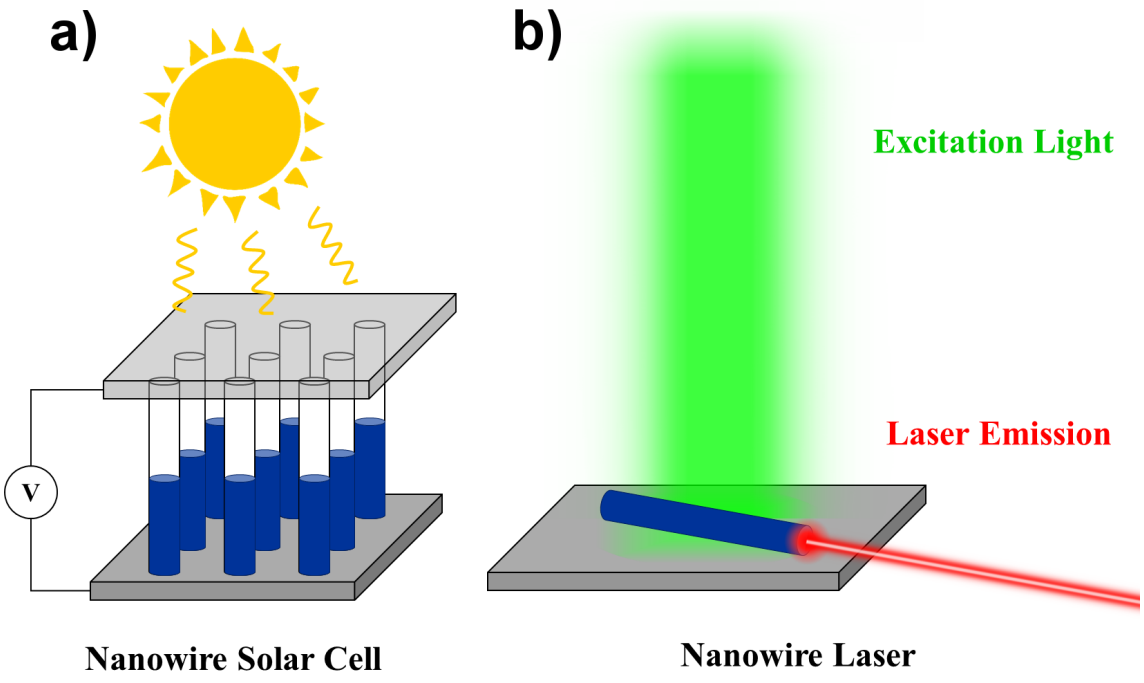

Figure 1.2: Examples of NWs applications. a) Scheme of a NW solar cell based on NWs with axial junction. Note that the upper electrode is transparent to let the solar radiation reach the NWs. b) Scheme of a NW laser. NWs can act as resonant cavities producing coherent laser radiation.

issue on transistor technology is the reduction of the channel dimensions. In NWFETs the channel is replaced by a semiconductor NW, thus acquiring the advantages of its bottom-up manufacture, i.e., the possibility of carefully controlling the size of the critical device dimensions (NW diameter), its reproducibility and the resulting crystalline quality of both the NW and its surface. Different approaches to this kind of devices have been afforded [2, 30, 31], based on both homogeneous and heterostructured NWs.

Light Sources

Semiconductor NWs can also be used as light sources, like lasers and LEDs [32–36], but also advanced photonic devices like single photon sources [37]. For lasing applications, group III-V NWs are preferred because they present direct bandgap, as well as better carrier mobilities as explained. On the other hand, the possibility of making heterojunctions as well as controlling the material doping facilitates bandgap engineering, which allows the control of the resulting light emitting properties on the final device. Simultaneously, the reduced dimension of the NWs makes them behave as waveguides (even in the subwavelength regime), having the versatility of confining and transporting the generated light as needed.

Thermoelectric Conversion

Thermoelectric conversion takes advantage of the Seebeck effect to obtain electric energy directly from a temperature gradient. Its efficiency depends on the so-called *figure of merit*: $ZT = S^2T/\rho\kappa$, where S is the Seebeck coefficient, T the temperature, ρ the electrical resistivity and κ the thermal conductivity. Maximizing ZT means optimizing the power efficiency of the final device, and in order to do so ρ and κ should be as low as possible. In bulk materials, electric and thermal conductivity are coupled and when one tries to reduce κ, ρ increases, and vice-versa. However, semiconductor NWs allow to separate the contributions of electrons and phonons to κ, so that the thermal conductivity can be reduced by changing phonon scattering conditions without modifying the electrical properties [38–41]. This approach permits us to go beyond bulk material limitations on thermoelectric conversion devices.

Light and Chemical Sensors

Semiconductor NWs are also used is as light detectors [42, 43] and chemical sensors [44, 45]. The involved physical phenomenon is similar in both cases: when specific molecules or light of a particular wavelength interact with the NW the current passing through the NW for a fixed voltage is changed. Consequently, the sensing takes place as a measurement of the NW conductivity in the presence or absence of the corresponding chemicals or radiation, which has proven to be very sensitive in the appropriate conditions.

1.2 Framework of this Thesis

This thesis has been developed in the GdS Optronlab Group in the Condensed Matter Physics Department of the University of Valladolid. Optronlab Group is focused on the characterization of optoelectronic properties of semiconductors. The group has three main research branches: Characterization of Nanostructured Semiconductors, Thermal Transport at the Nanoscale and Characterization of Photovoltaic Materials. The present work is framed in the first branch, Characterization of Nanostructured Semiconductors, as it comprises all the research in nanoscale systems, such as nanowires. In previous works the group studied the thermal properties of Si and SiGe NWs by using μ-Raman Spectroscopy and Finite Element Methods simulations [46]. This thesis extends the methodology of experimental measurements in connection with simulations to study the optical properties of axially heterostructured NWs. At the same time, some work has been developed on the topic of the second branch, Thermal Transport at the Nanoscale. The methodology for the study of the EM field distribution in NWs can be applied to the quantum well structure of high power laser diodes. This allows investigating the generation of heat sources on these devices as well as the effect of such heat sources on the laser EM field and its degradation.

1.3 Objectives

As it has been mentioned, heterostructures are basic elements of many devices. The present thesis aims to study the optical properties of axially heterostructured nanowires, and, at the same time, to provide a reliable theoretical framework to better understand light-matter interaction on this kind of systems. In order to do this, the problem will be approached from two different points of view that fully complement each other: experimental measurement of the optical response of axially heterostructured NWs, and theoretical simulations of the light-NW interaction to reproduce the experimental results.

The **experimental analysis** will be focused on μ-Raman Scattering. The NWs are individually probed with a laser beam and the Raman spectra are recorded. As will be explained later on, Raman spectroscopy is extremely sensitive to the material structure (like composition, doping, and presence of defects). This allows detecting clearly distinguishable signals from the different materials forming the heterostructured NWs even beyond the optical diffraction limit. Moreover, the Raman signal is proportional to the light intensity (i.e., $|E|^2$). Therefore, the Raman spectrum can provide information about the intensity of the electromagnetic fields in the different materials forming the NW, leading to effective measurement of the electromagnetic field distribution inside and around the NW.

The **theoretical analysis** is made by solving Maxwell Equations for the laser beam / NW / surroundings system. In order to do this, Maxwell Equations are numerically solved by the finite element method (FEM). The analysis of the resulting electromagnetic field distributions provides a theoretical framework to understand the interaction between the NW and the incident electromagnetic field, and comprehend the novel effects that appear on nanoscale systems.

1.4 Structure of This Thesis

The present thesis is written as a compendium of publications. The obtained results are supported by seven scientific publications listed in Table 1.1 of the next section. Moreover, this thesis fulfills the requirements to be accredited with the **International Mention**.

The thesis is organized in 8 Chapters and 1 Appendix. Chapters 1 to 3 contain the necessary information to understand the body of the work.

Chapter 1 - Introduction. The first chapter starts with an overview of the thesis topic. It states the relevance and applications of semiconductor NWs, the importance of heterojunctions and their study, and the objectives and methodology of the thesis.

Chapter 2 - State of the Art. The second chapter is devoted to the State of the Art. It is focused on the theory of μ-Raman Scattering and its use as a probe of the electromagnetic field. This chapter also discusses the Maxwell equations and their solution using Finite Element Methods, and the Fourier Transform as a tool to analyse the electromagnetic field distributions induced inside the heterostructured NWs.

Chapter 3 - Experimental Methods and Sample Preparation. This chapter is dedicated to the experimental methods and sample preparation. The process to prepare the NWs for Raman measurements and the experimental methodology is revised. Furthermore, reference Raman spectra are provided to better understand the results of the Raman measurements of the subsequent chapters.

Chapters 4 to 7 contain the main results presented in this work. Each of them focuses on independent topics, except for chapter 7, which delves deeper into the study of the electromagnetic interaction in order to better understand the results of chapters 4 to 6. These sections contain both experimental measurements and the simulations results for different heterostructured NWs: Si/SiGe and Si/III-V.

Chapter 4 - Si/SiGe axially heterostructured NWs. Chapter 4 contains the vast majority of the results. It is devoted to the study of Si/SiGe axially heterostructured NWs. The electromagnetic enhancement effect was first discovered on these NWs, and this is the reason why they have been extensively studied. The experimental Raman enhancement at the HJ is correlated with the results of the FEM simulations.

Chapter 5 - Si/III-V axially heterostructured NWs. This chapter is devoted to the study of Si/III-V NWs. The main objective is to check that the electromagnetic enhancement effect is not related to the material itself, but it is a consequence of the material discontinuity at the HJ, and it appears in different NW heterostructures. As a result of the immiscibility of Si with III-V semiconductors, the HJ is atomically abrupt, and these NWs do not present Raman signal of any HJ material itself. Despite this crucial difference, a similar effect is detected on the material adjacent to the HJ, supporting the electromagnetic field enhancement and localization by the presence of the HJ.

Chapter 6 - Nanowire Growth Model. In this chapter, NW growth methods are analysed. First, the current growth methods and models are introduced. Then, a new model for the growth of SiGe alloys NWs is developed, and its repercussion on the fabrication of Si/SiGe axial heterojunctions is studied. The model permits to control the NW composition and HJ abruptness by modifying the growth parameters such as temperature, total gas pressure, or partial pressures of the precursor gases.

Chapter 7 - Theoretical study of the light enhancement effect. This chapter aims to go deeper into the understanding of the light-heterostructured NW interaction. The electromagnetic field distributions calculated on the previous chapters are analysed by Fourier Transform. This mathematical tool allows ascertaining the effect of the material discontinuity on the electromagnetic field and its repercussion on the Raman enhancement.

Chapter 8 - Conclusions. The last chapter consists of a recapitulation of the obtained results. The degree of accomplishment of the initial objectives is also appraised. Finally, the perspectives of future work are proposed to continue the study of systems of heterostructured NWs.

Appendix A - Catastrophic Optical Damage of high power laser diodes. This appendix is a compendium of the work developed about the study of Catastrophic Optical Damage (COD) of high power laser diodes. Despite it is not the main topic of the thesis, the model for the light/NW interaction can be used to study the distribution of the electromagnetic radiation inside the laser diodes. It is important to note that the underlying ideas are essentially the same. Laser diodes present a heterostructure arrangement and the active region, the quantum well (QW), is a 2-dimensional material. Consequently, the QW/light interaction takes place on a heterostructure under confinement conditions, which leads again to a non-trivial behaviour of the electromagnetic field. The appendix is focused on studying the effect of a highly confined damaged region of the laser diode on the laser light distribution, and its repercussion on the laser COD.

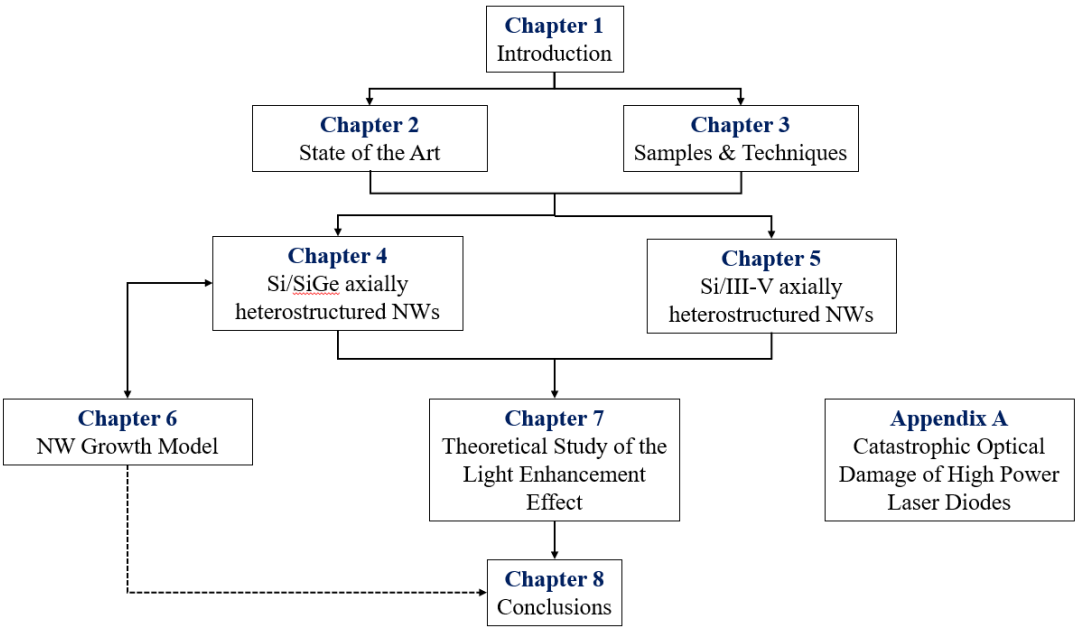

Figure 1.3: Diagram of the chapter distribution of this thesis.

1.5 Publications, Conferences, Stays and Research Projects

	Article Reference	Chapter
1	J. L. Pura, J. Anaya, J. Souto, A. C. Prieto, A. Rodríguez, T. Rodríguez and J. Jiménez. Local electric field enhancement at the heterojunction of Si/SiGe axially heterostructured nanowires under laser illumination. *Nanotechnology* **27**, 455709 (7pp), 2016	4
2	J. L. Pura, J. Anaya, J. Souto, A. C. Prieto, A. Rodríguez, T. Rodríguez, P. Periwal, T. Baron and J. Jiménez. Electromagnetic field enhancement effects in group IV semiconductor nanowires. A Raman spectroscopy approach. *J. Appl. Phys.* **123**, 114302, 2018	4
3	J. L. Pura, J. Souto, P. Periwal, T. Baron and J. Jiménez. Electromagnetic Field Enhancement on Axially Heterostructured NWs: The Role of the Heterojunctions. *J. Electron. Mater.* 2018	4
4	J. L. Pura, J. Anaya and J. Jiménez. About the Interaction Between a Laser Beam and Group IV Nanowires: A Study of the Electromagnetic Field Enhancement in Homogeneous and Heterostructured Nanowires. *Phys. Status Solidi A* **215**, 1800336, 2018	4
5	J. L. Pura, P. Periwal, T. Baron and J. Jiménez. Growth dynamics of SiGe nanowires by the vapour-liquid-solid method and its impact on SiGe/Si axial heterojunction abruptness. *Nanotechnology* **29**, 355602 (9pp), 2018	6
6	J. L. Pura, A. J. Magdaleno, D. Muñoz-Segovia, M. Glaser, A. Lugstein and J. Jiménez. Electromagnetic enhancement effect on the atomically abrupt heterojunction of Si/InAs heterostructured nanowires. *J. Appl. Phys.* **125**, 064303, 2019	5
7	J. L. Pura, J. Jiménez. Fourier Transform Study of the Complex Electric Field Induced on Axially Heterostructured NWs. *Submitted*	7

Table 1.1: Summary of the articles included in the thesis.

	Article Reference
1	J.Souto, J.L.Pura, M.Rodríguez, J.Anaya, A.Torres, J.Jiménez. Mechanisms driving the catastrophic optical damage in high power laser diodes. *Proc. of SPIE* **9348**, 93480O (7pp), 2015
2	J.Souto, J.L.Pura, A.Torres, J.Jiménez, M. Bettiati, F.J. Laruelle. Sequential Description of the Catastrophic Optical Damage of High Power Laser Diodes. *Proc. of SPIE* **9733**, 973306 (6pp), 2016
3	J.Souto, J.L.Pura, J.Jiménez. About the physical meaning of the critical temperature for catastrophic optical damage in high power laser diodes. *Laser Phys. Lett.* **13**, 025005 (6pp), 2016
4	J.Souto, J.L.Pura, J.Jiménez. Catastrophic optical damage of high power InGaAs/AlGaAs laser diodes. *Microelectron. Reliab.* **64**, 627-630, 2016
5	J. Souto, J.L.Pura, A. Torres, J.Jiménez. Thermomechanical degradation of single and multiple quantum well AlGaAs/GaAs laser diodes. *Microelectron. Reliab.* **76-77**, 588591, 2017
6	J.Souto, J.L.Pura, A.Torres, J.Jiménez. About the impact of the materials properties in the catastrophic degradation of high power GaAs based laser diodes. *Proc. of SPIE* **10086**, 100860P (6pp), 2017
7	J.Souto, J.L.Pura, J.Jiménez. Nanoscale effects on the thermal and mechanical properties of AlGaAs/GaAs quantum well laser diodes: influence on the catastrophic optical damage. *J. Phys. D: Appl. Phys.* **50**, 235101, 2017
8	J.Souto, J.L.Pura, J.Jiménez. Thermal and mechanical issues of high-power laser diode degradation. *MRS Commun.* **8 (3)**, 995-999, 2018
9	J.Souto, J.L.Pura, J.Jiménez. Thermomechanical Issues of High Power Laser Diode Catastrophic Optical Degradation. *J. Phys. D: Appl. Phys.*, **52** 343002, 2019 (Topical Review)
10	J. Souto, J. L. Pura, A. Torres, and J. Jimenéz. A comparative analysis of the catastrophic degradation of AlGaAs/GaAs and AlGaAs/InGaAs laser diodes: role of the strained QWs. *Proc. SPIE* **10900** , 2019
11	J. Martín-de León, J. L. Pura, V. Bernardo, M. Á. Rodríguez-Pérez. Transparent nanocellular PMMA: Characterization and modeling of the optical properties. *Polymer* **170**, 16-23 , 2019

Table 1.2: Summary of the articles written during the thesis that are not related with the main topic.

	Conference	Contribution
1	J.L.Pura, J.Jiménez. Thermal Transport in Nanostructures. *XVI Escuela Nacional de Materiales Moleculares* Santa Pola (Spain), February 1-6 2015	Oral
2	J.L.Pura, J.Jiménez. Enhanced Raman Scattering in Semiconductor Nanowires. *VIII European School on Molecular Nanoscience* Paris (France) October 25-29 2015	Oral
3	J.L.Pura, J.Jiménez. Enhanced Raman Signal at the Heterojunction Region of Si/SiGe Axially Heterostructured Nanowires. *EXMATEC 2016* Aveiro (Portugal) June 6-10 2016	Oral
4	J.L.Pura, J.Anaya, J.Souto, A.C.Prieto, A.Rodríguez, T.Rodríguez, T.Baron, J.Jiménez. Enhanced Raman signal at the heterojunction region of SiGe/Si axially heterostructured nanowires. *MRS Fall Meeting & Exhibit 2016* Boston (USA) November 27 - December 2 2016	Oral
5	J.L.Pura, J.Jiménez. Raman Enhancement on Si/SiGe Axially Heterostructured NWs. *SENM 2017* June 26-29 2017	Oral
6	J. L. Pura, J. Souto, P. Periwal, T. Baron, J. Jiménez. Electromagnetic Field Enhancement on axially heterostructured NWs: the role of the heterojunctions. *DRIP 2017* Valladolid (Spain) October 8 - 12 2017	Oral
7	J. L. Pura, M. Glaser, A. J. Magdaleno, A. C. Prieto, S. Rodríguez-Conde, A. Lugstein, J. Jiménez. Local electromagnetic field enhancement on Si/InAs axially heterostructured NWs. *DRIP 2017* Valladolid (Spain) October 8 - 12 2017	Poster
8	J. L. Pura, P. Periwal, T. Baron, J. Jiménez. Light absorption in axially heterostructured semiconductor NWs. *MRS Fall Meeting & Exhibit 2017* Boston (USA) November 26 - December 1 2017	Poster

Table 1.3: Summary of the conference attendances regarding the thesis topic.

	Conference	Contribution
1	J.Souto, J.L.Pura, M.Rodríguez, J.Anaya, A.Torres, J. Jiménez. Mechanisms driving the catastrophic optical damage in high power laser diodes. *Photonic West 2015* San Francisco (USA), February 7-12 2015	Oral
2	J.Souto, J.L.Pura, A.Torres, J. Jiménez, M..Bettiati, F.J. Laruelle. Sequential Description of the Catastrophic Optical Damage of High Power Laser Diodes. *Photonic West 2016* San Francisco (USA), January 28 - February 2 2016	Oral
3	J.Souto, J.L.Pura, A.Torres, J.Jiménez. Role of the Mechanical Strength of Quantum Wells in the Catastrophic Optical Damage of High Power Laser Diodes. *ESREF 2016* Halle (Germany) September 19-22 2016	Oral
4	J.Souto, J.L.Pura, A. Torres, J.Jiménez. About the impact of the materials properties in the catastrophic degradation of high power GaAs based laser diodes. *Photonic West 2017* San Francisco (USA) January 28 - February 2 2017	Oral
5	J. Souto, J. L. Pura, A. Torres, J. Jiménez. Thermomechanical model for the degradation of AlGaAs and InGaAs laser diodes: correlation with cathodoluminescence measurements. *DRIP 2017* Valladolid (Spain) October 8 - 12 2017	Poster
6	J.Souto, J.L.Pura, J.Jiménez. Materials issues for the catastrophic degradation of high power laser diodes. (Invited Talk) *2017 IEEE High Power Diode Lasers & Systems Conference* Coventry (UK) October 12 - 13 2017	Oral
7	J.Souto, J.L.Pura, J.Jiménez. Thermal and Mechanical Issues of High Power Laser Diode Degradation. (Invited Talk) *MRS Spring Meeting & Exhibit 2018* Phoenix (USA) April 2 - 6 2018	Oral
8	J. L. Pura. High School Excellence Projects: A Way to Introduce High School Students to University Research. *Edulearn 2018* Palma de Mallorca (Spain) July 2 - 4 2018	Virtual P.
9	J.Souto, J.L.Pura, A. Torres, J.Jiménez. A comparative analysis of the catastrophic degradation of AlGaAs/GaAs and AlGaAs/InGaAs laser diodes: role of the strained QWs. *Photonic West 2019* San Francisco (USA) February 2 - 7 2019	Oral

Table 1.4: Summary of other conference attendances.

Stays in Other Research Institutes
One month in the Applied Physics Department of the University of Málaga (Spain), June 2017
Topic: Elaboration of Pt contacts on Si/SiGe and Si/InAs heterostructured NWs for electrical and electro-optical characterization
Three months in the Cambridge Graphene Centre of the University of Cambridge (UK), September - November 2018
Topic: Measurement of the optical properties of heterostructured NWs deposited on top of grapheme & Exfoliation and characterization of GeSe thin layers

Table 1.5: Relation of the stays in other research centres.

	Research Projects
1	Nanohilos semiconductores para aplicaciones fotovoltaicas y de conversión termoeléctrica **Junta de Castilla y León: VA293U13**
2	Desarrollo de sistemas de imagen por electroluminiscencia para la inspección y mantenimiento de plantas solares **Junta de Castilla y León: VA283P18**
3	Caracterización óptica de obleas y células tandem de silicio de bajo coste para aplicaciones fotovoltaicas y de conversión termoeléctrica **MINECO (Spanish Government): ENE2014-56069-C4-4-R**
4	Diseño y desarrollo de un sistema de imagen por fotoluminiscencia para calificación de obleas y células solares de silicio multicristalino **Junta de Castilla y León: VA081U16**
5	Caracterización Eléctrica y lumínica de sustratos y células solares para la fabricación de módulos bifaciales de silicio solar **MINECO (Spanish Government): ENE2017-89561-C4-3-R**

Table 1.6: Participation on research projects during the thesis.

Bibliography

[1] A. B. Greytak, C. J. Barrelet, Y. Li, C. M. Lieber. Semiconductor nanowire laser and nanowire waveguide electro-optic modulators. *Applied Physics Letters*, **87** (15), 1–3 (2005). doi:10.1063/1.2089157

[2] W. Lu, P. Xie, C. M. Lieber. Nanowire transistor performance limits and applications. *IEEE Transactions on Electron Devices*, **55** (11), 2859–2876 (2008). doi:10.1109/TED.2008.2005158

[3] C. K. Chan, H. Peng, G. Liu, K. McIlwrath, X. F. Zhang, R. A. Huggins, Y. Cui. High-performance lithium battery anodes using silicon nanowires. *Nature Nanotechnology*, **3** (1), 31–35 (2007). doi:10.1038/nnano.2007.411

[4] B. Tian, X. Zheng, T. J. Kempa, Y. Fang, N. Yu, G. Yu, J. Huang, C. M. Lieber. Coaxial silicon nanowires as solar cells and nanoelectronic power sources. *Nature*, **449** (18), 885–889 (2007). doi:10.1038/nature06181

[5] X. Qu, P. J. J. Alvarez, Q. Li. Applications of nanotechnology in water and wastewater treatment. *Water Research*, **47** (12), 3931–3946 (2013). doi:10.1016/j.watres.2012.09.058

[6] M. Ferrari. Cancer nanotechnology: Opportunities and challenges. *Nature Reviews Cancer*, **5** (3), 161–171 (2005). doi:10.1038/nrc1566

[7] R. Rurali. Colloquium: Structural, electronic, and transport properties of silicon nanowires. *Reviews of Modern Physics*, **82** (1), 427–449 (2010). doi:10.1103/RevModPhys.82.427

[8] H. Kallel, A. Arbouet, G. Benassayag, A. Chehaidar, A. Potié, B. Salem, T. Baron, V. Paillard. Tunable enhancement of light absorption and scattering in Si 1-xGe x nanowires. *Physical Review B - Condensed Matter and Materials Physics*, **86** (8) (2012). doi:10.1103/PhysRevB.86.085318

[9] L. Cao, J. S. Park, P. Fan, B. Clemens, M. L. Brongersma. Resonant germanium nanoantenna photodetectors. *Nano Letters*, **10** (4), 1229–1233 (2010). doi:10.1021/nl9037278

[10] Z. V. Popovic, M. Cardona. Phonons in GaAs/AlAs superlattices grown along the [111] direction. *Physical Review B*, **41** (9), 5904–5913 (1990)

[11] K. W. Adu, H. R. Gutiérrez, U. J. Kim, G. U. Sumanasekera, P. C. Eklund. Confined Phonons in Si Nanowires. *Nano Letters*, **5** (3), 409–414 (2005). doi:10.1021/nl0486259

[12] R. Rinaldi, R. Cingolani, M. Lepore, M. Ferrara, I. M. Catalano, F. Rossi, L. Rota, E. Molinari, P. Lugli, U. Marti, D. Martin, F. Morier-Gemoud, P. Ruterana, F. K. Reinhart. Exciton Binding Energy in GaAs V-Shaped Quantum Wires. *Phys. Rev. Lett.*, **73** (21), 2899–2902 (1994)

[13] E. J. H. Lee, J. A. Varela, C. Ribeiro, E. R. Leite, E. Longo, T. R. Giraldi. Photoluminescence in quantum-confined SnO2 nanocrystals: Evidence of free exciton decay. *Applied Physics Letters*, **84** (10), 1745–1747 (2004). doi:10.1063/1.1655693

[14] P. Ramvall, S. Tanaka, S. Nomura, P. Riblet, Y. Aoyagi. Observation of confinement-dependent exciton binding energy of GaN quantum dots. *Applied Physics Letters*, **73** (8), 1104–1106 (1998). doi:10.1063/1.122098

[15] F. F. So, S. R. Forrest. Evidence for Exciton Confinement in Crystalline Organic Multiple Quantum Wells. *Phys. Rev. Lett.*, **66** (20), 2649–2652 (1991). doi:10.1038/2071238d0

[16] V. I. Vdovin, M. G. Mil'vidskii, T. G. Yugova, K. L. Lyutovich, S. M. Saidov. Effect of alloy composition on defect formation in GexSi(1-x)/Si heterostructures obtained by molecular beam epitaxy. *Journal of Crystal Growth*, **141**, 109–118 (1994)

[17] J. Narayan, K. Dovidenko, A. K. Sharma, S. Oktyabrsky. Defects and interfaces in epitaxial ZnO/α-Al2O3and AlN/ZnO/α-Al2O3heterostructures. *Journal of Applied Physics*, **84** (5), 2597–2601 (1998). doi:10.1063/1.368440

[18] V. Narayanan, K. Lorenz, W. Kim, S. Mahajan. Origins of threading dislocations in GaN epitaxial layers grown on sapphire by metalorganic chemical vapor deposition. *Applied Physics Letters*, **78** (11), 1544–1546 (2001). doi:10.1063/1.1352699

[19] M. J. Tambe, S. K. Lim, M. J. Smith, L. F. Allard, S. Gradečak. Realization of defect-free epitaxial core-shell GaAs/AlGaAs nanowire heterostructures. *Applied Physics Letters*, **93** (15), 2013–2016 (2008). doi:10.1063/1.3002299

[20] D. Ercolani, F. Rossi, A. Li, G. Salviati, V. Grillo, L. Sorba, F. Beltram, D. Ercolani, S. Roddaro, F. Rossi. InAs/InSb nanowire heterostructures grown by chemical beam epitaxy. *Nanotechnology*, **20** (50), 505605 (2009). doi:10.1088/0957-4484/20/50/505605

[21] X. Zhuang, C. Z. Ning, A. Pan. Composition and Bandgap-Graded Semiconductor Alloy Nanowires. *Advanced Materials*, **24** (1), 13–33 (2012). doi:10.1002/adma.201103191

[22] G. Otnes, M. T. Borgström. Towards high efficiency nanowire solar cells. *Nano Today*, **12**, 31–45 (2017). doi:10.1016/j.nantod.2016.10.007

[23] N. Anttu, H. Q. Xu. Efficient light management in vertical nanowire arrays for photovoltaics. *Optics Express*, **21** (S3), A558 (2013). doi:10.1364/OE.21.00A558

[24] E. Garnett, P. Yang. Light Trapping in Silicon Nanowire Solar Cells. *Nano Letters*, **10** (3), 1082–1087 (2010). doi:10.1021/nl100161z

[25] A. Nowzari, M. Heurlin, V. Jain, K. Storm, A. Hosseinnia, N. Anttu, M. T. Borgström, H. Pettersson, L. Samuelson. A Comparative Study of Absorption in Vertically and Laterally Oriented InP Core-Shell Nanowire Photovoltaic Devices. *Nano Letters*, **15** (3), 1809–1814 (2015). doi:10.1021/nl504559g

[26] G. Mariani, A. C. Scofield, C. H. Hung, D. L. Huffaker. GaAs nanopillar-array solar cells employing in situ surface passivation. *Nature Communications*, **4**, 1497 (2013). doi:10.1038/ncomms2509

[27] W. Wei, X.-y. Bao, C. Soci, Y. Ding, Z.-l. Wang, D. Wang. Direct Heteroepitaxy of Vertical InAs Nanowire Array on Si (111) Substrates for Broadband Photovoltaics and Photodetection. *Nano Letters*, **9** (8), 2926–2934 (2009)

[28] J. Wallentin, N. Anttu, D. Asoli, M. Huffman, I. Åberg, M. H. Magnusson, G. Siefer, P. Fuss-Kailuweit, F. Dimroth, B. Witzigmann, H. Q. Xu, L. Samuelson, K. Deppert, M. T. Borgström. InP Nanowire Array Solar Cells Achieving 13.8% Efficiency by Exceeding the Ray Optics Limit. *Science*, **339** (6123), 1057–1060 (2013). doi:10.1126/science.1230969

[29] L. Tsakalakos, J. Balch, J. Fronheiser, B. A. Korevaar. Silicon nanowire solar cells. *Applied Physics Letters*, **91**, 233117 (2007). doi:10.1007/978-3-319-69703-1_10

[30] T. Bryllert, L. E. Wernersson, L. E. Fröberg, L. Samuelson. Vertical high-mobility wrap-gated InAs nanowire transistor. *IEEE Electron Device Letters*, **27** (5), 323–325 (2006). doi:10.1109/LED.2006.873371

[31] K. Tomioka, M. Yoshimura, T. Fukui. A III-V nanowire channel on silicon for high-performance vertical transistors. *Nature*, **488** (7410), 189–192 (2012). doi:10.1038/nature11293

[32] F. Qian, Y. Li, S. Gradečak, H. G. Park, Y. Dong, Y. Ding, Z. L. Wang, C. M. Lieber. Multi-quantum-well nanowire heterostructures for wavelength-controlled lasers. *Nature Materials*, **7** (9), 701–706 (2008). doi:10.1038/nmat2253

[33] Y. J. Lu, C. Y. Wang, J. Kim, H. Y. Chen, M. Y. Lu, Y. C. Chen, W. H. Chang, L. J. Chen, M. I. Stockman, C. K. Shih, S. Gwo. All-color plasmonic nanolasers with ultralow thresholds: Autotuning mechanism for single-mode lasing. *Nano Letters*, **14** (8), 4381–4388 (2014). doi:10.1021/nl501273u

[34] Y. Zhang, J. Wu, M. Aagesen, H. Liu. III-V nanowires and nanowire optoelectronic devices. *Journal of Physics D: Applied Physics*, **48** (46), 463001 (29pp) (2015). doi:10.1088/0022-3727/48/46/463001

[35] H. Kim, W. J. Lee, A. C. Farrell, J. S. Morales, P. Senanayake, S. V. Prikhodko, T. J. Ochalski, D. L. Huffaker. Monolithic InGaAs Nanowire Array Lasers on Silicon-on-Insulator Operating at Room Temperature. *Nano Letters*, **17** (6), 3465–3470 (2017). doi:10.1021/acs.nanolett.7b00384

[36] F. Lu, I. Bhattacharya, H. Sun, T.-T. D. Tran, K. W. Ng, G. N. Malheiros-Silveira, C. Chang-Hasnain. Nanopillar quantum well lasers directly grown on silicon and emitting at silicon-transparent wavelengths. *Optica*, **4** (7), 717 (2017). doi:10.1364/OPTICA.4.000717

[37] T. M. Babinec, B. J. M. Hausmann, M. Khan, Y. Zhang, J. R. Maze, P. R. Hemmer, M. Lončar. A diamond nanowire single-photon source. *Nature Nanotechnology*, **5** (3), 195–199 (2010). doi:10.1038/nnano.2010.6

[38] A. I. Hochbaum, R. Chen, R. D. Delgado, W. Liang, E. C. Garnett, M. Najarian, A. Majumdar, P. Yang. Enhanced thermoelectric performance of rough silicon nanowires. *Nature*, **451** (7175), 163–167 (2008). doi:10.1038/nature06381

[39] N. Mingo. Thermoelectric figure of merit of II-VI semiconductor nanowires. *Applied Physics Letters*, **85** (24), 5986–5988 (2004). doi:10.1063/1.1829391

[40] L. Shi, D. Yao, G. Zhang, B. Li. Large thermoelectric figure of merit in Si1-x Gex nanowires. *Applied Physics Letters*, **96** (17), 1–4 (2010). doi:10.1063/1.3421543

[41] R. Kim, S. Datta, M. S. Lundstrom. Influence of dimensionality on thermoelectric device performance. *Journal of Applied Physics*, **105** (3) (2009). doi:10.1063/1.3074347

[42] H. Kind, H. Yan, B. Messer, M. Law, P. Yang. Nanowire Ultraviolet Photodetectors and Optical Switches. *Advanced Materials*, **14** (2), 158–160 (2002). doi:10.1002/1521-4095(20020116)14:2<158::aid-adma158>3.0.co;2-w

[43] T. Zhai, X. Fang, M. Liao, X. Xu, L. Li, B. Liu, Y. Koide. Fabrication of High-Quality In2Se3 Nanowire Arrays toward High-Performance Visible-Light Photodetectors. *ACS Nano*, **4** (3), 1596–1602 (2010). doi:10.1021/nn9012466

[44] Y. Hu, J. Zhou, P.-H. Yeh, Z. Li, T.-Y. Wei, Z. L. Wang. Supersensitive, Fast-Response Nanowire Sensors by Using Schottky Contacts. *Advanced Materials*, **22** (30), 3327–3332 (2010). doi:10.1002/adma.201000278

[45] A. Kolmakov, Y. Zhang, G. Cheng, M. Moskovits. Detection of CO and O2 using tin oxide nanowire sensors. *Advanced Materials*, **15** (12), 997–1000 (2003). doi:10.1002/adma.200304889

[46] J. Anaya Calvo. *Transporte térmico y caracterización Raman de Nanohilos Semiconductores de Silicio-Germanio*. Dissertation, Universidad de Valladolid (2013). doi:10.35376/10324/4451

Chapter

2

State of the Art

Mejor es ser admirado de los pocos sabios
que burlado de los muchos necios.
- Miguel de Cervantes -

2.1 Raman Scattering

Raman spectroscopy is widely used as an optical characterization tool for investigating semiconductors in bulk, thin film, nanostructured, and device forms [1–10]. When light interacts with a solid, three main processes can take place: reflection, absorption, and light scattering. The light scattering can be either elastic, when the frequency (energy) of the scattered light remains unaltered, called Rayleigh scattering, or inelastic otherwise. The Raman effect is a phenomenon of inelastic scattering in which phonons, the quasi-particles associated with the elementary excitations of the solid, are either created or absorbed by the incident electromagnetic wave. Lattice vibrations are extremely sensitive to the local atomic structure and lattice environment. As a result, Raman spectroscopy supplies useful information about the physical factors that could disturb the local order or modify the interatomic distances. A high number of fundamental properties of semiconductors can be studied by Raman spectroscopy, e.g., crystal orientation, lattice temperature, symmetry breakdown, strain, and chemical composition, among others. Moreover, electronic properties of semiconductors can also be probed with the use of this technique. Raman spectroscopy emerges as a valuable tool for device development and diagnosis, which is routinely used nowadays in the microelectronics industry, particularly, for the assessment of local stresses in microelectronic devices [11–13], but also for the local lattice temperature assessment in devices under operation [14]. The variety of information provided by Raman spectroscopy combined with the slightly sub-micrometric spatial resolution of the optical microscopy, the relative experimental simplicity, and its non-invasive character, make this an essential tool for the characterization of semiconductors and devices.

From the physical point of view, the Raman effect is based on the coupling of the electromagnetic field of the incident light with the lattice vibrations through an induced electric dipole moment. This can be studied from two different points of view: Classical Electromagnetism and Quantum Mechanics.

2.1.1 Semiclassical Description

The semiclassical description of the Raman effect is based on a purely electromagnetic approach. The analysis starts by representing the incident electromagnetic wave as a monochromatic linearly polarized plane wave:

$$\vec{E}(\omega_i) = \vec{E}_0 e^{i(\vec{k}_i \cdot \vec{x} - \omega_i t)} \tag{2.1}$$

Where $\vec{k}_i$ and ω_i are the wavevector and angular frequency of the incident light, respectively. The EM field will induce a polarization in the material

$$\vec{P}(\omega_s) = \chi \vec{E}(\omega_i) \tag{2.2}$$

This polarization will depend on the material susceptibility tensor χ. The normal modes of the atomic vibrations of the material, Q_j, can be represented as

$$Q_j = Q_{j0} e^{\pm(\vec{q}_j \cdot \vec{x} - \omega_j t)} \tag{2.3}$$

Where $\vec{q}_j$ and ω_j are the wavevector and angular frequency of the normal mode j. At this point, it is useful to perform a Taylor series expansion of the susceptibility tensor χ with respect to the normal modes Q_j

$$\chi = \chi_0 + \sum_j \left(\frac{\partial \chi}{\partial Q_j} \right)_0 Q_j + \frac{1}{2} \sum_{i,j} \left(\frac{\partial^2 \chi}{\partial Q_i \partial Q_j} \right)_0 Q_i Q_j + \dots \tag{2.4}$$

Where the sub-index 0 denotes the value of the magnitude at the point of no atomic movement. Now, by substituting 2.1, 2.3 and 2.4, on 2.2 the polarization vector can be computed

$$\vec{P}(\omega_s) = \chi_0 \vec{E}_0 e^{i(\vec{k}_i \cdot \vec{x} - \omega_i t)} + \vec{E}_0 \sum_j \left(\frac{\partial \chi}{\partial Q_j} \right)_0 Q_{j0} e^{i\left[(\vec{k}_i \pm \vec{q}_j) \cdot \vec{x} - (\omega_i \pm \omega_j) t\right]} + \dots \tag{2.5}$$

The first term of the polarization corresponds to Rayleigh Scattering, because it will produce radiation with the same frequency as the incident one. The second term corresponds to the Raman Scattering.

The scattered wavevector and angular frequency can be identified with the expressions on the exponent of the Raman term, denoted $\vec{k}_s$ and ω_s respectively. By applying energy and momentum conservation, the following equations are obtained

$$\begin{aligned} \hbar\vec{k}_s &= \hbar\vec{k}_i \pm \hbar\vec{q}_j \\ \hbar\omega_s &= \hbar\omega_i \pm \hbar\omega_j \end{aligned} \tag{2.6}$$

The minus and plus signs correspond to the so-called Stokes (S) and Anti-Stokes (AS) radiations, respectively. According to this, S and AS signals will provide the same information and will be symmetric with respect to the Rayleigh radiation, see Figure 2.1. S radiation corresponds to the excitation of a lattice (molecular) vibration, while AS corresponds to the absorption of the same pre-existing vibration.

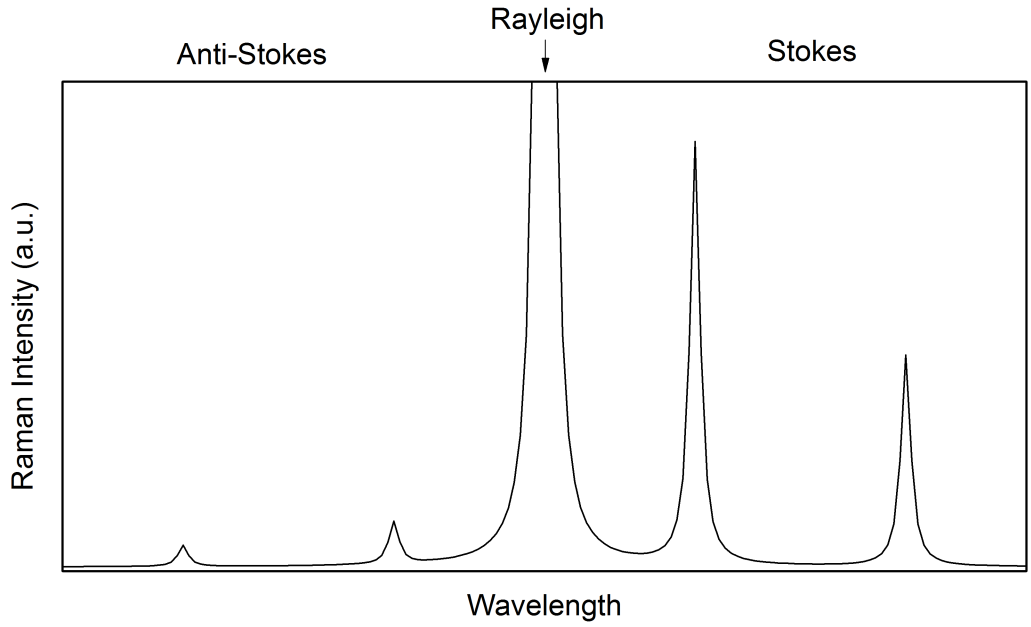

Figure 2.1: Example of an expected Raman spectrum of a simple substance. It shows the symmetric position of Stokes and Anti-Stokes radiations with respect to the Rayleigh radiation, and their different relative intensities.

Once the Raman polarization vector has been computed, Eq. (2.2), the Raman scattering cross-section can be calculated too [1]. The case of the S scattering reads

$$\frac{d\sigma}{d\Omega} = V^2 \omega_s^4 |\vec{e}_i \cdot R \cdot \vec{e}_j|^2 (n+1) \tag{2.7}$$

Where V is the excitation volume, $\vec{e}_i$ and $\vec{e}_j$ are the polarization vectors of the incident and scattered light, respectively, and n is the statistics of lattice vibrations, thus given by the Bose-Einstein distribution. The factor $(n+1)$ is replaced by n for AS scattering. Finally, R is the so-called Raman tensor, which contains all the information about the crystal (molecule) symmetry

$$R \propto \left(\frac{\partial \chi}{\partial Q_j} \right)_0 \tag{2.8}$$

Therefore, R will be a rank-3 tensor. By looking at (2.7) it is trivial that the Raman cross section will be non-zero only if the term $|\vec{e}_i \cdot R \cdot \vec{e}_j|^2 \neq 0$. This term depends on the crystal symmetry, contained in R, and the incident and scattering polarizations. These conditions give rise to systematic extinctions of certain Raman modes under specific laser polarizations and crystalline orientations. The conditions for the extinction of each Raman mode are gathered by the Raman selection rules, which will not be relevant for our experimental conditions. For more information about this, see Chapter 3 of Ref. [15].

2.1.2 Quantum Description

The use of Quantum Mechanics on the study of Raman spectroscopy has an immediate advantage, which is the use of a more powerful mathematical framework. This permits to study effects that cannot be easily explained with the Semiclassical Theory, such as Resonant Raman effects. Another advantage is the possibility of using the concepts of energy levels and (quasi) particles (photons, phonons, electrons, holes, etc.). With the correct use of these tools, the understanding of Raman spectroscopy is highly improved.

In this context, the Raman effect can be understood as the creation (S scattering) or annihilation (AS) of a lattice vibration quantum, i.e., a phonon, by the incident photon. This can also be explained with the help of an energy diagram like the one shown in Figure 2.2. In the case of Rayleigh Scattering, the incident photon excites the system to a higher energy state, which decays to the ground state emitting a photon with the same energy. In the case of S Raman scattering, the system is excited to a higher energy (virtual) state, but the system decays to a vibrationally excited state. As a result, the system emits radiation of lower energy and simultaneously creates a new phonon. Finally, if the system was in a vibrationally excited state at the beginning, when excited by the incident photon it can decay back to the ground state, emitting a higher energy photon while the pre-existing phonon vanishes, producing AS Raman scattering.

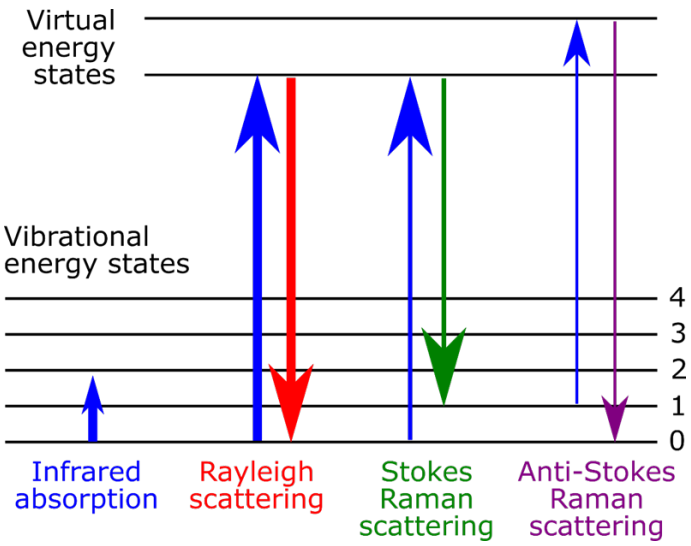

Figure 2.2: Energy Levels for different optical phenomena: Infrared absorption, Rayleigh Scattering, Stokes Raman Scattering and Anti-Stokes Raman Scattering.

In this picture, the main difference between S and AS radiations is crystal clear: AS needs the pre-existence of a phonon to be absorbed, while S does not. As a result, S Raman Scattering is much more probable than the AS one. The respective probabilities will depend on the phonon density, which can be directly calculated with the Bose-Einstein distribution.

$$n = \frac{1}{e^{\left(-\frac{\hbar\omega}{k_B T}\right)} - 1} \tag{2.9}$$

The quantum mechanics framework can easily explain the difference in the n and $(n+1)$ factors of Eq. (2.7). For AS radiation, the factor is n: the larger the number of phonons in the system, the higher is the probability of absorbing one of them. However, for S radiation this factor is $(n+1)$, the factor one accounts for the spontaneous occurrence of the inelastic scattering, while n accounts for the stimulated generation of phonons by the incident light. This relation between S and AS radiations is very useful for the application of Raman spectroscopy as a contact-less thermal probe. The ratio AS/S can be computed from (2.7) and (2.9)

$$\frac{I_{AS}}{I_S} \propto \frac{n}{n+1} = e^{\left(\frac{\hbar\omega}{kT}\right)} \tag{2.10}$$

This relation provides a simple way to measure the temperature of a sample avoiding the use of physical contact. This method is widely used for thermography of devices during operation, and it is possible to measure temperatures with a micrometric resolution if combined with a μ-Raman setup.

Finally, Quantum Mechanics provides another way to compute the Raman scattering probability by the use of Fermi's Golden Rule and third-order perturbation theory. The probability, W_{01}, of a Raman scattering event can be calculated with the following equation

$$W_{01} = \left(\frac{2\pi}{\hbar}\right) \left| \sum_{l,m} \frac{< 0 \,|H_{e-R}(\omega_i)|\, l >< l \,|H_{e-ph}|\, m >< m \,|H_{e-R}(\omega_s)|\, 1 >}{(\hbar\omega_i - \Delta E_{l0})(\hbar\omega_s - \Delta E_{m1})} \right|^2 \times \delta(\hbar\omega_i - \hbar\omega_{ph} - \hbar\omega_s) \tag{2.11}$$

Here $\mid 0 >$ represent the state with no initial phonons (ground state), $\mid l >$ and $\mid m >$ represent all the possible intermediate virtual states where the sum is taken, H_{e-R} and H_{e-ph} are the electron-radiation and electron-phonon terms of the Hamiltonian, respectively, and the δ function accounts for the energy conservation during the process. The physical interpretation of this formula is the occurrence of three "simultaneous" processes: first the absorption of the incident photon, then the creation of a new phonon, and finally the de-excitation of the system emitting a new photon with different energy as the incident one, each step of the process with the corresponding term of the Hamiltonian interaction.

The energies that appear in the denominator, ΔE_{l0} and ΔE_{m1}, represent the energy difference between each pair of involved states. This is one of the critical points of the quantum approach because it permits to account for the Resonant Raman effect. When the incident (or scattered) light energy is close to the energy difference between two stationary states the denominator of Eq. (2.11) will tend to zero, which results in a sharp increase of the Raman scattering cross-section. The most common way to achieve this situation when working with semiconductors is to excite the sample with light of the same wavelength as an interband transition. By doing this, the light will be exciting electrons from the valence band to the conduction band, which are stationary states, thus highly increasing the probability of Raman scattering. As a disadvantage, it will be fairly common that the generated electrons recombine producing photoluminescence (PL) that can overlap with the Raman spectrum making it more challenging to obtain a proper measurement. Therefore, resonance measurements must be done with photons of higher energy than the direct band gap.

2.1.3 Micro-Raman Spectroscopy as a nanoscale probe of the electromagnetic field

As was previously stated, μ-Raman spectroscopy is a powerful non-invasive technique that provides a wide range of information about the structural properties of a material. In this work, μ-Raman Spectroscopy is more than a standard characterization technique: μ-Raman spectroscopy can also be used as a probe of the EM field induced in heterostructured NWs. The dependence of the Raman signal with the excitation laser intensity can be computed from the total Raman scattering cross section (integrating Eq. (2.7) over the solid angle) obtaining the following dependence

$$I_R \propto \sigma I_i \propto |E_i|^2 \tag{2.12}$$

As expected, the dependence of the Raman intensity, I_R, is directly proportional to the excitation light intensity. As a result, it is also equivalent to the square modulus of the electric field of the incident light. This property by itself is not especially interesting; however, it becomes really important when working with NWs, and more in particular with heterostructured NWs, focusing on the study of the transition regions. When the laser beam is illuminating a heterostructured NW, the electromagnetic field adopts a particular distribution inside of it, according to Maxwell equations and the boundary conditions (see next Section). The Raman signal arising from each region will be proportional to the local value of the light intensity in this specific material. Since each material has an exclusive Raman signature on the spectrum, i.e., its phonon energies, the different Raman signals will provide us with information about the value of the EM field in their corresponding volumes.

2.2 Maxwell Equations and Finite Element Methods

In order to better understand the interaction between the incident EM field and the heterostructured NWs, the Maxwell equations have been solved when a laser beam is focused on a heterostructured semiconductor NW.

Typically, these calculations for homogeneous and core-shell heterostructured NWs have been carried out by means of the Lorenz-Mie theory, which provides the analytical solution for the light scattering by an infinitely long dielectric cylinder immersed in a homogeneous and isotropic non-absorbing medium [16]. In the frame of this formalism, the calculation of the absorption and scattering efficiencies, Q_{abs} and Q_{sc} respectively, has revealed a strong dependence of these coefficients with the NW diameter, presenting resonances for specific diameters [17, 18]. For homogeneous and core-shell NWs the translational symmetry along the NW axis allows for the simplification to a 2D problem, making it possible to study the section of the NW perpendicular to its axis. However,

the simulation of axially heterostructured NWs cannot be performed within this 2D approach because of axial symmetry breaking. First, the NWs are finite, which breaks the translational symmetry along its axis. Moreover, the presence of two different materials along the axis breaks the possible remaining specular symmetry. Second, the presence of a substrate under the NW eliminates the isotropy of the space surrounding the NW, thus breaking the cylindrical symmetry. These two features make it impossible to reduce the problem to a simple 2D framework; therefore, a full 3D model was solved. A 3D electromagnetic model was built for axially heterostructured NWs which can be adjusted to have the same characteristics as the NWs used in the experiments: diameter, length, materials, substrate, and position of the HJ. The model solves the Maxwell equations for a Gaussian beam illuminating the heterostructured NW, giving the EM field distribution inside the NW, which allows for the calculation of the expected Raman signal for that specific configuration.

The most general form of the Maxwell equations in vacuum is the following

$$\begin{aligned} \vec{\nabla} \cdot \vec{D} &= \rho \\ \vec{\nabla} \cdot \vec{B} &= 0 \\ \vec{\nabla} \times \vec{E} &= -\frac{\partial \vec{B}}{\partial t} \\ \vec{\nabla} \times \vec{H} &= \vec{j} + \frac{\partial \vec{D}}{\partial t} \end{aligned} \tag{2.13}$$

Where $\vec{E}$ is the electric field, $\vec{D}$ is the electric displacement, $\vec{H}$ is the magnetic field and $\vec{B}$ is the magnetic flux density. The field sources are represented by ρ and $\vec{j}$, charge and current densities, respectively. By solving these equations, the electric and magnetic fields can be obtained if their sources are known. However, when dealing with radiation in the absence of free charges and currents, it is common to reduce Maxwell equations to the Helmholtz equation, which is simpler and much more easily solvable. For this, ρ and $\vec{j}$ are set to zero, and by taking the rotational of the third Maxwell equation on 2.13 and operating, the very well-known wave equation can be found

$$\nabla^2 \vec{E} - \mu\varepsilon \frac{\partial^2 \vec{E}}{\partial t^2} = 0 \tag{2.14}$$

The same equation is satisfied by the magnetic field $\vec{H}$. Note that the magnetic permeability, μ, and electric susceptibility, ε, are those of the material in which the equation is being solved. From here on the materials are supposed to be linear and non-dispersive, otherwise more terms would appear in the equations. Finally, the fields are supposed to have a harmonic dependence with the time component (i.e., Fourier Transform in the time

coordinate is applied to the system): $\vec{E} = \vec{E}_0 e^{-i\omega t}$, which gives the Helmholtz equation

$$\nabla^2 \vec{E} + k^2 \vec{E} = 0 \tag{2.15}$$

where $k = \omega\sqrt{\varepsilon\mu} = \omega(n/c)$ is the wavevector modulus. Usually, all the calculations are performed for the electric field and, if the magnetic field is needed, it can be calculated from $\vec{\nabla} \times \vec{E}$ and the use of the third Maxwell equation on (2.13).

The Helmholtz equation is solved in our model by the Finite Element Methods (FEM) software. The FEM software takes the geometry of the model, Figure 2.3a, and automatically generates a mesh of tetrahedral elements, Figure 2.3b. Then the Helmholtz equation is solved numerically taking the elements of the mesh as evaluation points. As the number of mesh components increases, the result becomes more precise; however, the computational cost of the resolution (both in time and physical memory) increases dramatically. One should look for a compromise between an affordable time cost (hours-days) and a precise solution.

The specific conditions for the solution of the model are listed bellow.

1. Only half of the system is modelled because of the reflection symmetry with respect to the xz-plane. This plane has been set to a Perfect Magnetic Conductor condition, which acts as a mirror for this configuration.

2. The HJ between the two materials is simulated through a "Transition Boundary Condition", which simulates a thin layer of material as compared with the whole system. The properties of the thin layer are set to the intermediate value between the two homogeneous segments.

3. All the system has been surrounded by Perfectly Matched Layers (PMLs) to avoid secondary reflections of the outgoing waves.

4. The complex refractive index $(n + ik)$, or equivalently the complex electric permeability ε, of each material is used as the model input. The values of these magnitudes are summarized in Table 2.1.

The solution of the Helmholtz equation will provide the 3D distribution of the electromagnetic field $\vec{E}(\vec{x})$. For this, the model is fed with a background field, i.e., the laser beam excitation $\vec{E}_b$. If the materials in the model were all vacuum, nothing would happen but the laser beam would be travelling through them. However, the NW will be illuminated by the EM field, and $\vec{E}_b$ by itself will no longer satisfy Eq. (2.15) inside the materials. As a result, the excitation field will induce a scattering field, $\vec{E}_{sc}$, in the system that makes the full field, $\vec{E} = \vec{E}_b + \vec{E}_{sc}$, satisfy the Helmholtz equation again. Then the FEM software solves the Helmholtz equation with the boundary conditions and the background field to find the scattering field, and also the total EM field inside the NW.

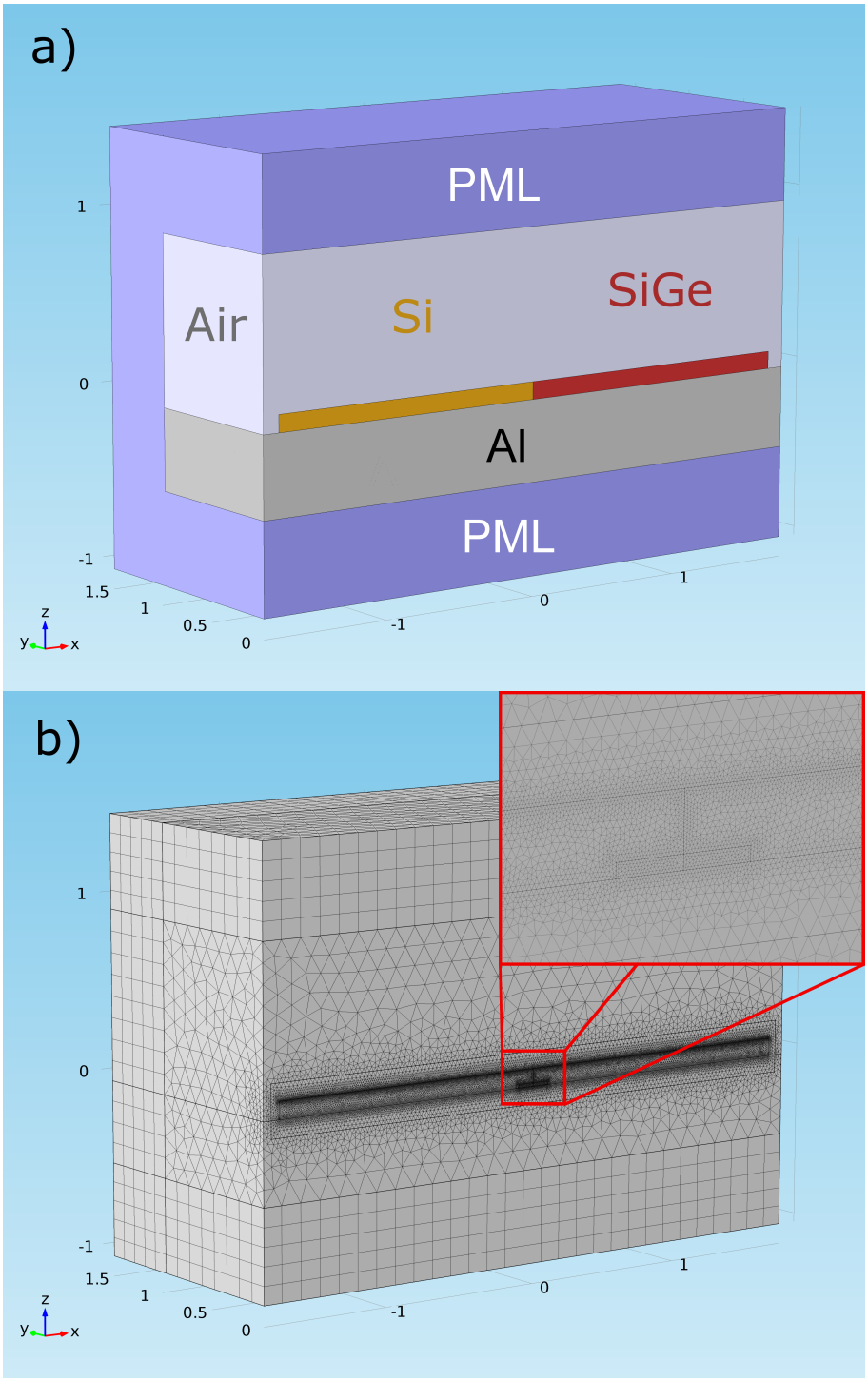

Figure 2.3: Scheme of the FEM model used to perform the EM simulations. a) Geometry and different regions of the model. b) Example of the model mesh used for the computation. The mesh resolution has been increased in certain regions (especially on the HJ) to achieve a higher precision on the solution.

	n	**k**
Au	0.467	2.407
Al	0.93877	6.4195
InAs	4.3736	1.0831
Si	4.1334	0.033258
Ge	4.92436	2.3734
$\mathbf{Si_{1-x}Ge_x}$	$4.1334+0.668619x+1.510779x^2$	$0.033258+0.204615x+1.621028x^2$

Table 2.1: Values of the complex refractive indexes, $n+ik$, used in the FEM model.

The choice of the background field is critical. Typically most of the calculations assume a plane wave excitation. That could be a good approximation for certain experiments with uniform illumination; however when doing μ-Raman measurements, the excitation laser beam is focused in a small region where the spot size is comparable to the size of the NW. In this situation, the distribution of the EM field inside the NW is far from that induced by a homogeneous illumination, and the plane wave approximation is not accurate.

In this work, plane wave illumination was used to obtain simple information about the system and the effect of the HJ on the EM field.

$$\vec{E}_b = E_0 e^{ikz}\vec{u}_x \tag{2.16}$$

However, in order to reproduce the experimental μ-Raman measurements, the background field has been modelled as a linearly polarized Gaussian beam, which is much more accurate than the plane wave. The equation for the field of a Gaussian laser beam propagating along the z-axis is the following [19–22]:

$$\vec{E} = E_0 \frac{w_0}{w(z)} \exp\left[\left(\frac{-r^2}{w^2(z)}\right) + \left(ik\frac{r^2}{2R(z)}\right) + i(kz-\omega t) + i\zeta(z)\right]\vec{u}_x \tag{2.17}$$

where cylindrical coordinates are used, r is the distance to the beam axis (z axis), and z is the position with respect to the focal plane ($z=0$). $R(z)$ is the radius of curvature of the wavefront at z, $\zeta(z)$ is the Gouy phase at z, typical of Gaussian and spherical wavefronts and $w(z)$ is the diameter of the Gaussian spot at z which depends on its value at the focus $w_0 = w(0)$, the so-called waist size.

These three previous functions are defined as follows

$$
\begin{aligned}
w(z) &= w_0\sqrt{1+\left(\frac{z\lambda}{\pi w_0^2}\right)} \\
R(z) &= z\left(1+\left(\frac{\pi w_0^2}{z\lambda}\right)^2\right) \\
\zeta(z) &= \arctan\left(\frac{z\lambda}{\pi w_0^2}\right)
\end{aligned}
\tag{2.18}
$$

When the distribution of the total EM field inside the NW is obtained from the FEM model, the expected Raman signal of each material of the NW can be calculated. The Raman signal emitted by a small volume of the material is proportional to the square of the electric field modulus, $|E|^2$, Eq. (2.12); therefore, once the distribution of the electric field is calculated, the total Raman signal produced by a particular region of the NW will be proportional to the integral of $|E|^2$ over the corresponding probe volume. By computing these integrals, the theoretical intensity of the signal emitted by each region of the NW can be estimated.

Finally, the model can be solved for different positions of the laser beam along the NW axis to reproduce the experimental measurements of a longitudinal laser beam scanning along the NW. In order to do this, the Raman intensities of each NW region are calculated as a function of the incident laser beam position.

2.3 Vapour-Liquid-Solid Method

Chemical Vapour Deposition (CVD) is one of the most extended growth techniques for the fabrication of high-quality semiconductors [23]. It was initially developed as a technique for thin-film coating of surfaces, but it can also be used to produce high-purity bulk materials. CVD involves the flow of precursor gases into a chamber containing the objects to be coated. The samples are heated so that chemical reactions occur on and near the hot surfaces, resulting in the deposition of a thin film on the object surface. As a result of the large variety of materials that can be deposited and the extensive number of applications, there are many variants of CVD depending on several variations of different aspects of the technique. For example, in Metal-Organic CVD (MO-CVD) the precursors are supplied to the chamber as metal-organic compounds, Plasma-Enhanced CVD (PE-CVD) uses plasma to enhance the chemical reaction of the reactants, or Low-Pressure CVD (LP-CVD) uses sub-atmospheric pressures to improve the uniformity of the film [24]. The NWs studied in this work have been manufactured by LP-CVD.

The crystalline structure of semiconductor NWs is always the same as the bulk form, i.e., they do not have any preferential growth direction. This is the principal difference with respect to molecular nanostructures, like graphene or carbon nanotubes, whose structure and dimensionality are determined by their atomic bonds. To obtain a 1-dimensional semiconductor NW, it is necessary to either favour one specific growth direction or to suppress the other two. There are two main approaches to this matter: the first one is by physically limiting the growth dimensions, i.e., using a template or a mask in which the material can only grow in the form of NWs, see Figure 2.4a. The second one, which is more versatile, consists of growing free-standing NWs from a nucleation point, Figure 2.4b. In order to do this, a catalyst droplet is commonly used, as well as a growth substrate, however there exist growing processes that do not need those two conditions. There are several different mechanisms based on free-standing growth by CVD, like Vapour Phase Epitaxy (VPE), Liquid Phase Epitaxy (LPE) or Molecular Beam Epitaxy (MBE) [25]. Nevertheless, the most extended and studied for NWs growth is the Vapour-Liquid-Solid (VLS) method, which will be the one discussed in this work.

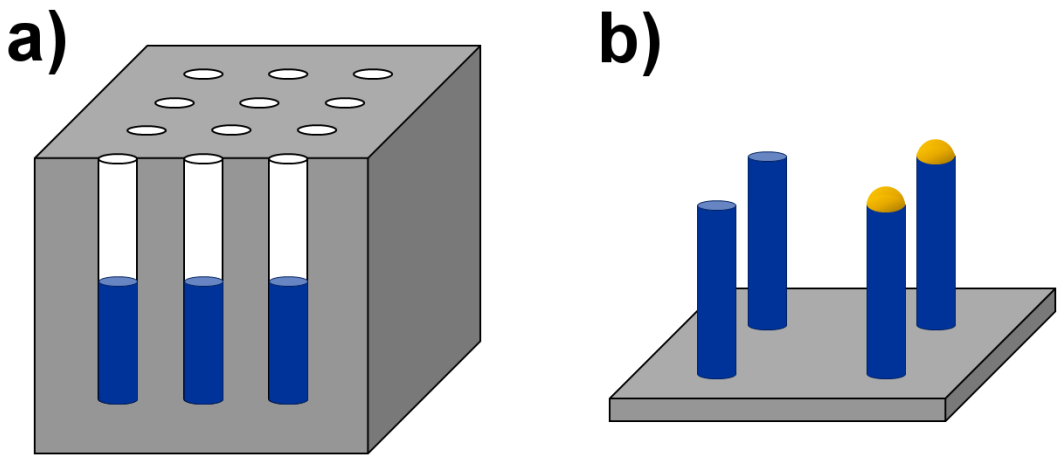

Figure 2.4: a) Example diagram of NW growth with the use of a template. b) Growth of free-standing NWs both with metal catalyst and without it.

2.3.1 Homogeneous NWs growth by VLS

The first NWs obtained by the VLS method were fabricated by Wagner and Ellis, who also proposed for the first time the VLS growth mechanism [26]. They obtained Si whiskers with a diameter of 100 nm grown with Au catalyst droplets. After this work, Givargizov proposed the first VLS model in 1975 [27], and the same method was applied to grow InAs NWs in the 90's [28]. During the last decades, the development and popularization of novel techniques allowed for more profound studies of the VLS method. For example, real-time growth studies by electron microscopy [29], or atomistic studies of the growth process [30].

The Vapour-Liquid-Solid Method is named after the presence of those three phases during the growth process. The vapour phase corresponds to the state of the precursors in the chamber. The liquid phase stands for the alloyed metal catalyst droplet (typically Au). Finally, the solid phase is the NW itself. To better understand the whole process, the growth of Si NWs will be used as an example, following the scheme on Figure 2.5.

The process starts with the precursors, typically SiH_4 or Si_2H_6 for Si NWs, that are supplied in vapour phase at a fixed rate. The precursor undergoes a dissociation process at the catalyst surface [1]. When the precursor molecule dissociates, the atoms of the growing material, Si in this example, are dissolved in the liquid catalyst droplet forming a eutectic mixture, Au-Si alloy. A eutectic system is characterized by a certain composition, the eutectic point, at which the solidification temperature is lower than those of the individual materials forming the alloy. If an alloy with the eutectic composition is cooled (slowly) both materials precipitate in solid form at the same time, usually in a layer-by-layer disposition. If the composition is different from the eutectic one, e.g., 50% for Au-Si, the liquid is cooled until it reaches the liquid alloy/solid Si curve (liquidus line). Then, solid Si will start to be deposited, the Si concentration will decrease, and the system will follow the equilibrium curve up to the eutectic point. The binary phase diagram of the Au-Si system [31] is provided in Figure 2.7a.

In the case of VLS growth, the process takes place at a constant temperature higher than the eutectic point (horizontal coloured line). The process starts in the pure liquid alloy phase, and the Si concentration grows as the precursors are supplied. When the equilibrium line is reached the system is said to be saturated, i.e., no more Si can be dissolved in the liquid droplet, and the material begins to precipitate at the liquid/solid interface making the NW grow. The process continues steadily as long as the precursors are being supplied, keeping the liquid droplet in a supersaturation state.

[1] It is still a matter of controversy if the metal droplet really acts as a catalyst by lowering the dissociation energy of the precursor

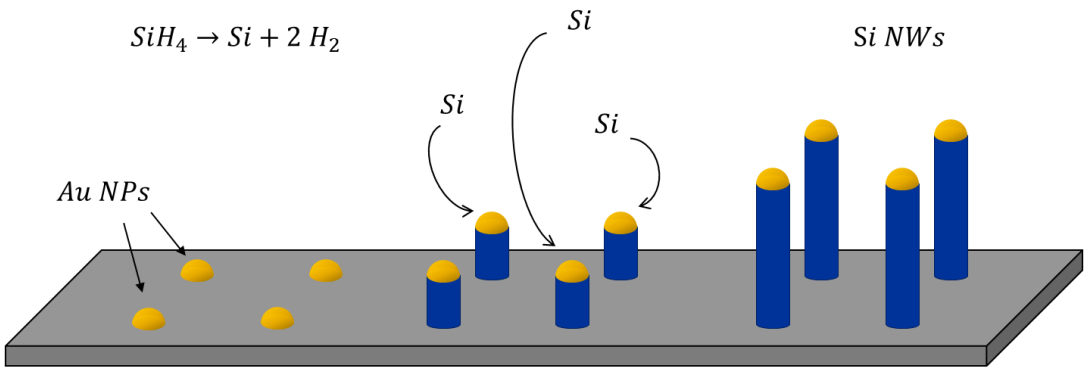

Figure 2.5: Scheme of Si WNs growth by VLS method. Au nanoparticles (NPs) are lying over the substrate. The chamber is fed with the precursor, SiH_4. Si dissolves in the Au droplet and then it is deposited on the catalyst/NW surface making the NW grow.

From the physical point of view, when dealing with processes of matter exchange, the most critical magnitude is the chemical potential μ. The chemical potential will be the driving force guiding the movement of atoms of the growing material. In fact, the attention should be focused on the difference of chemical potential between the liquid and solid phases, which controls either the deposition on the solid phase, making the NW growth, or the dissolution of the solid phase on the liquid, preventing NW growth. When the system is in equilibrium, $\Delta\mu = \mu_L - \mu_S = 0$, the number of atoms being deposited equals the number of them being dissolved. When the precursor dissociates on the liquid droplet new Si atoms are added to the liquid phase, thus increasing μ_L. If the number of dissolved atoms is higher than the solubility limit, the liquid will be supersaturated. In this state, $\Delta\mu > 0$ and the material starts to precipitate at the liquid/solid interface, making the NW grow. If a continuous flow of precursor is kept, the supersaturation state can be maintained, resulting in a constant growth rate.

It is important to note that the growth process takes place strictly out of equilibrium, since $\Delta\mu \neq 0$. This concept will prove very important later on, being a key point for the correct understanding of the HJ transition process. Mathematically, the dependence of $\Delta\mu$ on a system of two components is relatively simple

$$\Delta\mu = k_B T \log\left(\frac{C}{C_0}\right) \tag{2.19}$$

It depends on the temperature T and the composition of the liquid phase C, k_B stands for the Boltzmann constant and C_0 is the reference concentration. In this case, the reference concentration is that of the liquid/(solid + liquid) equilibrium (at which $\Delta\mu = 0$), it depends on temperature and can be computed from the binary phase diagram, Figure 2.7.

2.3.2 Heterostructured NWs growth by VLS

HJs are essential for device applications, and semiconductor NWs are not an exception. However, their use for device applications requires the presence of very abrupt HJs and, in order to achieve this, it is necessary to control the HJ growth process.

In the framework of the VLS method, the manufacture of axial heterojunctions during the NW growth is, a priori, quite straightforward; however, controlling this process in a precise manner is not even close to being simple. The growth of a heterostructured NW starts by growing a first segment of the NW by standard VLS, as explained in the previous section. To obtain a heterojunction, the fluxes of the precursors should be changed at a certain point, so that, a segment of a different material starts to grow following the first one. Figure 2.6 shows a scheme of an HJ growth process for a Si/SiGe NW. First, the Si segment is grown by keeping a constant flow of, for example, SiH_4. When the Si segment is long enough the GeH_4 flux is switched on, Ge reaches the liquid droplet, and a SiGe segment of the corresponding composition starts to grow. The final result is the desired heterostructured NW made of two different sections, in this example a Si/SiGe NW.

The versatility of this method lies in the possibility of adjusting the fluxes of the precursors to create many different types of HJs. For example, the process can start by growing Ge and then change to pure Si to obtain a Ge/Si NW. As well, NWs with more than one HJ can be created, like the SiGe/Si/SiGe NWs studied in this work. Moreover, the VLS method can be extended to a great variety of semiconductors. The combinations are only limited by our imagination and our control over the physics involved in the process.

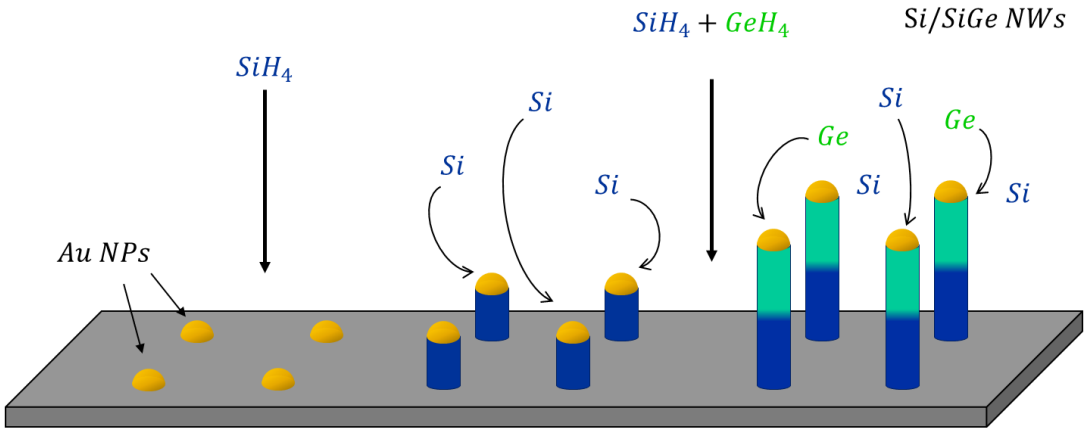

Figure 2.6: Scheme of the growth of Si/SiGe axially heterostructured NWs by VLS. The process starts by growing a Si NW, at a certain point, the Ge precursor is injected in the chamber. From this point on SiGe starts growing, forming the HJ and then the second SiGe segment.

As has been stated, the process is conceptually very simple, but it is not easy to control. Changes in the reactants partial pressures or slight differences in the chamber temperature when the fluxes are changed are fairly common. These fluctuations have a direct repercussion on the final result of the NW growth process. Typically, these variations can produce changes in the NW growth direction, inhibiting straight NW growth, modify the catalyst volume, which result in NW diameter changes, or even the suppression of the NW growth. Hence, a correct understanding of the VLS process is mandatory to control NW growth and obtain NWs with the desired properties.

The main difficulty lies in the non-linearity of thermodynamics when more than two components are present. For example, when a mixture of two liquids is studied, the entropy is not simply the sum of the individual liquids entropies, and a new term should be added regarding the entropy of mixing. In a similar fashion, when there are two or more different precursors, the chemical potential of each component in the liquid phase depends on the concentration of the other elements. In the case of Si and Ge with Au catalyst, the chemical potential can be computed as follows [32, 33]:

$$\Delta\mu_k = \mu_k^{pL} + k_B T \log C_k + \omega_{kj}(C_j)^2 + \omega_{kAu} C_{Au}^2 + C_j C_{Au}(\omega_{kj} + \omega_{kAu} - \omega_{jAu}) - \mu_k^S \quad (2.20)$$

Where the index k accounts for the corresponding atomic species (Si, Ge) and j stands for the other element (Ge, Si). The ω parameters account for the interatomic interactions in the liquid phase and depend on basic atomic properties [32]. The values of μ_k^{pL}, the chemical potential of the pure liquid, and μ_k^S, chemical potential in the solid phase, cannot be individually determined. However, their difference can be computed with the use of the binary phase diagrams, Figure 2.7. When the concentration of one of the components is set to zero, e.g., C_{Ge}, the dynamics should be that of the resulting binary compound (Au/Si), and from Figure 2.7 the concentration at which $\Delta\mu_k = 0$ is known, i.e., C_0 on equation (2.19). With this manipulation, the difference $(\mu_k^{pL} - \mu_k^S)$ can be computed for each material, and the remaining parameters can be determined.

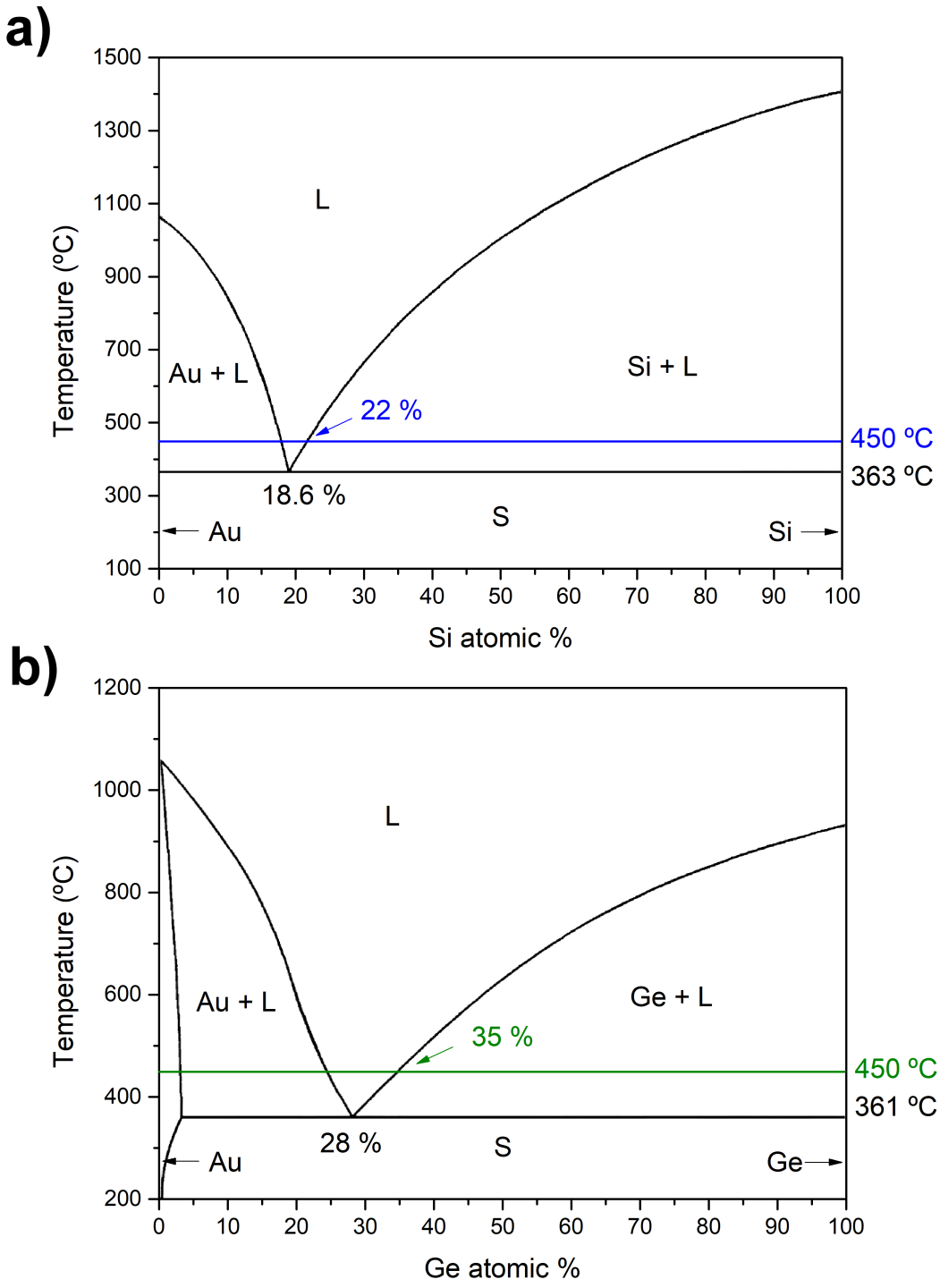

Figure 2.7: Binary phase diagrams of: a) Au/Si alloy, b) Au/Ge alloy. The colour lines represent the temperature at which VLS growth takes place. The intersection with the liquidus line gives the equilibrium concentration, C_0.

2.3.3 Si/III-V heterostructured NWs

As it has been shown, the VLS method is highly versatile, allowing for the growth of axially heterostructured NWs by merely changing the precursor gases during the growth process. This technique has proven to be very useful to grow heterojunctions of semiconductors with similar growth conditions, like Si and Ge or GaAs and $Al_xGa_{1-x}As$. However, it is not straightforward to change from a material like Si to another one with entirely different properties like GaAs. In fact, this kind of heterostructures is also very challenging even for other epitaxial growth techniques.

The major problem when trying to create a heterojunction of two different materials is the lattice mismatch. If the difference between the lattice parameters of the two materials is not small enough, after a certain number of primitive cells, mechanical stresses are relaxed. This results in the generation of dislocations or stacking faults, which diminish the crystalline quality, spoiling the whole growth process and consequently, the final properties of the material. In the case of group IV and III-V heterojunctions, there is another problem that prevents the easy integration of these semiconductors. Group IV semiconductors, like Si or Ge, are non-polar materials, i.e., their structure is given by covalent bonds. On the other hand, III-V semiconductors, like GaAs, InAs, etc., are always polar, because their bonds present a certain degree of ionic character. This makes the two types of semiconductors highly incompatible.

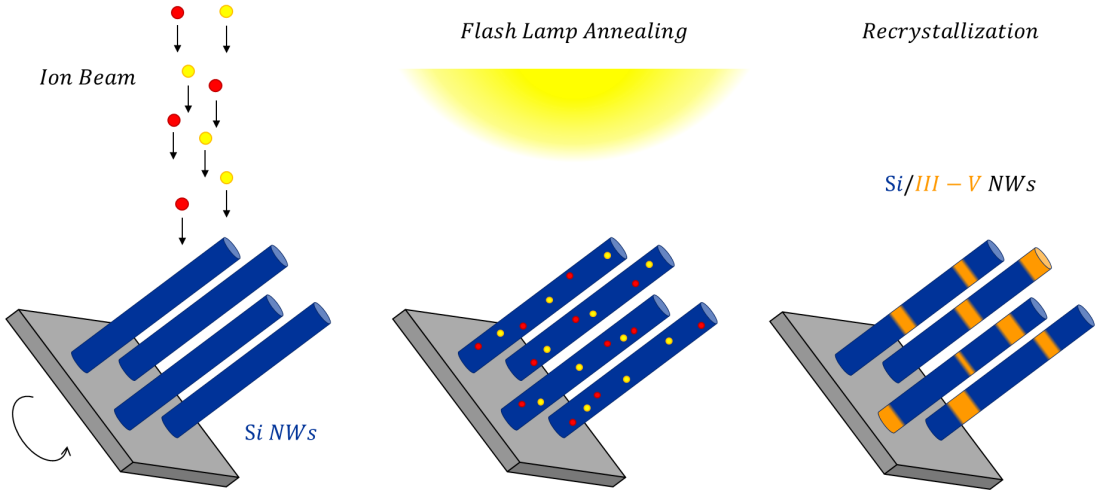

Figure 2.8: Scheme of the growth process of Si/III-V axially heterostructured NWs. The process starts by growing Si NWs by VLS; these NWs undergo an ion implantation process with the atoms of the III-V compound. Finally, the NWs are subjected to a flash annealing that triggers the diffusion of the III-V atoms and the recrystallization of the subsequent III-V segments along the Si NW.

Different approaches can be found to overcome this problem, like, for example, the defect-free nucleation of the III-V compound over a Si substrate [34] or directly by VLS method performing growth interruption [35]. For the growth of the Si/III-V heterostructured NWs studied in this thesis, a different process has been followed. The procedure starts with Si NWs grown by standard VLS method, as explained in the previous section. These Si NWs undergo an ion implantation process during which the atoms of the III-V compound, e.g., Ga and As, are introduced in the Si lattice. After this, the NWs are subjected to a flash lamp annealing (FLA) process. The NWs are illuminated with an optical flash of several milliseconds. During this last step, the high temperature induced in the material by the optical absorption allows for the fast diffusion of the implanted III-V atoms, which recrystallize forming the III-V segments. To maintain the NW integrity during the annealing process, the Si NWs are usually covered with a 20 nm SiO_2 layer, deposited by plasma enhanced chemical vapour deposition (CVD). A scheme of the whole process is summarized in Figure 2.8.

The Si/III-V heterostructured NWs studied in this thesis have been manufactured by the group of Alois Lugstein in the Technical University of Wien. In order to achieve a homogeneous implantation profile along the NWs, the samples were placed on a 45° tilted and continuously rotating stage during the ion implantation. In, Ga and As ions were implanted with an energy around 100 keV. The flash lamp annealing step was performed with a flash energy of about $50\,J^2\,cm^{-1}$. Si/GaAs, Si/InAs, and Si/InGaAs heterostructured NWs were respectively obtained. For further information about the manufacture of this kind of NWs see Refs. [36] and [37].

2.4 Fourier Transform

Fourier Transform (FT) is a handy mathematical tool extensively used in physics. The Fourier Transform of a particular function of time provides the decomposition of that function into its component frequencies. From a mathematical point of view, the Fourier Transform is a complex-valued function of frequency, the value of its modulus for a certain frequency represents the amount of that frequency contained in the original function. FT has a high number of applications such as analysis of differential equations (see the calculation of the wave equation in the previous section), signal processing, or spectroscopy, e.g., Fourier Transform Raman Spectroscopy or Fourier Transform Infrared Spectroscopy (FTIR)). Apart from these applications, the Fourier Transform is essential in fields like Quantum Mechanics. For example, the Heisenberg uncertainty principle is a direct consequence of the properties of FT as applied to any pair of canonical coordinates time-energy, position-velocity, etc.

The Fourier Transform of a function of time $f(t)$ can be defined as [38]

$$F(\omega) = \frac{1}{\sqrt{2\pi}} \int_{-\infty}^{\infty} f(t) e^{-i\omega t} dt \tag{2.21}$$

If the inverse operation is applied on $F(\omega)$ it restores the original function. Inverse Fourier Transform can be determined by the following definition

$$f(t) = \frac{1}{\sqrt{2\pi}} \int_{-\infty}^{\infty} F(\omega) e^{i\omega t} d\omega \tag{2.22}$$

Note that angular frequency $\omega = 2\pi\nu$ was used instead of frequency ν. A change between these two variables in equations 2.21 and 2.22 is straightforward. FT can also be applied to other variables provided that they form a pair of canonical coordinates, e.g., position x and linear momentum p (or wavevector $k = \hbar p$).

In Chapter 7, FT is applied to the complex-valued electric field distribution in 3D space $\vec{E}(\vec{x})$. As a result, the components in $\vec{k}$-space of the electric field distribution, $\vec{E}(\vec{k})$, can be obtained.

$$\vec{E}(\vec{k}) = \frac{1}{(2\pi)^{3/2}} \int \vec{E}(\vec{x}) e^{-i\vec{k}\cdot\vec{x}} d^3\vec{x} \tag{2.23}$$

In this case, the integral is taken over the whole real space $\mathbb{R}^3$.

2.4.1 Fast Fourier Transform

The theory mentioned above is useful when the function that is being studied is analytic. However, this is not always the case. For example, in signal analysis, the information is usually recorded with a certain sampling rate, which provides a finite array of function values and acquisition times. The electromagnetic field that will be studied in this work is computed by FEM. The output consists of an array of complex values of the electric (and magnetic) field. The fields are evaluated on a finite number of points defined by the FEM mesh. In this kind of situation, FT can still be used; however, its implementation is forcefully numerical instead of analytical. For this purpose, the Discrete Fourier Transform (DFT) can be defined in a similar way to Eq. 2.21, but replacing the integral by a sum:

$$F_k = \sum_{n=0}^{N-1} f_n e^{-i2\pi kn/N} \tag{2.24}$$

Where N is the total number of points and n and k are the indexes of real and transformed data, respectively.

To improve the performance of this calculation (especially for large amounts of data), several algorithms have been developed. These algorithms are referred to as Fast Fourier Transform (FFT), which require computation times of the order of $O(N \log N)$, whereas the direct solution of Eq. 2.24 takes a time of the order of $O(N^2)$.

In this work FFT calculations were performed by using the software Matlab, taking advantage of its built-in FFT functions [39].

FFT allows the study of the EM field components, thus helping to understand the effect of the HJ on the EM field distribution and the light/NW interaction.

Bibliography

[1] M. Cardona, G. Guntherodt. *Light Scattering in Solids I-VI*. Springer Verlag, Heildelberg (1975)

[2] P. Brüesch. *Phonons: Theory and Experiments I*. Springer Verlag, Berlin (1982)

[3] F. H. Pollak. *Analytical Raman Spectroscopy*. J. Wiley, New York (1991)

[4] W. Richter. *Resonant Raman Scattering in Semiconductors*. Springer Verlag, Berlin (1967)

[5] G. Abstreiter, E. Bauser, A. Fischer, K. Ploog. Raman spectroscopy-A versatile tool for characterization of thin films and heterostructures of GaAs and AlxGa1-xAs. *Applied Physics*, **16** (4), 345–352 (1978). doi:10.1007/BF00885858

[6] B. Prevot, J. Agner. Raman characterization of semiconducting materials. *Prog. Crystal Growth and Charact.*, **22**, 245–319 (1991)

[7] I. Zardo, G. Abstreiter, A. Fontcuberta. Raman Spectroscopy on Semiconductor Nanowires. In P. Prete, Herausgeber, *Nanowires*, March, S. 227–254. InTech, Rijeka (2010). ISBN 9789537619794. doi:10.5772/3457

[8] R. L. McCreery. *Raman Spectroscopy for Chemical Analysis*. J. Wiley, New York (2000)

[9] I. R. Lewis, H. Edwards, Herausgeber. *Handbook of Raman Spectroscopy: From the Research Laboratory to the Process Line*. Dekker, New York (2001)

[10] C. S. S. R. Kumar, Herausgeber. *Raman Spectroscopy for Nanomaterials Characterization*. Springer Verlag, Berlin-Heilderberg (2012)

[11] I. De Wolf, H. E. Maes, S. K. Jones. Stress measurements in silicon devices through Raman spectroscopy: Bridging the gap between theory and experiment. *Journal of Applied Physics*, **79** (9), 7148–7156 (1996). doi:10.1063/1.361485

[12] I. De Wolf. Stress measurements in Si microelectronics devices using Raman spectroscopy. *Journal of Raman Spectroscopy*, **30** (10), 877–883 (1999). doi:10.1002/(SICI)1097-4555(199910)30:10<877::AID-JRS464>3.3.CO;2-X

[13] T. Tada, V. Poborchii, T. Kanayama. Study of stress distribution in a cleaved Si shallow trench isolation structure using confocal micro-Raman system. *Journal of Applied Physics*, **107** (11), 113539 (5pp) (2010). doi:10.1063/1.3437628

[14] S. Todoroki. Influence of local heating on current-optical output power characteristics in Ga1-xAlxAs lasers. *Journal of Applied Physics*, **60** (1), 61–65 (1986). doi:10.1063/1.337628

[15] J. Jimenez, J. W. Tomm. *Spectroscopic Analysis of Optoelectronic Semiconductors*, Band 202. Springer Verlag, Switzerland (2016). ISBN 978-3-319-42347-0. doi:10.1007/978-3-319-42349-4

[16] G. Brönstrup, N. Jahr, C. Leiterer, A. Csáki, W. Fritzsche, S. Christiansen. Optical Properties of Individual Silicon Nanowires for Photonic Devices. *ACS Nano*, **4** (12), 7113–7122 (2010)

[17] J. Anaya, J. Jimenéz, A. Rodriguez, T. Rodriguez. Electromagnetic interaction between a laser beam and semiconductor nanowires deposited on different substrates: Raman enhancement in Si Nanowires. *MRS Symp. Proc.*, **1627** (2014)

[18] F. J. Lopez, J. K. Hyun, U. Givan, I. S. Kim, A. L. Holsteen, L. J. Lauhon. Diameter and Polarization-Dependent Raman Scattering Intensities of Semiconductor Nanowires (2012). doi:10.1021/nl204537d

[19] J. Anaya Calvo. *Transporte térmico y caracterización Raman de Nanohilos Semiconductores de Silicio-Germanio*. Dissertation, Universidad de Valladolid (2013). doi:10.35376/10324/4451

[20] O. Svelto, D. David, C. Hanna. *Principles of lasers*. Springer, Heilderberg, 5th Auflage (2010)

[21] B. E. A. Saleh, M. C. Teich. *Fundamentals of Photonics*. John Wiley & Sons, New York (1991)

[22] M. V. Berry. The electric and magnetic polarization singularities of paraxial waves. *Journal of Optics A: Pure and Applied Optics*, **6** (5), 475–481 (2004). doi:10.1088/1464-4258/6/5/030

[23] C. F. Powell, J. H. Oxley, J. M. Blocher. *Vapor Deposition*. Wiley, New York (1966)

[24] R. S. Rosler. Low pressure CVD production processes for poly, nitride, and oxide. *Solid State Technol.*, **20**, 63–70 (1977)

[25] K. A. Dick. A review of nanowire growth promoted by alloys and non-alloying elements with emphasis on Au-assisted III-V nanowires. *Progress in Crystal Growth and Characterization of Materials*, **54** (3-4), 138–173 (2008). doi:10.1016/j.pcrysgrow.2008.09.001

[26] R. S. Wagner, W. C. Ellis. Vapor-Liquid-Solid Mechanism of Single Crystal Growth. *Applied Physics Letters*, **4** (5), 89–90 (1964). doi:10.1063/1.1753975

[27] E. Givargizov. Fundamental Aspects of Vls Growth. *Journal of Crystal Growth*, **31**, 20–30 (1975). doi:10.1016/B978-1-4831-9854-5.50006-9

[28] M. Yazawa, M. Koguchi, A. Muto, M. Ozawa, K. Hiruma. Effect of one monolayer of surface gold atoms on the epitaxial growth of InAs nanowhiskers. *Applied Physics Letters*, **61** (17), 2051–2053 (1992). doi:10.1063/1.108329

[29] F. M. Ross. Controlling nanowire structures through real time growth studies. *Reports on Progress in Physics*, **73** (11), 114501 (2010). doi:10.1088/0034-4885/73/11/114501

[30] H. Wang, L. A. Zepeda-Ruiz, G. H. Gilmer, M. Upmanyu. Atomistics of vapour-liquid-solid nanowire growth. *Nature Communications*, **4** (1), 1956 (2013). doi:10.1038/ncomms2956

[31] T. B. Massalski. *Binary Alloy Phase Diagrams*. ASM International: Metals Park, Ohio, 2nd Auflage (1990). ISBN 978-0-87170-403-0

[32] G. B. Stringfellow. Calculation of ternary phase diagrams of III-V systems. *Journal of Physics and Chemistry of Solids*, **33** (3), 665–677 (1972). doi:10.1016/0022-3697(72)90075-3

[33] F. Glas. Chemical potentials for Au-assisted vapor-liquid-solid growth of III-V nanowires. *Journal of Applied Physics*, **108** (7), 073506 (2010). doi:10.1063/1.3488908

[34] K. Volz, A. Beyer, W. Witte, J. Ohlmann, I. Nmeth, B. Kunert, W. Stolz. GaP-nucleation on exact Si (0 0 1) substrates for III/V device integration. *Journal of Crystal Growth*, **315** (1), 37–47 (2011). doi:10.1016/j.jcrysgro.2010.10.036

[35] M. Hocevar, G. Immink, M. Verheijen, N. Akopian, V. Zwiller, L. Kouwenhoven, E. Bakkers. Growth and optical properties of axial hybrid III-V/silicon nanowires. *Nature Communications*, **3**, 1–6 (2012). doi:10.1038/ncomms2277

[36] S. Prucnal, M. Glaser, A. Lugstein, E. Bertagnolli, M. Stöger-Pollach, S. Zhou, M. Helm, D. Reichel, L. Rebohle, M. Turek, J. Zuk, W. Skorupa. III-V semiconductor nanocrystal formation in silicon nanowires via liquid-phase epitaxy. *Nano Research*, **7** (12), 1769–1776 (2014). doi:10.1007/s12274-014-0536-6

[37] M. Glaser, A. Kitzler, A. Johannes, S. Prucnal, H. Potts, S. Conesa-Boj, L. Filipovic, H. Kosina, W. Skorupa, E. Bertagnolli, C. Ronning, A. FontcubertaMorral, A. Lugstein. Synthesis, Morphological, and Electro-optical Characterizations of Metal/Semiconductor Nanowire Heterostructures. *Nano Letters*, **16** (6), 3507–3513 (2016). doi:10.1021/acs.nanolett.6b00315

[38] R. Bracewell. *The Fourier Transform and Its Applications*. McGraw-Hill, 3rd Auflage (1963). ISBN 0-07-116043-4

[39] https://es.mathworks.com/help/matlab/ref/fft.html

Chapter 3

Pick a flower on Earth and
you move the farthest star
- Paul Dirac -

Experimental and Samples

The heterostructured semiconductor NWs studied in this work were manufactured by three different groups. The groups of Tomás Rodríguez, Universidad Politécnica de Madrid, and Thierry Baron, Université de Grenoble, prepared the Si/SiGe NWs, with lower and higher Ge content, respectively. The group of Alois Lugstein, Technical University of Wien, manufactured the Si/III-V NWs. The specific details about both growth methods can be found in the previous chapter, Section 2.3.

The NWs are supplied upstanding on their growth substrate. In order to perform Raman measurements on individual NWs, they were removed from the substrate and deposited on an Al coated SiO_2 substrate. For this, the growth substrate full of NWs is submerged in methanol and placed in an ultrasonic bath for several minutes. The ultrasounds break the NWs on their base, separating them from the substrate and remaining suspended in the methanol solution. Next, the NWs are transferred onto the Al-coated substrate by drop-casting of the NW-methanol suspension. Finally, the solvent evaporates leaving the NWs lying flat over the Al. The full process is summarized in Figure 3.1.

The Al coated SiO_2 substrates are previously prepared by sputtering of Al over a thermally oxidized Si wafer ($\approx$ 300 - 400 nm of SiO_2). During the Al deposition, a mask is used to obtain either circular or square patterns of several hundreds of μm to ease the later localization of each individual NW. The Al layer is thick enough to block all the Raman signal that could be generated in the Si/SiO_2 substrate. Moreover, Al homogeneously covers the substrate without the presence of Al islands. This is very important to rule out any possible plasmonic effect during the Raman measurements. The use of an Al coated substrate will prove to be very important for the μ-Raman Spectroscopy experiments, as will be explained throughout this chapter.

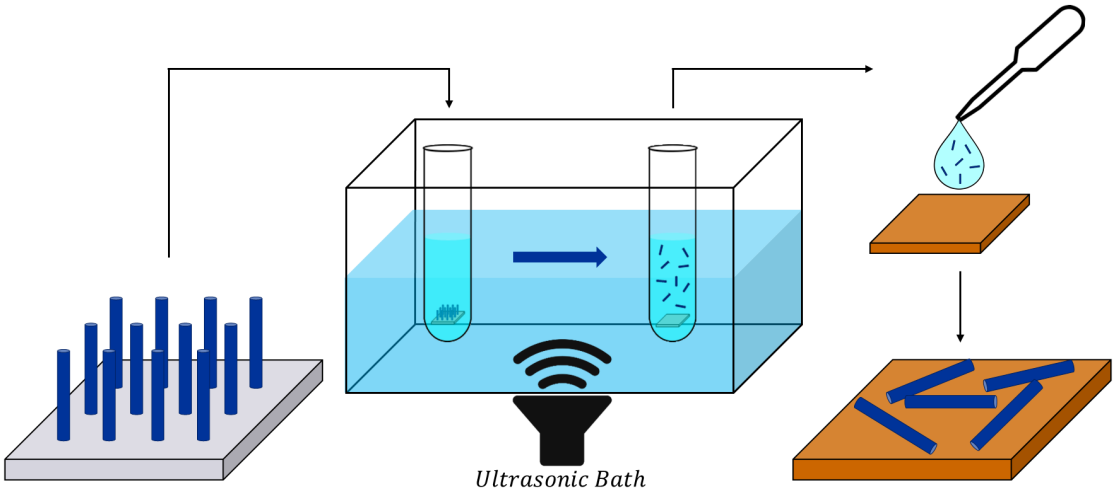

Figure 3.1: Scheme of the sample preparation. The as-grown NWs sample is submerged in methanol on an ultrasonic bath. The ultrasounds separate the NWs from the substrate, leaving them suspended in the methanol. Finally, the NWs in the suspension are deposited on the final substrate by drop-casting.

3.1 Scanning Electron Microscopy

In order to obtain proper and reliable Raman measurements, it is essential to know the morphology and environment of each studied NW. For this, the samples are examined by Scanning Electron Microscopy (SEM). This permits to ascertain the NW length, diameter, structure and the presence of any other features near the NW (like other NWs or contamination) that could disturb future measurements. Two different types of equipment have been used for this purpose: a field emission SEM, FESEM LEO 1530 Carl-Zeiss, used for fast assessment of the NWs, and an Environmental SEM, FEI Quanta 200FEG, with better image resolution used to measure the diameter and structure of the most interesting NWs as well as obtaining higher resolution microscopy images.

The later microscope is also equipped with an Energy Dispersive X-ray Spectroscopy (EDX) module. This characterization technique records the X-ray emission induced by the electron beam. The high energy electrons can excite electrons of the inner shells of the material's atoms, leaving an electron hole. Then, another electron decays to this lower energy state. These transitions result in an X-ray emission spectrum, which is unique of each atomic species. It is possible to use the excitation precision of the SEM with the analysis of the X-ray spectrum to obtain a nanometric resolution measurement of the NWs composition. This will be very important for a precise determination of the HJ region length. A proper ascertainment of this magnitude is essential to understand the enhancement of the Raman signal and to verify the HJ growth model of Chapter 6.

3.2 μ-Raman Spectroscopy

μ-Raman spectroscopy is the keystone of this work since it will let us study how the EM field distributes inside the heterostructured NWs. The equipment used for these measurements is a LabRam UV-HR 800 spectrometer from Horiba (Jovin Yvon). Its focal length is 0.8 m, the available laser excitations are 325, 532, and 633 nm. The vast majority of the measurements were done with the 532 nm light, obtained from a frequency doubled continuous wave (CW) Nd: YAG. The illumination and light collection is performed in a backscattering configuration through a 100x objective (0.95 NA). Two different diffraction gratings are used, depending on the needed spectral resolution: 1200 and 2400 lines/mm. Finally, the signal is recorded by a liquid nitrogen cooled Charge Coupled Device (CCD). As it was explained before, the NWs are lying on the Al substrate, then, the direction in which illumination takes place is always perpendicular to the NW axis. Regarding the incident laser polarization, it is always chosen to be parallel to the NWs axis (TM polarization) to obtain the maximum Raman signal.

It is important to note the relevance of the Al substrate, which has two different purposes for the Raman measurements. On the one hand, the Al is metallic and reflects both the incident and scattered radiation. This improves the signal collection in the backscattering configuration as compared to a transparent substrate like SiO_2. In fact, the interaction of the radiation with the substrate is not as simple as a reflection; nevertheless, the Raman signal can be highly improved by the use of a suitable substrate [1]. On the other hand, the Al substrate plays another fundamental role. The heat dissipation of semiconductor NWs is known to be highly reduced as compared with their bulk form [1]. Then, the excitation laser beam can induce heating in the NW that will be inefficiently dissipated. This has a direct and dramatic repercussion on the Raman signal by modifying the Raman bands and interfering with the later interpretation of the spectra. The presence of such an excellent thermal conductor like Al under the NWs enables a new route to dissipate the heat induced in the NWs by the laser absorption. As a result, the studied NWs can maintain a reasonably low temperature during Raman measurements if the laser power is low enough. Moreover, adequate laser power is higher for Al than for any other non-metallic substrate, improving the quality of the recorded Raman signal.

The measurements on the studied NWs are initially performed as single spectra on different points of the NWs. This aims to ascertain the NW composition and structure (presence of different materials and HJs). Next, a more in-depth study of the most interesting NWs is carried out by performing more detailed linear scans both along and across the NWs. The measurement step is chosen to ensure the maximum precision of the motorized stage, 200 nm for our experimental setup. This results in a significant number of Raman spectra (typically around 50) that should be analysed for each NW.

3.3 Raman Spectra Analysis

As anticipated, the high number of recorded Raman spectra for each NW scan is relatively large, which makes the analysis and representation of the results a real challenge. In order to present the results in the best possible way, all the spectra are subject to standard spectrum analysis. Each spectrum is fitted by a set of Lorentzian peaks depending on the Raman bands of the studied material. The fit provides as output parameters the Raman Shift, full width at half maximum (FWHM), height, and integrated area (Raman Intensity) of each Raman peak. Then, this magnitudes can be represented as a function of the incident laser beam position. The most representative data is the Raman intensity, as it can give us information about the variations of the Raman intensity for different illumination points along the NW, thus revealing the presence of either local enhancement or quenching. However, the other magnitudes must not be forgotten since they inform us about the nature of each peak and the reliability of the measurement, as well as other effects such as heating or disorder.

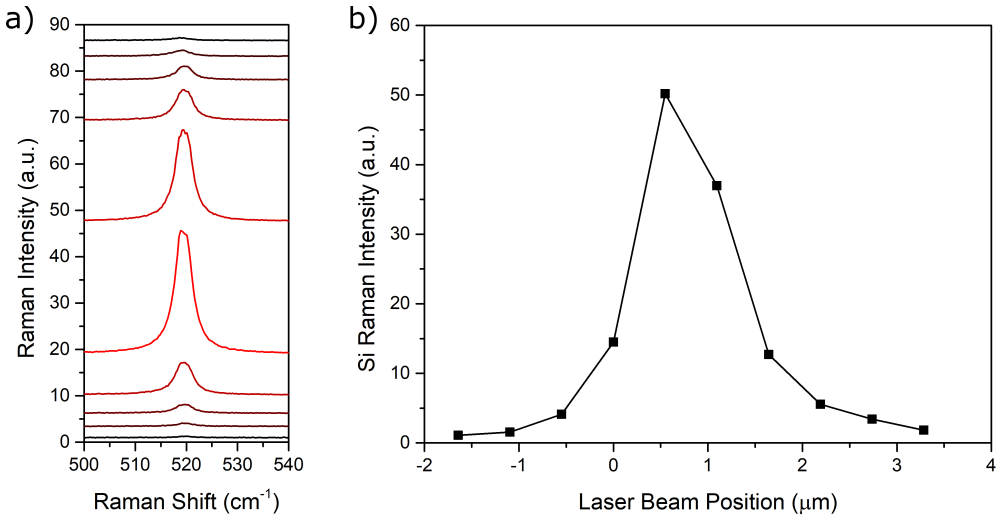

Figure 3.2: Example of the Raman spectra analysis on the transversal scan of a Si NW. a) Raw Raman spectra obtained for different positions of the laser beam across the NW. b) Integrated Si Raman signal as a function of the laser position obtained from the data plotted in a). In this simple case, the maximum corresponds to the illumination of the NW by the central region of the Gaussian spot, then the signal decays in both directions as the laser beam moves away from the NW.

3.4 Reference Raman Spectra

The final section of this chapter is intended to show reference Raman spectra of the different materials that will appear throughout this work. At the end of this last section Table 3.1 summarizes the Raman bands of all these materials.

3.4.1 Si

Silicon is a very well characterized material [2], apart from its great variety of applications, it is known for being the keystone of modern electronics. Silicon is commonly used In Raman spectroscopy as a reference sample for the calibration of spectrometers. It presents an excellent Raman intensity and cheap samples with outstanding crystalline quality are extraordinarily easy to obtain. Moreover, its first order Raman spectrum consists of only one peak, because of the degeneracy of the longitudinal (LO) and transversal (TO) optical modes at the Brillouin Zone Centre. This Raman peak is located at $\omega_{Si} = 520.6\,\mathrm{cm}^{-1}$ and can be observed in Figure 3.3. In addition to the clear first order Raman peak, there is a much weaker Raman band around $300\,\mathrm{cm}^{-1}$. This peak is associated with a second-order Raman scattering process, that involves the creation of two transverse acoustic (TA) phonons and will be referred to as Si (2TA).

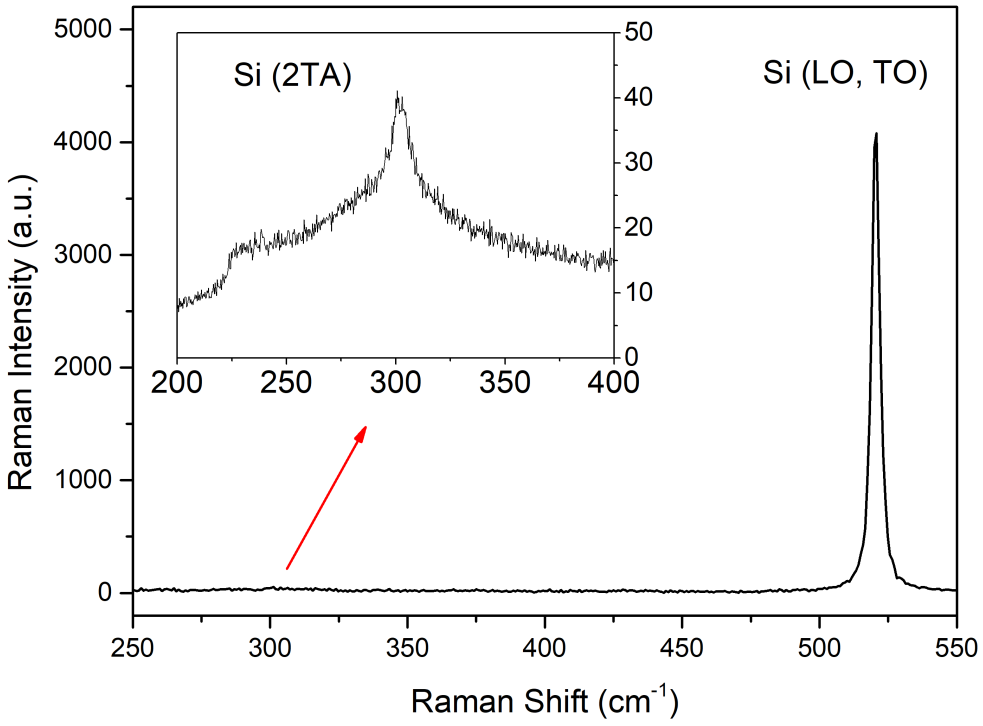

Figure 3.3: Raman spectra of bulk Si used as a reference.

3.4.2 Ge

Germanium is a group IV semiconductor like Si. The Raman spectrum of both materials are very similar, presenting only one degenerate peak, but Ge atoms are heavier than Si ones. Then, the vibrational frequency between Ge atoms will be smaller than that of Si atoms, and so will be the corresponding phonon energy. As a result, the degenerate Ge (LO, TO) peak can be observed at $\omega_{Ge} = 298\,\mathrm{cm}^{-1}$ [2].

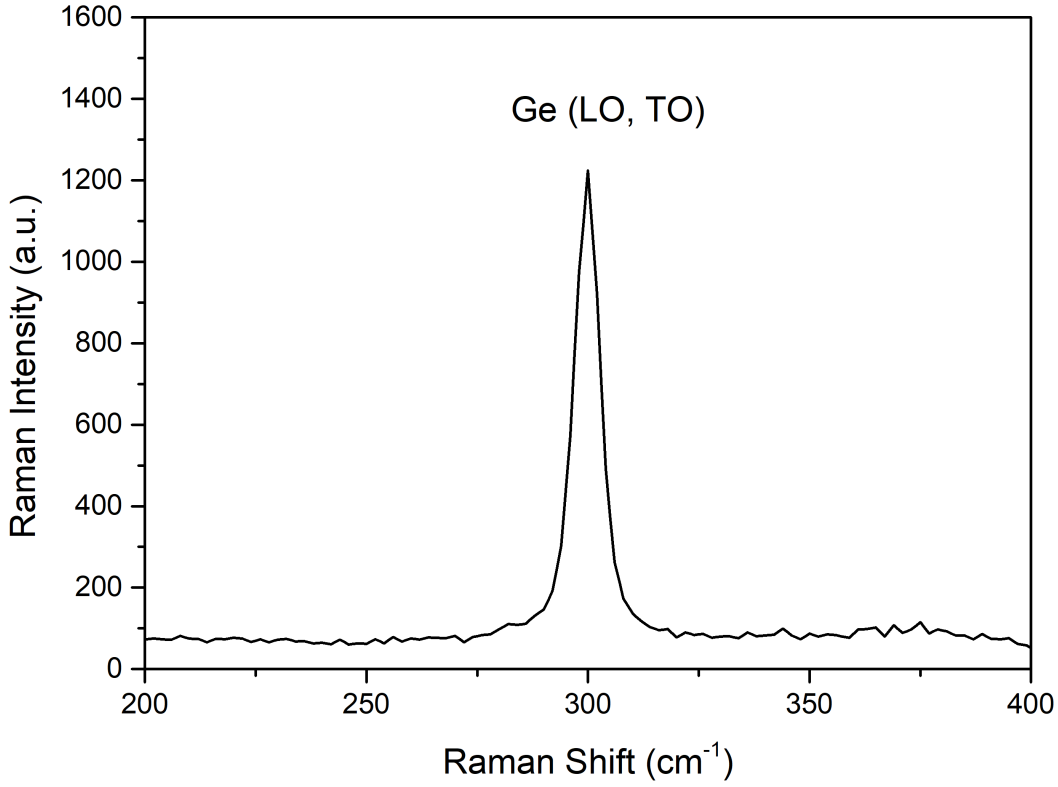

Figure 3.4: Raman spectra of bulk Ge used as a reference.

3.4.3 SiGe

The Si_xGe_{1-x} alloy (SiGe for short) presents much more complexity on its Raman spectrum than Si and Ge. SiGe has three principal Raman modes:

- Si-Si (SiGe) band: it is associated with the Si-Si vibration in the alloy, having a frequency close to the crystalline Si Raman peak but shifted towards lower energies because of the alloy disorder.
- Ge-Ge (SiGe) band: it is associated with the Ge-Ge vibration in the alloy, likewise, having a frequency near the crystalline Ge peak but shifted to lower energies.
- Si-Ge (SiGe) band: it is associated with the Si-Ge vibration in the alloy. It has an intermediate energy between those of Si-Si (SiGe) and Ge-Ge (SiGe) modes, $\omega_{Si-Ge} \approx 400\,\mathrm{cm}^{-1}$.

A Raman spectrum of reference SiGe is plotted on Figure 3.5.

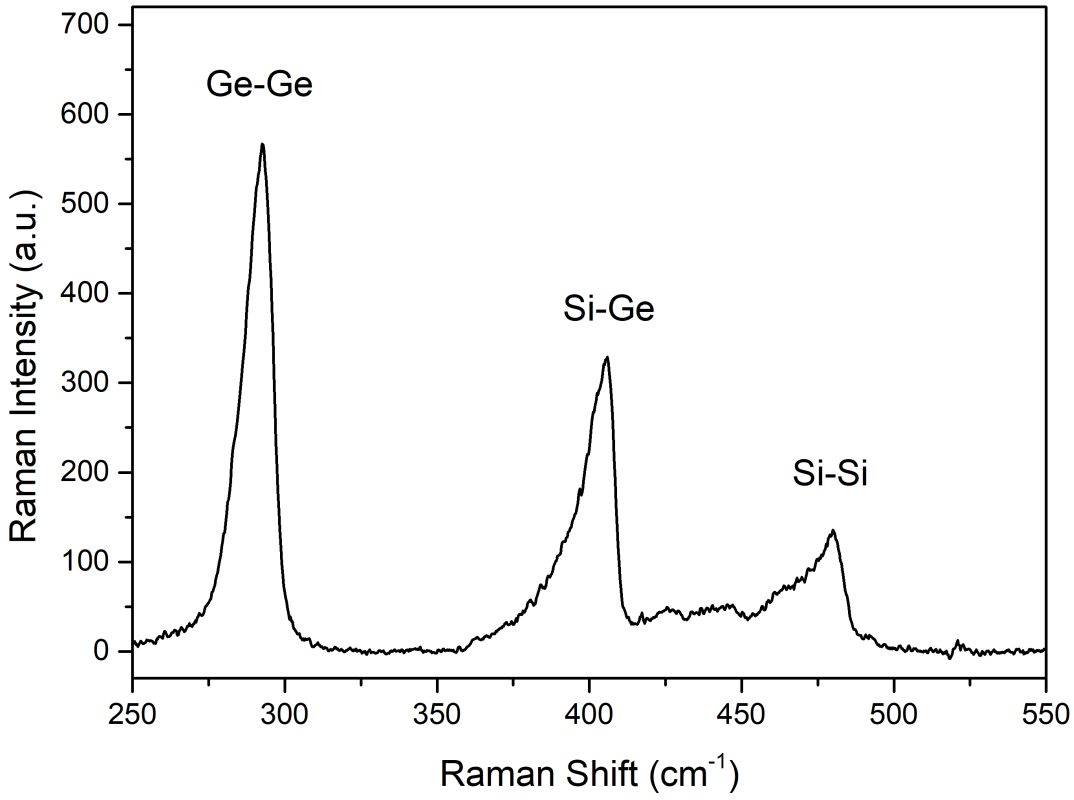

Figure 3.5: Raman spectra of SiGe used as a reference.

The down-shift of the alloy peaks is due to the presence of the other alloy material, e.g., the Si-Si (SiGe) peak is shifted to low energies as the Ge concentration on the alloy is increased, and vice versa. The explicit dependence of the Si-Si Raman Shift with Ge concentration can be summarized in the following equation [3–5]:

$$\omega_{Si-Si}(x) = 520.0 - 68x \ (cm^{-1}) \tag{3.1}$$

Which is very useful to determine the composition of a SiGe alloy from its Raman spectrum. A similar analysis can be performed with the Ge-Ge peak; however, the slope of the linear fit is smaller, resulting in a lower precision on the determination of the Ge concentration. It becomes useful when the Si-Si (SiGe) peak has not enough intensity, i.e., low Si concentrations [6].

$$\omega_{Ge-Ge}(x) = 280.3 - 19.4x \ (cm^{-1}) \tag{3.2}$$

In the case of the Si-Ge peak, its frequency depends in a non-linear way on the relative composition of Si and Ge, being more significant for intermediate concentrations. However, the variation with Ge composition is not very large, and the dependence is too complicated to be useful for determining the Ge concentration. In this case, a cubic relation with the Ge concentration can be found, resulting in the following equation [6].

$$\omega_{Si-Ge}(x) = 400.1 + 24.5x - 4.5x^2 - 33.5x^3 \ (cm^{-1}) \tag{3.3}$$

More information about these relations and other secondary peaks of the SiGe alloy can be found in references [3, 4, 7, 8].

3.4.4 GaAs

GaAs is a III-V semiconductor that presents two different Raman modes: LO and TO [9]. In this case, LO and TO modes are not degenerate at the Brillouin Zone Center. Their Raman Shifts are $\omega_{GaAs(TO)} = 268\,\mathrm{cm}^{-1}$ and $\omega_{GaAs(LO)} = 292\,\mathrm{cm}^{-1}$. Figure 3.6 shows an example Raman spectrum of a GaAs reference sample recorded on a (111) plane.

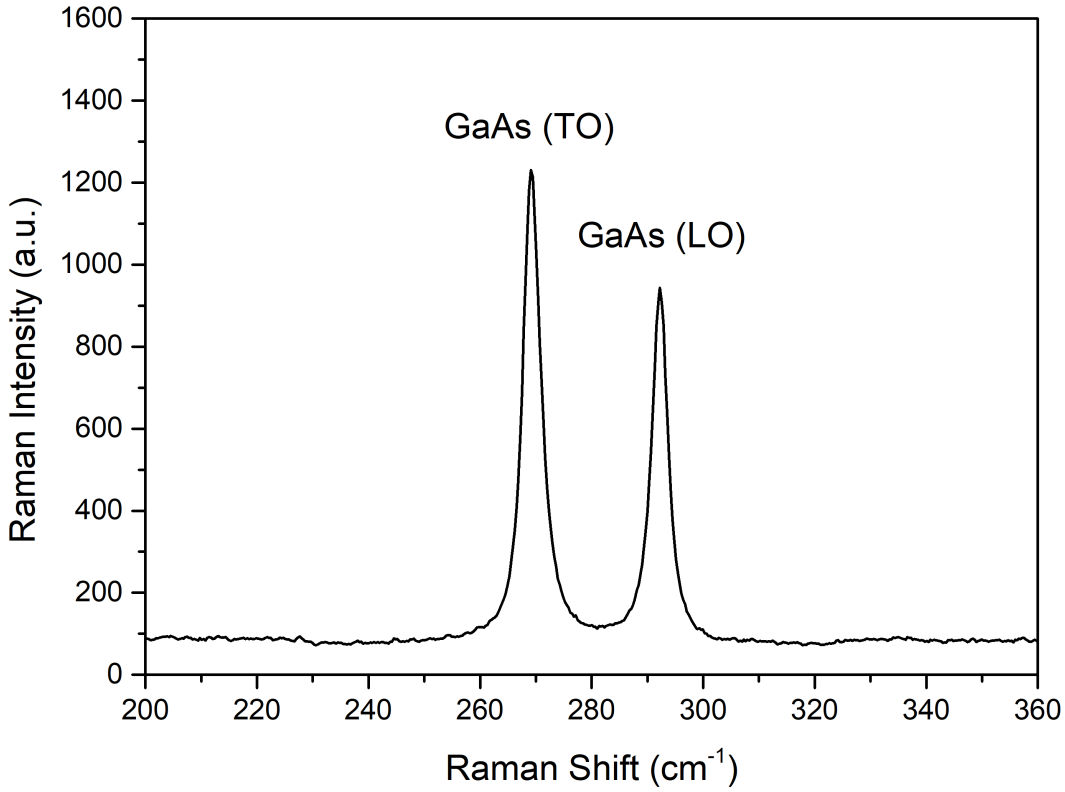

Figure 3.6: Raman spectra of GaAs used as a reference.

3.4.5 InAs

InAs presents the same structure as GaAs, with two first-order Raman peaks, but at different energies: $\omega_{InAs(TO)} = 220\,\mathrm{cm}^{-1}$ and $\omega_{InAs(LO)} = 242\,\mathrm{cm}^{-1}$ [10]. The spectrum is similar to that of GaAs, Figure 3.6, with other frequency values, see Figure 3.7.

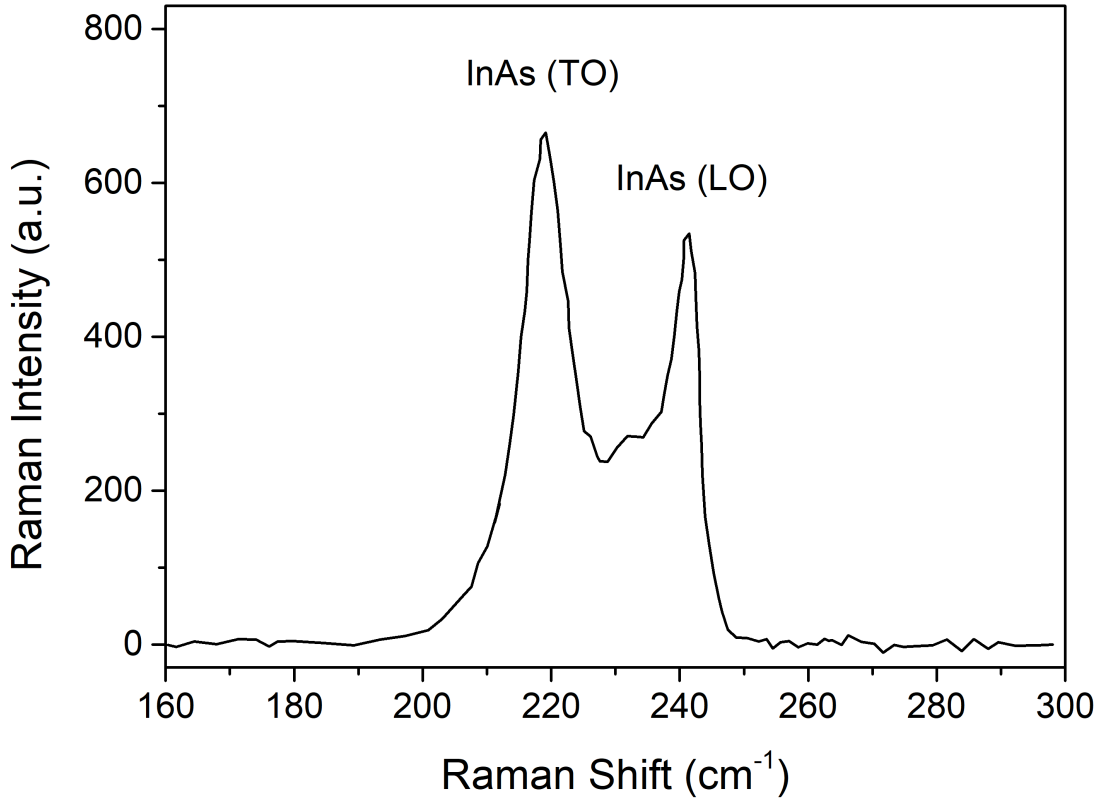

Figure 3.7: Raman spectra of InAs used as a reference.

3.4.6 InGaAs

The ternary compound $In_xGa_{1-x}As$ (InGaAs) presents four different Raman modes that are directly derived from the two binary compounds forming it: GaAs and InAs. Thus, two GaAs-like bands are found, called GaAs-like (LO) and GaAs-like (TO), and two InAs-like modes, namely InAs-like (LO) and InAs-like (TO). In all cases, the values of the Raman shifts are close to the respective modes of the binary compound, presenting possible displacements as a consequence of the composition or the presence of stress [11]. A reference spectrum is showed in Figure 3.8.

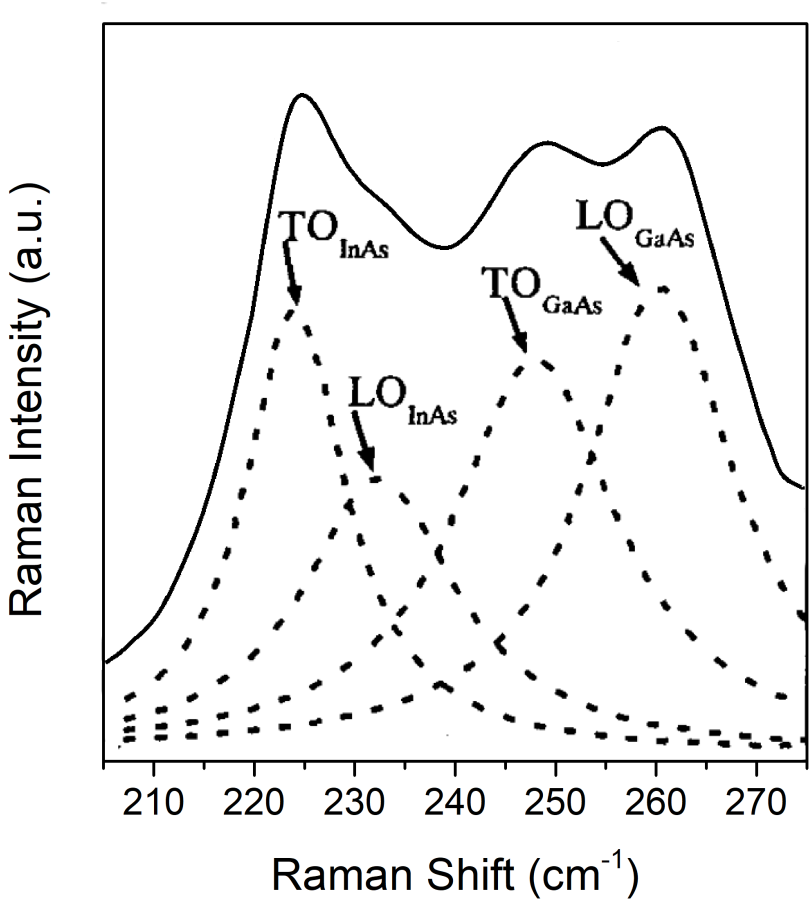

Figure 3.8: Raman spectra of InGaAs extracted from Ref. [11]. The four bands are very close to each other. Each component is extracted from the fit of the experimental data.

The Raman shift of InGaAs Raman peaks can be used (in the absence of stress) to calculate the In concentration x, equivalently to the SiGe alloy. In this case, the TO bands provide better precision as compared to the LO bands, so they are preferred for this purpose. The equations that relate the Raman shift of the four, LO and TO, modes and the In content, x, can be found in Ref. [11]:

$$\Delta\omega_{GaAs-like(TO)} = 268 - 30x \ (cm^{-1}) \tag{3.4}$$

$$\Delta\omega_{GaAs-like(LO)} = 291 - 53x \ (cm^{-1}) \tag{3.5}$$

$$\Delta\omega_{InAs-like(TO)} = 230 - 10x \ (cm^{-1}) \tag{3.6}$$

$$\Delta\omega_{InAs-like(LO)} = 230 + 8x \ (cm^{-1}) \tag{3.7}$$

3.4.7 Graphene

Graphene is a two-dimensional allotrope of carbon. It is formed by a single layer of carbon atoms connected by sp^2 bonds, giving rise to its representative honeycomb lattice. A reference graphene Raman spectrum is presented in Figure 3.9. It consists of two high intensity Raman bands labelled G and 2D, located at $\omega_G \approx 1580\,\mathrm{cm}^{-1}$ and $\omega_{2D} \approx 2700\,\mathrm{cm}^{-1}$ [12, 13]. The G band is the only band in graphene arising from a normal first-order Raman scattering process. It corresponds to the degenerate iTO and iLO phonons of graphene network at the Brillouin Zone Centre[1]. The graphene G band is the same Raman band observed in graphite. The 2D band is a second order resonant mode. It involves the generation of 2 iTO phonons as well as two resonant electronic transitions in momentum space between K and K' points, see Refs. [12, 13] for further details.

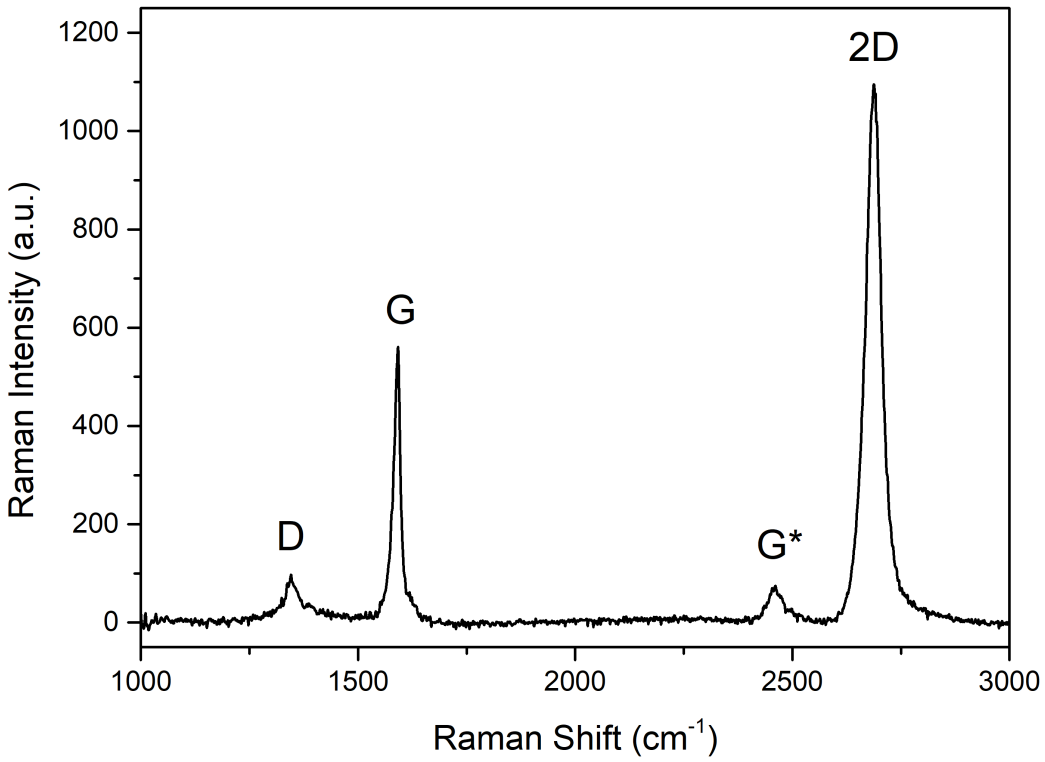

Figure 3.9: Raman spectra of graphene used as a reference.

[1]The prefix 'i' stands for in-plane vibrational modes, 'o' is used for out-of-plane vibrational modes. This differentiation is fundamental for 2D materials. In bulk materials, it is fairly common that the two transversal branches are degenerated. However, in 2D materials, the out-of-plane and in-plane vibrations are essentially different as a result of the dimensionality.

In addition to this, graphene also presents two secondary bands referred as D and G*, at Raman shifts $\omega_D \approx 1350\,\mathrm{cm}^{-1}$ and $\omega_{G*} \approx 2450\,\mathrm{cm}^{-1}$. The D band is associated with a defect-assisted Raman scattering for the generation of an iTO phonon. This reveals the origin of the relation $\omega_{2D} = 2\omega_D$. The defect-assisted transition involves one iTO phonon, and the resonant 2D transition involves two of them. The D Raman mode provides information about the crystalline quality of the graphene layer, being more intense when the graphene layer is richer in defects. Finally, the G* peak is a result of a more complex interaction which is not relevant for this analysis, further information about the origin of this Raman band can be found in Ref. [14].

Band	**Raman Shift / cm^{-1}**
InAs (TO)	220
InAs (LO)	242
GaAs (TO)	268
GaAs (LO)	292
Si (2TA)	$\approx$ 300
Ge (LO,TO)	298
Ge-Ge (SiGe)	$\approx$ 300
Si-Ge (SiGe)	$\approx$ 400
Si-Si (SiGe)	$\approx$ 450 - 520
Si (LO,TO)	520.6
D (Graphene)	$\approx$ 1350
G (Graphene)	$\approx$ 1580
G* (Graphene)	$\approx$ 2450
2D (Graphene)	$\approx$ 2700

Table 3.1: Principal Raman bands of all the studied materials and its respective values of the Raman Shift.

Bibliography

[1] J. Anaya Calvo. *Transporte térmico y caracterización Raman de Nanohilos Semiconductores de Silicio-Germanio*. Dissertation, Universidad de Valladolid (2013). doi:10.35376/10324/4451

[2] J. H. Parker, D. W. Feldman, M. Ashkin. Raman scattering by silicon and germanium. *Physical Review*, **155** (3), 712–714 (1967). doi:10.1103/PhysRev.155.712

[3] J. C. Tsang, P. M. Mooney, F. Dacol, J. O. Chu. Measurements of alloy composition and strain in thin Ge x Si 1-x layers. *Journal of Applied Physics*, **75** (12), 8098–8108 (1994). doi:10.1063/1.356554

[4] M. I. Alonso, K. Winer. Raman spectra of c-Si(1-x)Gex alloys. *Physical Review B*, **39** (14), 10056–10062 (1989)

[5] P. M. Mooney, F. H. Dacol, J. C. Tsang, J. O. Chu. Raman scattering analysis of relaxed Ge x Si 1-x alloy layers. *Applied Physics Letters*, **62** (17), 2069–2071 (1993). doi:10.1063/1.109481

[6] F. Pezzoli, L. Martinelli, E. Grilli, M. Guzzi, S. Sanguinetti, M. Bollani, H. D. Chrastina, G. Isella, H. Von Känel, E. Wintersberger, J. Stangl, G. Bauer. Raman spectroscopy of Si1-xGex epilayers. *Materials Science and Engineering B: Solid-State Materials for Advanced Technology*, **124-125** (SUPPL.), 127–131 (2005). doi:10.1016/j.mseb.2005.08.057

[7] W. Brya. Raman scattering in Ge-Si alloys. *Solid State Communications*, **12** (4), 253–257 (1973). doi:10.1016/0038-1098(73)90692-3

[8] T. S. Perova, J. Wasyluk, K. Lyutovich, E. Kasper, M. Oehme, K. Rode, A. Waldron. Composition and strain in thin Si1-xGex virtual substrates measured by micro-Raman spectroscopy and x-ray diffraction. *Journal of Applied Physics*, **109** (3), 033502 (2011). doi:10.1063/1.3536508

[9] D. Spirkoska, G. Abstreiter, A. Fontcuberta I Morral. Size and environment dependence of surface phonon modes of gallium arsenide nanowires as measured by Raman spectroscopy. *Nanotechnology*, **19** (43), 435704 (4pp) (2008). doi:10.1088/0957-4484/19/43/435704

[10] T. Li, Y. Chen, W. Lei, X. Zhou, S. Luo, Y. Hu, L. Wang, T. Yang, Z. Wang. Effect of growth temperature on the morphology and phonon properties of InAs nanowires on Si substrates. *Nanoscale Research Letters*, **6** (1), 463 (2011). doi:10.1186/1556-276x-6-463

[11] M. R. Islam, P. Verma, M. Yamada, M. Tatsumi, K. Kinoshita. Micro-Raman analysis of molar fraction in polycrystalline In/sub x/Ga/sub 1-x/ for traveling liquidus zone growth method. In *Conference Proceedings. 2001 International Conference on Indium Phosphide and Related Materials. 13th IPRM (Cat. No.01CH37198)*, S. 129–132 (2001). doi:10.1109/ICIPRM.2001.929046

[12] L. M. Malard, M. A. Pimenta, G. Dresselhaus, M. S. Dresselhaus. Raman spectroscopy in graphene. *Physics Reports*, **473** (5-6), 51–87 (2009). doi:10.1016/j.physrep.2009.02.003

[13] A. C. Ferrari, D. M. Basko. Raman spectroscopy as a versatile tool for studying the properties of graphene. *Nature nanotechnology*, **8** (4), 235–46 (2013). doi:10.1038/nnano.2013.46

[14] T. Shimada, T. Sugai, C. Fantini, M. Souza, L. G. Cançado, A. Jorio, M. A. Pimenta, R. Saito, A. Grüneis, G. Dresselhaus, M. S. Dresselhaus, Y. Ohno, T. Mizutani, H. Shinohara. Origin of the 2450 cm-1 Raman bands in HOPG, single-wall and double-wall carbon nanotubes. *Carbon*, **43** (5), 1049–1054 (2005). doi:10.1016/j.carbon.2004.11.044

Chapter 4

Study hard what interests you the most
in the most undisciplined, irreverent
and original manner possible
- Richard Feynman -

Si/SiGe axially heterostructured NWs

This chapter is devoted to the study of axially heterostructured NWs based on Si and SiGe. The analysis of these NWs by Raman spectroscopy revealed an enhancement of the Raman signal when the HJ region is being illuminated. This effect could prove to be very interesting for a great number of photonics applications. The localization and enhancement of an incident electromagnetic field at the HJ of these structures could improve already existing devices based on light/matter interaction and optoelectronics, like light sensors, solar cells, lasers, etc.

The present chapter is divided into three main sections. The first one is focused on SiGe/Si NWs with a single HJ and relatively low Ge concentration, around 10 %. These NWs were manufactured by the group of Tomás Rodríguez. The Raman enhancement effect was first discovered on these NWs; however, the analysis of the experimental results was rather complicated. This led to the second section, in which SiGe/Si and SiGe/Si/SiGe axially heterostructured NWs are analysed. The major advantage of these NWs is their higher Ge concentration, around 60 %. A larger Ge content produces a substantially higher shift of the Raman peaks, especially the Si-Si (SiGe) peak (see chapter 3.4.3), which makes the analysis of the results much more comfortable and evident. This group of NWs was provided by the group of Thierry Baron. The third section aims to explain the role of the HJ abruptness and why the enhancement effect is detected only in one HJ of the SiGe/Si/SiGe NWs, which led to the study of the heterostructured NWs growth process described in Chapter 6. The fourth and last section of the present chapter is devoted to the study of the previous axially heterostructured NWs laying over graphene. The aim of this experiment is to probe the EM field at the NW surface. This will let us investigate the near-field distribution of the NW, as a complement to the measurements of the internal field.

Four scientific papers are included in this chapter. Two of them, *"Local electric field enhancement at the heterojunction of Si/SiGe axially heterostructured nanowires under laser illumination"* (P1) and *"About the Interaction Between a Laser Beam and Group IV Nanowires: A Study of the Electromagnetic Field Enhancement in Homogeneous and Heterostructured Nanowires"* (P2), are attached to the first section. The first one is a short article presenting the detected enhancement effect for the first time. The second one contains an improved modelling of the effect that thoroughly explains the experimental results. The other two are focused on higher Ge concentration NWs and are included in the second section. The third paper, *"Electromagnetic field enhancement effects in group IV semiconductor nanowires. A Raman spectroscopy approach"* (P3), contains a full explanation of the enhancement effect, including new results of NWs with higher Ge concentrations. Finally, the fourth article, *Electromagnetic Field Enhancement on Axially Heterostructured NWs: The Role of the Heterojunctions* (P4), is focused on the improvement of the model, which is currently able to reproduce the experimental measurements with outstanding precision. Furthermore, this last article tries to explain the physics behind the model, paying particular attention to the role of the HJ and its direct effect on the electromagnetic field distribution.

4.1 SiGe/Si NWs - Low Ge Concentration

This first section comprises the earliest detection of the Raman enhancement on the HJ of SiGe/Si NWs. SiGe/Si NWs with Ge concentrations around 10 % were studied. The NWs were grown by VLS method using as precursors Si_2H_6 and GeH_4. During the growth process, the SiGe segment is grown first, and, at a certain point, the GeH_4 source is switched off, inducing the growth of the pure Si segment.

The NWs were studied by μ-Raman spectroscopy, and the spectra are collected very 200 nm. The resulting Raman spectra were fitted considering two Raman bands: one associated with the pure Si segment, located at $520.6\,\mathrm{cm}^{-1}$, and another one related to the SiGe segment around $514\,\mathrm{cm}^{-1}$ associated with the Si-Si vibrations, which corresponds to a $\approx 9\%$ of Ge, see Section 3.4.3. However, the experimental spectrum cannot be reproduced by the convolution of these two bands, see Figure 3 of paper P1. In order to obtain a reliable fit of the data, it is necessary to add a third band corresponding to an alloy composition between both homogeneous segments, which allows a satisfactory fit of the experimental spectrum when the laser beam shares the two segments and the HJ. When the fit is done in these conditions, the third band has a Raman shift corresponding to exactly intermediate composition between those of the Si and SiGe segments. Furthermore, the intensity of this third band is notably higher than the intensities of the bands arising from the homogeneous sections. We relate this band to the HJ, Since the signal has a Raman shift corresponding to an intermediate composition between the two segments, we related it to the HJ region, which is the only material with those characteristics. The interesting point is not the existence of this Raman band, but its unexpectedly huge Raman signal. The volume of the HJ is significantly smaller than the illuminated region of the homogeneous segments, but the experimental spectrum shows a higher Raman signal arising from the HJ than from the segments. According to the equations that allow calculating the Raman signal as a function of the excitation intensity, (2.7) and (2.12), the excitation electromagnetic field should be enhanced at the HJ with respect to the homogeneous segments in order to account for the high Raman intensity.

Local electric field enhancement at the heterojunction of Si/SiGe axially heterostructured nanowires under laser illumination

J. L. Pura[1], J. Souto[2,*], J. Souto[1], A. C. Prieto[1], A. Rodríguez[3], T. Rodríguez[3], and J. Jiménez[1]

[1] *GdS Optronlab, Dpt. Física de la Materia Condensada, ed. i+d, Parque Científico, Universidad de Valladolid, Paseo de Belén 1, 47011 Valladolid, Spain*

[2] *Centre for Device Thermography and Reliability, HH Wills Physics Laboratory, University of Bristol, Tyndall Avenue, BS8 1TL, Bristol, UK*

[3] *Ingeniería Electrónica, ETSI de Telecomunicación, Universidad Politécnica de Madrid,Avenida Complutense 30, 28040 Madrid, Spain.*

[*] *J.AnayaCalvo@bristol.ac.uk*

Keywords: Si/SiGe heterojunction, electromagnetic enhancement, nanowires, photogenerated carriers

Abstract

We present a phenomenon concerning the electromagnetic enhancement at the heterojunction region of axially heterostructured Si/SiGe nanowires when the nanowire is illuminated by a focused laser beam. The local electric field is sensed by micro Raman spectroscopy, which permits to reveal the enhancement of the Raman signal arising from the heterojunction region; the Raman signal per unit volume increases at least 10 times with respect to the homogeneous Si, and SiGe nanowire segments. In order to explore the physical meaning of this phenomenon, a 3-dimensional solution of the Maxwell equations of the interaction between the focused laser beam and the nanowire was carried out by finite element methods. A local enhancement of the electric field at the heterojunction was deduced; however, the magnitude of the electromagnetic field enhancement only approaches the experimental one when the free carriers are considered, showing enhanced absorption at the carrier depleted heterojunction region. The existence of this effect promises a way to improve the photon harvesting using axially heterostructured semiconductor NWs.

1 Introduction

Semiconductor nanowires (NWs) are attracting a great deal of attention because of the increasing number of potential applications based on their unique properties.[1] Most of these properties arise from the NW confined dimension, the diameter, as compared to some characteristic lengths, e.g. exciton Bohr radius, phonon mean free path, wavelength of the incident electromagnetic (EM) waves, etc.[2] In particular, there is a great interest in the interaction between semiconductor NWs and light, as their optical properties make of them the optimal candidates for nanophotonic devices. [3, 4] A broad range of unique optical properties of semiconductor NWs have been reported, e.g. waveguiding,[5] optical resonances,[6] antenna effects, among others.[7] All these effects emerge because light interacts with the NWs in different ways depending on the NW diameter, wavelength, and dielectric properties of the NW and the surrounding media. One of the most relevant properties concerning the light/NW interaction is the ability of NWs to enhance their optical absorption/scattering for certain diameters, which are characterized by large local electric fields inside the NW.[8] The absorption/scattering resonances deal with different phenomena recently reported, including, among other, the enhanced photocurrent response of the NWs,[7] enhanced elastic and inelastic light scattering by Si NWs,[9] light extinction,[10] light emission in different semiconductor NWs, [11, 12] and second harmonic generation. [5] Since the Raman intensity is proportional to the excitation light intensity and the scattering volume, the experimental study of the interaction of light with matter at the nanoscale can be carried out by its Raman response.[15] This makes of Raman spectroscopy an excellent probe for sensing the local electric field induced inside the NW under incident light. In addition, it is possible to take advantage of its capabilities as a powerful non-destructive technique for the characterization of the structure, composition, stress, thermal, electronic, and optical properties of semiconductor NWs.[6, 14–18] It is worth noting that up to now the research interest about the light/NWs interaction has been focused mainly on homogeneous single NWs and/or core-shell heterostructured NWs;[19] however, the response of axially heterostructured NWs to the electromagnetic waves is still unexplored. These kind of structures are attracting an increasing interest since heterojunctions (HJ) are necessary for the development of semiconductor NW based devices.[20] In the junction of these NWs a jump in the complex refractive index due the abrupt change of materials is expected, which therefore may change the electromagnetic (EM) response of the NW. Besides the HJ built-in electric field, which can locally change the polarizability, the oscillator strength and the presence of free carriers, either native or photogenerated, could also affect the electric field distribution inside the NW. To further advance in this subject, we present in this work a study of the distribution of the electromagnetic field in axially heterostructured Si/SiGe NWs, paying special attention to the role of the HJ in the optical response of the NW. This is carried out experimentally by using its Raman response as a sensor of the local electric field. The experimental data are compared to the output of a 3 dimensional (3D) solution of the Maxwell equations characterizing the electromagnetic laser/NW interaction by finite element methods (EM-FEM), enabling to explain the role of the HJ in the EM interaction.

2 Experimental description and samples

Axially-heterostructured NWs were grown by the vapour-liquid-solid (VLS) method, using Si_2H_6 and GeH_4 as precursor gases and alloyed Ga-Au metal droplets of different compositions as catalysts. The as-grown NWs were sonicated in an ultrasonic bath and suspended in methanol; subsequently the NWs were deposited on an Al substrate by drop-casting. For more details about the growth of these NWs see refs [21] and [22].

High resolution transmission electron microscopy (TEM) and energy dispersive X ray (EDX) analyses of the HJ was carried out. High resolution TEM images of the HJ region of SiGe/Si HJs did not show structural discontinuities at the junction, nor stacking faults, or other structural defects, Fig. 1a. The EDX profile shows a compositionally graded HJ with a width of around 30 nm, of the order of the NW diameter, $\approx$ 32 nm for the NW shown in Fig. 1b. The micro Raman spectra of several individual Si/SiGe NWs were recorded with a high resolution Labram UV-HR 800 Raman spectrometer from Horiba-JovinYvon. The excitation and the scattered light collection were performed by means of a confocal metallographic microscope with a high magnification objective (100X and 0.95 numerical

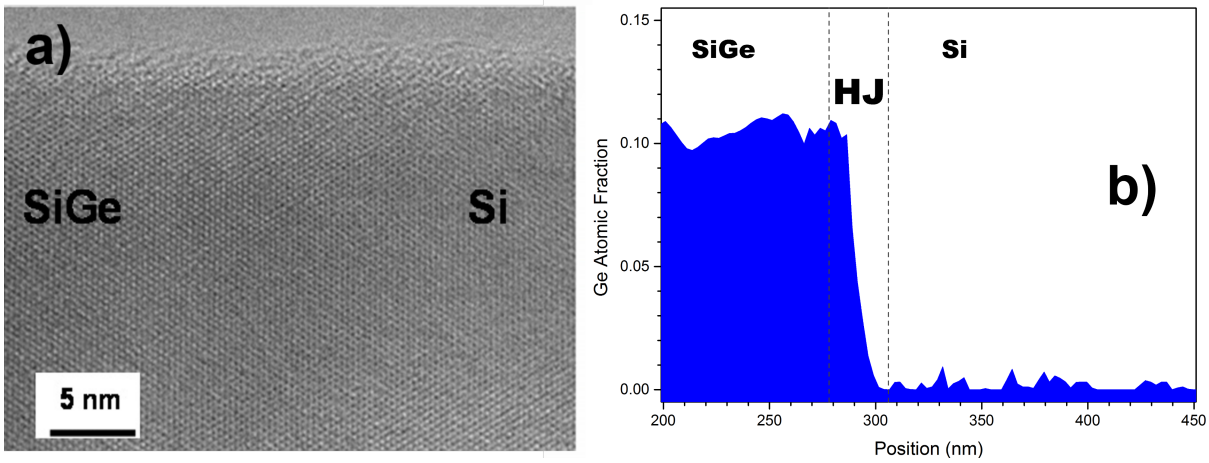

Figure 1: a) High resolution TEM image of the HJ. b) EDX Ge atomic fraction profile across the HJ.

aperture (NA)). The excitation was done with a frequency doubled Nd:YAG laser (532 nm). The measured laser beam diameter at the focal plane for these conditions is $\sim$ 1 μm, thus slightly bigger than the $\sim$ 700 nm given by the Abbe's formula ($w_0 \propto 1.22\lambda/NA$) and several times larger than the typical NW diameter studied here, which ranges from 30 to 100 nm. The NWs deposited on a metallic substrate were found to enhance the Raman signal with respect to the free standing NWs. The metallic substrate also allows a better heat dissipation, reducing the laser induced heating of the NWs.[23] The Ge concentration in the SiGe segment of the NW, measured by EDX and confirmed by the Raman measurements, lies around 10% for all the studied NWs. Prior to the Raman measurements the dimensions and morphology of the NWs were characterized in a scanning electron microscope (SEM).

The Raman spectra were acquired by scanning the laser beam along and across the NW axis in steps of 100 nm. The transverse scanning across the NW allows the optimization of the excitation conditions, i.e. maximum Raman signal with negligible laser induced heating.[23] The longitudinal scanning permits to localize the HJ, and also to study the Raman intensity profiles along the NW, and more interestingly around the HJ.

3 Experimental results

Four Raman spectra recorded at different positions along an axially heterostructured Si/SiGe NW are shown in Figure 2. Spectrum 1 was taken on the Si segment of the NW, while spectrum 4 was recorded on the SiGe segment. Spectra 2 and 3 were recorded with the laser beam sharing the two pure segments and the HJ. When these spectra are compared, a dramatic change is observed in the spectral shape of 2 and 3 with respect to 1 and 4. Spectra 1 and 4 show a typical Lorentzian peak, with the spectral parameters characteristic of $Si_{0.9}Ge_{0.1}$ and Si NWs respectively. [24, 25] Meanwhile, the spectra recorded in positions 2 and 3 appear broadened and asymmetric, as a consequence of the overlapping contribution to the Raman spectrum of the different regions of the NW being simultaneously excited by the laser beam. In order to analyze this signal, spectral deconvolution shall be thus carried out to ascertain the different contributions of the pure Si and SiGe segments of the NW, and also the contribution of the HJ region. For this deconvolution we used the spectra 1 and 4, corresponding unequivocally to the Si and $Si_{0.9}Ge_{0.1}$ pure NW segments, as the reference spectra for the fitting of the spectra 2 and 3. However when using a weighted Gaussian convolution –from the focused laser intensity distribution– of the two bands corresponding to the two pure segments it is not possible to reproduce the Raman recorded when the laser beam is sharing the three NW regions, i.e. spectra 2 and 3 (see Fig. 3 inset).

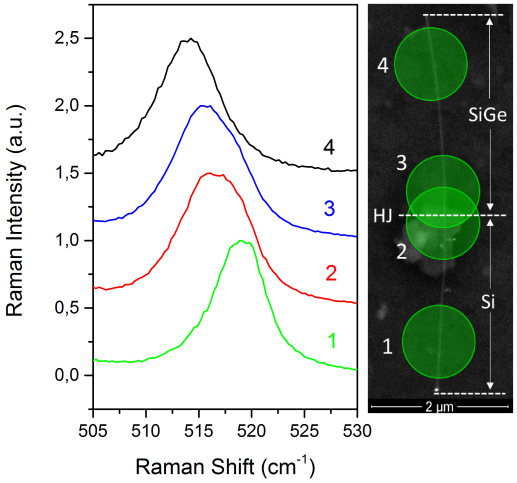

Figure 2: Raman spectra recorded at different positions along the heterostructured Si/SiGe NW. The positions of the laser spot along the NW are indicated in the SEM image. Spectrum 1 is taken on the Si segment, spectra 2 and 3 share the three regions of the NW and spectrum 4 is taken on the SiGe segment.

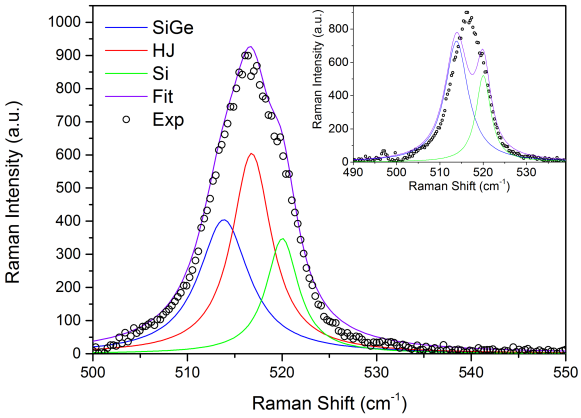

Figure 3: Fitting of the Raman signal corresponding to an intermediate composition between the two NW segments, a satisfactory fitting can only be achieved by using a third Raman band. (Inset) Fitting of a Raman spectrum sharing the three NW regions using only two bands with the spectral parameters of the Raman bands of the pure Si and SiGe segments respectively, this fitting neglects the contribution of the HJ.

Fig. 3 shows that a third band is necessary to achieve a satisfactory fit of the spectra recorded with the participation of the HJ, e.g. 2 and 3. This third contribution, which has a peak width and frequency intermediate between those recorded for the pure $Si_{0.9}Ge_{0.1}$ and Si NW segments, should arise exclusively from the very narrow HJ region. It should be noted that the HJ region in VLS NW growth does not present a sharp composition change, but it follows a compositionally graded transition from the nominal 10% Ge of the SiGe segment to the pure Si segment (see Fig. 1b). The thickness of this transition region is of the same order of magnitude as the NW diameter, and it is consequence of the Ge reservoir effect on the catalyst droplet. Once the GeH_4 gas source had been switched-off this reservoir continues depositing Ge during the growth up to the Ge exhaustion in the catalysts droplet.[3, 26, 27] Thus, in order to explain the Raman signal detected in the HJ region, we should first consider this transition volume as the source of the observed third band in the Raman spectrum.

The Raman intensity is correlated to the volume of the material probed by the laser beam, [14] which in our case gives a ratio of $\sim$ 1:0.1:1 (Si:HJ:SiGe) between the three probed regions for a 50 nm diameter NW when the laser beam spot is sharing the three parts of the NW (when it is centered around the HJ). Therefore, the high intensity of the Raman band arising from the HJ region (see Fig. 3), which is similar in amplitude to the ones corresponding to the Si and SiGe NW segments, cannot be explained in terms of a simple convolution of the signals weighted by their scattering volumes.

Indeed, the high intensity recorded in the HJ when translated in terms of Raman intensity per unit volume, results in a Raman signal enhancement for the HJ contribution of at least one order of magnitude with respect to the signals recorded in the two single NWs segments. This means that there is a significant enhancement of the induced local electromagnetic field at the HJ of the NW. Furthermore, the Raman intensity along the heterostructured NW is not only amplified at the HJ, but the presence of the HJ seems to pull up of the overall Raman signal. This is shown in Fig. 4, in which the integrated Raman intensities of the different contributions, - namely Si, HJ and SiGe - as determined from the deconvolution of the experimental Raman spectra are plotted as a function of the position of the laser beam along the NW. Here the Raman intensity reaches a maximum when

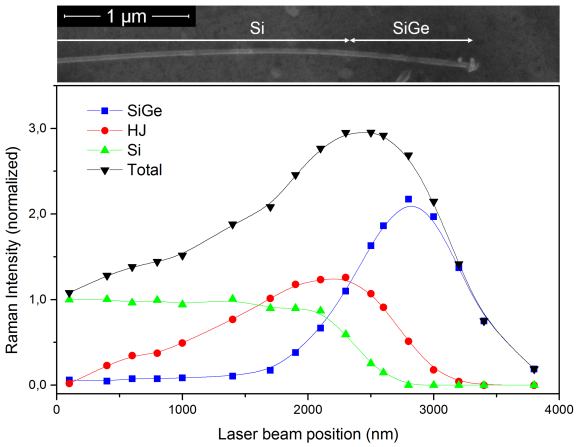

Figure 4: Intensity profiles along the NW axis for the overall Raman signal and for the deconvoluted bands corresponding to the three regions of the NW, showing the enhancement under the influence of the HJ. The points correspond to the positions of the laser beam center where the Raman spectra were recorded. The data have been normalized to the one corresponding to the pure Si region to better illustrate the enhancement in Raman signal.

the laser beam is crossing the HJ, evidencing that the presence of the HJ is enhancing the overall Raman intensity, and thus affecting the distribution of the electric field inside the NW even when the laser beam is not directly illuminating the HJ.

We should note that this behaviour was observed for all of the several axially heterostructured NWs that we have studied. On the other hand, the decrease of the SiGe signal at the right side of the plot of Fig. 4 is the consequence of the reduced scattering volume and Gaussian intensity profile of the laser at the end of the NW (see the SEM image of Fig. 4). The same effect occurs on the other end of the NW (Si segment) but it is not plotted here.

4 Laser/NW interaction by finite element method (EM-FEM) simulations

To study the quantitative interaction between the focused laser beam and the NWs, and thus to unravel the distribution of the electromagnetic field inside the HJ NW, one needs to solve the Maxwell equations for the laser/NW system. This has been typically carried out by means of the Lorenz-Mie theory, in which the NW is described as an infinitely long cylinder immersed in a homogeneous and isotropic non absorbing medium. [28] In the frame of this formalism, the calculation of the absorption, and scattering efficiencies, Q_{abs} and Q_{sc} respectively, has revealed a strong dependence of these coefficients with the NW diameter, presenting resonances for certain diameters.[6, 17]

Alternatively, we have analyzed the NW/laser beam interaction by solving the equivalent 2D Maxwell equations using the radio-frequency (RF) module of the COMSOL Multiphysics simulation software, contrasting our results with the solution of the Lorentz-Mie equations and obtaining an excellent agreement.[29] However, because of symmetry-breaking in the presence of the HJ, the simulation of the axially heterostructured NWs cannot be performed by a 2D approach like the ones typically used when studying the light/NW interaction for homogeneous NWs and core-shell heterostructured NWs.[14, 15] Instead, here we solved a 3D model accounting for the axial HJ and the finite length of the NW, as well as the presence of the metallic substrate. The electromagnetic model used here reproduces a HJ-NW with the same characteristics as the one shown in Fig. 4, deposited on a metallic (Al) substrate and surrounded by air. The NW is illuminated by the same 532 nm Gaussian laser beam used in the experiments. The air/NW/substrate system was limited by Cartesian perfectly matched layers (PMLs), which absorb all the outgoing radiation, thus eliminating secondary reflections on the boundaries. The complex refractive indexes were obtained from Sopra database.[30] In a first step the response of a perfectly dielectric NW was calculated. This model was solved for different positions of the excitation laser beam along the NW axis in order to reproduce the experimental profile of Fig. 4.

A particular solution of the model is shown in Fig. 5, where one observes the 3D distribution of the relative electric field intensity, defined as $E_r^2 = |E|^2/|E_{Incident}|^2$ (i.e., the electric field enhancement over the incident laser electromagnetic field), inside the heterostructured NW. In the same figure we also included the profile of this magnitude along the NW axis, highlighting the local enhancement at the HJ region. For each position of the laser beam the electromagnetic field distribution inside the NW is calculated. The volume integrals of the square of the electric field, $|E|^2$, in the three different regions: Si segment, SiGe segment and the HJ, are

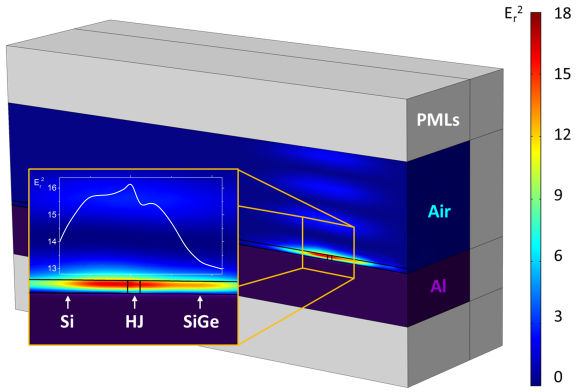

Figure 5: 3D representation of a solution of the model for a similar heterostructured NW than the ones experimentally studied. A magnification of the HJ region with the E_r^2 relative intensity axial profile showing enhancement at the HJ is also represented.

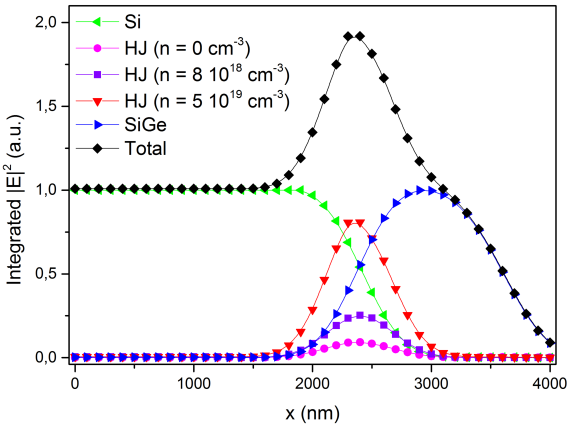

Figure 6: Integrated values of $|E|^2$ (proportional to the Raman signal) along a NW with the same compositional and geometrical properties as the NW of Fig. 4. Results are shown for a perfectly dielectric NW ($n = 0$), and two different carrier densities. The calculated total signal corresponds to $n = 5\ 10^{19} cm^{-3}$.

then calculated. The value of these integrals should therefore be proportional to the theoretical Raman signal arising from each NW region under the excitation beam.[13] It is remarkable that this model shows a similar amplification and localization of the EM field in the HJ region, see Fig. 5; however, the estimated amplification for the HJ region was lower than the one deduced from the experimental data (see Fig 6, pink dots).

In order to explain this discrepancy, a more complete model accounting for the effect of the photogenerated carriers in the solution of the Maxwell equations was considered. This is needed since the presence of free carriers will contribute to the dielectric losses. For the excitation conditions of our measurements and a Surface Recombination Velocity (SRV) of $S \approx 3\ 10^5\ cm/s$, [31] it results in a photogenerated carrier concentration of $n \approx 10^{19}\ cm^{-3}$, in agreement with other experimental estimations. [31] The dielectric losses will mainly affect the regions with free carriers, i.e. the two NW segments; but as a consequence of the carrier depletion at the HJ, this region will be free of the losses associated with the presence of free carriers. As a result, the dielectric losses will modify the electric field distribution inside the NW, lowering the electric field in the homogeneous segments with respect to the HJ, which yields an effective amplification of the HJ signal.

Once the free carriers were considered the model was solved for a carrier density ranging from 10^{16} to $10^{20}\ cm^{-3}$. The results obtained for two representative carrier densities, $n = 8\ 10^{18}\ cm^{-3}$ and $n = 5\ 10^{19}\ cm^{-3}$, are shown in Fig. 6. From here it is clear that by including the effect of the photogenerated carriers in the model, the electromagnetic field is strongly localised in the HJ region, well approaching the contribution observed in the experimental data of Fig. 4, and therefore explaining the origin of anomalous effect observed in the experiments. However we should note that the experimental intensity of the SiGe segment is higher than the intensity measured for the Si segment, as opposed to what is observed in the EM-FEM model, which shows similar values for both segments. This discrepancy might arise by a difference of a few nanometers in the diameter of both segments, which due to the diameter dependent resonance in the Raman intensity, can be responsible for the observed difference;[29] in fact, diameter changes in the presence of axial HJs are common. Here to simplify the problem, the data of Fig. 6 were calculated for an ideal cylindrical NW, without diameter change and therefore the model does not account for these subtle differences in geometry.

Finally, and to fully validate the model, the hypothesis of including the photogenerated carriers as an important player to explain the observed Raman intensity needs to be tested experimentally. In nanoscale systems the photogenerated carrier con-

centration is dominated by the surface recombination; therefore, by modifying the surface condition, one can change the surface recombination velocity (SRV) which in return will induce a change in the free carrier density. Taking this into account, Si NWs were dipped in a 4% HF solution in order to remove the native oxide layer, changing their SRV. The chemical treatment removes the native SiO_2 external layer and does not react with the crystalline Si core, leaving a clean Si NW. The NWs were immediately deposited in the metallic substrate, and kept in a N_2 atmosphere up to the first Raman measurement. After this point the N_2 source is switched off and the oxidation process starts at room temperature. Immediately after the removal of the oxide layer the surface recombination states will be nearly suppressed, then the equilibrium photogenerated carrier density will raise, lowering the Raman signal because of the free carrier associated losses. As time goes on and the spontaneous oxidation process takes place, new surface recombination centers are created and the SRV increases, with the reduction of the free carrier density and the concomitant increase of the Raman signal. In our experiment, the Raman spectrum was periodically recorded for one week of measurements, albeit the Raman signal became fully stable after the second day. The Raman signal evolution for this Si NW can be seen in Fig. 7, showing that the intensity is starting to reach a stable value after the first 24 hours. This is in good agreement with the time needed for the formation of the first stable oxide layer in Si at room temperature, which lies around 25-30 hours.[32] This therefore shows the evolution of the Raman signal with the change of the SRV, which progressively increased due to the oxidation. It should be noted that this experimental configuration warrants the same excitation conditions and photogeneration rate for all the measurements and thus shows that the change in the photogenerated carrier concentration is controlled by the SRV. Besides, the Raman signal raises rather fast in the first hours of oxidation, suggesting that the creation of a full oxide layer is not needed to enhance the surface recombination, but the creation of sparse defects at the surface is enough to spoil the homogeneity of the Si surface, and create surface states. With the presence of surface states, the equilibrium photocarrier concentration decreases and the Raman signal is progressively recovered. Therefore this result highlights the role played by the free carriers in the laser/NW interaction, and supports the good agreement observed between theoretical and experimental results obtained in the heterostructured NWs when the photogenerated carriers are considered in the electromagnetic interaction.

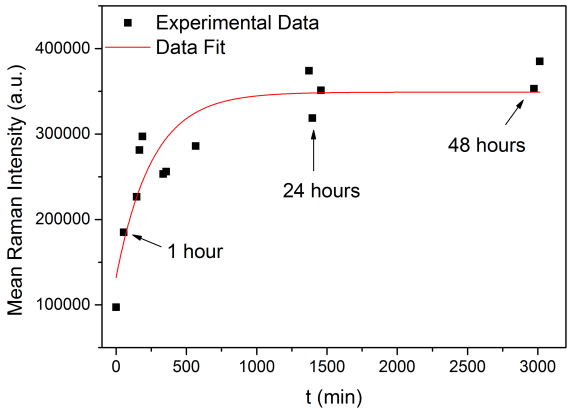

Figure 7: Evolution of the mean Raman Intensity of a Si NW as a function of the oxidation time. The intensity becomes stable 25-30 hours after the oxidation began, which coincides with the formation of the first stable oxide layer.[32]

5 Summary

We have presented here a local electromagnetic amplification phenomenon in the HJ region of axially heterostructured Si/SiGe NWs when interacting with a laser beam. This nano-scale effect has been systematically studied by recording the Raman signals of the heterostructured NWs, which show a significant enhancement at the HJ region with respect to those obtained in compositionally homogeneous NWs of the same dimensions. The Raman intensity of the HJ presents an intensity per unit volume at least 10 times higher than the pure segments of the NW. These experimental observations were contrasted with the results obtained by the 3D solution of the Maxwell equations for the interaction between the dielectric NW and the focused laser beam using an EM-FEM model. The model accounts for the above experimental observations, and shows the possibility of locally modify the electromagnetic in the HJ; however, the calculated electric field enhancement at the HJ is substantially lower than the one observed experimentally by the Raman signal. A more complete physical description considering the contribution of the photogen-

erated free carriers has been implemented, showing a good agreement with the experimental observations. The role of the photogenerated carriers on the Raman response of the NWs observed in the model has been revealed by experiments changing the photocarrier recombination dynamics by modifying the surface recombination velocity. The local electric field inside the NW can be modulated by the presence of the HJ and the surface states. This electromagnetic field enhancement at the HJ of axially heterostructured NWs suggests a path to optimize light-sensitive devices as photodetectors, sensors, solar cells, among other.

6 Acknowledgements

This work was funded by Junta de Castilla y León (Project VA293U13), Spanish Government (CICYT MAT2010-20441-C02 (01 and 02)) and FEDER (MINECO -ENE 2014-56069-C4-4-R) . J.L. Pura was granted by the FPU programme (Spanish Government)(FPU14/00916. We also acknowledge Prof. C.Ballesteros (Universidad Carlos III, Madrid) for providing the EDX and TEM results.

References

[1] Y. Cui, C. M. Lieber. Functional Nanoscale Electronic Devices Assembled Using Silicon Nanowire Building Blocks. *Science*, **291** (5505), 851–853 (2001). doi:10.1126/science.291.5505.851

[2] R. Rurali. *Colloquium* : Structural, electronic, and transport properties of silicon nanowires. *Rev. Mod. Phys.*, **82**, 427–449 (2010). doi:10.1103/RevModPhys.82.427

[3] R. Yan, D. Gargas, P. Yang. Nanowire photonics. *Nat Photon*, **3** (10), 569–576 (2009). doi:10.1038/nphoton.2009.184

[4] B. Loitsch, D. Rudolph, S. Morkötter, M. Döblinger, G. Grimaldi, L. Hanschke, S. Matich, E. Parzinger, U. Wurstbauer, G. Abstreiter, J. J. Finley, G. Koblmüller. Tunable Quantum Confinement in Ultrathin, Optically Active Semiconductor Nanowires Via Reverse-Reaction Growth. *Advanced Materials*, **27** (13), 2195–2202 (2015). doi:10.1002/adma.201404900

[5] M. Law, D. J. Sirbuly, J. C. Johnson, J. Goldberger, R. J. Saykally, P. Yang. Nanoribbon Waveguides for Subwavelength Photonics Integration. *Science*, **305** (5688), 1269–1273 (2004). doi:10.1126/science.1100999

[6] H. Kallel, A. Arbouet, G. BenAssayag, A. Chehaidar, A. Potié, B. Salem, T. Baron, V. Paillard. Tunable enhancement of light absorption and scattering in $Si_{1-x}Ge_x$ nanowires. *Phys. Rev. B*, **86**, 085318 (2012). doi:10.1103/PhysRevB.86.085318

[7] L. Cao, P. Fan, A. P. Vasudev, J. S. White, Z. Yu, W. Cai, J. A. Schuller, S. Fan, M. L. Brongersma. Semiconductor Nanowire Optical Antenna Solar Absorbers. *Nano Letters*, **10** (2), 439–445 (2010). doi:10.1021/nl9036627. PMID: 20078065

[8] R. Ruppin. Electromagnetic energy inside an irradiated cylinder. *J. Opt. Soc. Am. A*, **15** (7), 1891–1895 (1998). doi:10.1364/JOSAA.15.001891

[9] L. Cao, P. Fan, E. S. Barnard, A. M. Brown, M. L. Brongersma. Tuning the Color of Silicon Nanostructures. *Nano Letters*, **10** (7), 2649–2654 (2010). doi:10.1021/nl1013794. PMID: 20507083

[10] J. A. Schuller, R. Zia, T. Taubner, M. L. Brongersma. Dielectric Metamaterials Based on Electric and Magnetic Resonances of Silicon Carbide Particles. *Phys. Rev. Lett.*, **99**, 107401 (2007). doi:10.1103/PhysRevLett.99.107401

[11] T. Nobis, E. M. Kaidashev, A. Rahm, M. Lorenz, M. Grundmann. Whispering Gallery Modes in Nanosized Dielectric Resonators with Hexagonal Cross Section. *Phys. Rev. Lett.*, **93**, 103903 (2004). doi:10.1103/PhysRevLett.93.103903

[12] D. van Dam, D. R. Abujetas, R. Paniagua-Domínguez, J. A. Sánchez-Gil, E. P. A. M. Bakkers, J. E. M. Haverkort, J. G. Rivas. Directional and Polarized Emission from Nanowire Arrays. *Nano Letters*, **15** (7), 4557–4563 (2015). doi:10.1021/acs.nanolett.5b01135. PMID: 26043200

[13] F. R. Aussenegg, M. E. Lippitsch. On the electric field dependence of Raman scattering.

Journal of Raman Spectroscopy, **17** (1), 45–49 (1986). doi:10.1002/jrs.1250170110

[14] F. J. Lopez, J. K. Hyun, U. Givan, I. S. Kim, A. L. Holsteen, L. J. Lauhon. Diameter and Polarization-Dependent Raman Scattering Intensities of Semiconductor Nanowires. *Nano Letters*, **12** (5), 2266–2271 (2012). doi:10.1021/nl204537d. PMID: 22497202

[15] Q. Xiong, G. Chen, H. Gutierrez, P. Eklund. Raman scattering studies of individual polar semiconducting nanowires: phonon splitting and antenna effects. *Applied Physics A*, **85** (3), 299–305 (2006). doi:10.1007/s00339-006-3717-7

[16] G. S. Doerk, C. Carraro, R. Maboudian. Raman Spectroscopy for Characterization of Semiconducting Nanowires. In *Raman Spectroscopy for Nanomaterials Characterization*, S. 477–506. Springer (2012)

[17] L. Cao, B. Nabet, J. E. Spanier. Enhanced Raman Scattering from Individual Semiconductor Nanocones and Nanowires. *Phys. Rev. Lett.*, **96**, 157402 (2006). doi:10.1103/PhysRevLett.96.157402

[18] A. Torres, A. Martín-Martín, O. Martínez, A. C. Prieto, V. Hortelano, J. Jiménez, A. Rodríguez, J. Sangrador, T. Rodríguez. Micro-Raman spectroscopy of Si nanowires: Influence of diameter and temperature. *Applied Physics Letters*, **96** (1), 011904 (2010). doi:http://dx.doi.org/10.1063/1.3284647

[19] L. J. Lauhon, M. S. Gudiksen, D. Wang, C. M. Lieber. Epitaxial core-shell and core-multishell nanowire heterostructures. *Nature*, **420** (6911), 57–61 (2002). doi:10.1038/nature01141

[20] S. T. Le, P. Jannaty, X. Luo, A. Zaslavsky, D. E. Perea, S. A. Dayeh, S. T. Picraux. Axial SiGe Heteronanowire Tunneling Field-Effect Transistors. *Nano Letters*, **12** (11), 5850–5855 (2012). doi:10.1021/nl3032058. PMID: 23113718

[21] A. Rodríguez, J. Sangrador, T. Rodríguez, C. Ballesteros, C. Prieto, J. Jiménez. SiGe Nanowires Grown by LPCVD: Morphological and Structural Analysis. *MRS Proceedings*, **1258**, 1258–P05–05 (2010). doi:10.1557/PROC-1258-P05-05

[22] A. Rodríguez, T. Rodríguez, C. Ballesteros, J. Jiménez. SiGe/Si Nanowire Axial Heterostructures Grown by LPCVD Using Ga-Au. *MRS Proceedings*, **1510**, mrsf12–1510–dd06–05 (2013). doi:10.1557/opl.2013.273

[23] J. Anaya, A. Torres, V. Hortelano, J. Jiménez, A. C. Prieto, A. Rodríguez, T. Rodríguez, R. Rogel, L. Pichon. Raman spectrum of Si nanowires: temperature and phonon confinement effects. *Applied Physics A*, **114** (4), 1321–1331 (2013). doi:10.1007/s00339-013-7966-y

[24] M. I. Alonso, K. Winer. Raman spectra of c -$Si_{1-x}Ge_x$ alloys. *Phys. Rev. B*, **39**, 10056–10062 (1989). doi:10.1103/PhysRevB.39.10056

[25] T. P. Pearsall. Silicon-germanium alloys and heterostructures: Optical and electronic properties. *Critical Reviews in Solid State and Materials Sciences*, **15** (6), 551–600 (1989). doi:10.1080/10408438908243745

[26] P. Periwal, N. V. Sibirev, G. Patriarche, B. Salem, F. Bassani, V. G. Dubrovskii, T. Baron. Composition-Dependent Interfacial Abruptness in Au-Catalyzed Si1-xGex/Si/Si1-xGex Nanowire Heterostructures. *Nano Letters*, **14** (9), 5140–5147 (2014). doi:10.1021/nl5019707. PMID: 25118977

[27] T. E. Clark, P. Nimmatoori, K.-K. Lew, L. Pan, J. M. Redwing, E. C. Dickey. Diameter Dependent Growth Rate and Interfacial Abruptness in Vapor-Liquid-Solid Si/Si1-xGex Heterostructure Nanowires. *Nano Letters*, **8** (4), 1246–1252 (2008). doi:10.1021/nl072849k. PMID: 18321076

[28] G. Brönstrup, N. Jahr, C. Leiterer, A. Csáki, W. Fritzsche, S. Christiansen. Optical Properties of Individual Silicon Nanowires for Photonic Devices. *ACS Nano*, **4** (12), 7113–7122 (2010). doi:10.1021/nn101076t

[29] J. Anaya, J. Jiménez, A. Rodríguez, T. Rodríguez. Electromagnetic interaction between a laser beam and semiconductor nanowires deposited on different substrates: Raman enhancement in Si Nanowires. In *Symposium L, Photonic and Plasmonic Materials for Enhanced Optoelectronic Performance*, Band 1627 von *MRS Proceedings* (2014). doi:10.1557/opl.2014.250

[30] SOPRA. SOPRA DATABASE (2016)

[31] A. J. Sabbah, D. M. Riffe. Measurement of silicon surface recombination velocity using ultrafast pump-probe reflectivity in the near infrared. *Journal of Applied Physics*, **88** (11), 6954–6956 (2000). doi:http://dx.doi.org/10.1063/1.1316047

[32] M. Morita, T. Ohmi, E. Hasegawa, M. Kawakami, M. Ohwada. Growth of native oxide on a silicon surface. *Journal of Applied Physics*, **68** (3), 1272–1281 (1990). doi:http://dx.doi.org/10.1063/1.347181

About the interaction between a laser beam and group IV nanowires: a study of the electromagnetic field enhancement in homogeneous and heterostructured nanowires

J. L. Pura[1], J. Anaya[2], and J. Jiménez[1,*]

[1] *GdS Optronlab, Dpt. Física de la Materia Condensada, ed. LUCIA Universidad de Valladolid, Paseo de Belén 19, 47011 Valladolid, Spain*
[2] *MTC- Manufacturing Technology Centre, Ansty Park, Coventry CV79JU, UK*
[*] *jimenez@fmc.uva.es*

Keywords: Raman spectroscopy, group IV semiconductor nanowires, light/nanowire interaction, optical resonances, axially heterostructured nanowires

Abstract

The optical properties of semiconductor nanowires are object of study because they are the building blocks of the future nanophotonic devices. The high refractive index and its reduced dimension, make them suitable for photon engineering. The study of the interaction between nanowires and visible light has revealed resonances of the light absorption/scattering by the nanowires. Micro-Raman spectroscopy is used as a characterization method of semiconductor nanowires. The relation between the Raman intensity and the incident electromagnetic field permits to study the light/nanowire interaction through the micro-Raman spectra of individual nanowires. As compared to either metallic or dielectric nanowires, the semiconductor nanowires add additional tools to modify its interaction with light, e.g., the composition, the presence of heterostructures, both axial and radial, doping, and the surface morphology. One presents herein a study of the optical response of group IV semiconductor nanowires to visible photons. The study is experimentally carried out through the micro-Raman spectroscopy of different group IV nanowires, both homogeneous and heterostructured (SiGe/Si), and the results are analyzed in terms of the electromagnetic modelling of the light/nanowire interaction using finite element methods. The heterostructures are seen to produce additional resonances allowing new photonic capacities to the semiconductor nanowires.

P2

1 Introduction

Semiconductor nanowires (NWs) attract the attention of the scientific community because of the increasing number of applications based on their unique properties [1]. These properties arise from the confined dimension, the diameter, as compared to some characteristic lengths. Among other, the radius of the Bohr exciton for quantum confinement, the phonon mean free path for thermal conductivity, or the wavelength of the incident electromagnetic (EM) waves for optical antenna effects [1]. There is a great interest about the interaction between semiconductor NWs and light, because the optical properties of the NWs make of them the optimal candidates for the future nanophotonic devices.

Several unique optical properties of semiconductor NWs have been reported lately, e.g. waveguiding [2], optical resonances [3], antenna effects [4], etc. These effects are modulated by the NW diameter, the laser wavelength, and the dielectric properties of the NW and its surrounding medium. For certain NW diameters, resonant optical absorption /scattering takes place, resulting in large local electromagnetic fields inside the NW [5, 6], which can be experimentally investigated by microRaman spectroscopy [3, 7–9].

Up until now, most of the research effort has been focused on homogeneous NWs; however, heterostructured NWs are necessary for the fabrication of advanced devices. Some effort has been focused on core/shell heterostructured NWs, mainly focused on the stress assessment [10, 11], but much less effort has been devoted to the optical properties of axially heterostructured NWs.

In previous papers, we demonstrated the need of studying individual NWs [12], mainly because of the optical response of bundles of NWs is disturbed by the very different NWs dimensions probed by the laser beam, as well as by their spatial distribution within the laser beam spot. The main issue with this approach, i.e. using individual NWs, is that the Raman signal would be notably weak. Individual NWs have a very small scattering volume as compared to a bulk sample; therefore, one could expect a very low Raman signal arising from them. Fortunately, as we will show later on, the unique properties of the NWs come to help us and the Raman signal of an individual NW can be almost equivalent to the Raman signal arising from the corresponding bulk semiconductor under the same experimental conditions. The interaction between a NW and light can be analyzed in the frame of the Lorenz-Mie theory [13], or more accurately by solving the full Maxwell equations for this interaction. Here we have solved the electromagnetic equations by finite element methods (FEM) for different NW configurations, i.e. homogeneous group IV NWs, core/shell SiGe/Ge NWs, and axially heterostructured SiGe/Si NWs and the results are compared to the experimental micro-Raman results.

2 Experimental

We have studied the light/ NW interaction in group IV semiconductor NWs, both homogeneous Si NWs, and axially heterostructured SiGe/Si NWs, grown by the vapour-liquid-solid (VLS) method, using Si_2H_6 and GeH_4 as precursor gases and Au metal droplets as the catalysts. VLS growth is the most extended method to grow bottom up NWs; however, it does not provide abrupt axial SiGe/Si heterojunctions, because of the high solubility of group IV semiconductors in Au. Once the gas sources are switched-off to change the NW composition, the reservoir effect, due to the remaining atoms solved in the catalysts droplet, avoids the formation of sharp interfaces [14, 15].

The heterojunction appears as a region of graded composition from the nominal Ge concentration of the SiGe segment to the pure Si of the Si segment. In this framework, it is usually claimed that the HJ width is roughly equivalent to the diameter of the NW [14, 15]. Micro-Raman spectra of several individual Si/SiGe NWs were acquired with a Labram UV-HR 800 Raman spectrometer from Horiba-Jovin Yvon. The excitation light was provided by a frequency doubled Nd:YAG laser (532 nm). The excitation and the scattered light collection are performed by means of a confocal metallographic microscope with a high magnification objective (X100) and 0.95 numerical aperture. Under these conditions, the laser beam diameter at the focal plane is $\approx 1\mu m$, which is several times larger than the typical NW diameters, which range from 40 to 150 nm.

The Raman spectra were acquired by scanning the laser beam along the NW axis in steps of 100 nm, and under TM light polarization with respect to the NW axis, i.e. the electric field parallel to the NW axis. This orientation is selected because the NWs behave as electric dipoles face to the incident laser beam, and the Raman intensity as a

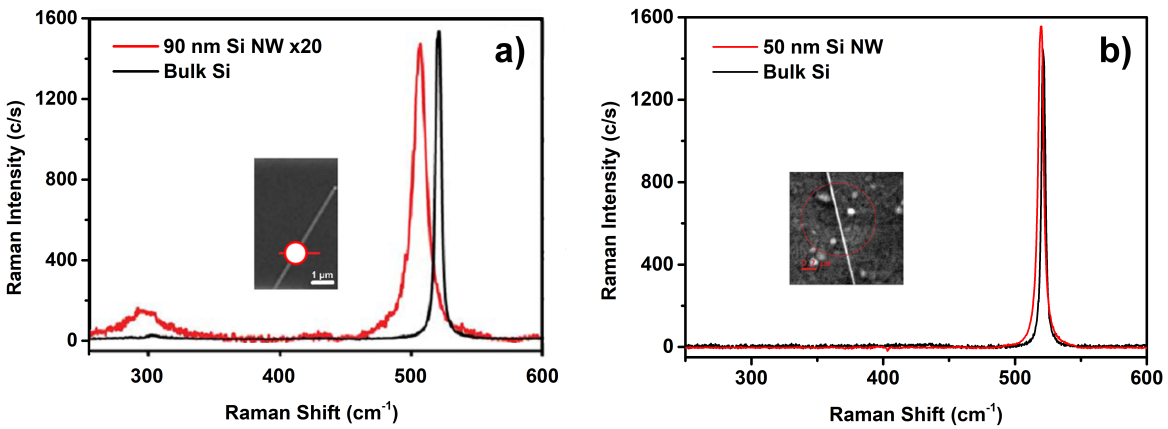

Figure 1: a) Raman spectra of a free standing Si NW and a bare Si bulk substrate, b) Raman spectra of a Si NW deposited on a metallic substrate and a bare Si bulk substrate. The red circles are the laser beam spots.

function of the angle formed by the NW axis and the light polarization axis reveals an electric dipole behavior.[16] The maximum Raman signal is therefore obtained for TM polarization with respect to the NW axis. On the other hand, the longitudinal scanning permits to precisely locate and study the electromagnetic response of the axial HJ.

An important issue is to avoid NW heating by the laser beam. When NWs surrounded by air, free standing NWs, are excited by a focused laser beam a substantial heating of the NW is done, because of its very low thermal conductivity, greatly reduced with respect to the bulk figures. The low thermal conductivity is due to both the low dimensionality and the surface morphology [17, 18]. Therefore, the Raman spectrum can be affected by the laser induced heating of the NW and care must be taken on the interpretation of such spectra [19]. The deposition of the NWs on a metallic substrate permits to minimize the NW heating. Additionally, we observed that the Raman signal was enhanced by the presence of the metallic substrate. In our Raman experiments we used an Al substrate, which permits the optimization of the Raman signal, but also acts as an efficient heat-sink avoiding the NW heating. The laser power was optimized to prevent any heating on the NWs [16]. The Raman measurements were carried out under laser power densities around $5\ 10^8\ W/m^2$, for which laser heating was negligible.

3 Results and discussion

The Raman spectrum of a Si NW compared to the Raman signal arising from bulk Si obtained under the same experimental conditions is shown in Figure 1. Figure 1a compares the spectrum of the free standing NW with respect to that of bulk Si. The typical Raman signature of Si at high temperature is observed in the free standing NW, with a clear downshift with respect to the 300 K Si Raman frequency. In Figure 1b the spectrum of the NW deposited on an Al substrate and that of bulk Si are shown, all of them obtained under the same excitation conditions. Interestingly, the two Raman signals are roughly equivalent in this case, in spite of a scattering volume ratio of near 100 times between bulk and NW when excited with a focused laser beam with a diameter of $\approx 1\mu m$. Therefore, taking into account the corresponding scattering volumes it is possible to estimate an enhancement in the Raman intensity per unit volume of roughly a factor 100 in the NW with respect to the bulk material. This resonance behavior allows achieving exhaustive Raman studies using individual semiconductor NWs. Note that the Al substrate enhances the Raman signal of the NW with respect to the Raman signal of the free standing NW, and effectively dissipates the heat generated by the laser beam absorption.

P2

Modeling the electromagnetic interaction between the laser beam and the NWs is the complement to the micro-Raman experiments. This model is solved by finite element methods using COMSOL Multiphysics. The Maxwell equations are solved for the NW and its surrounding space when excited by a focused laser beam in similar conditions to the micro-Raman experiments [16, 20]. The system formed by the air/NW/substrate was limited by cartesian perfectly matched layers (PMLs), which absorb the outgoing radiation eliminating secondary reflections, Figure 2. The complex refractive indexes used in the calculations were taken from Sopra database.[21] Details of the calculation procedure are in refs. [16] and [20].

The solution of the model provides the electromagnetic field intensity, $|E|^2$, distribution inside the NW. Since The Raman signal is directly proportional to the field intensity $|E|^2$, it is possible to analyze the Raman signal arising from the NW in terms of $|E|^2$ to compare it to the experimental values. In the case of homogeneous NWs this can be achieved by using a two dimensional (2D) model because of the axial symmetry, which allows to calculate the distribution of the electric field inside the NW as a function of the NW diameter, as we show in Figure 2.

The electric field distribution exhibits different patterns depending on the NW diameter. For diameters around 40 nm a nearly radial symmetry distribution is observed; for increasing diameters the electric field presents a lobular distribution with two or more lobes depending on the NW diameter. If one integrates the electric field to the full NW section one observes diameter resonances of $|E|^2$, which depend on the laser wavelength and the composition of the NW. The role of the NW composition is shown in Figures. 3 and 4, where the electric field was calculated for different SiGe NW compositions. The field distribution is similar for all of them, but the integrated intensity decreases with the Ge content for 532 nm light excitation, while it presents the opposite behavior for excitation with 632 nm. This holds for a NW diameter of 50 nm, Figure 3. For different diameters the results change, e.g for a diameter of 100 nm the opposite behavior happens, as shown in Figure 4.

In certain SiGe NWs the Raman spectrum reveals the existence of inhomogeneous composition inside the NW, with pure Ge regions in the NWs as shown in Figure 5, where one can appreciate the Raman peak of pure Ge (300 cm^{-1}), together with

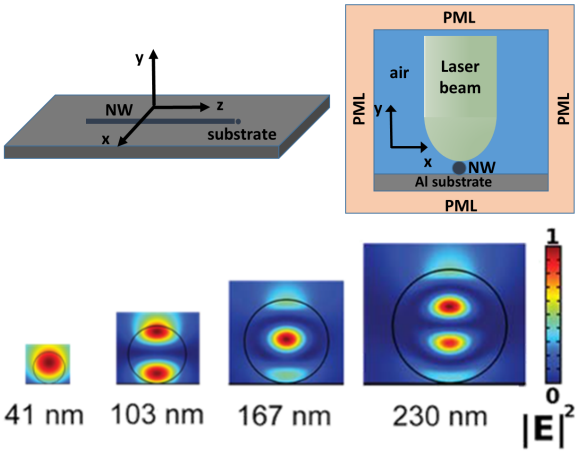

Figure 2: Scheme of the 2D modelling of the system NW/Substrate/ laser beam, the PLMS are perfect matching layers (upper panel). Calculated electromagnetic field intensity distribution inside Si NWs of different diameters deposited on an Al substrate. The simulation is done for a Gaussian laser beam with wavelength of 532 nm. The black circles represent the perimeter of the NWs with different diameters (lower panel).

the SiGe related bands. It should be noted that in SiGe it is frequently observed the segregation of Ge because of the Si oxidation creating a germanium rich layer [21, 22]. What is interesting here is that the Raman band associated with pure Ge ($\approx$ 300 cm^{-1}) modifies its intensity depending on the transversal position of the laser beam with respect to the NW axis. To analyse this behaviour we modelled the NW as a core-shell structure with a thin shell of segregated pure Ge. The $|E|^2$ distribution inside the NW ($\approx$ 85 nm diameter) is not homogeneous; in particular, it looks like two spatially opposed lobes strongly localised near the NW outer shell. This region in which $|E|^2$ is strongly localised will contribute the most to the Raman signal, being possible to explain the anomalous Raman spectrum by the presence of a Ge rich outer shell, which the contribution to the Raman signal is overrepresented because of the $|E|^2$ distribution. In Figure 5 we also show the results of the simulated laser cross walk experiment. This simulation shows that the localised $|E|^2$ distribution lobes rotate when the laser beam position across the NW changes, therefore, the Raman signal arises from different zones of the NW outer shell depending on the transverse

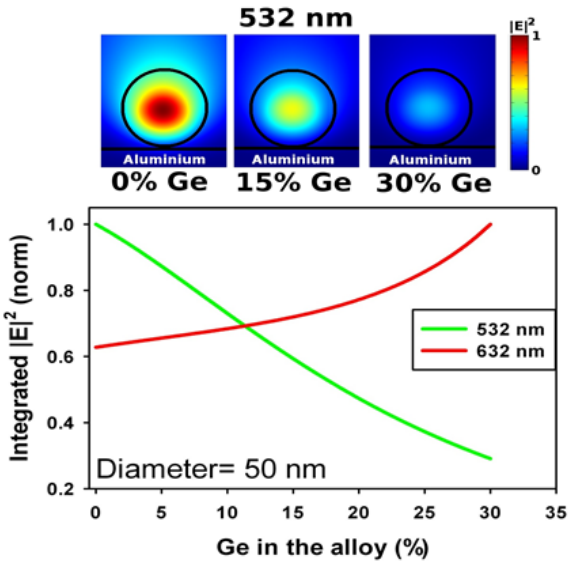

Figure 3: Calculated electromagnetic field intensity distribution inside an SiGe NW (50 nm diameter) as a function of the Ge content (%) for an excitation wavelength of 532 nm (upper panel). Integrated intensity vs Ge content for 532 nm and 632 nm excitations (lower panel).

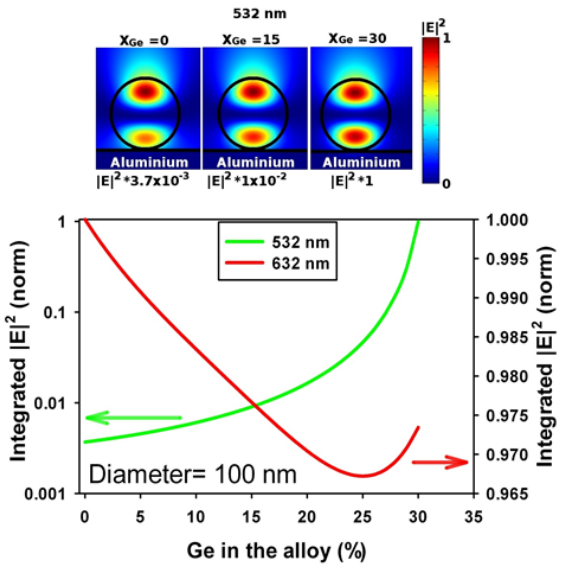

Figure 4: Calculated electromagnetic field intensity distribution inside a SiGe NW (100 nm diameter) as a function of the Ge content (%) for an excitation wavelength of 532 nm (upper panel). Integrated intensity vs Ge content for 532 nm and 632 nm excitations (lower panel).

laser position with respect to the NW axis, Figure 5. Therefore, the variation of the Ge related Raman band intensity with respect the position of the laser beam across the NW suggests that the Ge rich outer shell is non-homogeneous. The rotation of the localised $|E|^2$ lobes and the non uniformity of the Ge-rich layer can explain why the Raman spectra of the NW can be different for the three transverse positions of the laser beam represented in Figure 5, even when a similar volume of the NW is being probed for the three laser beam positions. The inhomogeneous Ge rich outer shell can be due to the oxidation of the NW [22, 23], but also to parasitic nucleation of Ge. The transmission electron microscopy (TEM) image and transverse electron dispersive X-Ray spectroscopy (EDX) scan of an SiGe NW are shown in Figure 6, showing the existence of a non uniform Ge rich outer shell.

The presence of the axial heterojunction breaks the longitudinal symmetry of the NW. Therefore, a 3D model must be applied, instead of the 2D model used for NWs without axial discontinuities, either homogeneous NWs or core/shell heterostructured NWs [16, 20]. The 3D model accounts for the presence of the axial HJ; and also takes account of the finite length of the NW. The modelled system consists of an axially heterostructured NW deposited on a metallic (Al) substrate, surrounded by air and illuminated by the 532 nm laser line focused on the NW by the microscope objective, in a similar configuration as the one used in the Raman experiments. Fig. 7.

The axial heterojunction in SiGe/Si NWs is not abrupt. The transition between the two segments is not sharp, but it appears as a region with graded composition [14, 15]. Usually, it is assumed to have a thickness of the order of the NW diameter; although it is more appropriate to say that the HJ width is a fraction of the NW diameter, depending on the growth conditions [24]. Therefore, when the laser beam impacts on the heterojunction it is probing the Si segment, the SiGe segment, and the HJ itself. These three regions of different composition shall contribute to the Raman spectrum. The Raman spectra of the heterostructured NWs are recorded along the NW axis in steps of 100 nm. The spectra recorded on the homogeneous Si and SiGe segments show the typical Lorentzian peaks, with the spectral parameters characteristic of Si and

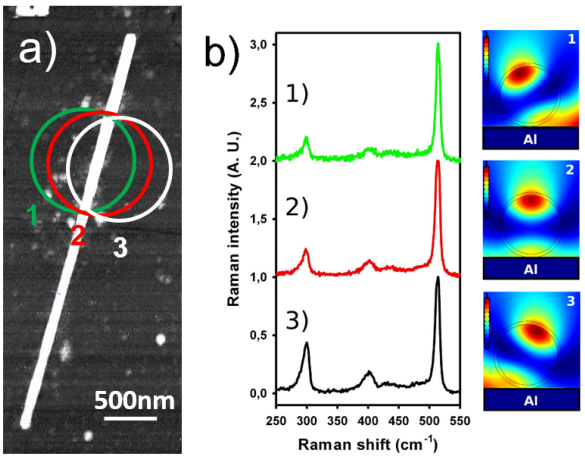

Figure 5: a) AFM image of a SiGe NW (85 nm diameter). The three circles correspond to the transversal positions of the laser beam. b) Raman spectra for the three positions of the laser beam, and field intensity distribution calculated for each of the three configurations, showing the rotation of the field pattern with the position of the laser beam with respect to the NW axis.

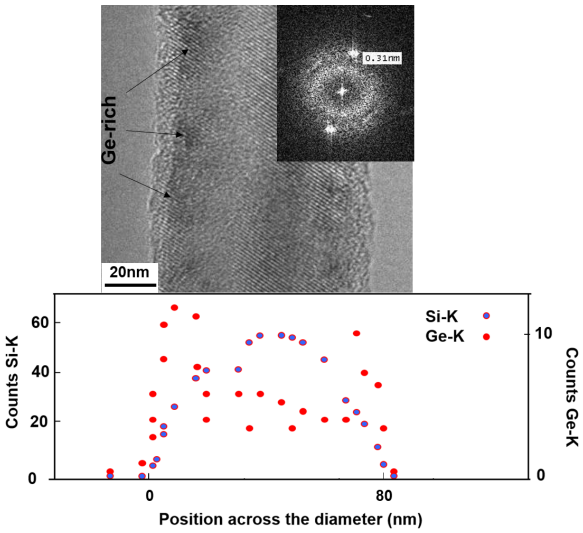

Figure 6: TEM image of a NW showing Ge rich clusters in the NW periphery (upper panel). EDX profile across the diameter showing Ge accumulation at the periphery.

SiGe pure NWs, respectively. Meanwhile, the spectra obtained when the laser beam shares the HJ and the neighbouring NW segments appear broadened and asymmetric, Figure 8. Furthermore, the overall Raman intensity is enhanced with respect to the homogeneous segments. This is the consequence of the overlapping between the Raman contributions arising from the different regions of the NW probed by the laser beam. The spectral deconvolution reveals the contribution to the experimental Raman band of the two NW segments, Si and SiGe, and an additional Raman peak arising from the HJ itself. When this deconvolution is done with only two Raman peaks, those corresponding to the two homogenous segments, one cannot achieve a satisfactory fitting of the Raman spectrum. It is necessary to add a third peak to achieve the fitting of the Raman spectrum of the region including the HJ. This third peak has spectral characteristics in between those of the Si and SiGe segments of the NW. It arises from the HJ itself, which is a compositionally graded NW rod. It is important to recall that the HJ width is close or below to the NW diameter ($\approx$ 50 nm in this case) [14, 15, 24], while the excited length of the two homogeneous segments of the NW lies around 500 nm (approximately half of the laser spot diameter) for a laser beam centred on the HJ. As a result, the probed volume of each of the homogeneous segments is at least 10 times larger than that of the HJ; however, the intensity of the Raman signal associated with the HJ is of the same order of magnitude, or even higher, as the signals arising from the homogeneous segments, see Figure 8. Translating this result into Raman intensity per unit of scattering volume, it results in an enhance-

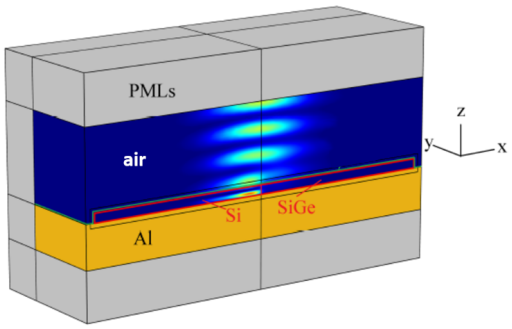

Figure 7: 3D model used for solving the interaction between the laser beam and the heterostructured NW.

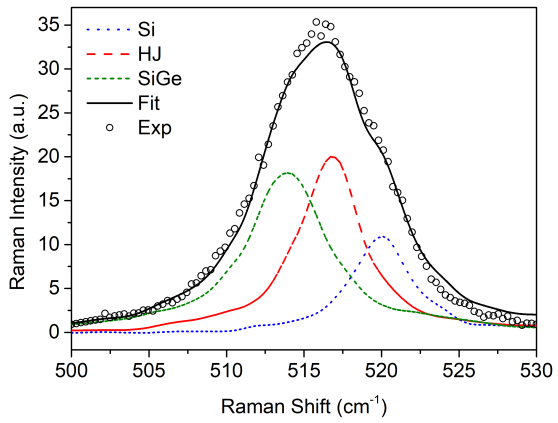

Figure 8: Raman spectrum obtained when the laser beam shares the two NW segments and the HJ. The three peaks obtained by deconvolution of the spectrum correspond to the SiGe segment, the HJ itself and the Si segment. (λ_{exc} = 532 nm)

ment of 10-20 times in the HJ region with respect to the homogeneous segments, depending on the studied NW. In ref. [16] one can see the spectrum at the HJ of a SiGe/Si axially heterostructured NW with higher concentration of Ge (60%), where one can clearly appreciate the HJ contribution.

The calculated results obtained from the solution of the EM model were contrasted to the experimental results. The Raman intensity profiles along the NW axis are plotted in Figure 9, where one establish the comparison between the experimental Raman profile, Figure 9a, showing the Raman intensity of the Si segment, the SiGe segment and the HJ, as a function of the laser beam position; and the calculated Raman profile. The Raman intensity is proportional to $|E|^2$, which is obtained from the distribution of the electric field along the NW by integrating over the volume of the NW probed by the laser beam at each beam position, Figure 9b. The Raman profiles evidence the signal enhancement that takes place at the HJ. We can see that the signal of the HJ region is comparable to that of the homogeneous segments, despite the difference of a factor 10 in volume, as it was aforementioned.

The simulations are in good agreement with the experimental measurements, reproducing the Raman experiments and the electromagnetic enhancement effect. Note that the spread out of the Raman signal around the HJ is due to the size of the laser beam. The decrease of the Raman intensity of the Si and SiGe segments toward the ends is due to the fact that the laser beam is partially out of the NW. The NW studied in Fig. 9 was longer on the Si side than in the SiGe side. One observes the decrease of the Raman intensity from the SiGe segment when laser beam starts to overrun the NW end.

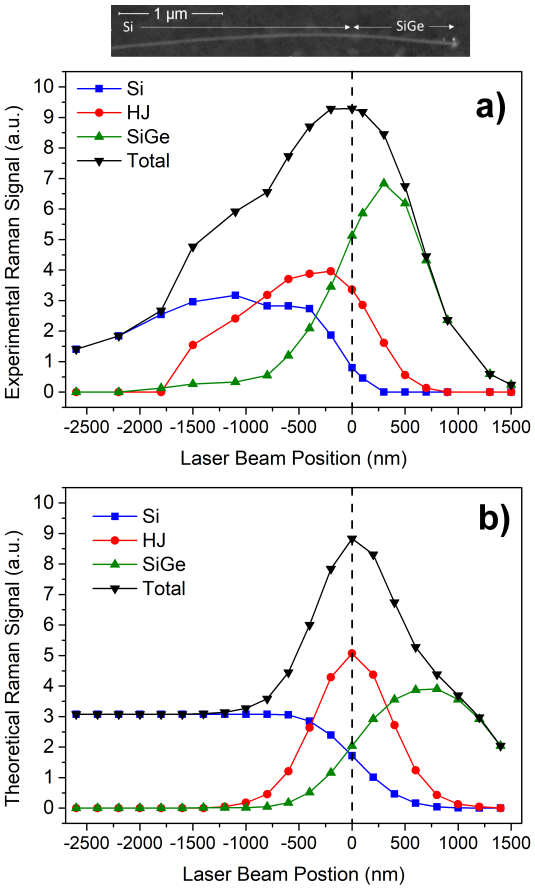

Figure 9: a) Experimental Raman profiles along a heterostructured Si/SiGe NW. b) Theoretical Raman profile of the simulated NW with similar characteristics to the experimental one. Note that the NW extends away a few more micrometers on the Si side.

P2

4 Conclusions

We have described the main effects resulting from the interaction between group IV semiconductor NWs and a focused laser beam. The influence of the NW diameter, NW composition, NW structure, in particular axially heterostructured SiGe/Si NWs, on the optical response of the NWs has been studied by both experimental micro-Raman spectroscopy, and the FEM solution of the Maxwell equations. Both experimental and modeling results are in good agreement, and permit to account for the very interesting optical properties of the NWs. The sensitivity of the optical properties of the NWs to those geometric, compositional and structural factors suggests a great potential of the NW for photon handling.

Achnowledgements

This work was funded by Junta de Castilla y León (Project VA293U13). J.L Pura was granted by Spanish Government, FPU program (FPU14/00916).

Supporting Information

Transverse scan of the SiGe NW, showing non homogeneous Ge-rich outershell (complementary to Fig. 5)

References

[1] G. Brönstrup, N. Jahr, C. Leiterer, A. Csáki, W. Fritzsche, S. Christiansen. Optical Properties of Individual Silicon Nanowires for Photonic Devices. *ACS Nano*, **4** (12), 7113–7122 (2010)

[2] M. Law, D. J. Sirbuly, J. C. Johnson, J. Goldberger, R. J. Saykally, P. Yang. Nanoribbon waveguides for subwavelength photonics integration. *Science (New York, N.Y.)*, **305** (5688), 1269–73 (2004). doi:10.1126/science.1100999

[3] H. Kallel, A. Arbouet, G. Benassayag, A. Chehaidar, A. Potié, B. Salem, T. Baron, V. Paillard. Tunable enhancement of light absorption and scattering in Si 1-xGe x nanowires. *Physical Review B - Condensed Matter and Materials Physics*, **86** (8) (2012). doi:10.1103/PhysRevB.86.085318

[4] L. Cao, J. S. Park, P. Fan, B. Clemens, M. L. Brongersma. Resonant germanium nanoantenna photodetectors. *Nano Letters*, **10** (4), 1229–1233 (2010). doi:10.1021/nl9037278

[5] L. Cao, J. S. White, J.-S. Park, J. a. Schuller, B. M. Clemens, M. L. Brongersma. Engineering light absorption in semiconductor nanowire devices. *Nature materials*, **8** (8), 643–647 (2009). doi:10.1038/nmat2477

[6] R. Ruppin. Electromagnetic energy inside an irradiated cylinder. *J. Opt. Soc. Am. A*, **15** (7), 1891–1895 (1998). doi:10.1364/JOSAA.15.001891

[7] L. Cao, B. Nabet, J. E. Spanier. Enhanced Raman Scattering from Individual Semiconductor Nanocones and Nanowires. *Physical Review Letters*, **96** (15), 157402 (2006). doi:10.1103/PhysRevLett.96.157402

[8] G. S. Doerk, C. Carraro, R. Maboudian. Single nanowire thermal conductivity measurements by raman thermography. *ACS Nano*, **4** (8), 4908–4914 (2010). doi:10.1021/nn1012429

[9] F. J. Lopez, J. K. Hyun, U. Givan, I. S. Kim, A. L. Holsteen, L. J. Lauhon. Diameter and polarization-dependent raman scattering intensities of semiconductor nanowires. *Nano Letters*, **12** (5), 2266–2271 (2012). doi:10.1021/nl204537d

[10] Z. Zhang, D. C. Dillen, E. Tutuc, E. T. Yu. Strain and Hole Gas Induced Raman Shifts in Ge-Si x Ge 1-x Core-Shell Nanowires Using Tip-Enhanced Raman Spectroscopy. *Nano Letters*, S. 150609142006005 (2015). doi:10.1021/acs.nanolett.5b00176

[11] D. C. Dillen, K. M. Varahramyan, C. M. Corbet, E. Tutuc. Raman spectroscopy and strain mapping in individual Ge-Si x Ge 1 - x core-shell nanowires. *Physical Review B*, **86** (4), 045311 (2012). doi:10.1103/PhysRevB.86.045311

[12] J. Anaya, A. Torres, V. Hortelano, J. Jim??nez, A. C. Prieto, A. Rodr??guez, T. Rodr??guez, R. Rogel, L. Pichon. Raman spectrum of Si nanowires: Temperature and phonon confinement effects. *Applied Physics A: Materials Science and Processing*, **114** (4), 1321–1331 (2014). doi:10.1007/s00339-013-7966-y

[13] M. Kerker. *The scattering of light : and other electromagnetic radiation.* ISBN 9781483191744

[14] T. E. Clark, P. Nimmatoori, K.-k. Lew, L. Pan, J. M. Redwing, E. C. Dickey. Diameter Dependent Growth Rate and Interfacial Abruptness in Vapor - Liquid - Solid Si / Si 1 - x Ge x Heterostructure Nanowires. *Nano Letters*, **8** (4), 1246–1252 (2008)

[15] P. Periwal, N. V. Sibirev, G. Patriarche, B. Salem, F. Bassani, V. G. Dubrovskii, T. Baron. Composition-Dependent Interfacial Abruptness in Au-Catalyzed Si1-xGex/Si/Si1-xGex Nanowire Heterostructures. *Nano Letters*, **14**, 5140–5147 (2014)

[16] J. L. Pura, J. Anaya, J. Souto, A. C. Prieto, A. Rodríguez, T. Rodríguez, P. Periwal, T. Baron, J. Jiménez. Electromagnetic field enhancement effects in group IV semiconductor nanowires. A Raman spectroscopy approach. *Journal of Applied Physics*, **123** (11), 114302 (2018). doi:10.1063/1.5012987

[17] D. Li, Y. Wu, P. Kim, L. Shi, P. Yang, A. Majumdar. Thermal conductivity of individual silicon nanowires. *Applied Physics Letters*, **83** (14), 2934–2936 (2003). doi:10.1063/1.1616981

[18] J. Anaya, T. Rodríguez, J. Jiménez. Predictive Model for the Thermal Conductivity of Rough and Smooth Silicon Nanowires. *Science of Advanced Materials*, **7** (6), 1097–1107 (2015). doi:10.1166/sam.2015.2154

[19] A. Torres, A. Martín-Martín, O. Martínez, A. C. Prieto, V. Hortelano, J. Jiménez, A. Rodríguez, J. Sangrador, T. Rodríguez. Micro-Raman spectroscopy of Si nanowires: Influence of diameter and temperature. *Applied Physics Letters*, **96** (1), 011904 (2010). doi:10.1063/1.3284647

[20] J. L. Pura, J. Anaya, J. Souto, Á. C. Prieto, A. Rodríguez, T. Rodríguez, J. Jiménez. Local electric field enhancement at the heterojunction of Si/SiGe axially heterostructured nanowires under laser illumination. *Nanotechnology*, **27** (45), 455709 (2016). doi:10.1088/0957-4484/27/45/455709

[21] Sopra database S A, France. www.sspectra.com/sopra

[22] F. K. LeGoues, R. Rosenberg, T. Nguyen, F. Himpsel, B. S. Meyerson. Oxidation studies of SiGe. *Journal of Applied Physics*, **65** (4), 1724–1728 (1989). doi:10.1063/1.342945

[23] N. Sugiyama, T. Tezuka, T. Mizuno, M. Suzuki, Y. Ishikawa, N. Shibata, S. Takagi. Temperature effects on Ge condensation by thermal oxidation of SiGe-on-insulator structures. *Journal of Applied Physics*, **95** (8), 4007–4011 (2004). doi:10.1063/1.1649812

[24] J. Pura, P. Periwal, T. Baron, J. Jiménez. Growth dynamics of SiGe nanowires by the vapour-liquid-solid method and its impact on SiGe/Si axial heterojunction abruptness. *Nanotechnology*, **29** (35), 355602 (9pp) (2018). doi:10.1088/1361-6528/aaca74

P2

Supporting Information

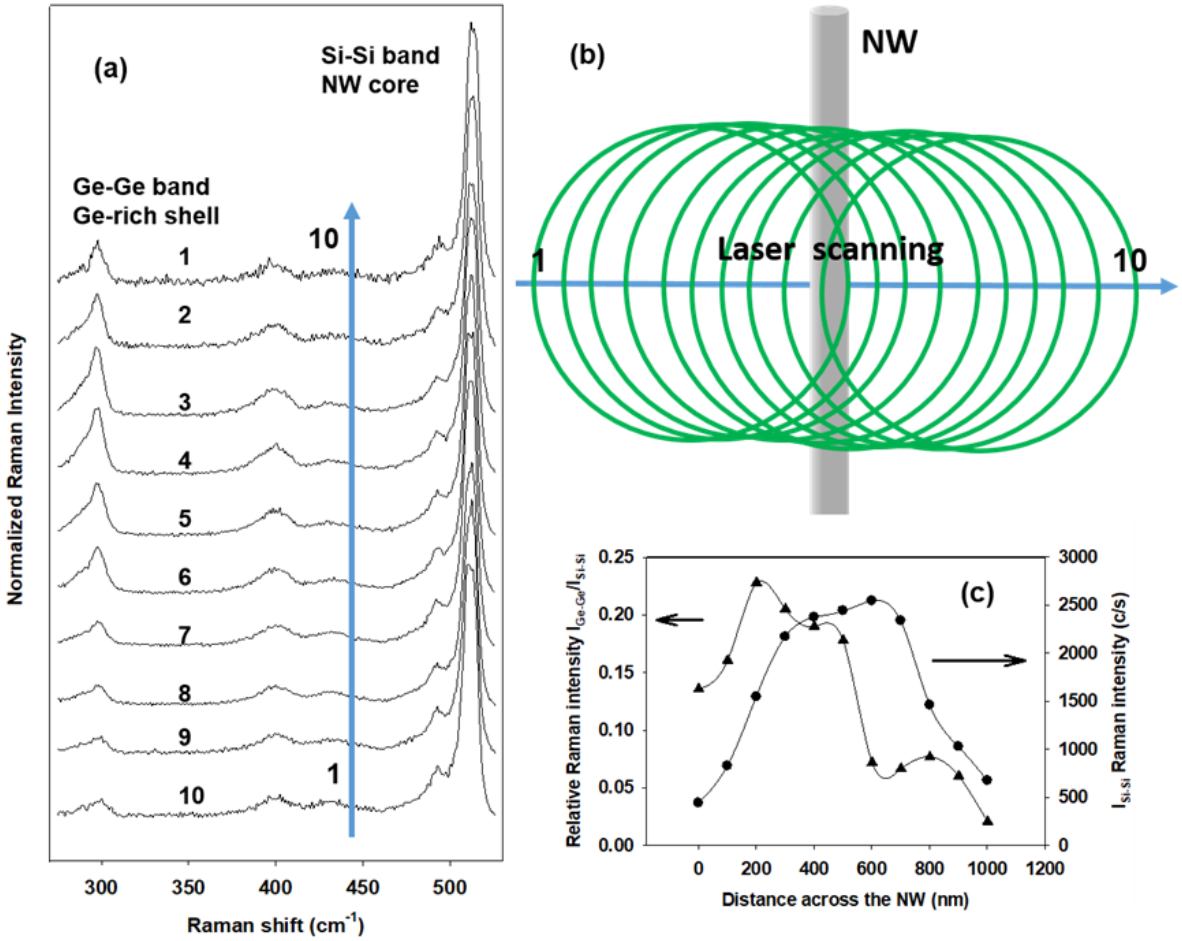

S1: a) Ten spectra acquired by scanning the laser beam across the NW, see b) the spectra are normalized to the intensity of the Si-Si Raman band. b) Scheme of the Raman spectra acquisition. c) Intensity of the Si-Si Raman band arising from the SiGe alloy forming the NW core, and relative intensity of the Ge-Ge band (298 cm^{-1}) arising from the Ge-rich clusters localized in the outer shell of the NW. The intensity of the Si-Si band ($\approx$ 513 cm^{-1}, corresponding to a Ge fraction in the alloy of 15%) roughly follows the Gaussian laser power distribution, while the Ge-Ge band does not follow because of the non homogeneous distribution of the Ge-rich clusters in the outer shell of the NW.

4.2 SiGe/Si/SiGe NWs - High Ge Concentration

In the second section of this chapter, the Raman enhancement effect is further explored. To do this, NWs with higher Ge concentration have been investigated. These NWs have been manufactured by the group of Thierry Baron from the University of Grenoble Alpes using the VLS method. The Ge concentration in the SiGe segments is $\approx 60\%$ and the NW structure is SiGe/Si/SiGe, presenting two different HJs. According to the higher Ge concentration the Raman peak of the Si-Si(SiGe) band is shifted to around $480\,\mathrm{cm}^{-1}$ which is well separated from the $520.6\,\mathrm{cm}^{-1}$ of the Si phonon, see Section 3.4.3. The higher shift removes any compositional ambiguity that could appear for the low Ge concentration NWs. This allows to clearly distinguish both contributions without the need for a complicated deconvolution. This is a great advantage since the Raman spectra analysis is significantly simplified, and the enhancement effect becomes clearer and stronger. Furthermore, the detection of the same effect on NWs with different composition reinforces our explanation of the phenomenon.

Regarding the simulations, the FEM model was further refined thanks to the new experimental data provided by the higher Ge concentration NWs. Currently, the FEM model is able to reproduce the experimental measurements with an excellent agreement. Also, the correlation between the model data and the experiments is not only qualitative, but the model can reproduce the enhancement on these NWs quantitatively.

Electromagnetic field enhancement effects in group IV semiconductor nanowires. A Raman spectroscopy approach

J. L. Pura[1], J. Anaya[2], J. Souto[1], A.C. Prieto[1], A. Rodríguez[3], T. Rodríguez[3], P. Periwal[4], T. Baron[4], and J. Jiménez[1,*]

[1] *GdS Optronlab, Dpt. Física de la Materia Condensada, ed. LUCIA Universidad de Valladolid, Paseo de Belén 19, 47011 Valladolid, Spain*
[2] *HH Wills physics Laboratory, University of Bristol, Tyndall Avenue, BS* 1TL, Bristol, UK*
[3] *Ingeniería Electrónica, ETSIT, Universidad Politécnica de Madrid, 28040 Madrid, Spain*
[4] *University Grenoble Alpes, LTM, F-38000 Grenoble, France and CNRS, LTM, F-38000 Grenoble, France*
[*] *jimenez@fmc.uva.es*

P3

Keywords: Nanowires, heterojunctions, light-matter interaction, Raman, Si, SiGe, electromagnetic enhancement

Abstract

Semiconductor nanowires are the building blocks of the future nanoelectronic devices. Furthermore, its large refractive index and its reduced dimension, make them suitable for nanophotonics. The study of the interaction between nanowires and visible light reveals resonances that promise light absorption/scattering engineering for photonic applications. Micro-Raman spectroscopy has been used as a characterization tool of semiconductor nanowires. The light/nanowire interaction can be experimentally assessed through the micro-Raman spectra of individual nanowires. As compared to both metallic and dielectric nanowires, semiconductor nanowires add additional tools for photon engineering. In particular, one can grow heterostructured nanowires, both axial and radial, also one could modulate the doping level and the surface condition, among other factors than can affect the light/NW interaction. We present herein a study of the optical response of group IV semiconductor nanowires to visible photons. The study is experimentally carried out through the micro-Raman spectroscopy of different group IV nanowires, both homogeneous and axially heterostructured (SiGe/Si). The results are analyzed in terms of the electromagnetic modelling of the light/nanowire interaction using finite element methods. The presence of axial heterostructures is shown to produce electromagnetic resonances promising new photon engineering capacities of semiconductor nanowires.

P3

1 Introduction

Semiconductor nanowires (NWs) are one-dimensional structures allowing the engineering of photons, phonons, electrons, and plasmons, which grants them a paramount role on nanodevice development. Significant differences with the behaviour of the bulk materials are enabled by the large aspect ratio and the size of the confined dimension, the NW diameter [1–4]. In particular, the interaction of semiconductor NWs with light presents very promising features for advanced photonic devices; e.g. photovoltaic cells, photo detectors, and light emitters, including lasers. In this frame, a broad spectrum of amazing optical properties has been reported for deep subwavelength diameter semiconductor NWs, e.g. waveguiding [4], optical resonances [5], antenna effects [6], etc. It has been shown that light couples to NWs in different ways depending on the NW diameter, NW composition, light wavelength, and the dielectric mismatch between the NW and the surrounding media [7]. All these variables allow tuning the optical properties of the NWs. One of the most relevant properties concerning the light/NW interaction is the ability of NWs to enhance the optical absorption/scattering for certain NW diameters [4–6, 8–11]. Different phenomena related to such resonance effect have been reported, e.g. enhanced photocurrent in Ge NWs [8], enhanced elastic and inelastic light scattering by Si NWs [12], light extinction [13], enhanced light emission [14–17], second harmonic generation [18], optical annealing of Si NWs [19], among other.

Compared to either dielectric micro-resonators or metal cavities, semiconductor NWs present additional chances for engineering the optical resonances. In particular, its suitability for fabricating complex structures as heterojunctions (HJs), quantum wells, superlattices or selective doping, should provide additional means to engineer the light/NW interaction. HJs are a fundamental for most electronic and optoelectronic devices, such as sensors, solar cells, thermoelectric devices, etc. The proper characterization of the HJs optical properties is essential to improve the performance of optoelectronic devices.

Quantitative analysis of the interaction between the electromagnetic (EM) radiation and NWs has been carried out by the extension to NWs of the Lorenz-Mie theory, developed for the study of the electromagnetic behavior of resonant micro-spheres [20]. In this theory, the NWs are described as infinitely long cylinders immersed in a homogeneous and isotropic non absorbing medium. The calculation of the absorption and scattering efficiencies of NWs, Qabs and Qsc respectively, has revealed a strong dependence of these magnitudes with the NW diameter and the light wavelength [10]. Numerical solutions of the problem by the finite difference in time domain (FDTD) method showed that the electric field inside the NW is not homogeneously distributed, but a pattern of lobed like structures, which distribution depends on the NW diameter, is observed [7].

We study herein the interaction between a laser beam focused through a high magnification microscope objective and group IV semiconductor NWs, both compositionally homogeneous and axially heterostructured. This interaction is experimentally monitored by micro-Raman spectroscopy, and the results are contrasted with the solution of the Maxwell equations using finite element methods (FEM). In section 2, we describe the samples and the experimental procedure, section 3 deals with the Raman analysis of these NWs, section 4 is devoted to the FEM modelling of the light/NW coupling, and, finally, section 5 presents the discussion of the results, highlighting the role of the axial heterojunctions as optical enhancers.

2 Experimental and Samples

Group IV NWs were grown by the vapour-liquid-solid (VLS) method using a commercial low pressure chemical vapor deposition (LPCVD) reactor. Either SiH_4 or Si_2H_6 and GeH_4 were used as precursor gases and Au metal droplets were used as catalysts [21].

Single Si NWs were grown at 470 °C using Si_2H_6 as a precursor; while the SiGe NWs (with a nominal Ge atomic fraction close to 0.1) were grown at 430 °C. The carrier gas was H_2, preserving for the different precursor flow ratios a total pressure of 400 mTorr all over the growth run [21]. Under these growth conditions straight NWs with uniform diameters ranging from 30 to 100 nm were obtained. A crucial issue concerns the HJ, in a previous work the different growth approaches followed to achieve the matching between the SiGe and Si segments in the axially heterostructured NWs were discussed [22]. The best way to achieve a good junction between SiGe and Si was by switching off the GeH4 source, while keeping a continuous flow of Si_2H_6.

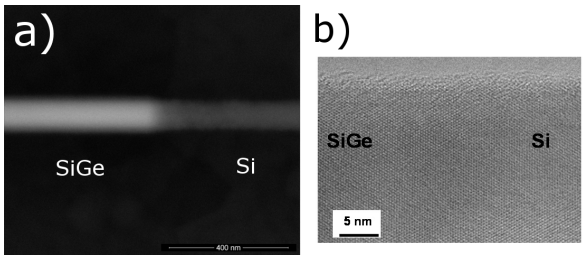

Figure 1: a) Backscattering SEM image of a heterostructured SiGe/Si NW (diameter ≈ 110 nm). b) HR-TEM image of the HJ region of a SiGe/Si axially heterostructured NW showing the excellent crystalline quality of the transition and the absence of any kind of defects.

The morphological features of the NWs were studied in a high resolution field emission scanning electron microscope (FESEM). The NWs lengths varied from 2 to 5 μm, and they appear as straight cylinders without appreciable tapering. Transmission Electron Microscopy (TEM) showed the excellent crystallinity of the NWs, figure 1b. In particular, high resolution TEM images of the HJ region of SiGe/Si HJs did not show structural discontinuities at the junction, nor stacking faults, or other structural defects [21, 22].

It is claimed that in VLS growth the abruptness of the HJ depends on the solubility of the atomic species in the catalysts metal. Due to the reservoir effect in the catalysts droplet once the precursor gas source is switched-off to shift to the composition of the next NW segment, the remaining atoms solved in the catalysts droplet continue to be deposited up to reaching a sub-saturation concentration. The result is a compositionally graded junction, with composition varying between the compositions of the two NW segments, $Si_{1-x}Ge_x$ and Si respectively. This effect is particularly relevant in the SiGe system because of the high solubility of Ge in Au. According to this, the SiGe/Si HJ presents a characteristic trailing gradual composition. The trailing HJ width was claimed to be roughly equivalent to the NW diameter [23–25], thus, the axially heterostructured NWs consist of a $Si_{1-x}Ge_x$ segment, a narrow $Si_{1-y}Ge_y$ HJ layer with a graded Ge composition ($x \leq y \leq 0$), and a Si segment. Atomic resolution high-angle annular dark-field scanning transmission electron microscopy (HAADF-STEM) reveals the existence of the compositionally graded HJ [24], which can be also observed by high resolution energy dispersive X-Ray spectroscopy (EDS), though a precise estimation of the composition gradient is not easy to be achieved because of the e-beam size.

As grown NWs were separated from the substrate in an ultrasonic bath, and suspended in methanol. Droplets of this suspension were spread out on an Al coated Si substrate for the micro-Raman (μ-R) measurements. The choice of the substrates is based on the optimization of the Raman signal, which is enhanced by the presence of the metallic substrate with respect to free standing NWs. Also, but not less important, the presence of the metallic substrate improves the thermal management of the NW allowing to minimize the laser induced heating during the μ-R experiments. Al coated substrates were satisfactory from both the thermal point of view, and the enhancement of the Raman signal. Therefore, they were used as the standard substrate for our micro-Raman measurements. The Al coating was around 0.5 μm thick, enough to block any optical signal arising from the Si substrate. This thickness also guarantees a continuous Al layer with no Al islands, ruling out any Al related plasmon enhancement of the Raman signal.

μ-R spectra were recorded with a Labram UV-HR 800 Raman spectrometer from Horiba - Jobin Yvon. The excitation and the scattered light collection were performed by means of a confocal metallographic microscope with a high magnification objective (X100) and 0.95 numerical aperture. A frequency doubled Nd:YAG laser (532 nm) was used as the excitation source. The laser beam diameter at the focal plane is slightly below 1 μm according to the Abbe's formula ($\phi = 1.22\lambda/NA$), which is several times larger than the diameter of the studied NWs, that typically ranges from 30 to 100 nm. It is important to note that the effective excitation power on the NW depends on its position inside the Gaussian power distribution of the focused laser beam [26, 27]. Prior to the Raman measurements the dimensions and morphology of each NW were characterized in a field emission scanning electron microscope (FESEM).

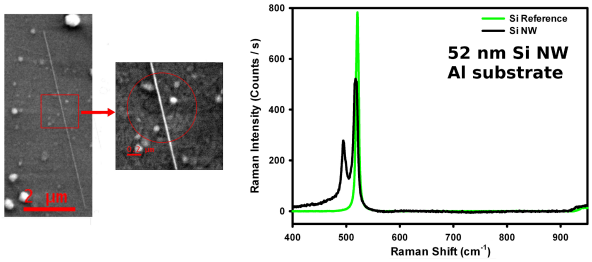

Figure 2: a) SEM image of a Si NW (52 nm diameter). The red circle represents the laser beam spot. b) Raman spectrum of a bare Si substrate and a Si NW on an Al substrate, respectively, showing comparable intensities in spite of the different scattering volumes. The low frequency peak at 495 cm^{-1} observed in the Si NW is associated with either a surface phonon or a hexagonal polytype. Its presence does not alter the course of the discussion, and the debate about it is out of the scope of this work.

P3

3 Experimental Results

μ-Raman spectroscopy has demonstrated to be a powerful non-destructive technique for the characterization of semiconductor NWs. It provides information about several relevant aspects of the NWs, e.g. the structure, composition, stress, and thermal, electronic, and optical properties [5, 7, 28–32]. Some of the above mentioned properties depend on the NW dimension. Therefore, in order to give sense to the Raman spectrum one needs to work with individual NWs instead of ensembles of NWs, which give a Raman spectrum averaged over a certain population of NWs with a distribution of diameters and lengths. Furthermore, the Raman signal is proportional to the excitation light intensity (i.e. $\propto |E|^2$), this makes Raman scattering an excellent tool to catch sight of the electromagnetic interaction between NWs and light.

A priori, the measurement of the Raman spectrum of individual NWs is challenging because of the low efficiency of Raman scattering, which is a second order optical process. This results in weak Raman signal when dealing with small sampling volumes, as it can be the case of individual NWs. On the other hand, NWs are not efficient thermal carriers [2, 3], therefore, in order to avoid laser induced heating, one has to keep low excitation laser power densities. Laser heating might modify the shape of the Raman spectrum leading to misinterpretations, in particular, free standing NWs are substantially heated up during Raman experiments because of the poor heat dissipation across them [2, 3, 26, 27, 31]. Laser induced heating is almost negligible under our experimental conditions because of the use of a metallic substrate, namely Al coated Si, and the adequate excitation conditions.

When the NWs are deposited on certain substrates, e.g., Al coated Si, they can be directly observed at the optical microscope in spite of their deeply subwavelength diameter, which evidences that the NWs behave as nanolenses for visible light. Furthermore, the observation of the NWs in the optical microscope depends on its orientation with respect to the light polarization axis, showing that the NW is a very anisotropic optical object [16, 17].

All these optical behaviors point to an unusual interaction between the NW and light. This is well observed when one measures the Raman spectrum of individual Si NWs. Regardless of the small sampling volume, when the NWs were deposited on different substrates the Raman intensities recorded for individual NWs reached the same order of magnitude as the intensity recorded for bulk Si under similar excitation conditions, figure 2. Note that in terms of Raman intensity per unit of scattering volume the Raman signal arising from the NW presents a significant enhancement with respect to the bulk Si signal, about two orders of magnitude. The NWs behave as optical nano-antennas rendering the Raman spectrum of individual NWs measurable under low laser power excitation for resonant diameters [28–30]. Therefore, μ-R spectra of individual NWs without external perturbations, e.g. heating, can be recorded if one adopts the appropriate experimental configuration.

As mentioned above, the NWs are optically anisotropic, as a result, the Raman signal will depend strongly on the polarization of the incident light. A polar plot of the recorded Raman intensity with respect to the angle formed between the light polarization and the NW axis will show a dipolar behavior in which the maximum signal is observed when the electric field of the incident light is aligned parallel to the NW axis, figure 3. All the Raman spectra of the NWs presented here were recorded in this configuration to optimize the signal/noise ratio.

The full characterization of the NWs was carried out by acquiring the Raman spectra by scanning the laser beam either along or across the NW axis in steps of 50-100 nanometers. Transverse laser scans across the NW permit to establish the Raman response of the NW to the laser intensity. In pre-

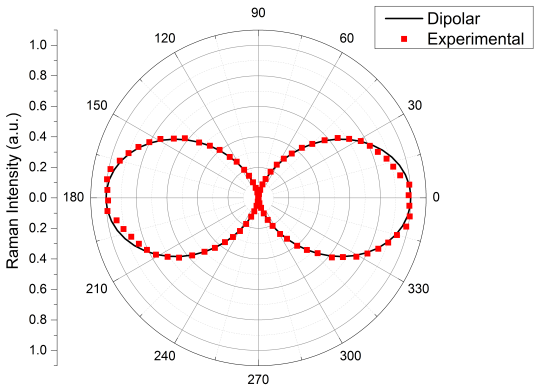

Figure 3: Polar plot of the normalized Raman intensity of the HJ region of a Si/SiGe heterostructured NW recorded for different polarization angles of the incident light with respect to the NW axis. The plot shows a clear dipolar behaviour, and the result is the same for all Raman signals coming from the NW.

vious works, we studied the effective excitation intensity depending on the position of the NW inside the Gaussian power distribution of a focused laser beam [26, 27]. When the Raman peak frequency remains unchanged across the transverse scan, one can assume that there is not noticeable heating of the NW by the laser beam for that selected laser power. The Raman peak frequencies obtained from the transverse scan across a Si NW are shown in figure 4b. One observes that there is a negligible frequency shift along the scanning line, which means that the NW is not heated by the laser beam within the range of powers drawn by the laser power Gaussian profile, see the temperature conversion in figure 4c. When the laser power increases one observes the typical peak frequency downshift and broadening associated with increased temperature. Therefore, taking into account the temperature profiles of figure 4, one can ascertain that for laser powers below 50 μW (532 nm) one can work in conditions of negligible laser induced heating. Therefore, transverse scans across the NW are suitable for fixing the optimal excitation conditions, also permit to align the NW with the beam axis.

3.1 Axially heterostructured NWs

Up until now, most of the research interest about the light/NWs interaction has focused on homogeneous single NWs [5, 6, 10]], while the role of the heterojunctions on the light/NW interaction has been scarcely studied, and mainly focused on core/shell HJs [33]. The analysis of the axially heterostructured NWs was done by scanning the laser beam along the NW axis in steps of 100 nm. As mentioned above, the trailing SiGe/Si HJ consists of a compositionally graded layer with a thickness roughly equivalent to the NW diameter [22–25, 34]. A priori, when the focused laser beam shares the two NW segments and the HJ, the Raman signal arising from the HJ layer must be much less intense than the Raman signals arising from the two NW segments, in terms of scattering volume figures. Under normal conditions it should be scarcely detected, because of the very small sampling volume of the HJ.

The sampling volumes of the three NW regions simultaneously shared by the laser beam, $Si_{1-x}Ge_x/Si_{1-y}Ge_y(HJ)/Si$, obey to a ratio $\approx$ 1:0.08:1 for a 40 nm diameter NW, assuming a HJ width equivalent to the NW diameter. Once the volume ratio is corrected by the Gaussian laser power distribution, assuming that the HJ is placed in the laser beam center, the integrated laser power ratio for the three sampled volumes scales to $\approx$ 1:0.1:1, which is still greatly unfavourable for the HJ region in terms of effective excitation.

Typical Raman spectra (only the Si-Si Raman mode of the SiGe alloy is shown) obtained along a 50 nm diameter axially heterostructured SiGe/Si NW deposited on an Al coated Si substrate can be seen on figure 2 of ref. [39]. One observes the typical Raman spectrum of a Si NW for the laser beam focused on the Si segment. When it is focused on the $Si_{1-x}Ge_x$ segment one observes the Raman spectrum of the SiGe alloy with the nominal Ge composition, which in this case is $\approx$ 10%. This has been confirmed by the peak frequency shift of the Si-Si Raman mode [35, 36], and also by EDS measurements in the TEM. Note that the studied NWs have diameters ($d > 30$ nm) for which phonon confinement does not occur [37, 38], then, Raman bands are not disturbed by size effects.

Regarding the Raman spectrum recorded when the laser beam shares the two NW segments and the HJ, one observes a band peaking at an intermediate frequency between the ones of the Si and $Si_{1-x}Ge_x$ NW segments. While the spectra taken in the sin-

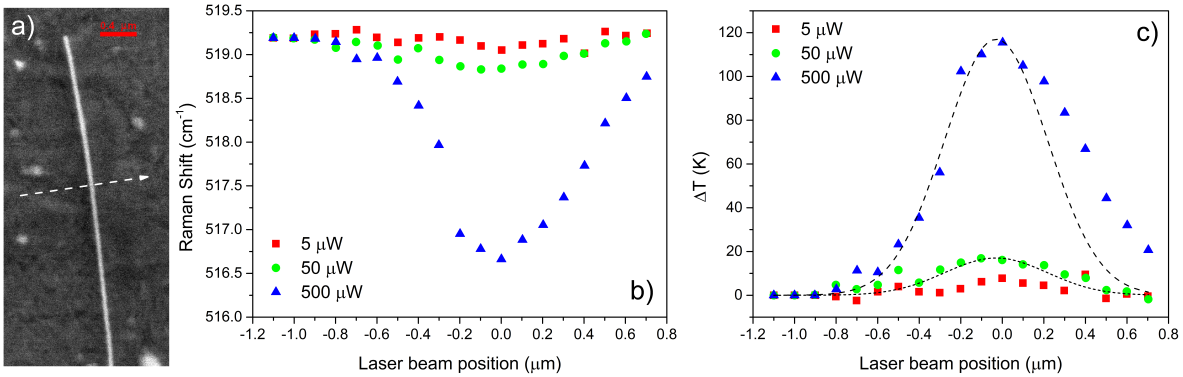

Figure 4: a) SEM image of a Si NW. The arrow indicates the scanning line crossing the NW, b) Raman shift profiles for different excitation conditions, see the symbols on the right side of the figure. c) Estimated temperature deduced from the Raman shift. Note that as the NW position is closer to the beam axis the effective excitation laser power density is enhanced because of the Gaussian laser power distribution. One observes that laser powers up to 50 μW (532 nm) permit to work without significant NW heating, while for higher laser powers, the temperature starts to increase under the laser exposure. Because of the Gaussian power distribution the effective excitation laser power depends on the position of the NW with respect to the laser beam axis. These scans permit to fix the conditions for which the temperature enhancement can be neglected.

P3

gle NW segments are fitted by only one Lorentzian curve, the spectrum sharing the HJ needs three Lorentzian curves to be satisfactorily fitted. Each of the three bands resulting from the deconvolution correspond respectively to the $Si_{1-x}Ge_x$ segment, the Si segment, and the HJ layer itself. In the case of the HJ the Raman spectrum looks like the SiGe spectrum corresponding to an intermediate composition in between those of the two homogeneous segments, see figure 3 of ref. [39]. Surprisingly, the Raman intensity arising from the HJ is as intense, or even higher, than the Raman intensities arising from the two NW segments, instead of the expected 1:0.1:1 volume ratio previously. Therefore, a significant Raman enhancement, at least 10 to 20 times, shall be localized at the HJ, which points to a significant local electromagnetic enhancement at the very HJ region [39].

This is better observed in a $Si_{1-x}Ge_x/Si$ axially heterostructured NW with higher Ge content, $x \approx 0.6$ in this case [40]. The larger shift of the Si-Si peak of the SiGe alloy permits to observe the different contributions with minimum overlapping. In these NWs a dramatic spectral change occurs when the laser beam crosses the HJ region, figure 5. One observes a change in the relative intensities and a shift of the peak frequencies of the Raman bands of the SiGe alloy, both clear evidences of compositional changes at the HJ with respect to the two NW segments. Once again, the spectrum collected at the HJ, identified through its Raman spectrum, shows a much higher intensity than it should correspond to its volume, figure 5.

The relevant point is that the Raman spectrum of the HJ is clearly seen in spite of the small scattering volume associated with the HJ. For these NWs, the measured Raman intensity per unit volume arising from the HJ is enhanced by a factor of about 60 with respect to the Raman signal collected in the pure NW segments. This evidences that the HJ provides an additional contribution to the coupling between the laser beam and the NW. In other words, the axial HJ concentrates the electromagnetic field under visible illumination, which appears very suitable for photonic applications, e.g. photon harvesting in solar cells or photon detectors.

Note that this is not a mere compositional effect. In fact, the Raman signal of $Si_{1-x}Ge_x$ with $x = 0.7-0.8$ presents a resonance for 532 nm excitation [41]. This resonance is progressively quenched for decreasing x; therefore, if we were observing a simple compositional resonance the Raman collected from the SiGe segment ($x \approx 0.6$) will supply a higher intensity than the HJ, where the value of x

progressively decreases, being out of compositional resonance. It is worth mentioning that the Raman signal arising from the HJ of the heterostructured Si/Ge NWs were also observed by Wang et al [42].

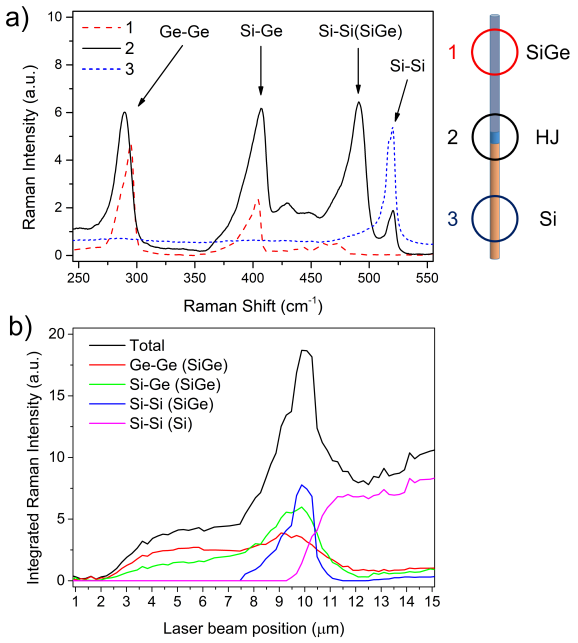

Figure 5: a) Raman spectra in SiGe/Si heterostructured NW 100 nm in diameter with a nominal Ge concentration of ≈ 60%. The dramatic changes in the spectrum when the HJ is probed provides evidence of the composition change. b) Raman intensity profiles of the Raman bands of Si and SiGe as a function of the laser beam position along the NW, showing the enhancement of the Raman signal at the HJ.

4 Modelling of the laser/NW interaction

The understanding of the light/NW interaction demands of the solution of the Maxwell equations of the system formed by the laser beam, the NW, and the hosting medium. The experimental conditions must be carefully considered when one acquires the spectrum of a NW with a micro Raman apparatus (far field). First, the laser beam is focused by a high magnification optical microscope objective with a large numerical aperture, which gives a focused Gaussian-like laser intensity distribution. Secondly, as mentioned in the experimental section, the NWs have finite length and an optical discontinuity due to the HJ. Finally, the NWs can be either free standing surrounded by air, or lying on a substrate. All of this shall be consider in the modelling.

The problem of the interaction of the EM wave and the NW is usually studied in terms of the Mie scattering theory. For this, an ideal homogeneous and infinitely long NW is considered, neglecting the influence of the NW ends. Most of the simulations rely on the illumination with polarized plane waves, while only a few studies have considered focused laser beams [7]. The presence of the NW ends and the HJ are not compatible with the infinite and homogeneous NW of the Mie theory. In this work, Maxwell equations in 3-dimensional space were solved using the Electromagnetic Waves in Frequency Domain module of COMSOL Multiphysics.

In the simulation an heterostructured NW is placed on the substrate, which fills the inferior half-space, while the space surrounding the NW is set up to be air. The laser beam is described as a focused Gaussian beam, instead of the usual approach of a plane wave. In this situation, the distribution of the EM field inside the NW is far from what a homogeneous illumination would induce, and the plane wave approximation is no longer valid. The equations accounting for the electric field in a Gaussian laser beam propagating along the z axis are written as follows:

$$E_x = E_0 \frac{w_0}{w(z)} e^{\left(\frac{-r^2}{w^2(z)}\right)} e^{\left(ik\frac{r^2}{2R(z)}\right)} e^{i(kz-\omega t)} e^{i\zeta(z)} \quad (1)$$

$$w(z) = w_0 \sqrt{1 + \left(\frac{z\lambda}{\pi w_0^2}\right)} \quad (2)$$

$$R(z) = z\left(1 + \left(\frac{\pi w_0^2}{z\lambda}\right)^2\right) \quad (3)$$

$$\zeta(z) = \arctan\left(\frac{z\lambda}{\pi w_0^2}\right) \quad (4)$$

cylindrical coordinates are used: r is the distance to the beam axis (z axis), and z the position with respect to the focal plane ($z = 0$). $R(z)$ is the radius of curvature of the wavefront at z, $\zeta(z)$ is called the Guoy phase at z, typical of Gaussian and spherical wavefronts, $w(z)$ is the diameter of the Gaussian spot at z, which depends on its value at the focus $w_0 = w(0)$, the so called waist size. Let

us remind that the NW is lying on the x-y plane. According to the Abbe's formula, the beam waist size, w_0, is determined by the laser wavelength and the numerical aperture of the objective:

$$w_0 \propto \frac{1.22\lambda}{NA} \tag{5}$$

Once the excitation laser beam and the system have been modelled, the FEM software solves the equations of the scattered field. The scattered field, E_{sc}, is defined as the EM field generated by the system when the excitation field, E_b, is applied, in order to create a total EM field satisfying the Maxwell equations

$$\vec{E}_{tot} = \vec{E}_b + \vec{E}_{sc} \leftrightarrow \vec{E}_{sc} = \vec{E}_{tot} - \vec{E}_b \tag{6}$$

When the distribution of the total EM field inside the NW is known the expected Raman signal of each segment of the NW can be calculated since the emitted Raman signal is proportional to the EM field intensity, $I_R \propto |E|^2$. Therefore, once we have calculated the distribution of the electric field inside the NW, the Raman signal arising from a certain region of the NW will be proportional to the integral of $|E|^2$ over the corresponding sampling volume. By computing these integrals we can plot the corresponding theoretical Raman signal along the NW. Finally, the model is solved for different positions of the laser beam along the NW axis in order to reproduce the experimental longitudinal scans of the NW. This allows to calculate the Raman intensities of the NW as a function of the laser beam position. The optical parameters used for the calculations are resumed in Table 1, and were extracted from Sopra database [43].

5 Discussion

The tunability of the optical absorption by NWs requires the control of the different factors contributing to the enhancement of the optical absorption or scattering. The FEM model permits to analyze the impact of the enhancement factors, namely the NW dimension, the substrate, the light wavelength and polarization, and the NW nature and structure.

We solved the problem for different substrates characterized by different complex refractive indexes. In particular, the results obtained for Au, Al, Ge and air are shown in figure 6 for 532 nm wavelength. This figure shows the diameter dependent resonances for $|E|^2$. If the integrated $|E|^2$ is plotted as a function of the NW diameter one observes

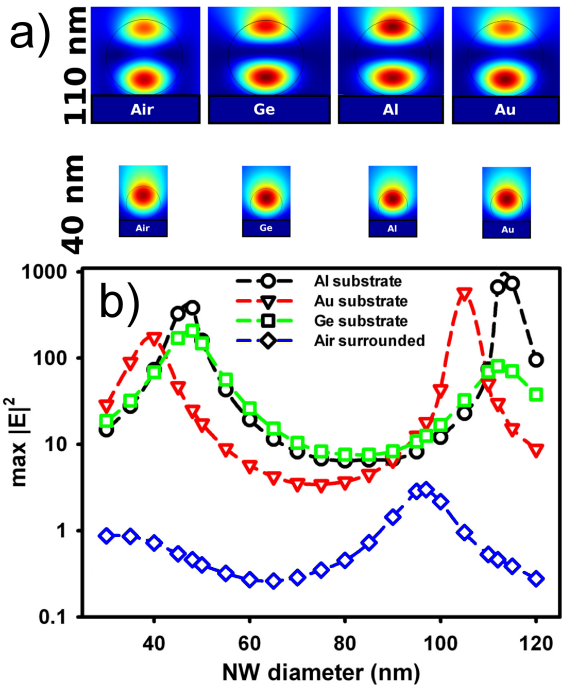

Figure 6: a) Electromagnetic field distributions for two Si NWs with diameter 40, and 110 nm, with different NW/substrate configurations. b) $|E|^2$ vs NW diameter for the different configurations.

the enhancement of $|E|^2$, up to one order of magnitude for the NWs standing in air with respect to the incident electromagnetic field, and up to 2 additional orders of magnitude for the NWs lying on the metallic substrate. The reflection of both the excitation and the Raman radiation by the metallic substrate can contribute to this enhancement by a theoretical factor of 4, the remaining amplification is due to the EM interaction between light and the NW-substrate system. The substrate acts by improving the antenna effect already present in free standing NWs. Figure 6 also shows that the resonance diameters depend on the substrate. There is a shift of the resonances to lower diameters for Au with respect to Al, and a further shift to lower diameters for the free standing NW in air, as it was already shown in ref. [7] using FDTD calculations. The resonances for the Ge substrate closely match those of the Al substrate, but with lower electromagnetic enhancement. According to this, the optical response of the NWs can be tuned by using different diameters and substrates characterized by different optical constants.

	Au	Al	Si	Ge	$Si_{(1-x)}Ge_x$
n	0.467	0.93877	4.1334	4.92436	$4.1334 + 0.668619x + 1.510779x^2$
k	2.407	6.4195	0.033258	2.3734	$0.033258 + 0.204615x + 1.621028x^2$

Table 1: Real (n) and imaginary (k) parts of the complex refractive indexes of the different materials used in the FEM calculations for 532 nm radiation [43].

5.1 Axial heterojunctions

The study of axial heterostructures demands of a 3D solution of the Maxwell equations in order to reveal the role of the HJ. We have solved the Maxwell equations for a NW with a SiGe/Si axial HJ interacting with the focused Gaussian laser beam. The 3D solution of the Maxwell equations reveals the enhancement of the electric field at the HJ region, in agreement with the Raman measurements, figure 7. The 3D simulation also reveals that the electromagnetic field profile along the NW axis exhibits a series of longitudinal resonant modes overlapped with the Gaussian distribution. This longitudinal modes can be clearly seen when a plane wave excitation is considered on a pure Si NW of finite length, but they are hidden by the Gaussian beam distribution in the local excitation case. However, in the presence of the HJ they are clearly revealed, evidencing that the HJ produces a significant disturbance of the electromagnetic field inside the NW. In addition, the HJ raises the electromagnetic field intensity inside the NW, this overall enhancement is also experimentally observed in the Raman scans along the NW axis, in figure 5b a higher Raman intensity is observed in the presence of the HJ.

In order to confirm that the $|E|^2$ resonance at the HJ is related to the presence of the HJ itself, and it is not an effect of the mere difference in the resonance behaviour between the two NW segments, we modelled two different scenarios for a 40 nm diameter NW. The first one is a pure Si NW with a SiGe ($x = 0.075$) thin slab (6 nm width) in its

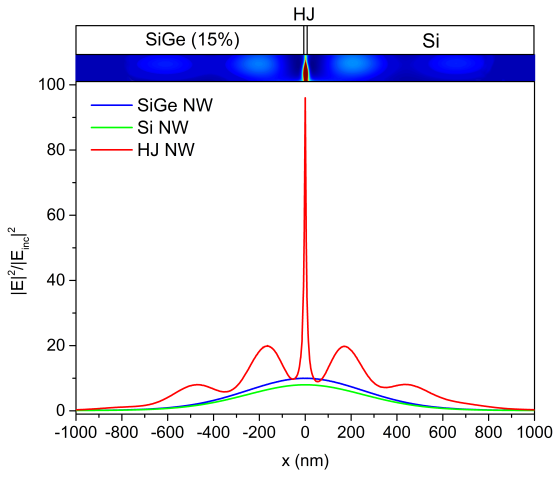

Figure 7: Profiles of the normalized value of $|E|^2$ along the HJ NW axis under a focused Gaussian beam excitation, showing the enhancement at the HJ. The response of single Si and SiGe NWs are also plotted for comparison. The simulated NW diameter is 40 nm. The heterostructured NW shows a few longitudinal modes, which are scarcely appreciated in the Si NW.

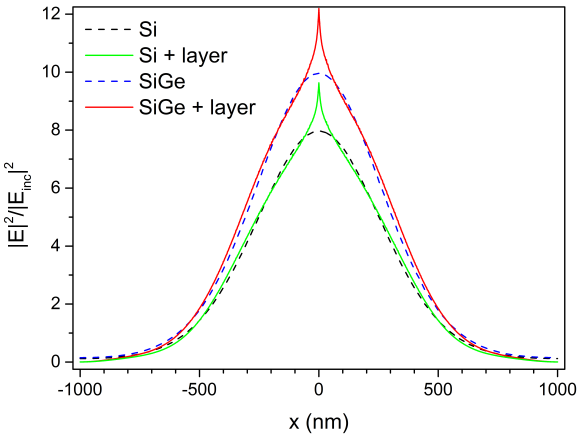

Figure 8: Relative electromagnetic field intensity distribution inside Si and SiGe (15% Ge) NWs (40 diameter nm), black and blue dashed lines. Green and red lines represent the same magnitude for the same NWs with an axial thin layer (6 nm) of SiGe (7.5% Ge). The figure shows how the presence of a different material enhances the EM field in its vicinity, regardless of the Ge composition difference.

center, the second one is a pure SiGe ($x = 0.15$) with the same SiGe ($x = 0.075$) slab. If we were dealing with a mere compositional effect both cases should exhibit opposite behaviours in the HJ region. However, the local enhancement of the electric field at the HJ is observed for both NW configurations, which points to the electromagnetic field enhancement by the presence of the HJ, figure 8.

Finally, the calculated enhancement factor of $|E|^2$ at the HJ of a Si/SiGe NW with the same structure as the experimentally measured ones is 63. This value is in very good agreement with the mean value of 60 experimentally measured by μ-Raman spectroscopy.

P3

6 Conclusions

An exhaustive analysis of the NW/light coupling has been carried out combining electromagnetic modelling and micro-Raman experiments on individual NWs, aiming to understand the light/NW interaction. The Raman experiments evidenced different optical enhancement phenomena, some of them already known, while other as the enhancement associated with the axial HJs are new. The Raman experiments have demonstrated the possibility of tuning the light/NW interaction by varying different configurations of the NWs, namely, diameter, substrate, length, composition, and NW structure, in particular, the presence of HJs. A description of different micro-Raman experiments on NWs revealing the different optical effects is provided.

Numerical solutions of the Maxwell equations for the different experimental configurations of the light/NW system have been carried out. The laser beam/heterostructured NW interaction has been numerically analyzed by 3-D finite difference solutions of the Maxwell equations. Furthermore, instead of an infinite plane wave a focused laser beam with a Gaussian intensity distribution has been used, more accorded to the comparison to the micro-Raman experiment. Additionally, we have considered different substrates supporting the NWs, since the resonance properties of the NWs depend on the electromagnetic properties of the surrounding medium as well.

The results presented herein show different possibilities for tuning the optical properties of the NWs. In addition to the diameter and composition dependence of the optical properties of the NWs, further consideration must be given to the NW length, the presence of HJs, and the surrounding medium. All of them would provide suitable means for tailoring the optical absorption (scattering) of semiconductor NWs. This locally enhanced EM absorption might open interesting perspectives for photon engineering with heterostructured NWs, in particular, it seems very promising for photovoltaics and light detectors.

Achnowledgements

This work was funded by Junta de Castilla y León (Projects VA293U13, and VA081U16), and Spanish Government (CICYT MAT2010-20441-C02 (01 and 02) and ENE 2014-56069-C4-4-R). J L Pura was granted by the FPU programme (Spanish Government) (FPU14/00916).

References

[1] G. Brönstrup, N. Jahr, C. Leiterer, A. Csáki, W. Fritzsche, S. Christiansen. Optical Properties of Individual Silicon Nanowires for Photonic Devices. *ACS Nano*, **4** (12), 7113–7122 (2010)

[2] D. Li, Y. Wu, P. Kim, L. Shi, P. Yang, A. Majumdar. Thermal conductivity of individual silicon nanowires. *Applied Physics Letters*, **83** (14), 2934–2936 (2003). doi:10.1063/1.1616981

[3] J. Anaya, T. Rodríguez, J. Jiménez. Predictive Model for the Thermal Conductivity of Rough and Smooth Silicon Nanowires. *Science of Advanced Materials*, **7** (6), 1097–1107 (2015). doi:10.1166/sam.2015.2154

[4] M. Law, D. J. Sirbuly, J. C. Johnson, J. Goldberger, R. J. Saykally, P. Yang. Nanoribbon waveguides for subwavelength photonics integration. *Science (New York, N.Y.)*, **305** (5688), 1269–73 (2004). doi:10.1126/science.1100999

[5] H. Kallel, A. Arbouet, G. Benassayag, A. Chehaidar, A. Potié, B. Salem, T. Baron, V. Paillard. Tunable enhancement of light absorption and scattering in $Si_{1-x}Ge_x$ nanowires. *Physical Review B - Condensed Matter and Materials Physics*, **86** (8) (2012). doi:10.1103/PhysRevB.86.085318

[6] L. Cao, J. S. Park, P. Fan, B. Clemens, M. L. Brongersma. Resonant germanium nanoantenna photodetectors. *Nano Letters*, **10** (4), 1229–1233 (2010). doi:10.1021/nl9037278

[7] F. J. Lopez, J. K. Hyun, U. Givan, I. S. Kim, A. L. Holsteen, L. J. Lauhon. Diameter and polarization-dependent raman scattering intensities of semiconductor nanowires. *Nano Letters*, **12** (5), 2266–2271 (2012). doi:10.1021/nl204537d

[8] L. Cao, J. S. White, J.-S. Park, J. a. Schuller, B. M. Clemens, M. L. Brongersma. Engineering light absorption in semiconductor nanowire devices. *Nature materials*, **8** (8), 643–647 (2009). doi:10.1038/nmat2477

[9] R. Ruppin. Electromagnetic energy inside an irradiated cylinder. *J. Opt. Soc. Am. A*, **15** (7), 1891–1895 (1998). doi:10.1364/JOSAA.15.001891

[10] G. S. Doerk, C. Carraro, R. Maboudian. Single nanowire thermal conductivity measurements by raman thermography. *ACS Nano*, **4** (8), 4908–4914 (2010). doi:10.1021/nn1012429

[11] M. Heiss, A. Fontcuberta I Morral. Fundamental limits in the external quantum efficiency of single nanowire solar cells. *Applied Physics Letters*, **99** (26), 3–6 (2011). doi:10.1063/1.3672168

[12] L. Cao, P. Fan, A. P. Vasudev, J. S. White, Z. Yu, W. Cai, J. a. Schuller, S. Fan, M. L. Brongersma. Semiconductor nanowire optical antenna solar absorbers. *Nano Letters*, **10** (2), 439–445 (2010). doi:10.1021/nl9036627

[13] J. A. Schuller, R. Zia, T. Taubner, M. L. Brongersma. Dielectric Metamaterials Based on Electric and Magnetic Resonances of Silicon Carbide Particles. *Physical Review Letters*, **99** (10), 107401 (2007). doi:10.1103/PhysRevLett.99.107401

[14] T. Nobis, E. M. Kaidashev, A. Rahm, M. Lorenz, M. Grundmann. Whispering gallery modes in nanosized dielectric resonators with hexagonal cross section. *Physical Review Letters*, **93** (10), 1–4 (2004). doi:10.1103/PhysRevLett.93.103903

[15] D. van Dam, D. R. Abujetas, R. Paniagua-Domínguez, J. a. Sánchez-Gil, E. P. a. M. Bakkers, J. E. M. Haverkort, J. Gómez Rivas. Directional and Polarized Emission from Nanowire Arrays. *Nano letters*, **ASAP**, 150608160137007 (2015). doi:10.1021/acs.nanolett.5b01135

[16] H. E. Ruda, A. Shik. Polarization-sensitive optical phenomena in thick semiconducting nanowires. *Journal of Applied Physics*, **100** (2), 024314 (2006). doi:10.1063/1.2216879

[17] H. E. Ruda, A. Shik. Polarization-sensitive optical phenomena in semiconducting and metallic nanowires. *Physical Review B - Condensed Matter and Materials Physics*, **72** (11), 1–11 (2005). doi:10.1103/PhysRevB.72.115308

[18] R. Grange, G. Brönstrup, M. Kiometzis, A. Sergeyev, J. Richter, C. Leiterer, W. Fritzsche, C. Gutsche, A. Lysov, W. Prost, F. J. Tegude, T. Pertsch, A. Tünnermann, S. Christiansen. Far-field imaging for direct visualization of light interferences in GaAs nanowires. *Nano Letters*, **12** (10), 5412–5417 (2012). doi:10.1021/nl302896n

[19] G. H. Ding, C. T. Chan, Z. Q. Zhang, P. Sheng. Resonance-enhanced optical annealing of silicon nanowires. *Physical Review B - Condensed Matter and Materials Physics*, **71** (20), 1–5 (2005). doi:10.1103/PhysRevB.71.205302

[20] M. Kerker. *The scattering of light and other electromagnetic radiation.* ISBN 9781483191744

[21] A. Rodríguez, J. Sangrador, T. Rodríguez, C. Ballesteros, C. Prieto, J. Jimenez. SiGe Nanowires Grown by LPCVD: Morphological and Structural Analysis. *MRS Proceedings*, **1258**, 1258–P05–05 (2010). doi:10.1557/PROC-1258-P05-05

[22] A. Rodríguez, T. Rodríguez, C. Ballesteros, J. Jiménez. SiGe/Si Nanowire Axial Heterostructures Grown by LPCVD Using Ga-Au. *MRS Proceedings*, **1510**, mrsf12–1510–dd06–05 (2013). doi:10.1557/opl.2013.273

[23] P. Periwal, N. V. Sibirev, G. Patriarche, B. Salem, F. Bassani, V. G. Dubrovskii, T. Baron. Composition-Dependent Interfacial Abruptness in Au-Catalyzed $Si_{1-x}Ge_x/Si/Si_{1-x}Ge_x$ Nanowire Heterostructures. *Nano Letters*, **14** (9), 5140–5147 (2014). doi:10.1021/nl5019707

P3

[24] T. E. Clark, P. Nimmatoori, K.-k. Lew, L. Pan, J. M. Redwing, E. C. Dickey. Diameter Dependent Growth Rate and Interfacial Abruptness in Vapor-Liquid-Solid $Si/Si_{1-x}Ge_x$ Heterostructure Nanowires. *Nano Letters*, **8** (4), 1246–1252 (2008). doi:10.1021/nl072849k

[25] D. E. Perea, N. Li, R. M. Dickerson, A. Misra, S. T. Picraux. Controlling heterojunction abruptness in VLS-grown semiconductor nanowires via in situ catalyst alloying. *Nano Letters*, **11** (8), 3117–3122 (2011). doi:10.1021/nl201124y

[26] J. Anaya, A. Torres, A. Martín-Martín, J. Souto, J. Jiménez, A. Rodríguez, T. Rodríguez. Study of the temperature distribution in Si nanowires under microscopic laser beam excitation. *Applied Physics A: Materials Science and Processing*, **113** (1), 167–176 (2013). doi:10.1007/s00339-012-7509-y

[27] J. Anaya, A. Torres, V. Hortelano, J. Jiménez, A. C. Prieto, A. Rodríguez, T. Rodríguez, R. Rogel, L. Pichon. Raman spectrum of Si nanowires: Temperature and phonon confinement effects. *Applied Physics A: Materials Science and Processing*, **114** (4), 1321–1331 (2014). doi:10.1007/s00339-013-7966-y

[28] Q. Xiong, G. Chen, H. R. Gutierrez, P. C. Eklund. Raman scattering studies of individual polar semiconducting nanowires: Phonon splitting and antenna effects. *Applied Physics A: Materials Science and Processing*, **85** (3), 299–305 (2006). doi:10.1007/s00339-006-3717-7

[29] G. S. Doerk, C. Carraro, R. Maboudian. Raman Spectroscopy for Characterization of Semiconducting Nanowires. In *Raman Spectroscopy for Nanomaterials Characterization*, S. 477–506. Springer Berlin Heidelberg, Berlin, Heidelberg (2012). doi:10.1007/978-3-642-20620-7_17

[30] L. Cao, B. Nabet, J. E. Spanier. Enhanced Raman Scattering from Individual Semiconductor Nanocones and Nanowires. *Physical Review Letters*, **96** (15), 157402 (2006). doi:10.1103/PhysRevLett.96.157402

[31] A. Torres, A. Martín-Martín, O. Martínez, A. C. Prieto, V. Hortelano, J. Jiménez, A. Rodríguez, J. Sangrador, T. Rodríguez. Micro-Raman spectroscopy of Si nanowires: Influence of diameter and temperature. *Applied Physics Letters*, **96** (1), 011904 (2010). doi:10.1063/1.3284647

[32] R. Singh, E. J. Dailey, J. Drucker, J. Menéndez. Raman scattering from Ge-Si core-shell nanowires: Validity of analytical strain models. *Journal of Applied Physics*, **110** (12), 124305 (2011). doi:10.1063/1.3667125

[33] Z. Zhang, D. C. Dillen, E. Tutuc, E. T. Yu. Strain and Hole Gas Induced Raman Shifts in Ge - Si_xGe_{1-x} Core-Shell Nanowires Using Tip-Enhanced Raman Spectroscopy. *Nano Letters*, S. 150609142006005 (2015). doi:10.1021/acs.nanolett.5b00176

[34] J. Anaya, J. Jimenéz, A. Rodriguez, T. Rodriguez. Electromagnetic interaction between a laser beam and semiconductor nanowires deposited on different substrates: Raman enhancement in Si Nanowires. *MRS Symp. Proc.*, **1627** (2014)

[35] M. I. Alonso, K. Winer. Raman spectra of c - $Si_{1-x}Ge_x$ alloys. *Physical Review B*, **39** (14), 10056–10062 (1989). doi:10.1103/PhysRevB.39.10056

[36] J. C. Tsang, P. M. Mooney, F. Dacol, J. O. Chu. Measurements of alloy composition and strain in thin GeSi layers. *Journal of Applied Physics*, **75** (12), 8098 (1994). doi:10.1063/1.356554

[37] I. Campbell, P. Fauchet. The effects of microcrystal size and shape on the one phonon Raman spectra of crystalline semiconductors. *Solid State Communications*, **58** (10), 739–741 (1986). doi:10.1016/0038-1098(86)90513-2

[38] S. Piscanec, M. Cantoro, A. C. Ferrari, J. A. Zapien, Y. Lifshitz, S. T. Lee, S. Hofmann, J. Robertson. Raman spectroscopy of silicon nanowires. *Physical Review B*, **68** (24), 241312 (2003). doi:10.1103/PhysRevB.68.241312

[39] J. L. Pura, J. Anaya, J. Souto, Á. C. Prieto, A. Rodríguez, T. Rodríguez, J. Jiménez. Local electric field enhancement at the heterojunction of Si/SiGe axially heterostructured nanowires under laser illumination. *Nanotechnology*, **27** (45), 455709 (2016). doi:10.1088/0957-4484/27/45/455709

[40] A. Potié, T. Baron, L. Latu-Romain, G. Rosaz, B. Salem, L. Montès, P. Gentile, J. Kreisel, H. Roussel. Controlled growth of SiGe nanowires by addition of HCl in the gas phase. *Journal of Applied Physics*, **110** (2), 024311 (2011). doi:10.1063/1.3610409

[41] A. Picco, E. Bonera, E. Grilli, M. Guzzi, M. Giarola, G. Mariotto, D. Chrastina, G. Isella. Raman efficiency in SiGe alloys. *Physical Review B*, **82** (11), 115317 (2010). doi:10.1103/PhysRevB.82.115317

[42] X. Wang, L. Tsybeskov, T. I. Kamins, X. Wu, D. J. Lockwood. Structural and optical properties of axial silicon-germanium nanowire heterojunctions. *Journal of Applied Physics*, **118** (23), 0–8 (2015). doi:10.1063/1.4937345

[43] Sopra database S A, France. www.sspectra.com/sopra

Electromagnetic Field Enhancement on axially heterostructured NWs: the role of the heterojunctions

J. L. Pura[1,*], J. Souto[1], P. Periwal[2], T. Baron[2], and J. Jiménez[1]

[1] *GdS Optronlab, Dpt. Física de la Materia Condensada, ed. LUCIA Universidad de Valladolid, Paseo de Belén 19, 47011 Valladolid, Spain*

[2] *University Grenoble Alpes, LTM, F-38000 Grenoble, France and CNRS, LTM, F-38000 Grenoble, France*

[*] *jlpura@fmc.uva.es*

Keywords: nanowires, silicon, light-matter interaction, light enhancement, heterojunctions

Abstract

Semiconductor nanowires are the building blocks of the future nanoelectronic devices. The study of the interaction between nanowires and visible light reveals resonances that promise light absorption/scattering engineering for photonic applications. The experimental measurements are carried out through the micro-Raman spectroscopy of different group IV nanowires, both homogeneous Si nanowires and axially heterostructured SiGe/Si nanowires. These experimental measurements show an enhancement of the Raman signal in the vicinity of the heterojunction of SiGe/Si nanowires. The results are analysed in terms of the electromagnetic modelling of the light/nanowire interaction using finite element methods. The presence of axial heterostructures is shown to produce novel electromagnetic resonances, and the results are understood as a consequence of a finite change in the relative permittivity of the material at the SiGe/Si heterojunction. This effect opens a new path to control light matter interaction at the nanoscale with direct applications in photonic nanodevices.

1 Introduction

Semiconductor nanowires (NWs) have received a great deal of attention in recent years. One of their main fields of interest concerns photonics, as it has been shown that light couples to NWs in different ways depending on the NW diameter, NW composition, light wavelength, and the dielectric mismatch between the NW and the surrounding media [1]. As a result, all these variables allow to tune the optical properties of NWs. One of the most relevant properties concerning the light/NW interaction is the ability of NWs to enhance the optical absorption/ scattering for certain diameters [2]. Up to now the research has been focused on both homogeneous and core-shell NWs, while less attention has been paid to the optical properties of axially heterostructured NWs. We aim to unravel the amazing effects that appear when an axially heterostructured NW interacts with an electromagnetic field. For this, micro-Raman (μ-R) spectroscopy is used as a local probe of the electromagnetic field. Since the Raman signal is proportional to the excitation light intensity, i.e. $|E|^2$, the Raman signal arising from each region of the heterostructured NW provides a measurement of the mean value of the electromagnetic (EM) field distribution in this specific region. As a result, μ-Raman spectroscopy is a very suitable tool to detect the EM field distribution induced inside heterostructured NWs by an incident laser beam.

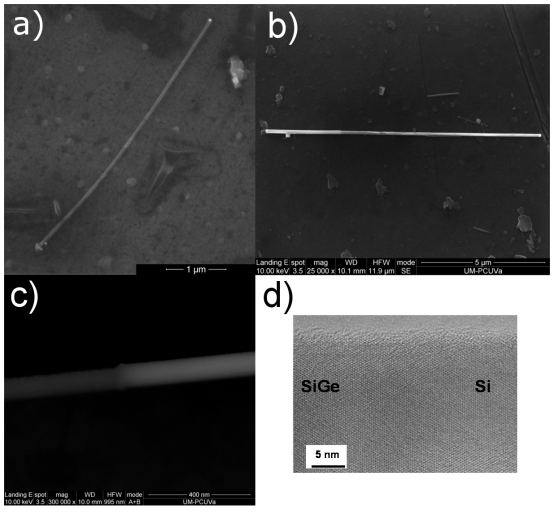

Figure 1: a) SEM image of a Si NW (diameter ≈ 30 nm) b) HR-TEM image of the HJ region of a SiGe/Si axially hetersostructured NW showing the excellent crystalline quality and absence of defects.

2 Experimental and Samples

μ-Raman spectra were recorded with a Labram UV-HR 800 Raman spectrometer from Horiba-Jobin Yvon. The excitation and the scattered light collection were performed by means of a confocal metallographic microscope with a high magnification objective (X100) and 0.95 numerical aperture (NA). A frequency doubled Nd:YAG laser (532 nm) was used as the excitation source. The laser beam diameter at the focal plane is slightly below 1 μm according to the Abbe's formula ($\phi = 1.22\ \lambda/\mathrm{NA}$), which is several times larger than the diameter of the studied NWs, that typically ranges from 30 to 100 nm. The Raman spectra are recorded at different positions along the NWs, in steps of 100 nm. It is important to note that the effective excitation power on the NW depends on its position inside the Gaussian power distribution of the focused laser beam [3, 4].

Group IV heterostructured NWs were grown by the Au-catalized vapour-liquid-solid (VLS) method using a hot-wall CVD reactor (Easy Tube 3000 First Nano, a divison of CVD Equipment Corporation). Either 50 nm Au colloid nanoparticles or a 2 nm thick Au layer were deposited on a Si (111) substrate for the NW growth, SiH_4 and GeH_4 were used as precursors, and HCl as carrier gas. For further details on the NWs growth see [5].

Prior to the Raman measurements the dimensions and morphological features of each NW were studied in a high resolution field emission scanning electron microscope (FESEM), Figure 1a. The NWs lengths varied from 2 to 12 μm, and they appear as straight cylinders without appreciable tapering. Transmission Electron Microscopy (TEM) showed the excellent crystallinity of the NWs, Figure 1b. In particular, high resolution TEM images of the HJ region of SiGe/Si HJs did not show structural discontinuities at the junction, nor stacking faults, or other structural defects [5].

As grown NWs were separated from the substrate in an ultrasonic bath, and suspended in methanol. Droplets of this suspension were spread out on an Al coated Si substrate for the μ-R measurements. The choice of the substrates is based on the optimization of the Raman signal, which is enhanced by the presence of a metallic substrate with respect to free standing NWs. Also, but not less important, the presence of the metallic substrate improves the thermal management of the NW allowing to minimize the laser induced heating during

the μ-R experiments. Al coated substrates proved to be optimal in order to meet both requirements, then they were used as the standard substrate for the experimental measurements. The Al coating was thick enough to block any optical signal arising from the Si substrate.

3 Experimental Results

The longitudinal scans along several heterostructured NWs show a clear enhancement of the Raman signal at the HJ region, see Figure 2. It can be seen that the signal of the Si-Si (SiGe) Raman mode is greatly enhanced when the laser beam excites the HJ. The Raman shift of this mode corresponds to an intermediate Ge composition between that of Si and SiGe ($\approx$ 60% Ge) homogeneous segments, so we deduce that it arises from the transition region, i.e. the HJ. In fact, this Raman band is not detected in the homogeneous segments. Moreover, we have to consider the scattering volume of each region of the NW. The transition region between Si and SiGe is not an abrupt transition but a gradual change from one material to the other as a result of the reservoir effect of the catalyst droplet [5, 6]. According to the reservoir effect the HJ extension ranges in the order of magnitude of the NW diameter, so it can be estimated to be around 50 nm, or less. Meanwhile, when the laser beam is focused on the HJ the homogeneous segments of the NW will be sharing the beam spot, this results in around 500 nm of each segment under illumination. According to this estimation the scattering volume ratio between homogeneous segments and the HJ is approximately 1 to 10, i.e. the HJ volume is 10 times smaller than each of the illuminated homogeneous segments. However, we detect a Raman signal from the HJ higher than that of the Si and SiGe segments. It can be argued that the Raman signal at the HJ is being enhanced by a factor of at least 10 times. A more detailed calculation with the experimental data of these specific SiGe/Si heterostructured NWs gives an experimental enhancement factor of circa 63.

The enhancement effect in these NWs with a greater Ge composition ($\approx$ 60% Ge) is more intense than that of NWs with lower Ge composition [7]. Moreover, due to the higher Ge composition of the NWs the Raman bands are clearly separated and there is no need of a deconvolution of the Raman spectra.

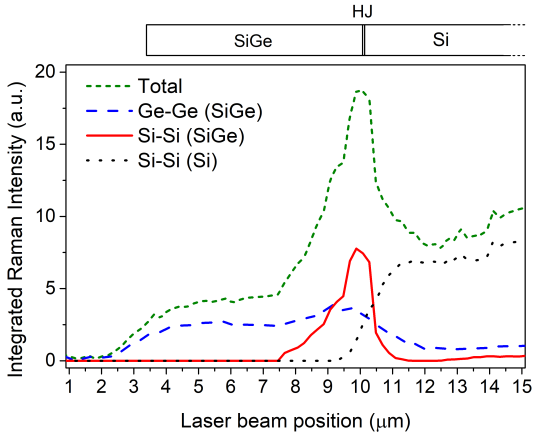

Figure 2: Raman intensity profiles along a SiGe/Si heterostructured NW showing the enhancement of the signal arising from the HJ. The three Raman modes of the $Si_{1-x}Ge_x$ alloy are represented as well as the Raman signal arising from pure Si, and the total Raman signal.

4 Finite Element Methods Simulations

Parallel to the Raman spectroscopy measurements, the light/NW interaction has been studied by means of Finite Element Methods (FEM) simulations. For this the "Electromagnetic Waves in Frequency Domain" module of COMSOL Multiphysics software has been used. In our model a finite heterostructured NW, with similar characteristics to the experimentally studied ones, is located on an aluminium substrate and surrounded by air. All the system is limited by Cartesian Perfectly Matched Layers (PMLs), and illuminated by a linearly polarized Gaussian laser beam with 532 nm wavelength and around 1 μm spot size, to reproduce the experimental conditions of the Raman spectra. The position of the excitation beam axis can be varied to reproduce the experimental profile measurements. The electromagnetic field distribution inside the HJ NW is calculated as a function of the position of the excitation laser beam. In this situation, the value of the square of the electric field modulus $|E|^2$ will be proportional to the local light intensity, as a consequence it will be proportional to the lo-

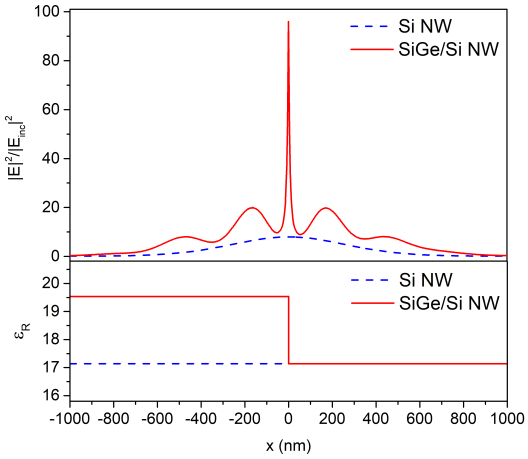

Figure 3: EM field distribution inside a homogeneous Si NWs, and a SiGe/Si heterostructured NW. The presence of a discontinuity on the relative permittivity in the heterostructured NW induces the enhancement of the incident field near the HJ region as compared to the homogeneous NWs.

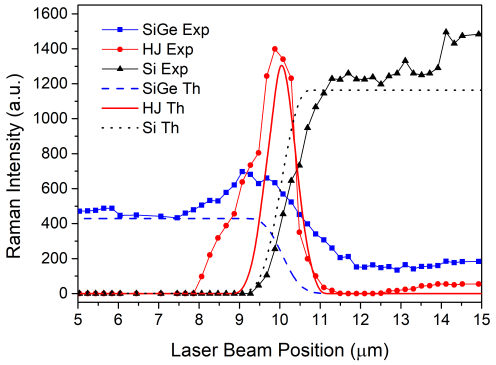

Figure 4: Simulation of the longitudinal Raman profile measurements along a heterostructured SiGe/Si NW. The results of the simulation are represented by dashed lines and compared with the experimental data of Figure 2, plotted with continuous lines. The simulations are in quite a good agreement with the experimental Raman measurements.

P4

cally generated Raman signal. Then, by integrating $|E|^2$ over the different regions of the heterostructured NW for each position of the laser beam one can calculate the theoretical Raman profile along the NW axis for comparison with the experimental profile.

The FEM results for these NWs are summarized in Figures 3 and 4. Figure 3 shows the EM field distribution inside the heterostructured NW computed when the laser beam is centred on the HJ region. The EM field distribution is compared with that of a homogeneous Si NW, where there is no change in the relative permittivity, ε. According to this, the EM field distribution inside the Si NW resembles the Gaussian distribution of the incident laser beam. In the case of the heterostructured NW the system has a finite jump discontinuity in its relative permittivity, when Maxwell equations are solved this results in a local enhancement of the EM field distribution right at the HJ. Once the model is defined, the excitation beam position is varied to reproduce the experimental longitudinal scanning measurement. The EM field distribution is computed for each position of the laser beam, then the theoretical Raman intensities of all NW regions can be calculated from the field distribution. In Figure 4 the theoretical Raman intensity profile is plotted and compared with the experimental measurements of Figure 2. We can see a very good agreement between both data, moreover, if we compute the theoretical Raman enhancement of the HJ signal with this model the calculated value is 60, quite close to the experimental value of circa 63. We can conclude that the model accounts for the experimentally observed Raman enhancement and provides an accurate framework to understand the physics of the light/ heterostructured NW interaction.

5 Conclusions

Heterostructured Si/SiGe NWs present an enhancement of the EM field at the HJ transition region. This effect has been measured by μ-Raman spectroscopy detecting an enhancement of the Raman signal arising from the HJ up to a factor of 60. Moreover, the experimentally measured longitudinal Raman profiles show a high increase of the total Raman signal when the excitation beam is crossing the HJ region. The experimental results have been contrasted by a FEM model, in which the Maxwell equations are solved to find the EM field distribution inside the studied NWs. This model allows to simulate the experimental Raman measurements, and has been proved to explain the EM field localization at the HJ region. At the same

time the model reproduces with a good agreement the Raman longitudinal profiles. As a summary, the change in the relative electric permittivity that takes places at the HJ is shown to be responsible for the EM field localization and enhancement at this region. The control of this EM field enhancement effect with the use of HJs opens the path to improve the performance of a great variety of photonic nanodevices by using heterostructured NWs.

Acknowledgements

This work was funded by Junta de Castilla y León (Projects VA293U13, and VA081U16), and Spanish Government (CICYT MAT2010-20441-C02 (01 and 02)). J. L. Pura was granted by the FPU programme (Spanish Government FPU14/00916).

References

[1] F. J. Lopez, J. K. Hyun, U. Givan, I. S. Kim, A. L. Holsteen, L. J. Lauhon. Diameter and Polarization-Dependent Raman Scattering Intensities of Semiconductor Nanowires (2012). doi:10.1021/nl204537d

[2] L. Cao, J. S. White, J.-S. Park, J. a. Schuller, B. M. Clemens, M. L. Brongersma. Engineering light absorption in semiconductor nanowire devices. *Nature materials*, **8** (8), 643–647 (2009). doi:10.1038/nmat2477

[3] J. Anaya, A. Torres, A. Martín-Martín, J. Souto, J. Jiménez, A. Rodríguez, T. Rodríguez. Study of the temperature distribution in Si nanowires under microscopic laser beam excitation. *Applied Physics A: Materials Science and Processing*, **113** (1), 167–176 (2013). doi:10.1007/s00339-012-7509-y

[4] J. Anaya, A. Torres, V. Hortelano, J. Jiménez, A. C. Prieto, A. Rodríguez, T. Rodríguez, R. Rogel, L. Pichon. Raman spectrum of Si nanowires: Temperature and phonon confinement effects. *Applied Physics A: Materials Science and Processing*, **114** (4), 1321–1331 (2014). doi:10.1007/s00339-013-7966-y

[5] P. Periwal, N. V. Sibirev, G. Patriarche, B. Salem, F. Bassani, V. G. Dubrovskii, T. Baron. Composition-Dependent Interfacial Abruptness in Au-Catalyzed $Si_{1-x}Ge_x/Si/Si_{1-x}Ge_x$ Nanowire Heterostructures. *Nano Letters*, **14** (9), 5140–5147 (2014). doi:10.1021/nl5019707

[6] T. E. Clark, P. Nimmatoori, K.-k. Lew, L. Pan, J. M. Redwing, E. C. Dickey. Diameter Dependent Growth Rate and Interfacial Abruptness in Vapor-Liquid-Solid $Si/Si_{1-x}Ge_x$ Heterostructure Nanowires. *Nano Letters*, **8** (4), 1246–1252 (2008). doi:10.1021/nl072849k

[7] J. L. Pura, J. Anaya, J. Souto, Á. C. Prieto, A. Rodríguez, T. Rodríguez, J. Jiménez. Local electric field enhancement at the heterojunction of Si/SiGe axially heterostructured nanowires under laser illumination. *Nanotechnology*, **27** (45), 455709 (2016). doi:10.1088/0957-4484/27/45/455709

4.3 Influence of the HJ abruptness

One of the critical factors of the Raman enhancement is the HJ abruptness. SiGe/Si/SiGe NWs are an excellent example of this, where only one of the two HJs produces Raman enhancement. An SEM image of this NW is shown in Figure 4.1. Figure 4.2 shows the Raman intensities of one of these NWs as a function of the laser beam position along the NW axis. Taking the signal of the central Si segment as a reference (blue data of Figure 4.2), we precisely know the location of the two HJs. It can be seen that the Raman signal of the SiGe alloy on the right hand HJ is enhanced, while this is not the case of the left hand HJ. These two HJs are morphologically different and can be discriminated accordingly with the growth direction, which can be ascertained from the SEM image of Figure 4.1. The bright ball on the right end of the NW is the Au catalyst droplet. This is telling us that the right part of the NW was grown later than the left one, i.e., it started growing on the left side. As a result, the first HJ takes place from SiGe to Si, called *trailing* HJ, while the right one takes place from Si back to SiGe, called *leading* HJ.

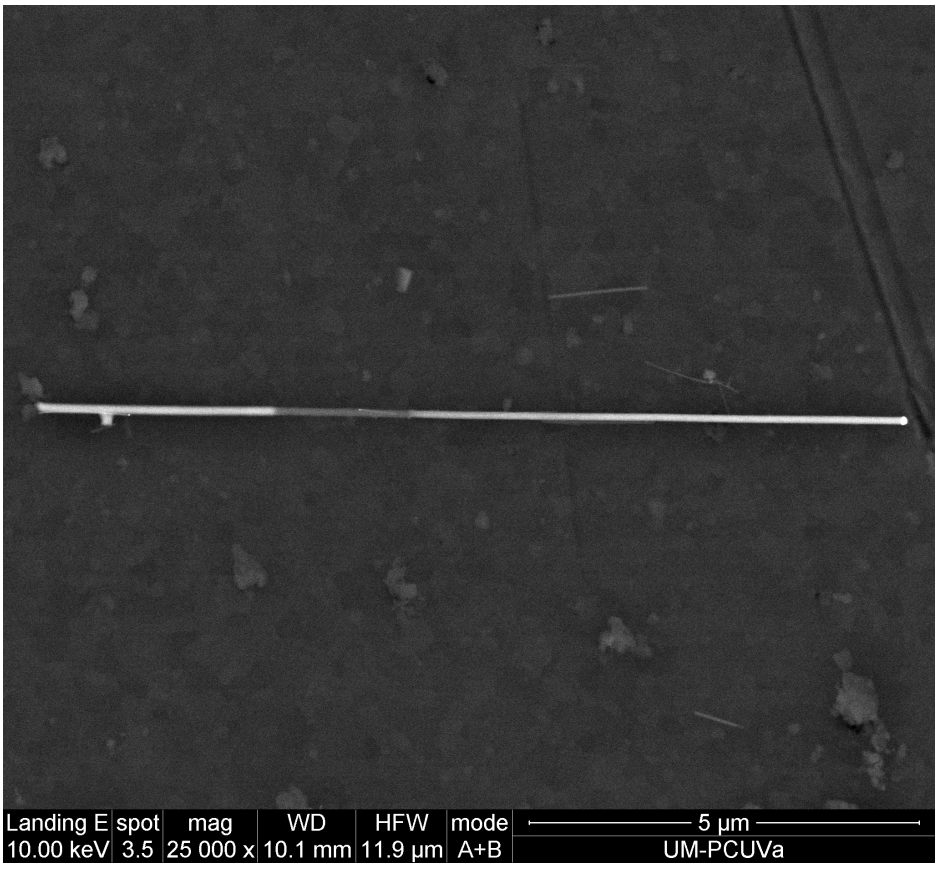

Figure 4.1: SEM image of one of the SiGe/Si/SiGe axially heterostructured NWs. The results of the Raman measurements of this NW are summarized in Fig. 4.2

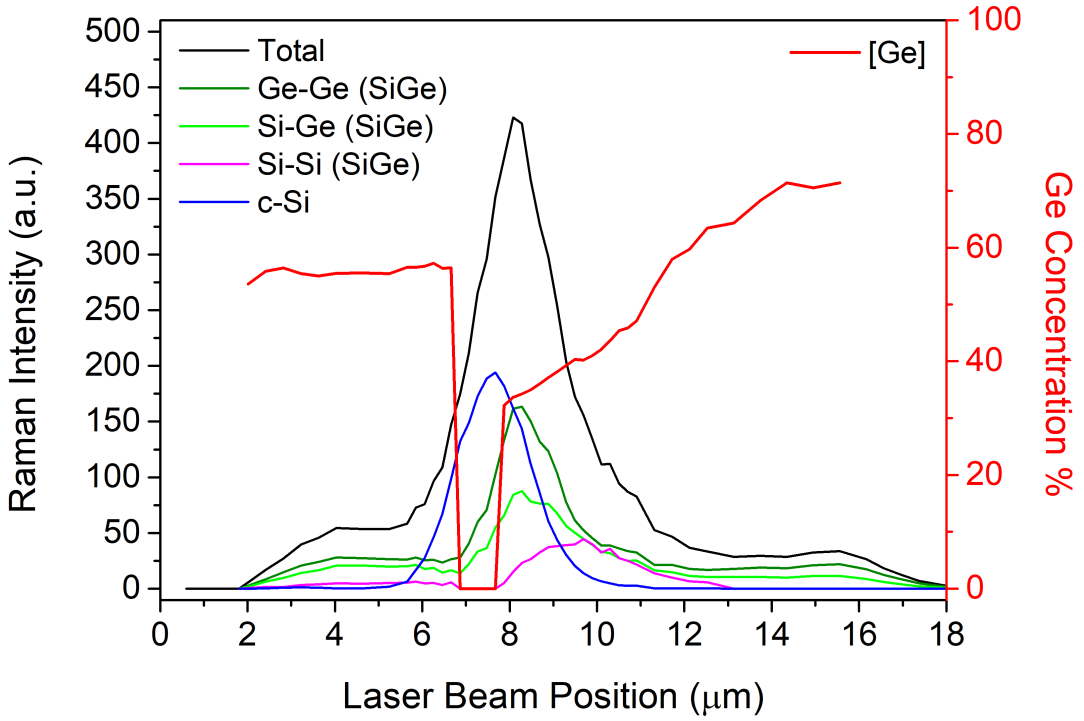

Figure 4.2: Raman measurement of the axially heterostructured NW of Figure 4.1. The plot shows the enhancement of the Raman signal, which is only present on one of the two heterojunctions (right HJ in the picture). The enhancement effect is only observed when there is a gradual change in Ge composition; this progressive change is not present in the HJ without enhancement. This points out to the presence of a highly abrupt heterojunction on the left side (trailing HJ).

Typically, the leading HJ has been thought to be more abrupt than the trailing one. The argument used is the reservoir effect explained in section 2.3. In the case of the trailing HJ, the Ge keeps being deposited on the solid phase until exhaustion. However, for the leading HJ, the Ge is rapidly reincorporated to the liquid phase reaching the steady growth of SiGe segment much faster. If we look at the Ge concentration, obtained from the Si-Si (SiGe) peak and the use of equation (3.1), represented by the red line in Figure 4.2, we can appreciate that in the trailing HJ (left) there is no signal from any intermediate composition of the SiGe alloy. However, in the leading HJ (right) we can see a continuous change from the absence of Ge in the central Si segment, to the final homogeneous composition of the last SiGe segment.

The experimental measurements suggest that the trailing HJ behaves as a very abrupt HJ, while the leading one presents a more extended composition profile, presenting Raman signals of intermediate SiGe compositions. This picture seems to be in a flagrant contradiction with the current paradigm of HJ growth process, which led us to revise the existing models for VLS growth. We assume that during the growth of the trailing HJ,

Ge atoms do not need to be exhausted, but they stop being deposited once the Ge concentration in the droplet is under saturation. According to this, the trailing HJ appears much more abrupt than expected, and it is also shorter than the leading one in all cases. This will be discussed in detail in Chapter 6.

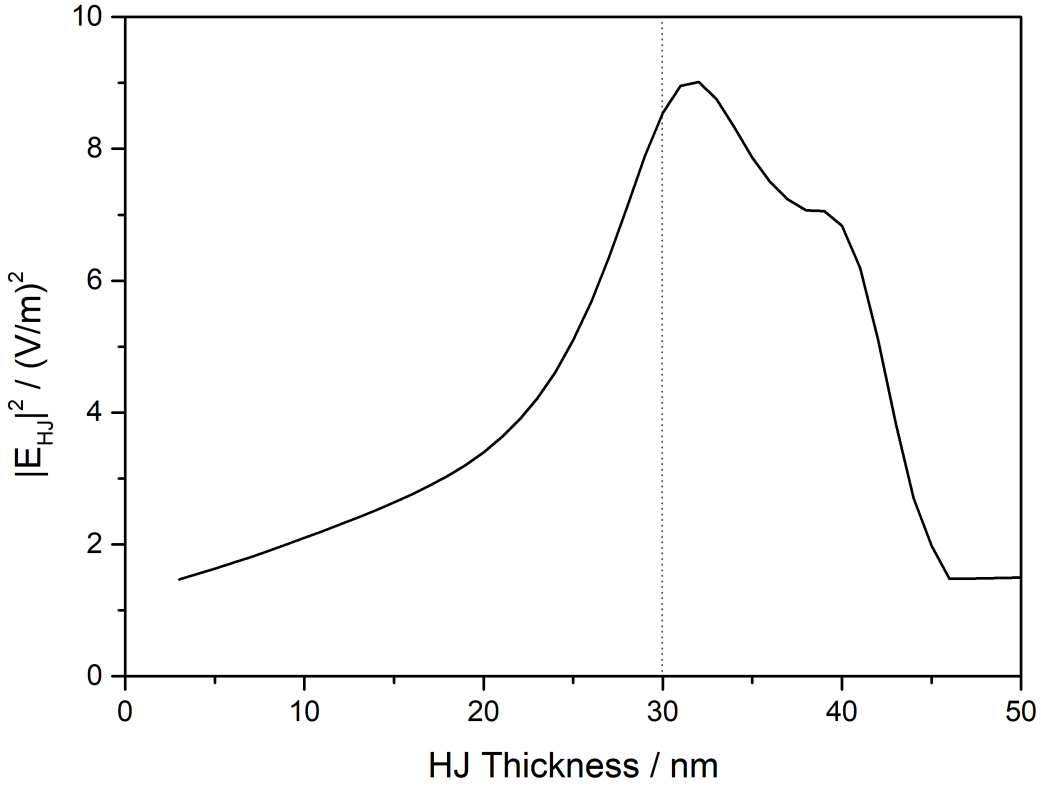

Figure 4.3: Representation of the maximum value of $|E|^2$ at the HJ as a function of the HJ thickness. As the HJ width is being reduced the field intensity at the HJ tends to unity, which means no enhancement. Furthermore, for values higher than 40 nm the behaviour is not reliable, because the calculation presumes a thickness of the HJ much lower than the NW length, and the approximation is not valid for that range.

On the other hand, we studied the dependence of the enhancement effect with the HJ thickness by FEM simulations. The results are summarized in Figure 4.3, showing an absence of the enhancement effect when the HJ thickness tends to zero. This is in perfect agreement with the behaviour observed in the experimental data, Figure 4.2, where no signal of the HJ region can be appreciated in the trailing HJ. Note that when the HJ thickness is reduced, two different contributions are being decreased simultaneously: first, the volume of the HJ is linearly reduced, lowering its expected Raman signal; second, the enhancement itself is being reduced, with the concomitant decrease of the Raman output. These two effects take place simultaneously, multiplying their effects.

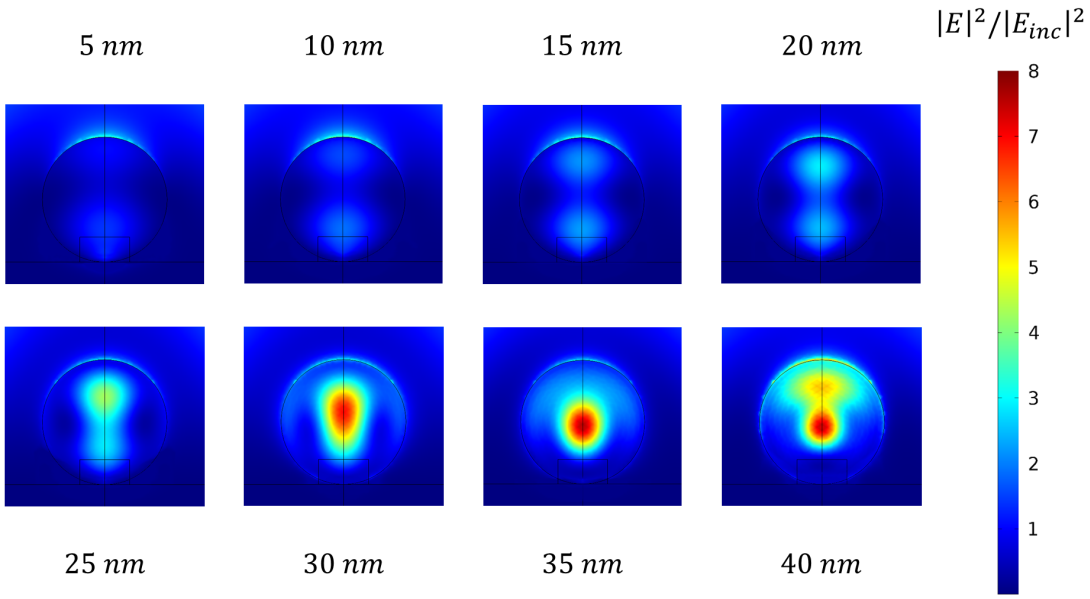

Figure 4.4: Electromagnetic field distribution on a transversal section of the simulated NW at the HJ for different values of the HJ thickness. The plot shows that the EM field is reduced as the HJ thickness approaches zero. Furthermore, for values near the maximum observed in figure 4.3 the EM field changes to a one-lobe distribution, being localized at the centre of the NW. For larger values of the HJ thickness ($\geq$ 40 nm) the model begins to provide non-accurate solutions for the EM field.

Figure 4.4 shows the electromagnetic field distribution on a transversal section of the NW for different values of the HJ thickness. The transversal section is obtained by a plane perpendicular to the NW and going through the HJ position. The plot contains the same information as figure 4.3: the EM field is reduced as the HJ thickness approaches zero, and the model is not accurate for high values of the HJ thickness ($\geq$ 40 nm) when the thin layer approximation is no longer valid. It is essential to note the localization of the EM field on the centre of the NW as the enhancement reaches its maximum. We can observe that for 30-35 nm the field mode is highly localized and has changed its shape to a one-lobe distribution.

The information provided by Figures 4.3 and 4.4 can be complemented with that of Figure 4.5. The latter shows the EM field distribution for 30 nm HJ thickness at different points along the heterostructured NW: at the Si segment and the HJ. The reference points on the Si segment is 200 nm away from the HJ. We can see in Figure 4.5 that the radial mode is drastically different for the two situations. The Si segment shows a near two-lobe distribution, while the field at the HJ is formed by just one localized lobe in the centre of the NW. Something similar can be appreciated in Figure 4.4, where the EM distribution

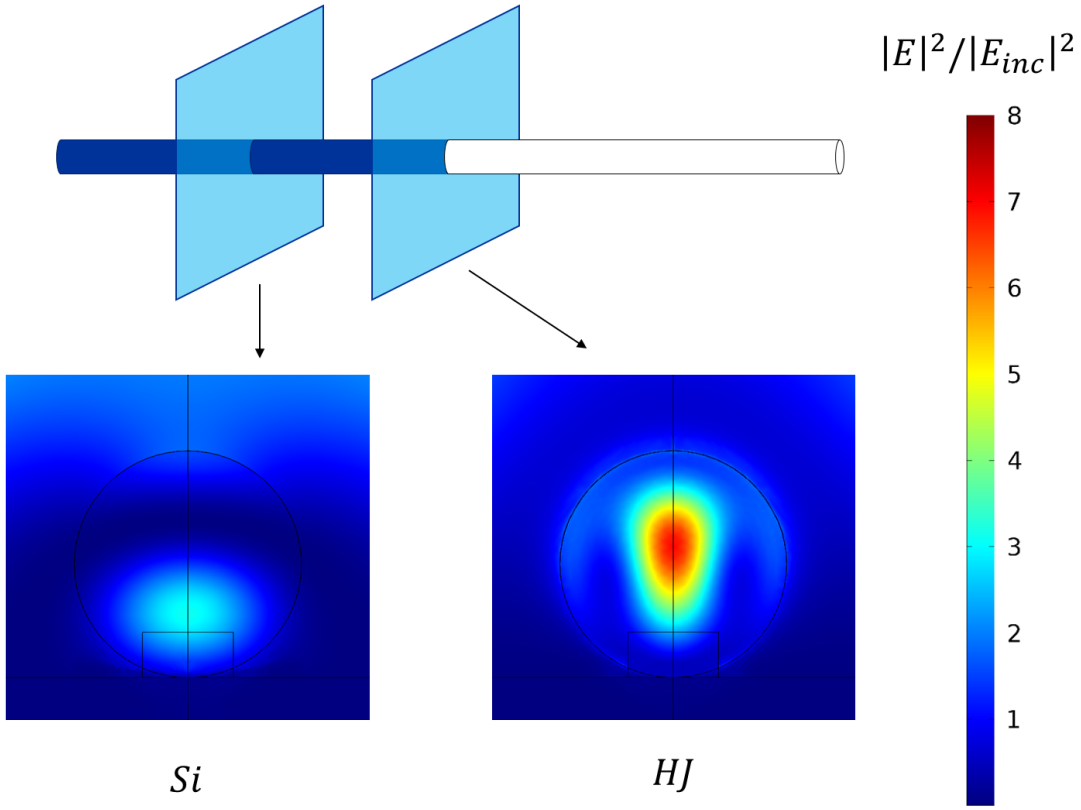

Figure 4.5: EM field distribution for three different positions along the NW axis: Si segment, the HJ, and the SiGe segment. The planes on the homogeneous segments are both 200 nm away from the HJ plane. The plot shows the localization of the EM on the NW centre at the HJ.

at the HJ tends to the two-lobed shape of the homogeneous segments as the HJ thickness is reduced. This illustrates again that the thinner the HJ, the less effect on the EM field distribution.

All this description does correlate perfectly with the experimental observation of the enhancement effect only present on the leading HJ. The experimental measurements do not show any compositional transition on the trailing HJ, neither an enhancement effect. Moreover, the simulations of fully abrupt HJs report the absence of enhancement on this scenario, supporting the experimental data.

4.4 SiGe/Si/SiGe NWs over Graphene

The last section of this chapter aimed at studying the EM field on the immediate vicinity of the NWs. To do this, we used the most renowned 2D material: graphene. Graphene provides us with the possibility of having a one-atom layer of material near the NW, allowing to measure the local EM field exceptionally close to the NW surface. For this experiment, a single layer of CVD graphene was deposited on an Al coated SiO_2 substrate, see Figure 4.6 diagram. After this, SiGe/Si/SiGe NWs are placed over the graphene layer by standard drop-casting.

The first measurements of these samples over the SiO_2 substrate revealed a typical graphene Raman spectrum, see section 3.4.7. However, when these measurements are repeated over the Al the graphene Raman signal is dramatically lowered. Figure 4.6 shows a Raman profile from a region of SiO_2 to Al, showing the fading of the graphene Raman signal as the laser beam moves to the Al substrate. This can be easily explained because Al is a metal, so that, the electric field of an incident light wave should vanish at its surface. Since graphene is a one-atom layer the excitation field on it should be extremely low according to its distance to the metal. This behaviour is not observed on SiO_2 because it is an insulator and transparent to visible light.

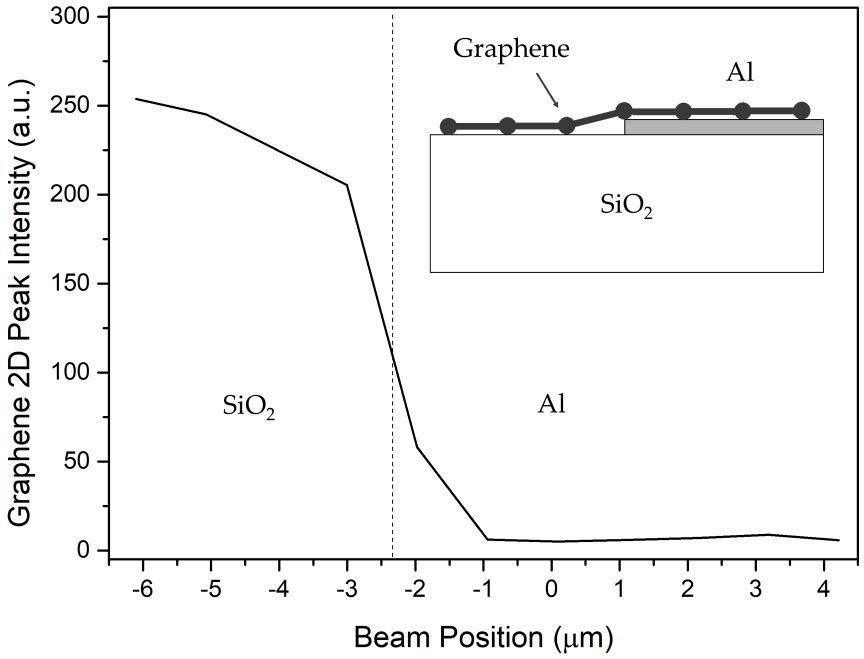

Figure 4.6: Raman profile of graphene over the transition from the SiO_2 substrate to Al. The Raman signal is quenched on Al because of its metallic nature.

The most exciting features appear when we study the NWs lying over graphene. Surprisingly, the Raman signal of graphene is retrieved when a NW is lying over the graphene layer on Al. Figure 4.7 shows a transversal scanning of a SiGe/Si/SiGe NW on one of its SiGe segments. The signals of the Si-Ge peak from SiGe and the graphene 2D peak are represented. There is a clear correlation between both of them: they are reduced when the laser beam does not reach the NW, and both grow when it is illuminated by the laser beam. This figure displays the recovering of the graphene Raman signal by the presence of the NW, even over the surface of a metal like Al.

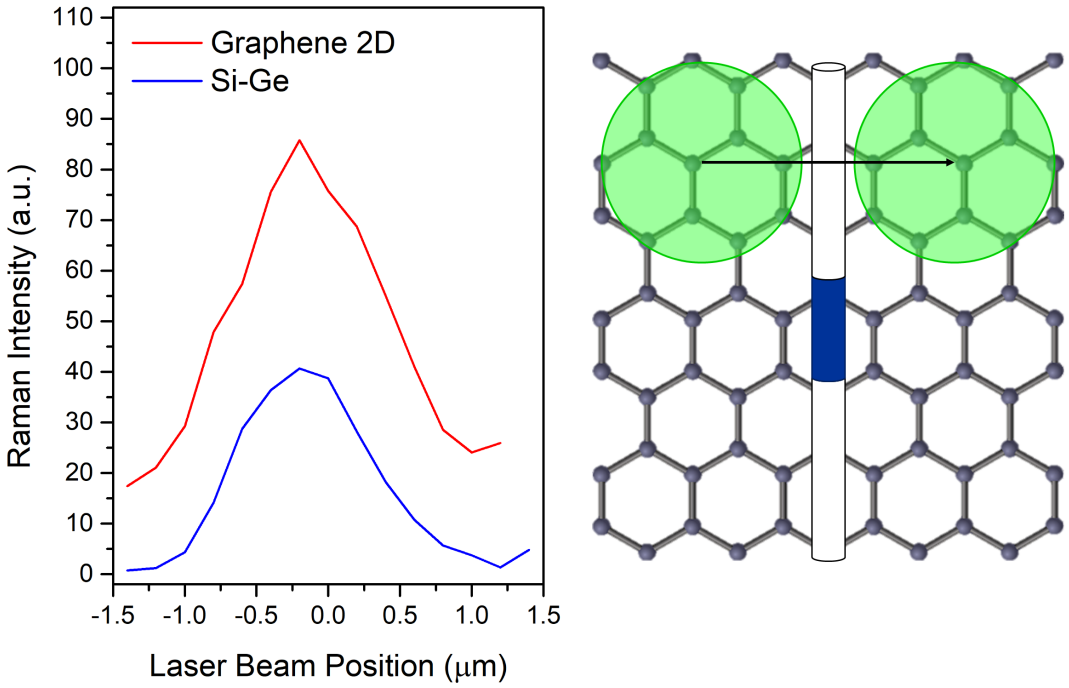

Figure 4.7: Transversal Raman profile of a SiGe/Si/SiGe NW over graphene lying on an Al substrate. The Si-Ge peak of SiGe is used as a reference of the NW signal and the 2D peak is the reference for graphene. The signals of the NW and graphene have a very good correlation being substantially lower outside of the NW.

After this experience, a longitudinal scan of the NW was performed; the results are presented in Figure 4.8. The response of the NW itself is analogous to that of previous NWs, e.g., Figure 4.2. Nevertheless, if we pay attention to the graphene Raman signal, represented by the 2D Raman band, we observe that this signal is higher when the NW is illuminated, in accordance with the transversal scan on Figure 4.7. The graphene signal level is rather homogeneous along the NW; however, a clear minimum can be observed when the laser beam is illuminating the right HJ. A priori we could expect the graphene Raman signal to be enhanced by the HJ, in a similar way as it increases the NW signal.

However, if we recall the results of Figure 4.5, the EM field on the HJ region is localized in the center of the NW, following the single-lobe pattern. Meanwhile, the homogeneous segments present a more spread distribution. This localization of the EM in the NW interior explains why the graphene Raman signal of these samples has never been enhanced by the HJ in the experimental measurements. Indeed, when the EM field is localized in the NW interior the near field on the NW surface is lowered, reducing the graphene Raman signal.

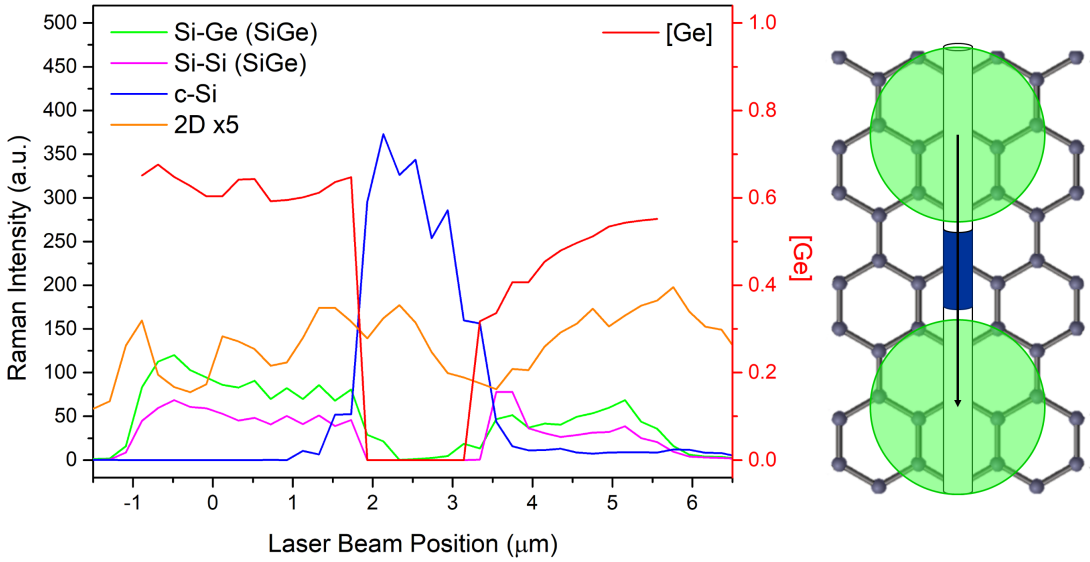

Figure 4.8: Longitudinal Raman profile of a SiGe/Si/SiGe NW over graphene lying on an Al substrate. The enhancement on the right HJ (leading) can be detected on the Si-Si (SiGe) signal, that occurs with a continuous change in composition, see Fig. 4.2. The graphene 2D band is rather homogeneous presenting a minimum that coincides with the HJ enhancement.

4.5 Conclusions

In this chapter, we have presented a new effect of Raman enhancement on SiGe/Si axially heterostructured NWs. The enhancement effect is first presented on single HJ SiGe/Si NWs with low Ge concentration. After this, a similar effect is observed in one of the HJs of SiGe/Si/SiGe NWs, and the FEM model is improved to fully reproduce the experimental results. The Raman response of each HJ is radically different: the trailing HJ behaves as a fully abrupt HJ with no signal of intermediate compositions or enhancement effect; on the other hand, the trailing HJ presents a gradual composition change and an enhancement of the Raman signal. This is in good agreement with the FEM simulations, showing that a fully abrupt HJ does not present any increase of the Raman signal.

Finally, the axially heterostructured NWs have been measured over CVD graphene on top of an Al coated SiO_2 substrate. The results show that the NWs are able to recover the Raman signal of graphene that should be lost because of metallic Al. This points to the NW acting in a similar fashion to a nanolens, by localizing the EM field on its vicinity, allowing for a successful Raman measurement. During the study of the HJ region in this scenario, a lowering of the graphene Raman signal was detected. Even if it may look counterintuitive at first, this is in perfect accordance with the simulations. As it has been shown, the model predicts a localization of the EM field inside the NW at the HJ, lowering its value on the NW surface. These light/matter interactions could be the basis for applications of this kind of NWs as near field probes for molecules or other materials near their surface.

Chapter 5

Any fool can know
The point is to understand
- Albert Einstein -

Si/III-V axially heterostructured NWs

The aim of this section is to find out whether the Raman enhancement effect appears in axially heterostructured NWs manufactured with different materials. According to the FEM model, an EM enhancement on the HJ should be expected regardless of the materials forming the NW, as long as there is a change in the refractive index.

The selection of Si/III-V axially heterostructured NWs responds to the useful applications of III-V semiconductors and their complementarity with group IV semiconductors. The integration of group IV (Si) and III-V semiconductors has been a really active topic for the last decades. On the one hand, Si technology has been broadly studied, allowing very cheap, fast, and reliable fabrication of a great variety of devices. Its main drawbacks are the low carrier mobility, which results in relatively low speed of the final device, as well as the absence of a direct band gap, which restricts its use on light emitting devices. On the other hand, III-V semiconductors like GaAs, InAs, or InP, have higher carrier mobilities and a significant number of them also present direct band gap, making up for the weak points of Si technology. Their main drawback is that III-V semiconductors are more expensive and their manufacture is much more difficult. It is also very interesting to consider Si/III-V heterostructured NWs because they present a different HJ structure, which in this case is atomically abrupt rather than showing a continuous compositional change. This provides an entirely new scenario for the study of heterostructured NWs, as well as highly valuable information for the development of a correct physical understanding of the Raman enhancement phenomenon.

In order to obtain a broad range of results, three different groups of Si/III-V semiconductor NWs have been studied in this section: Si/GaAs, Si/InAs and Si/InGaAs.

5.1 Si/GaAs NWs

The study of Si/III-V heterostructured NWs started with Si/GaAs NWs. Unfortunately, we were unable to measure GaAs signal in any of the studied NWs, and only Raman signal of crystalline Si could be detected. It is interesting to note that the Si peak was slightly broader ($\approx$ 5 cm^{-1}) than what is expected for monocrystalline Si ($\approx$ 3-4 cm^{-1}). Furthermore, the Si band shape showed a subtle asymmetry. These two features point to a lack of crystalline quality of the Si phase, which may be a direct consequence of the flash lamp annealing and subsequent recrystallization process.

The SEM images of the NWs reinforced the Raman results, see Figure 5.1. The NWs do not show fully formed GaAs segments, only small bits of GaAs that seem to be located mainly at the NW surface and do not cover the whole NW diameter. The presence of Ga and As has been confirmed by EDX measurements [1].

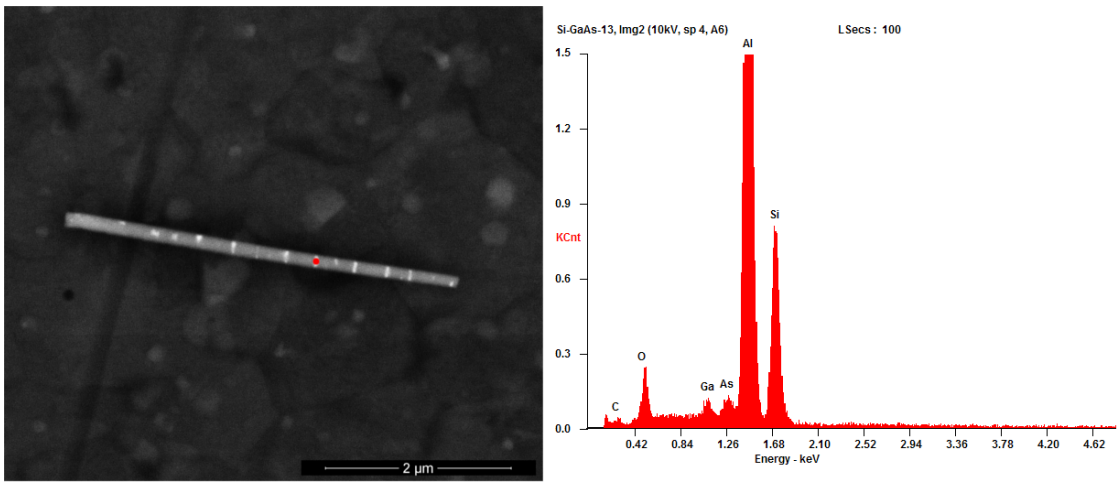

Figure 5.1: SEM micrograph of one of the Si/GaAs NWs showing the absence of complete GaAs segments.

We can conclude that Si/GaAs NWs did not contain fully formed GaAs segments along the NW axis, but only GaAs nanoparticles that do not produce any measurable Raman signal. Moreover, the crystalline quality of the Si may have been degraded during the annealing process.

[1] A.J. Magdaleno. *Estudio y caracterización Raman de nanohilos heteroestructurados*. Trabajo Fin de Grado, Universidad de Valladolid (2017)

5.2 Si/InAs NWs

Unlike their Si/GaAs counterparts, Si/InAs NWs present clear InAs segments along the NW axis. This was determined by both SEM and Raman spectroscopy. The presence of well-formed InAs segments in a significant number of NWs resulted in outstanding statistics and reproducibility of the experimental measurements. The main results of this section are gathered in the scientific paper: *Electromagnetic enhancement effect on the atomically abrupt heterojunction of Si/InAs heterostructured nanowires* (P5).

The μ-Raman spectroscopy scanning of several Si/InAs NWs revealed a similar phenomenon to that observed on SiGe/Si heterostructured NWs. Indeed, the presence of a Raman enhancement effect has been detected, in accordance with the FEM simulations. However, in these samples, the enhancement effect emerges differently, even if the underlying physical interaction is the same.

In the case of Si/InAs NWs the HJ is atomically abrupt because of the immiscibility of these two types of semiconductors, see Section 2.3. Then, there is no HJ volume that can produce Raman signal like in the case of SiGe/Si NWs, where a continuous transition can be found. Si/InAs NWs also present an enhancement of the incident EM field when the HJ region is illuminated by the incident laser beam. However, in this case, the enhancement effect is detected in the Raman signal of the homogeneous Si segment. When the laser beam is focused over the Si segment of the NW, a uniform Raman intensity is obtained. When the laser beam reaches the transition region from Si to the InAs segment, the signal arising from the Si segment is enhanced up to 25 times. Two examples are shown in Figure 3 of P5.

If we look at the FEM simulations for these NWs, the EM field/NW interaction does not result in a sharp and localized enhancement precisely at the HJ. Instead, the EM field is enhanced in the region immediately adjacent to the HJ, see Figure 4 of P5. This perfectly agrees with the Raman measurements obtained for all the NWs with InAs segments. Note that the FEM simulations, Figure 4, predict a localization of the EM field in a reduced region ($\leq$ 300 nm) next to the HJ. This means that a very reduced volume of material is producing the majority of the enhanced signal, although, the extension of this region and the corresponding enhancement factor are very difficult to determine with enough reliability. We could also expect a similar effect in the InAs segment. However, the imaginary part of the refractive index of InAs is noticeably higher than that of Si ($k_{InAs} \approx 1 >> k_{Si} \approx 0.03$), see Table 2.1, and, therefore, the dielectric losses increase. This, together with the typical short length of the InAs segments, makes the possibly existing enhancement on InAs much more difficult to be clearly detected.

There is a contradictory behaviour in the enhancement observed in Si/InAs NWs with respect to the SiGe/Si NWs. In fact, we have shown that the enhancement in the SiGe/Si HJ depends on the HJ thickness, being low for abrupt HJs. However, in the case of Si/InAs, the HJ is atomically abrupt, and one observes the localization and enhancement of the EM field in the region of the Si segment next to the HJ. This result confirms the importance of the discontinuity of the refractive index for the electromagnetic field distribution around the HJ. In the case of the SiGe/Si HJ, the refractive index differences are small and one needs a certain volume of HJ, in which the enhancement takes place. Meanwhile, the difference in the refractive indexes in the Si/InAs HJ is more significant and the enhancement on the Si segment is achieved despite the abrupt nature of the HJ.

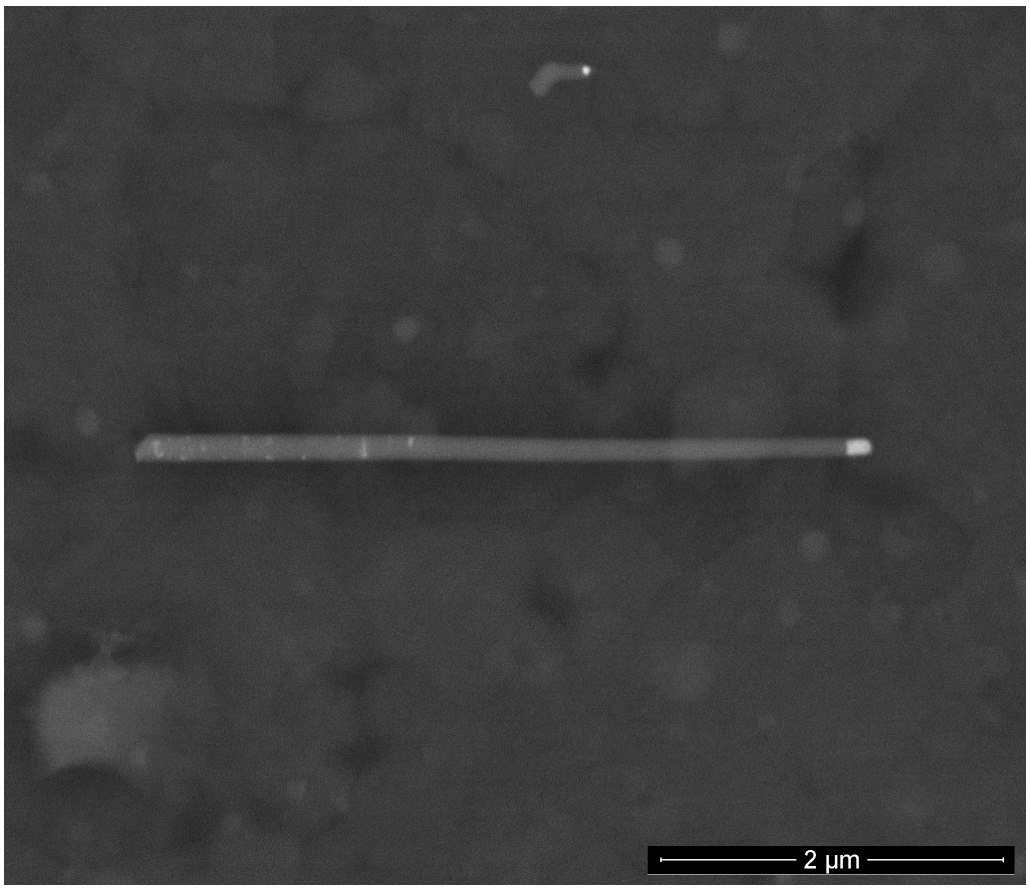

Figure 5.2: Back scattering SEM image of a Si/InAs NWs showing a clearly visible segment of InAs (bright region) on its right side. Some traces of InAs can also be observed on the left side over the NW surface.

5.3 Si/InGaAs NWs

Finally, we analyzed axially heterostructured NWs based on the ternary compound InGaAs. The enhancement effect has been detected in a similar way to that in InAs NWs. However, the analysis of the Raman spectra of these NWs is much more complex, and the effect is much more difficult to see in the final results. This is due to two different reasons. First, InGaAs presents four different Raman modes that are relatively close to each other, see Figure 3.8 and Table 3.1, increasing the difficulty of obtaining an acceptable fit of the Raman spectra. Second, the Raman intensity of these NWs is much lower than that of InAs NWs, resulting in a worse signal-to-noise ratio and the subsequent complication of the data analysis. Nevertheless, the Raman signal of InGaAs has been clearly detected in a good number of NWs, guaranteeing the presence of InGaAs segments, see Figure 5.3. All the studied NWs exhibit an In composition $x \approx 50-60\%$ [2].

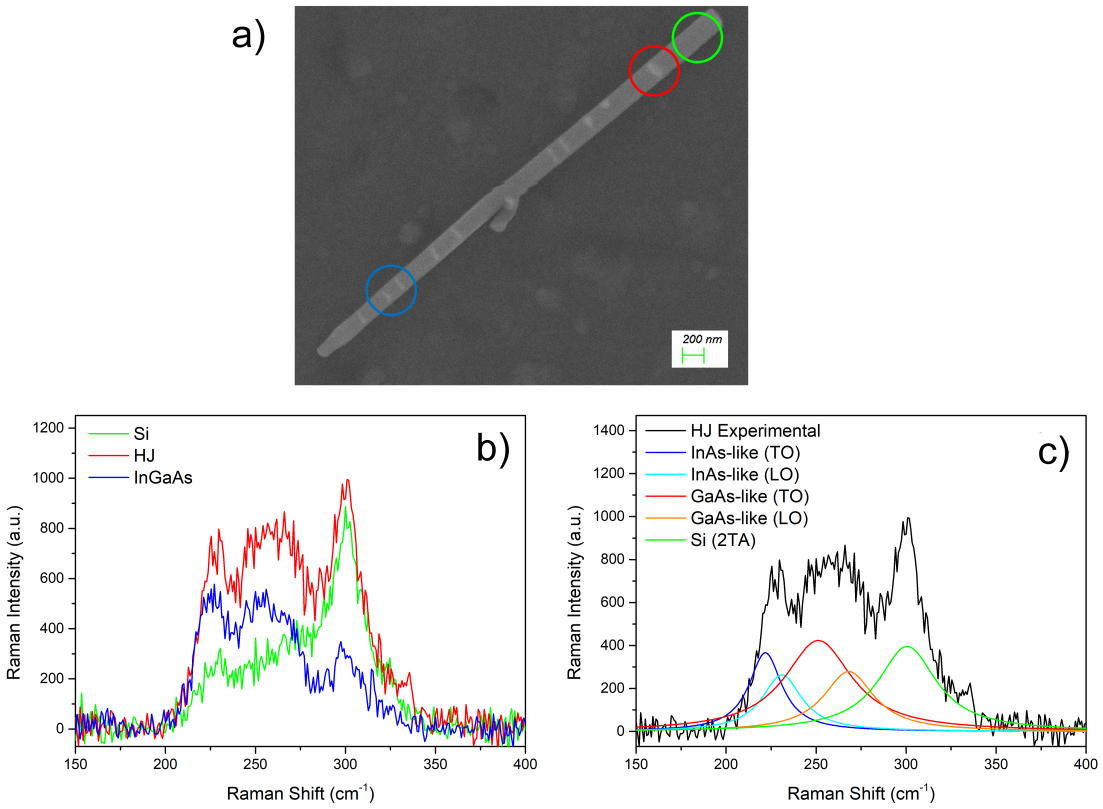

Figure 5.3: a) SEM image of one of the studied Si/InGaAs NWs, showing clearly visible thin segments of InGaAs. b) Three Raman spectra obtained for the Si/InGaAs NW on the marked regions of the SEM image. c) Exmple of the band deconvolution of the spectrum recorded at the HJ region.

[2] D. Muñoz-Segovia. *Estudio de la interacción del campo electromagnético con nanohilos semiconductores heteroestructurados*. Trabajo Fin de Grado, Universidad de Valladolid (2018)

The second order mode of isolated Si, Si (2TA), as well as the four Raman bands of InGaAs, can be identified in Figure 5.3b. This ensures the existence of clear InGaAs segments, as mentioned. Figure 5.3c shows the deconvolution of one of the spectra from the HJ region with the five previously mentioned bands. The weakness of all the Raman signals, when compared with previous experimental measurements, can also be appreciated. We should also mention another difficulty in the analysis of these spectra: the non-Lorentzian shape of the Si (2TA) peak. Indeed, if we look at the shape of this peak, a shoulder on its left side can be observed, which is typical of this Raman band, see Figure 3.3. The shoulder comprises the full region in which the InGaAs Raman signal is detected, thus making it further challenging to analyse the spectra.

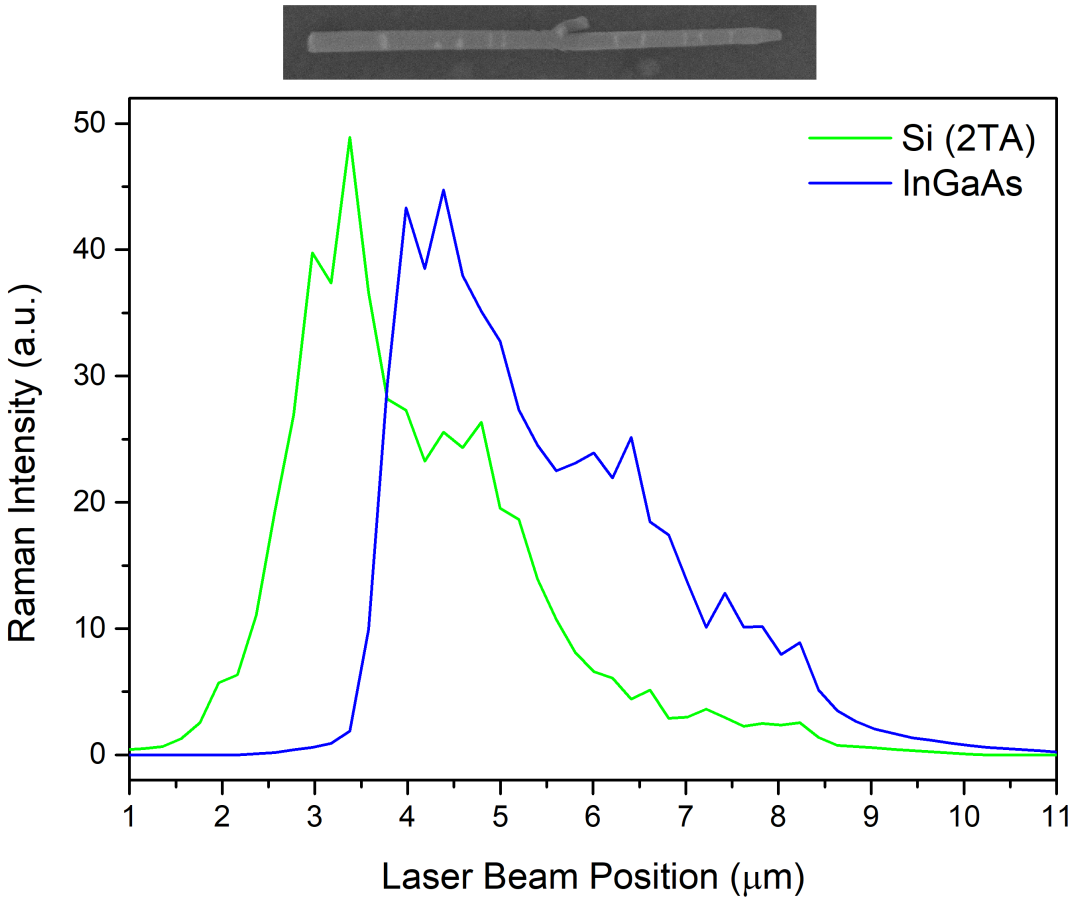

Figure 5.4: Raman mapping along the axis of a Si/InGaAs heterostructured NW. The Raman intensity shows an enhancement of all the Raman signals around the first and longer InGaAs segment. The InGaAs signal shows more fluctuations because of the presence of thinner InGaAs segments along the NW.

The NWs were studied by SEM in order to double check the presence of well-formed InGaAs segment. Figure 5.3a shows the existence of brighter thin sections of InGaAs, whose position correlate perfectly with the longitudinal Raman profile.

Finally, we performed the longitudinal Raman mapping of several of these NWs. The results for a representative one are summarized in Figure 5.4. We can observe the absence of InGaAs Raman signal at the NW ends, reproducing the NW structure of the SEM image. The enhancement effect is similar to that in Si/InAs NWs: the maximum Raman signal of Si is detected just before reaching the first InGaAs segment. Both Si and InGaAs signals slightly decrease after the first segment and recover again when entering the next two segments forming a pair. Finally, both signals fall and become homogeneous on the right side of the NW, which has more InGaAs sections.

It is also interesting that the results for these NWs are somehow intermediate between GaAs and InAs based NWs. On the one hand, we could measure a clear signal of the ternary III-V compound, and an enhancement of the Raman signal is observed near the InGaAs segments. On the other hand, the segments are not reduced in number and relatively long, but numerous and thin, yet detectable. This may be due to different diffusion and segregation properties of In and Ga, which result in a different NW structure after the flash lamp annealing.

5.4 Conclusions

According to the results of this chapter, we can conclude that Si/InAs and Si/InGaAs NWs present the Raman enhancement effect. However, it is different from the SiGe/Si NWs in the sense that the Raman enhancement is detected next to the HJ, rather than on the HJ itself. Si/GaAs NWs did not present this effect; moreover, no GaAs signal at all has been recorded in any of the studied NWs of this kind. Taking into account that the In based compounds do present the effect and also well defined III-V segments, it can be argued that In could play an essential role in the recrystallization process of these heterostructures. As a matter of fact, segregated In has been detected in some of the NWs here studied. The study of this relation could be interesting to understand and control the recrystallization process and the formation of clear segments.

The detection of the enhancement effect on new heterostructured NWs reveals the link between the NW axial structure and the origin of the Raman enhancement, rather than being a consequence of the exact materials forming the NW. In the same way, the FEM model can reproduce the observed phenomena by merely specifying the properties of the new materials. This is proof of excellent reliability in the robustness of the FEM model.

Electromagnetic enhancement effect on the atomically abrupt heterojunction of Si/InAs heterostructured nanowires

J. L. Pura[1,*], A. J. Magdaleno[1], D. Muñoz-Segovia[1], M. Glaser[2], A. Lugstein[2], and J. Jiménez[1]

[1] *GdS Optronlab, Dpt. Física de la Materia Condensada, ed. LUCIA Universidad de Valladolid, Paseo de Belén 19, 47011 Valladolid, Spain*

[2] *Institute for Solid State Electronics, Vienna University of Technology, Floragasse 7, 1040 Vienna, Austria*

[*] *jlpura@fmc.uva.es*

Keywords: nanowires, axial heterostructures, Si, InAs, Raman, electromagnetic enhancement

Abstract

Semiconductor nanowires (NWs) present a great number of unique optical properties associated with their reduced dimension and internal structure. NWs are suitable for the fabrication of defect free Si/III-V heterostructures, allowing the combination of the properties of both Si and III-V compounds. We present here a study of the electromagnetic (EM) resonances on the atomically abrupt heterojunction of Si/InAs axially heterostructured NWs. We studied the electromagnetic response of Si/InAs heterojunctions sensed by means of Micro-Raman spectroscopy. These measurements reveal a high enhancement of the Si Raman signal when the incident laser beam is focused right on the Si/InAs interface. The experimental Raman observations are compared to finite element methods (FEM) simulations for the interaction of the focused laser beam with the heterostructured NW. The simulations explain why the enhancement is detected on the Si signal when illuminating the HJ and also provide a physical framework to understand the interaction between the incident EM field and the heterostructured NW. The understanding of this process opens the possibility of controlling the light absorption/scattering on semiconductor NWs with the use of heterostructures, while taking advantage of the properties of both Si and III-V semiconductors. This is important for current NW based photonic nanodevices, such as light sensors, but also for the design of new optoelectronic devices based on NWs.

1 Introduction

Semiconductor nanowires (NWs) exhibit unique physical properties as a consequence of their confined dimension, the diameter. Besides, the presence of heterojunctions (HJ) is necessary for building up electronic and optoelectronic nanodevices [1–4]. Among all the possible heterostructured NWs, those based on Si are especially interesting because of its useful properties for solar applications, versatility and the possibility of their integration with the already existing Complementary Metal Oxide Semiconductor (CMOS) technology. According to this, a great variety of Si NW based devices has been produced, e.g. Si NW near-infrared photodetectors [5] or double-gated Si NW FET sensors [6]. On the other hand, III-V semiconductors present higher values of the carrier mobility and improved optical properties with respect to their group IV counterparts, thus making up for Si drawbacks. The integration of Si/III-V heterostructures in a single NW would allow combining the advantages of both Si and III-V semiconductors with the unique optical properties of semiconductor NWs [7–11].

III-V semiconductor NWs are being extensively investigated for its possible applications on nanowire solar cells [12, 13], and light sources, including lasers [14–18]. There are excellent studies of InP NWs, based on their optical properties and resonances [19], and its high efficiency as solar cells [20]. Also, as an example of Si/III-V integration, InAs NWs deposited on a Si substrate were used in photovoltaics and photodetectors. [21] In previous works, we reported the enhancement of the Raman signal at the heterojunction of axially heterostructured Si/SiGe nanowires [22]. We demonstrated that the enhancement effect appears as a result of the interaction between the incident electromagnetic (EM) field and the dielectric discontinuity at the heterojunction [23, 24]. According to this, the EM enhancement effect is expected to appear in any kind of axially heterostructured NW. In this work we will study the electromagnetic behaviour of heterostructured Si/InAs NWs using micro-Raman spectroscopy as a probe of the EM field inside the NW. A theoretical framework of the problem is established by solving the Maxwell equations of the light/ NW system by Finite Element Methods (FEM). Finally, the results of the simulations are contrasted with the micro-Raman experiments.

2 Experimental and Samples

The Si/InAs heterostructured NWs were fabricated with an ion implantation and flash annealing procedure, similar to the one presented in reference [4]. The $< 111 >$ oriented Si NWs were epitaxially grown on Si (111) substrates by applying the gold-catalyzed vapour-liquid-solid (VLS) method. After removal of gold by wet chemical etching, approx. 20 nm SiO_2 was deposited on the NWs by plasma enhanced chemical vapour deposition, acting as a protecting layer for the following steps. In order to achieve homogeneous implantation profiles along the NWs, samples were placed on a 45° tilted and continuously rotating stage during ion implantation. In and As ions were implanted alternatingly with an energy of 120 keV and 90 keV, respectively. The recrystallization along with the phase separation and formation of Si/InAs heterostructures within the NW core was finally achieved by applying a 20 ms flash lamp annealing step with a flash energy of about 50 J/cm^2.

The NW morphology and structure were studied in a high-resolution Field Emission Scanning Electron Microscope (FESEM). The heterostructured NWs appear as straight cylinders with slight tapering. The InAs segment is shorter than the Si segment, namely 200 - 500 nm vs 3 - 4 μm. Energy-Dispersive X-ray Spectroscopy (EDS) was used to determine the NW composition, revealing that the brighter regions in the SEM micrographs are indeed InAs, while the darker contrast segment consists of Si, as expected from the different atomic number (see Fig. 1).

Raman spectra profiles along the axes of several Si/InAs NWs were obtained in order to study the effect of the heterojunction on the Raman signal. The laser excitation was performed with a continuous wave frequency doubled Nd:YAG laser (532 nm) going through a 100X objective, this gives a laser spot of ≈ 1 μm. The maximum laser power was 450 μW (≈ 14 kW/cm^2), non-linear effect are not detected at this power level (although they might appear for higher power). During the Raman measurements the NWs are lying over an Al coated Si substrate, so the excitation beam is always perpendicular to the NW axis and the substrate. The laser polarization is always parallel to the NW axis in order to record the maximum Raman signal. The Raman spectra were recorded along the NW axis in steps of 200 nm. Further details about the experimental method followed for the characterization of the heterostruc-

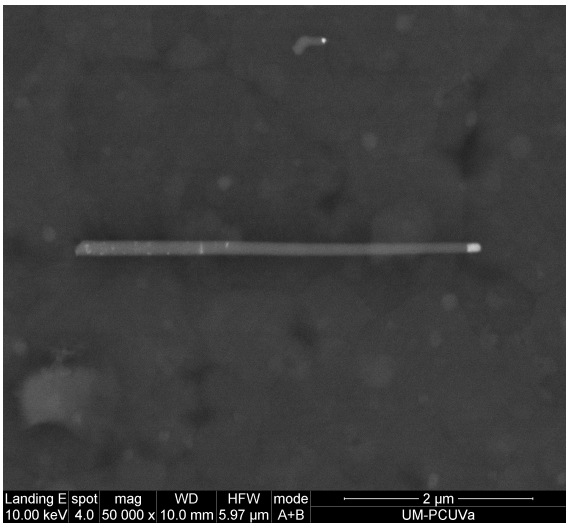

Figure 1: SEM image of a typical Si/InAs heterostructured NW. The InAs segment can be detected on the right side as a brighter region on the NW.

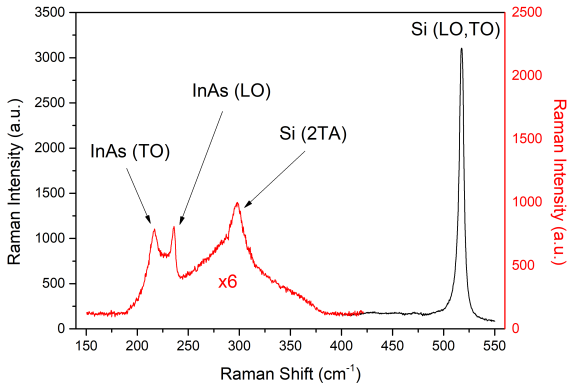

Figure 2: Typical Raman spectrum of a Si/InAs NW when the HJ region is illuminated. It shows the principal Raman bands of both NW segments, Si and InAs.

tured NWs can be found elsewhere [22, 23]. The typical Raman spectrum of these NWs when the HJ is being excited by the laser beam will contain the Raman bands of both crystalline Si and InAs, Figure 2. When each individual segment of the NW is illuminated only the signal of the semiconductor forming the segment is recorded. The spectrum of the Si NW segment consists of the degenerated LO and TO modes located at 520.6 cm^{-1}, labelled Si (LO,TO), and the much less intense second order transverse acoustic mode around 300 cm^{-1}, labelled Si (2TA). For the InAs segment, we can observe the LO and TO modes at 217.3 cm^{-1} and 238.6 cm^{-1}, respectively [25].

3 Results

We acquired the Raman profiles along the axis of several Si/InAs NWs. Then, the intensities of the different Raman bands were extracted from each spectrum. This allows visualizing the dependence of the Raman signals as a function of the laser beam position along the NW. Two examples of the Raman intensity profiles are shown in Figure 3, corresponding to two different Si/InAs heterostructured NWs.

Both profiles show that the Raman intensities arising from the Si segment are enhanced when the HJ region is illuminated by the laser beam, giving enhancement factors of 25 and 10 times, respectively. This enhancement factor is calculated as the ratio between the maximum Raman intensity recorded next to the HJ, with respect to the one recorded on the homogeneous Si segment of the NW. This proves that the enhancement effect is also present in Si/InAs heterostructured NWs, in spite of some differences with respect to the same effect observed in Si/SiGe NWs previously studied [11, 12]. In the case of SiGe/Si heterostructured NWs, Si and Ge are both non-polar semiconductors and the SiGe alloy is stable for any Si/Ge ratio. The full miscibility of Ge and Si, and its high solubility in the catalyst metal, are responsible for the graded HJs extending several tens of nanometres depending on the NW diameter [26]. The SiGe/Si heterojunction is not abrupt, but a continuous transition between the compositions of the two NW segments constitutes the heterojunction. Therefore, one can associate a certain volume of material to the HJ region itself, which is chemically recognizable, and the Raman signal arising from this volume forming the HJ permitted to study the true local field enhancement (intensity per unit scattering volume). This situation does not apply to Si/InAs NWs, because the immiscibility between polar InAs and non-polar Si makes the Si/InAs heterojunction atomically abrupt [27]. For this reason, one cannot extract a spectrally differentiated signal arising from the HJ itself; however, the EM enhancement effect is clearly observed around the HJ in the profiles of Figure 3. The Raman intensity of Si is

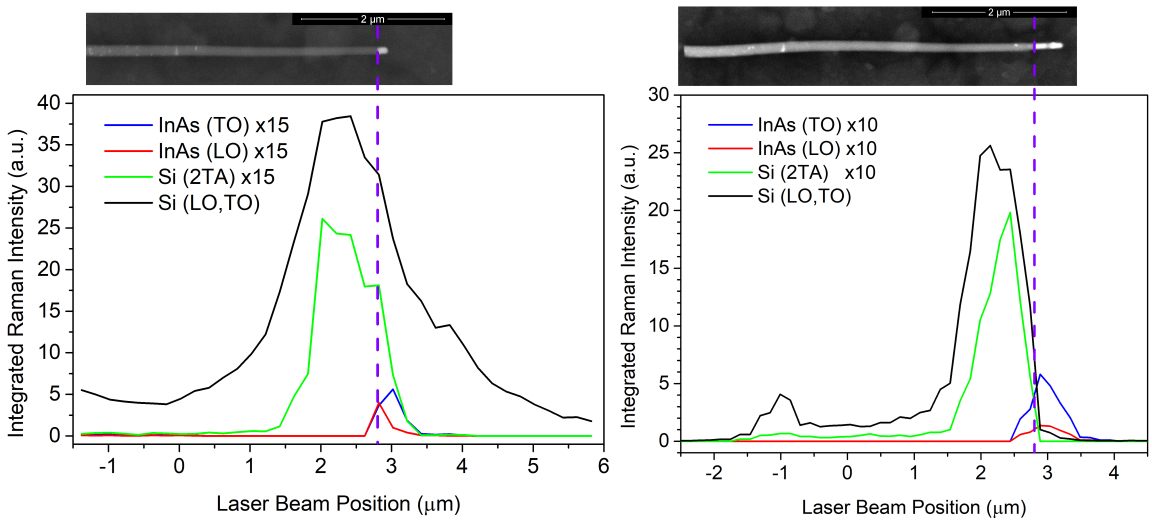

Figure 3: Raman intensity profiles of two different Si/InAs heterostructured NWs. The upper SEM images have the same scale as the plots and show the position of the HJ. A strong enhancement of the Si signal arising from the Si region adjacent to the HJ can be seen.

strongly enhanced in the region of the Si NW segment adjacent to the heterojunction. The true EM enhancement per unit scattering volume is difficult to estimate, because of the limited spatial resolution of the micro-Raman probe. However, the increase of the Raman intensity around the HJ can be unambiguously appreciated in Figure 3. It is important to note that any effect of the electronic states, or resonance with the band gap energy, have been ruled out. This is because Si and InAs bandgaps are in the IR and far-IR regions, respectively, and the band alignment between both of them is type II [28]. As a result, any possible interaction between carriers will need both a change in momentum and position which will drastically reduce its efficiency.

The experimental results have been contrasted with the EM field calculated by Finite Element Methods (FEM) simulations. The Maxwell equations were solved for the substrate /NW system, the FEM calculation provides us with the distribution of the electric field intensity, $|E|^2$, inside the NW. A more detailed explanation of the developed FEM model can be found in previous papers [22, 23]. There are two main differences in Si/InAs heterostructured NWs with respect to Si/SiGe heterostructured NWs. First, as we mentioned, the axial heterojunctions for both types of NWs are different, graded for SiGe/Si and abrupt for InAs/Si. Second, InAs presents much higher dielectric losses (imaginary part of the refractive index, k) than Si or the SiGe alloy for light in the visible range, Table 1. The values of the optical constants of InAs can be found in Ref. [29]. The dimensions of the heterostructured NW used in the simulations are 100 nm diameter, 500 nm the length of the InAs segment and 3500 nm the length of the Si segment.

The main results of the simulations are summarized in Figure 4. The solution of the Maxwell equations provides the distribution of the EM field inside the NW. Figure 4a shows the volume distribution of the relative EM field intensity on the NW and its environment when the laser beam is focused on the HJ. The relative EM field is defined as the value of the EM field divided by the incident field, $|E|^2/|Einc|^2$. Figure 4b shows the distribution of the same magnitude along the NW axis. We can see that the effect of the higher dielectric losses on the InAs side consists of a marked reduction of the EM field intensity with respect to the Si side next to the HJ. It explains the low InAs Raman signal detected on the experimental measurements, even next to the heterojunction. On the other hand, we can see the enhancement and localization of the incident field on the Si side. The EM field is enhanced by more than 3 times in a small region of about 300 nm, close to the heterojunction. One can establish here

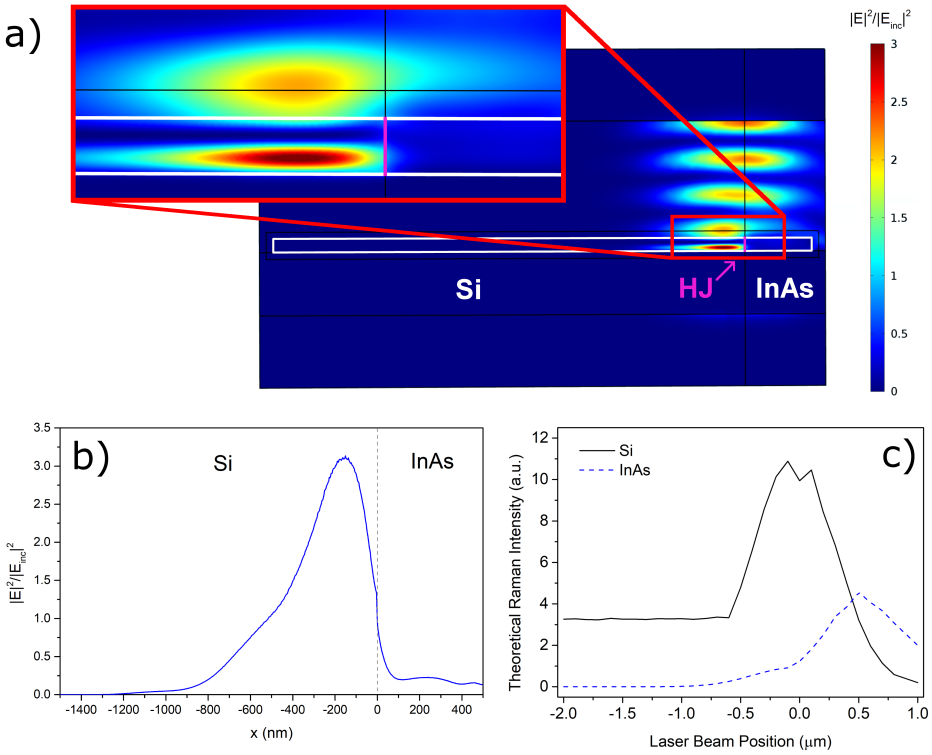

Figure 4: a) EM field distribution induced in a Si/InAs NW with 100 nm diameter when the incident laser beam is focused on the HJ. The incident field is enhanced more than 3 times in a region of ≈ 300 nm next to the HJ on the Si side. b) Profile of the EM field distribution along the NW axis. c) Simulation of the Theoretical Raman Signal as a function of the laser beam position, to reproduce the experimental measurements of Fig. 3. Note that the high dielectric loses of InAs [29] ($k \approx 1$) result in a highly reduced field intensity in the InAs side.

an estimation for the dimension of the NW region where the EM enhancement takes place, therefore one can estimate the Raman intensity per unit volume to bring up the true EM enhancement at the HJ. Figure 4c presents the theoretical Raman intensity, which should be proportional to the excitation field intensity i.e. $|E|^2$. This value is obtained from the simulation by varying the laser beam position along the NW axis and integrating on each of the NW segments. We can see that the intensity of the Si signal is enhanced when the laser beam approaches the HJ as compared to the calculated intensity obtained when illuminating the homogeneous Si segment. These results are in very good agreement with the experimental measurements of Figure 3, both showing the enhancement of the Si Raman signal as a consequence of the illumination of the Si/InAs HJ by the focused laser beam.

Finally, it is worth noting that the exact calculation of the experimental enhancement is difficult for two main reasons. First, the enhancement depends on the NW diameter. According to this, the response of a pure Si NW has been investigated. Figure 5 shows the average relative electric field inside a homogeneous Si NW as a function of its diameter.

Si/InAs heterostructured NWs present a slight tapering (see Figure 1), as a result the diameter of the homogeneous Si segment becomes larger as it moves away from the HJ. Near the HJ the NW diameter is around 100-120 nm which coincides with a diameter resonance of Si, see Figure 5. However, the NW diameter increases as we move away from the HJ, slightly deviating from the diameter resonance peak. This would explain the higher experimental values of the enhancement as compared to the homogeneous segment signal. The ratio be-

	InAs	**Si**	$\mathbf{Si_{(1-x)}Ge_x}$
n	4.3736	4.1334	$4.1334 + 0.668619x + 1.510779x^2$
k	1.0831	0.033258	$0.033258 + 0.204615x + 1.621028x^2$

Table 1: Real (n) and imaginary (k) parts of the complex refractive indexes of the different materials used in the FEM calculations for 532 nm radiation.

tween the two regions of Figure 5 has a mean value of 5, which accounts for the observed difference between the experimental and theoretical values (a maximum value of 10 could be obtained when the diameter coincides exactly with the maximum of the resonance). On the other hand, the NW is not homogenous, and it is covered by a SiO_2 outer shell, making the exact determination of the diameter even more difficult.

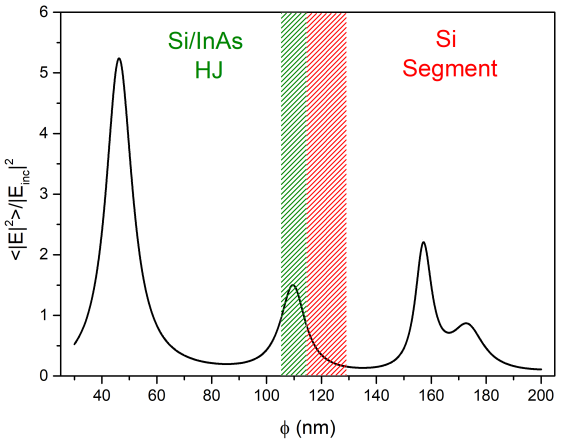

Figure 5: Dependence of the mean value of the relative electric field intensity inside a pure Si NW as a function of its diameter. The studied Si/InAs NWs are tapered, as a result the Si segment presents a smaller diameter in the region next to the HJ than in the region far away from the HJ. These two diameter ranges are represented by the shadowed regions, showing how a small diameter variation can shift out the diameter resonance of the Si segment in this case.

4 Conclusions

The Raman intensity is enhanced on the heterojunction of axially heterostructured Si/InAs NWs. The observation of this effect on different axially heterostructured NWs formed by different materials accounts for the description of this phenomenon as an EM effect associated with the dielectric discontinuity at the heterojunction. However, the detailed behaviour of the EM enhancement effect strongly depends on the materials forming the HJ and the structure of the HJ itself. In the case of Si/SiGe NWs, the enhancement was detected on the signal arising from the HJ itself, which has a finite dimension. Alternatively, in Si/InAs NWs with abrupt HJs the electromagnetic enhancement is observed in the region of the Si segment right next to the HJ. Note that the same effect also appears in the InAs side, but the high dielectric losses and reduced length of the InAs segment do not allow us to see the effect as clear as in the Si side. Both, experimental and theoretical profiles of the EM field intensity along the NW show a higher intensity of the Si signal in the immediate vicinity of the HJ. The existence of this effect and its observation on very different materials suggests the possibility of detecting similar effects on other nanostructured systems with HJs. Finally, the enhanced absorption/scattering at the HJs in axially heterostructured NWs, and its dependence with the NW composition and structure opens interesting ways of photon handling using complex heterostructured NWs, with application in photon detection and photovoltaics, among other.

Achnowledgements

This work was funded by Junta de Castilla y León (Projects VA293U13, and VA081U16), and Spanish Government (CICYT MAT2010-20441-C02 (01 and 02) and ENE 2014-56069-C4-4-R). J L Pura was granted by the FPU programme (Spanish Government) (FPU14/00916).

References

[1] Y. Li, F. Qian, J. Xiang, C. M. Lieber. Nanowire electronic and optoelectronic devices. *Materials Today*, **9** (10), 18–27 (2006). doi:10.1016/S1369-7021(06)71650-9

[2] Y. Cui, Z. Zhong, D. Wang, W. U. Wang, C. M. Lieber. High performance silicon nanowire field effect transistors. *Nano Letters*, **3** (2), 149–152 (2003). doi:10.1021/nl025875l

[3] J. Xiang, W. Lu, Y. Hu, Y. Wu, H. Yan, C. M. Lieber. Ge/Si nanowire heterostructures as high-performance field-effect transistors. *Nature*, **441** (7092), 489–493 (2006). doi:10.1038/nature04796

[4] M. Glaser, A. Kitzler, A. Johannes, S. Prucnal, H. Potts, S. Conesa-Boj, L. Filipovic, H. Kosina, W. Skorupa, E. Bertagnolli, C. Ronning, A. FontcubertaMorral, A. Lugstein. Synthesis, Morphological, and Electro-optical Characterizations of Metal/Semiconductor Nanowire Heterostructures. *Nano Letters*, **16** (6), 3507–3513 (2016). doi:10.1021/acs.nanolett.6b00315

[5] K. Das, S. Mukherjee, S. Manna, S. K. Ray, A. K. Raychaudhuri. Single Si nanowire (diameter $\leq$ 100 nm) based polarization sensitive near-infrared photodetector with ultra-high responsivity. *Nanoscale*, **6** (19), 11232–11239 (2014). doi:10.1039/c4nr03170a

[6] F. Gasparyan, H. Khondkaryan, A. Arakelyan, I. Zadorozhnyi, S. Pud, S. Vitusevich. Double-gated Si NW FET sensors: Low-frequency noise and photoelectric properties. *Journal of Applied Physics*, **120** (6), 064902 (8pp) (2016). doi:10.1063/1.4960704

[7] K. Tomioka, M. Yoshimura, T. Fukui. A III-V nanowire channel on silicon for high-performance vertical transistors. *Nature*, **488** (7410), 189–192 (2012). doi:10.1038/nature11293

[8] M. Hocevar, G. Immink, M. Verheijen, N. Akopian, V. Zwiller, L. Kouwenhoven, E. Bakkers. Growth and optical properties of axial hybrid III-V/silicon nanowires. *Nature Communications*, **3**, 1–6 (2012). doi:10.1038/ncomms2277

[9] J. Justice, C. Bower, M. Meitl, M. B. Mooney, M. A. Gubbins, B. Corbett. Wafer-scale integration of group III-V lasers on silicon using transfer printing of epitaxial layers. *Nature Photonics*, **6** (9), 610–614 (2012). doi:10.1038/nphoton.2012.204

[10] C. D. Bessire, M. T. Björk, H. Schmid, A. Schenk, K. B. Reuter, H. Riel. Trap-assisted tunneling in Si-InAs nanowire heterojunction tunnel diodes. *Nano Letters*, **11** (10), 4195–4199 (2011). doi:10.1021/nl202103a

[11] W. S. Ko, I. Bhattacharya, T. T. D. Tran, K. W. Ng, S. Adair Gerke, C. Chang-Hasnain. Ultrahigh Responsivity-Bandwidth Product in a Compact InP Nanopillar Phototransistor Directly Grown on Silicon. *Scientific Reports*, **6** (March), 1–11 (2016). doi:10.1038/srep33368

[12] G. Otnes, M. T. Borgström. Towards high efficiency nanowire solar cells. *Nano Today*, **12**, 31–45 (2017). doi:10.1016/j.nantod.2016.10.007

[13] G. Mariani, A. C. Scofield, C. H. Hung, D. L. Huffaker. GaAs nanopillar-array solar cells employing in situ surface passivation. *Nature Communications*, **4**, 1497 (2013). doi:10.1038/ncomms2509

[14] F. Qian, Y. Li, S. Gradečak, H. G. Park, Y. Dong, Y. Ding, Z. L. Wang, C. M. Lieber. Multi-quantum-well nanowire heterostructures for wavelength-controlled lasers. *Nature Materials*, **7** (9), 701–706 (2008). doi:10.1038/nmat2253

[15] Y. J. Lu, C. Y. Wang, J. Kim, H. Y. Chen, M. Y. Lu, Y. C. Chen, W. H. Chang, L. J. Chen, M. I. Stockman, C. K. Shih, S. Gwo. All-color plasmonic nanolasers with ultralow thresholds: Autotuning mechanism for single-mode lasing. *Nano Letters*, **14** (8), 4381–4388 (2014). doi:10.1021/nl501273u

[16] Y. Zhang, J. Wu, M. Aagesen, H. Liu. III-V nanowires and nanowire optoelectronic devices. *Journal of Physics D: Applied Physics*, **48** (46), 463001 (29pp) (2015). doi:10.1088/0022-3727/48/46/463001

[17] H. Kim, W. J. Lee, A. C. Farrell, J. S. Morales, P. Senanayake, S. V. Prikhodko, T. J. Ochalski, D. L. Huffaker. Monolithic InGaAs Nanowire Array Lasers on Silicon-on-Insulator Operating at Room Temperature. *Nano Letters*, **17** (6), 3465–3470 (2017). doi:10.1021/acs.nanolett.7b00384

[18] F. Lu, I. Bhattacharya, H. Sun, T.-T. D. Tran, K. W. Ng, G. N. Malheiros-Silveira, C. Chang-Hasnain. Nanopillar quantum well lasers directly grown on silicon and emitting at silicon-transparent wavelengths. *Optica*, **4** (7), 717 (2017). doi:10.1364/OPTICA.4.000717

[19] N. Anttu, H. Q. Xu. Efficient light management in vertical nanowire arrays for photovoltaics. *Optics Express*, **21** (S3), A558 (2013). doi:10.1364/OE.21.00A558

[20] J. Wallentin, N. Anttu, D. Asoli, M. Huffman, I. Åberg, M. H. Magnusson, G. Siefer, P. Fuss-Kailuweit, F. Dimroth, B. Witzigmann, H. Q. Xu, L. Samuelson, K. Deppert, M. T. Borgström. InP Nanowire Array Solar Cells Achieving 13.8% Efficiency by Exceeding the Ray Optics Limit. *Science*, **339** (6123), 1057–1060 (2013). doi:10.1126/science.1230969

[21] W. Wei, X.-Y. Bao, C. Soci, Y. Ding, Z.-L. Wang, D. Wang. Direct Heteroepitaxy of Vertical InAs Nanowires on Si Substrates for Broad Band Photovoltaics and Photodetection. *Nano Letters*, **9** (8), 2926–2934 (2009). doi:10.1021/nl901270n

[22] J. L. Pura, J. Anaya, J. Souto, Á. C. Prieto, A. Rodríguez, T. Rodríguez, J. Jiménez. Local electric field enhancement at the heterojunction of Si/SiGe axially heterostructured nanowires under laser illumination. *Nanotechnology*, **27** (45), 455709 (2016). doi:10.1088/0957-4484/27/45/455709

[23] J. L. Pura, J. Anaya, J. Souto, A. C. Prieto, A. Rodríguez, T. Rodríguez, P. Periwal, T. Baron, J. Jiménez. Electromagnetic field enhancement effects in group IV semiconductor nanowires. A Raman spectroscopy approach. *Journal of Applied Physics*, **123** (11), 114302 (2018). doi:10.1063/1.5012987

[24] J. L. Pura, J. Souto, P. Periwal, T. Baron, J. Jiménez. Electromagnetic Field Enhancement on Axially Heterostructured NWs: The Role of the Heterojunctions. *Journal of Electronic Materials* (2018). doi:10.1007/s11664-018-6356-9

[25] K. Aoki, E. Anastassakis, M. Cardona. Dependence of Raman frequencies and scattering intensities on pressure in GaSb, InAs, and InSb semiconductors. *Physical Review B*, **30** (2), 681–687 (1984). doi:10.1103/PhysRevB.30.681

[26] J. Pura, P. Periwal, T. Baron, J. Jiménez. Growth dynamics of SiGe nanowires by the vapour-liquid-solid method and its impact on SiGe/Si axial heterojunction abruptness. *Nanotechnology*, **29** (35), 355602 (9pp) (2018). doi:10.1088/1361-6528/aaca74

[27] S. Prucnal, M. Glaser, A. Lugstein, E. Bertagnolli, M. Stöger-Pollach, S. Zhou, M. Helm, D. Reichel, L. Rebohle, M. Turek, J. Zuk, W. Skorupa. III-V semiconductor nanocrystal formation in silicon nanowires via liquid-phase epitaxy. *Nano Research*, **7** (12), 1769–1776 (2014). doi:10.1007/s12274-014-0536-6

[28] C. Bru-Chevallier, A. El Akra, D. Pelloux-Gervais, H. Dumont, B. Canut, N. Chauvin, P. Regreny, M. Gendry, G. Patriarche, J. M. Jancu, J. Even, P. Noe, V. Calvo, B. Salem. InGaAs Quantum Dots Grown by Molecular Beam Epitaxy for Light Emission on Si Substrates. *Journal of Nanoscience and Nanotechnology*, **11** (10), 9153–9159 (2011). doi:10.1166/jnn.2011.4282

[29] S. Adachi. Optical dispersion relations for GaP, GaAs, GaSb, InP, InAs, InSb, $Al_xGa_{1-x}As$ and $In_{1-x}Ga_xAs_yP_{1-y}$. *Journal of Applied Physics*, **66** (12), 6030–6040 (1989). doi:10.1063/1.343580

P5

Chapter 6

Never make a calculation until you know the answer
- John Wheeler -

Nanowire Growth Model

Despite encompassing more than 50 years of history, the VLS growth method is not fully understood. There exist several models and approaches to its study, but also some inconsistencies between models and experimental data, for example, in Chapter 4 the experimental measurements showed that the trailing HJ could be more abrupt than initially expected. This is a crucial matter regarding the applications of NWs on devices. In order to be able to achieve an optimal operation, it is necessary to fabricate abrupt heterojunctions on NW heterostructures. For all these reasons, a correct understanding of the heterojunctions growth process is fundamental.

The main limiting factor of the HJ abruptness is the *reservoir effect* [20, 21]. When one of the reactant fluxes is switched off, the vapour phase can be flushed of the remaining atoms relatively fast. However, the atoms that are dissolved in the catalyst droplet will continue being deposited until the liquid phase leaves the supersaturation state. This will limit the minimum physical extension in which one material completely changes to the other during growth. In the case of III-V compounds, the solubility of group V semiconductors in the liquid droplet is typically much lower ($\approx 10^{-5}$ times) than the group III ones. This makes the fabrication of abrupt III-V heterojunctions relatively easy. However, group IV materials like Si and Ge present very high values of the solubility on Au and similar metals. As a result, a significant number of atoms are stored in the liquid droplet, and they are deposited during the HJ transition, producing less abrupt HJs. Several techniques have been proposed to overcome this problem, usually focusing on catalysts with lower Ge solubility like Au/Al or Au/Ag [15, 16].

For the development of the following model, we propose a deeper study of the growth dynamics to better understand NW growth by the VLS method. Specifically, the model is intended for its application to HJs growth and the study of the interface extension. The model is based on the chemical potentials of Si and Ge in the Si/Ge/Au alloy as described in Section 2.3, equation (2.20). The chemical potentials are the driving forces of atomic movement through phase boundaries; this allows to compute the deposition rates of the two components on the solid growing phase. At the same time, the composition of the liquid phase can be updated if the atomic deposition rates and the incoming fluxes are known. The model computes the composition of each atomic layer of the NW during the process, establishing the evolution of the NW composition during growth, which permits the calculation of the transition region length.

The calculated HJ profiles and lengths are in good agreement with experimental data, both those presented in this thesis, Chapter 4, as well as previous experimental measurements [32]. Nevertheless, the major advance of the model is the capability of controlling the NW growth composition given the liquid droplet conditions. The model can explain the exact growth composition as well as the HJ profile by the use of a composition map derived from the chemical potentials. This permits to calculate the expected growth composition as a function of the initial conditions of the liquid droplet, which can be derived from the experimental conditions: partial pressures of the precursors, temperature, gas flow rates, etc.

The model also predicts the existence of a *critical point*, characterized by the growth temperature and a particular composition of the liquid droplet (C_{Si}, C_{Ge}). This thermodynamic point is determined by the equilibrium of the liquid phase with solid Si, Ge, and SiGe, simultaneously. The model shows that when the growth process takes place near this point, the transition from one material to the other is more abrupt. This is coherent with the strategy of reducing the material solubility since states closer to equilibrium correspond to lower material concentrations in the liquid phase. Furthermore, the proposed methodology can be applied to any other materials following the same dynamics by simply substituting the corresponding material parameters on the chemical potentials.

The model is described with full detail in the attached paper: *Growth dynamics of SiGe nanowires by the Vapour Liquid Solid method and its impact on SiGe/Si axial heterojunction abruptness* (P6).

Growth dynamics of SiGe nanowires by the Vapour Liquid Solid method and its impact on SiGe/Si axial heterojunction abruptness

J. L. Pura[1], P. Periwal[2], T. Baron[2], and J. Jiménez[1]

[1] *GdS Optronlab, Dpt. Física de la Materia Condensada, ed. LUCIA Universidad de Valladolid, Paseo de Belén 19, 47011 Valladolid, Spain*

[2] *University Grenoble Alpes, LTM, F-38000 Grenoble, France and CNRS, LTM, F-38000 Grenoble, France*

Keywords: SiGe, Si, nanowires, heterojunctions, VLS, growth dynamics

Abstract

The Vapour Liquid Solid (VLS) method is by far the most extended procedure for bottom-up nanowire growth. This method also allows for the manufacture of nanowire axial heterojunctions in a straightforward way. To do this, during the growth process the precursor gases are switched on/off to obtain the desired change in the nanowire composition. Using this technique axially heterostructured nanowires can be grown, which are crucial for the fabrication of electronic and optoelectronic devices. SiGe/Si nanowires are compatible with Complementary Metal Oxide Semiconductor (CMOS) technology, this improves their versatility and the possibility of integration with the current electronic technologies. Abrupt heterointerfaces are fundamental for the development and correct operation of electronic and optoelectronic devices. Unfortunately, VLS growth of SiGe/Si heterojunctions does not provide abrupt transitions because of the high solubility of group IV semiconductors in Au, with the corresponding reservoir effect that precludes the growth of sharp interfaces. In this work, we studied the growth dynamics of SiGe/Si heterojunctions based on already developed models for VLS growth. A composition map of the Si-Ge-Au liquid alloy is proposed to better understand the impact of the growing conditions on the nanowire growth process and the heterojunction formation. The solution of our model provides heterojunction profiles in good agreement with experimental measurements. Finally, the in-depth study of the composition map provides a practical approach to reduce drastically the heterojunction abruptness by reducing the Si and Ge concentrations in the catalyst droplet. This converges with previous approaches that use catalysts aiming to reduce the solubility of the atomic species. This analysis opens new paths to reduce the heterojunction abruptness using Au catalysts, but the model can be naturally extended to other catalysts and semiconductors.

1 Introduction

Heterostructured semiconductor nanowires (NWs) are the building blocks of the future nanodevices. In particular, axially heterostructured NWs promise new devices in electronics, [1, 2] photonics [3] and thermoelectric conversion, [4] among other applications. A key issue concerns the control of the heterojunctions, which is crucial to the performance of those devices. Generally, one needs abrupt interfaces for the optimal operation of the devices, [5] especially those that rely on quantum wells and quantum confinement effects. [6, 7]

Most semiconductor NWs are grown in a bottom up approach by means of the Vapour Liquid Solid (VLS) technique.[8] In VLS the constituent elements of the NW are incorporated to a metallic droplet (catalyst) forming a supersaturated liquid alloy, from which epitaxial layer by layer deposition at the solid (NW)/ liquid (catalyst droplet) interface takes place. The growth rate is governed by the difference of chemical potentials of the constituent elements between their liquid and solid phases. Axially heterostructured NWs are very promising for growing complex devices with multi-junctions, [9] suitable for one-dimensional electronic and optoelectronic devices. Axially heterostructured NWs are manufactured by switching off/on the vapour phase reactants during the VLS growth. [10] These heterostructured NWs have been grown with different combinations of III-V compounds, III-Vs and Si, and also group IV semiconductors, like Si/Ge and Si/SiGe heterojunctions. While sharp heterointerfaces have been reported for III-V heterostructured NWs,[11, 12] group IV NW heterointerfaces are more gradual, forming a relatively broad compositionally graded transition between the two extreme compositions of the NW.[13] However, atomically abrupt Si/SiGe interfaces have been recently achieved by using other methods or catalysts like Sn catalysed solvent vapour (SVG) growth (VLS) [14] or Au/Al [15] and Ag/Au [16] catalysed vapour solid solid (VSS) growth. Such a different behaviour between III-V and group IV axially heterostructured NWs has been related to the different solubilities of the constituent elements in the metallic droplet.[17] The high solubility of Ge and Si in Au results in a reservoir effect of those atomic species in the catalyst droplet. After switching off the reactant gas source, the remaining atomic species still continue to be deposited until they reach equilibrium. As a result, the deposition of the remaining atomic species should prevent step-like interfaces. For III-V semiconductors, the low solubility of the column V elements in the catalysts droplet suppresses the reservoir effect by a great amount, which will result in much sharper heterointerfaces. In recent work, we have shown that axially heterostructured Si/SiGe NWs present potential qualities for photon engineering. Indeed, a strong enhancement of the optical absorption/ scattering at the heterojunction of these NWs was observed by Raman spectroscopy.[18, 19] Electromagnetic calculations suggest that the absorption/scattering by the axially heterostructured NWs can be tuned by engineering the heterointerfaces. This opens an interesting way for photon harvesting based on the control of the composition of axial NW heterointerfaces. Heterostructured Si/SiGe NWs present two different heterointerfaces: SiGe/Si and Si/SiGe in growth direction, labelled trailing and leading interfaces, respectively. The interface abruptness refers to the width of the transition region between the two homogeneous segments of the NW. The growth mechanisms for axially heterostructured NWs are far from being fully understood, in spite of the existence of a few models that roughly fit the scarce experimental data concerning the abruptness of the axial NW heterojunctions. We present herein an analysis of the growth of both trailing and leading heterointerfaces in axially heterostructured Si/SiGe NWs. Our study is based on already developed models, from which we establish a full composition growth map describing the formation of the heterointerfaces in Au catalysed VLS Si/SiGe NWs.

2 Growth Model

Alloyed SiGe NWs are grown by the VLS method using SiH4 and GeH4 vapour reactants. The reactants diffuse onto the Au droplet surface and dissociate releasing the constituents in the liquid droplet, then they diffuse towards the liquid-solid interface. The growth of axial heterointerfaces is obtained by switching-off/on the gas sources of the reactants according to the desired compositional change. However, a sudden switch of the reactant flux is not synonymous of an abrupt interface, because the remaining atomic species solved in the droplet at the instant of the switch-off are still in supersaturation and will keep being deposited at the liquid-solid interface. As the heterojunction starts growing a compositionally graded transition takes place as far as the excess atoms in the droplet are deposited and

progressively replaced in the metallic droplet by the constituent atoms forming the next NW segment. A discussion about the abruptness of the heterointerfaces and the consequences of the reservoir effect in the catalyst droplet can be found in [20, 21]. However, the analysis of the heterointerfaces and the growth conditions for controlling them is still a matter of controversy. Our model is based on layer-by-layer growth without considering details about the layer nucleation and the monolayer growth dynamics. For detailed analyses of these aspects see Refs. [22–26]. Here, we will focus on gold catalysts, which are by far the most commonly used. Anyway, the model can be easily extended to other metals. For the development of the model we have applied the growth principles described in Refs. [17, 20]. In this model the growth rate of a monolayer (ML) at the solid-liquid interface is proportional to the difference in the chemical potentials of the liquid and the solid alloy phases. Therefore, the deposition rates of pure Ge and pure Si can be written as

$$v_{Ge}^{(i)} = \Gamma_{Ge}\Delta\mu_{Ge}^{(i)} \quad ; \quad v_{Si}^{(i)} = \Gamma_{Si}\Delta\mu_{Si}^{(i)} \qquad (1)$$

Where $\Delta\mu_{Ge(Si)}$ is the difference between the chemical potentials of the liquid and solid phases for Ge and Si, respectively. The kinetic parameters, Γ_{Ge} and Γ_{Si}, are related to the equilibrium concentration of the corresponding atomic species, therefore, they are basically determined by the solubility of each element in Au. According to this, we can define a parameter $B = \Gamma_{Si}/\Gamma_{Ge}$, which should be smaller than 1 because of the higher solubility of Ge than Si in Au.

The discrete index i numbers the successive monolayers forming the interface, because in the heterointerface the Ge concentration is gradually varying from each ML to the next one. As Si and Ge concentrations in the catalyst droplet are changing, the composition of each ML will depend on the composition of the precedent one. The chemical potentials of the solid phase and the kinetic parameters might slightly vary depending on the ML position at the heterointerface, because of the concentration variation. In our calculations, we assume that both parameters do not depend on the ML position for a sake of simplicity, but also because of the lack of data about its dependence with the composition. Accordingly, the Ge concentration of the i-th layer can be calculated as:

$$x_i = \frac{v_{Ge}^{(i)}}{v_{Ge}^{(i)} + v_{Si}^{(i)}} = \frac{\Gamma_{Ge}\Delta\mu_{Ge}^{(i)}}{\Gamma_{Ge}\Delta\mu_{Ge}^{(i)} + \Gamma_{Si}\Delta\mu_{Si}^{(i)}} = \\ = \frac{1}{1 + B\frac{\Delta\mu_{Si}^{(i)}}{\Delta\mu_{Ge}^{(i)}}} \qquad (2)$$

The chemical potentials are calculated according to the Glas model [27] for the III-V NW growth based on the Stringfellow ternary phase diagrams, [28] and adapted to the SiGe alloy system as:

$$\Delta\mu_k^{(i)} = \mu_k^{pL} + k_B T \ln C_k^{(i)} + \omega_{kj}\left[C_j^{(i)}\right]^2 + \\ + C_j^{(i)} C_{Au}(\omega_{kj} + \omega_{kAu} - \omega_{jAu}) - \mu_j^S \qquad (3)$$

Where C_{Si} and C_{Ge} are the Si and Ge concentrations in the liquid droplet, while $C_{Au} = (1 - C_{Si} - C_{Ge})$ is the Au concentration. μ_k^{pL} and μ_k^S are, respectively, the chemical potentials of the pure liquid and pure solid phases. The ω parameters account for the interatomic interactions in the liquid phase and are given by:

$$\omega_{\alpha\beta} = \frac{1}{N_A}\frac{V_\alpha V_\beta}{C_\alpha V_\alpha + C_\beta V_\beta} \times \\ \times \left[(\delta_\alpha - \delta_\beta)^2 - F\frac{(\chi_\alpha - \chi_\beta)^2}{(V_\alpha V_\beta)^{1/2}}\right] \qquad (4)$$

where $V_\alpha = M_\alpha/\rho_\alpha N_A$ is the molar volume and $M_\alpha, \rho_\alpha, \chi_\alpha, \delta_\alpha$ denote molar mass, density, Pauling electronegativity, and Hildebrand solubility parameter of species α and β, respectively, N_A is the Avogadro number, and $F = 1.256 \times 10^5$ if all quantities are in SI units. The solubility parameter δ_α is taken as: $\delta_\alpha = [(\Delta H_\alpha^{at} - RT)/V_\alpha]^{1/2}$ here ΔH^{at} is the molar heat of atomization. All other coefficients except μ_k^S can be found in reference books. [22, 27, 29] The numerical values of the parameters used in our calculations can be found in the supporting information S1. The unknown values of $\mu_{Si/Ge}^{pL}$ and $\mu_{Si/Ge}^S$ were fixed by the conditions that the corresponding difference of chemical potential is zero at the equilibrium concentration of Si/Au and Ge/Au alloys respectively. Therefore, we put $\Delta\mu_{Si} = 0$ at $C_{Ge} = 0$, $C_{Si} = 0.22$, $C_{Au} = 0.78$, and $\Delta\mu_{Ge} = 0$ at $C_{Si} = 0$, $C_{Ge} = 0.35$ and $C_{Au} = 0.65$ at the growth temperature $T = 450°C$.[29] Thus $\mu_{Si/Ge}^S$ are approximately taken as independent of i, i.e. independent of the layer composition.

The heterointerface width in a transition from $Si_{(1-x)}Ge_x$ to Si is calculated as the distance between the monolayers with Ge concentrations $x = (1-\delta)x_0$ and $x = \delta x_0$, for $\delta = 0.1$, where x_0 is the Ge concentration of the homogeneous SiGe segment. By solving this model we can establish a complete description of the growth of both heterointerfaces, leading and trailing, allowing to select the experimental growth conditions required for obtaining a predefined heterointerface abruptness.

3 Results

In order to understand the growth of the interfaces we will analyse the growth dynamics in a continuous compositional change. First, we start by studying the Ge concentration of the NW solid phase x, as a function of Si and Ge concentrations in the liquid droplet, C_{Si} and C_{Ge}, Eq. (2). A 3D representation of this magnitude can be seen in Figure 1.

Figure 1 shows the growth concentration of the solid phase, x, as a function of both Si and Ge concentrations in the liquid droplet. We can observe

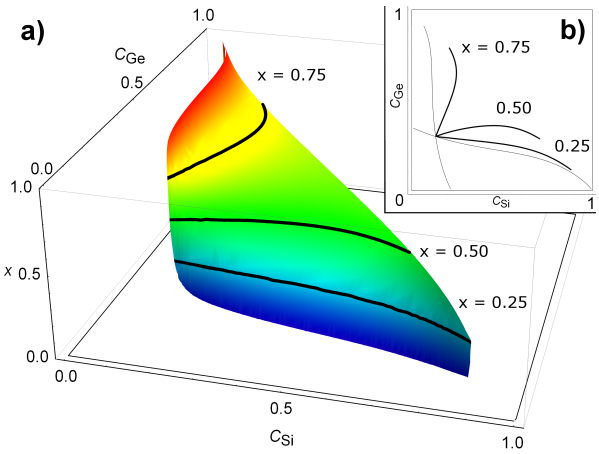

Figure 1: a) 3D map of the NW growing composition, x, as a function of Si and Ge concentrations in the Au catalyst droplet. The black curves represent the pairs of concentrations resulting in the same solid phase composition x, three of them are plotted as an example: $x = 0.25$, $x = 0.50$ and $x = 0.75$ from bottom to top. b) Plane projection of Figure 1a, showing the previously mentioned curves, and the limiting curves for $x = 0$ and $x = 1$ (gray curves).

two limiting regions: one for x approaching 1 (red colour in the 3D plot), which corresponds to low C_{Si}, close to the pure Ge NW growth. The other limiting region appears for x approaching 0 (blue colour in the 3D plot), which corresponds to low C_{Ge} values approaching the pure Si growth. These two limiting regions are described by two curves in the (C_{Si}, C_{Ge}) plane, corresponding to the liquid-solid equilibrium for Si and Ge, respectively. These curves can be easily computed by finding the concentrations at which $\Delta\mu_{Si} = 0$, no Si deposition ($x = 1$ in the solid phase); and $\Delta\mu_{Ge} = 0$, no Ge deposition ($x = 0$ in the solid phase). Between these two limiting curves there is a curve for each growing composition ranging from 0 to 1. These curves represent the degenerated pairs of Si and Ge concentrations in the liquid phase that result in the growth of the same Ge concentration in the solid phase. Three of these curves are plotted in Figure 1 as an example ($x = 0.25$, 0.50 and 0.75).

Figure 2 shows a projection of Figure 1 on the $C_{Ge} - C_{Si}$ plane where we can see the two equilibrium curves as well as the curve for x = 0.5, providing us with a composition map for the growth of the heterointerface of a $Si_{1-x}Ge_x$/Si NW for a concentration $x = 0.5$, which will be used as an example. It is important to note that the Au droplet remains in liquid state regardless of the Si and Ge concentrations, also, the total number of Au atoms in the droplet is assumed to remain unchanged during the growth process. Remind that any significant Au losses in the catalysts droplet will modify the growth dynamics and induce NW diameter changes.

The two curves corresponding to $\Delta\mu_{Si} = 0$ (red) and $\Delta\mu_{Ge} = 0$ (blue) define four regions in the (C_{Si}, C_{Ge}) plane, numbered I to IV.

Region I is the region of interest for the heterostructured NW growth purposes, where the liquid Au/Si/Ge alloy (L) coexists with the $Si_{1-x}Ge_x$ solid phase (S($Si_{1-x}Ge_x$)) of a certain concentration x (L + S($Si_{1-x}Ge_x$)). In region II $\Delta\mu_{Si} < 0$, then Si tends to dissolve in the droplet and cannot be deposited in the solid phase, therefore, only the Ge NWs can be grown for such low Si concentration (L + S(Ge)). Region III is the analogue to region II, but interchanging Si and Ge roles (L + S(Si)). Finally, in region IV the liquid phase is thermodynamically more stable for both Si and Ge, and there is no nucleation of the solid phase (L). This plot conforms a composition map for the growth of $Si_{1-x}Ge_x$ NWs at 450 °C.

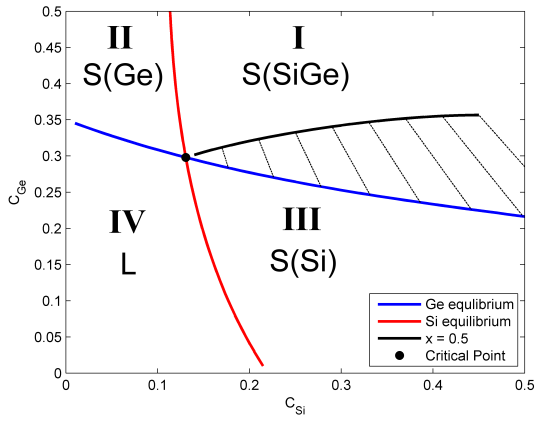

Figure 2: Composition map of the Au/Si/Ge alloy, as a function of Si and Ge concentrations in the liquid phase. Note that the region of interest is that of $C_{Si} + C_{Ge} \leq 1$, however only the region near the critical point is represented since it contains all the relevant information.

It is important to note the existence of a critical point, defined by the intersection of the two equilibrium curves, which is located at coordinates $(C_{Si}, C_{Ge}) \approx (0.1307, 0.2980)$. This point corresponds to the perfect equilibrium between liquid and solid phases of both atomic species. The simultaneous equilibrium of Si and Ge implies the equilibrium of two phases: the $Si_{1-x}Ge_x$ solid phase for any composition, x, and the liquid Au/Si/Ge alloy. According to this, fast compositional transitions shall occur with only little changes in the concentration when the system is in the vicinity of this critical point. This will directly affect the interfacial abruptness as we will see later on.

Now, we will analyse the two types of heterointerfaces: the trailing one, in which SiGe is growing and the Ge flow is switched off, and the leading one in which pure Si is growing and the nominal Ge flow is restored.

3.1 Trailing HJ

The so called trailing HJ profile corresponds to the heterointerface resulting from the transition from $Si_{1-x}Ge_x$ to pure Si. It is frequently claimed that the trailing HJ should be relatively extended because of the reservoir effect due to the high solubility of Ge in liquid Au. However, it should be noted that Ge stops its deposition once the Ge concentration in the droplet is under the saturation value. In this context, pure Si means that traces of Au and/or Ge might be present in the Si segment by stochastic incorporation, but in very low concentrations, $< 1\%$, which do not alter the Si structure. The exact concentration of Ge in the Si segment is not easy to calculate; however, we can make a rough estimation assuming that the adsorption and desorption probabilities of the Ge atoms on the solid phase are similar once the Ge is under saturation in the metal droplet. In this case, we can expect, on average, the incorporation of one Ge atom per bilayer as an upper bound, which results in a Ge/Si concentration ratio around 10-5 for a NW with 100 nm diameter.

According to the composition map of Figure 2, during the growth of the homogeneous $Si_{1-x}Ge_x$ segment the system is located at a certain point of the curve corresponding to concentration x (black line in Figure 2 for $x = 0.5$). The exact point on such curve will depend on the growth conditions, i.e. on the amount of Si and Ge dissolved in the Au droplet. This amount is determined by the Si and Ge fluxes and also their corresponding solubilities in the catalysts droplet, which depend on temperature and pressure. Once the Ge source is switched-off, the Ge in the catalysts droplet will keep being deposited, but no more Ge is fed into the droplet from the vapour phase. This will progressively reduce the Ge concentration in the droplet, following one of the dashed curves of Figure 2, until the Ge equilibrium curve is reached (blue curve in Figure 2), beyond this point no more Ge is deposited. On the other hand, the relative Si concentration will slightly increase during the transition, because of the reduction of the total amount of Ge atoms in the droplet, which are progressively replaced by Si atoms. Once the Ge equilibrium concentration is reached the Ge deposition stops, even if there is still Ge in the catalyst droplet; this dynamics would result in a trailing HJ sharper than expected if Ge in the droplet was exhausted. In fact, the analysis of the catalyst droplet still evidences the presence of Ge, once the Ge source was switched-off, and the Si segment was grown. [30] The droplet composition dynamics can be summarized in the following two equations

$$C_{Ge}^{i+1} = C_{Ge}^{i} - x_i(C_{Si}^{i}, C_{Ge}^{i})\frac{3h}{d} \tag{5}$$

$$C_{Si}^{i+1} = C_{Si}^{i}\frac{(1 - C_{Ge}^{i+1})}{(1 - C_{Ge}^{i})} \tag{6}$$

Where h is the height of one SiGe monolayer $\approx 0.5nm$, d is the NW diameter, x_i the Ge composition of the i-th monolayer, and C_{Si} and C_{Ge} the Si and Ge concentrations on the liquid droplet. Eq. (5) describes the change in C_{Ge} as Ge is being deposited, Eq. (6) accounts for the change in C_{Si} as a result of the change in C_{Ge}. Given the initial conditions of the system (C_{Si}, C_{Ge}), the iterative solution of these two equations provides the composition profile of the transition from SiGe to Si.

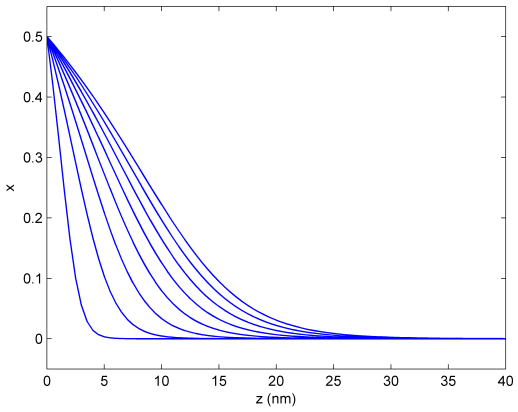

Figure 3: Calculated composition profiles of several trailing HJs as a function of the position along the growing direction z (NW axis). Each curve corresponds to one of the dashed lines of Figure 2, with the most abrupt profiles corresponding to initial conditions near the critical point.

Figure 3 shows a series of trailing HJ profiles from x = 0.5 ($Si_{0.5}Ge_{0.5}$ NW segment) to $x = 0$ (Si segment) calculated for different starting points along the $x = 0.5$ curve (black line in Figure 2), $B = 0.5$ and $d = 100nm$. The calculated heterointerface composition profiles correspond to the transitions from the black line of Figure 2 to the Ge equilibrium curve (blue), each process takes place along one of the black dashed lines in Figure 2. One can observe that the abruptness of the heterointerface strongly depends on the starting point over the black line, which is determined by the growth conditions, mainly Si and Ge fluxes, however all the conditions derived here will depend on the selected temperature and pressure. The HJ becomes broader as the starting point moves away from the critical point. This behaviour shows a way to tailor the HJ sharpness, it also shows the possibility of creating abrupt SiGe/Si heterointerfaces with extensions of only a few nanometres by adjusting the growth conditions as closer as possible to the critical point during VLS growth.

3.2 Leading HJ

The leading HJ is the opposite of the trailing HJ, the NW growth is switched from Si to $Si_{1-x}Ge_x$. In this case the system is located at a certain point below the Ge equilibrium curve (no Ge deposition), as a result only Si is being deposited in the solid phase (L + S(Si) equilibrium). Once the Ge source is switched-on, the Ge concentration in the liquid droplet increases up to supersaturation, then the system starts moving to the equilibrium curve of the target composition. The composition dynamics are the same as that of the trailing case, Eq. (5), but one has to take account of the dependence of C_{Ge} with the incoming Ge flux, ϕ_{Ge}. This term can be easily calculated because we know that the composition variation when the equilibrium curve is reached must be zero, i.e. $C_{Ge}^{i+1} = C_{Ge}^{i}$ and $\phi_{Ge} - x_0 \frac{3h}{d} = 0$, so it can be simply replaced by a term proportional to the final composition x_0

$$\begin{aligned} C_{Ge}^{i+1} =& C_{Ge}^{i} + \phi_{Ge} - x_i(C_{Si}^{i}, C_{Ge}^{i})\frac{3h}{d} = \\ =& C_{Ge}^{i} + (x_0 - x_i(C_{Si}^{i}, C_{Ge}^{i}))\frac{3h}{d} \end{aligned} \quad (7)$$

Si concentration, C_{Si}, follows Eq. (6).

The paths followed by the system are analogous to those of the trailing case but the system moves along them in the opposite direction, from the blue curve to the black one.

The simulated leading heterointerface profiles for a composition $x = 0.5$ are plotted in Figure 4 (same B and d values as for the trailing case, Figure 3), showing that also the leading heterointerface becomes sharper as the growth conditions approach the critical point.

Note the different profiles of the trailing and leading heterointerfaces, consequence of the different starting points. While the reservoir effect governs the trailing interface, showing initially a slow decrease of the Ge concentration followed from a faster decrease, the leading heterointerface evidences a continuous increase of the Ge concentration. Note that both interfaces start from opposite situations, the trailing heterointerface departs from a Ge supersaturation situation, while the leading heterointerface starts from a Ge subsaturation situation,

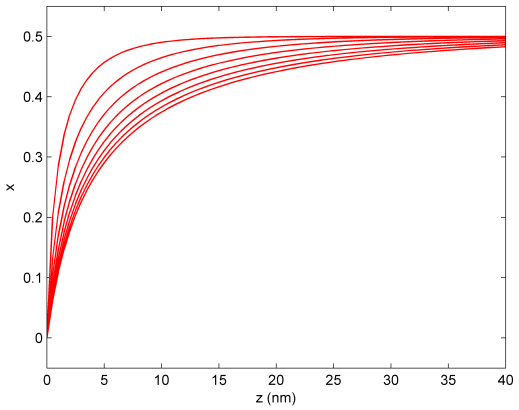

Figure 4: Composition profiles of several leading HJs as a function of the position along the growing direction (NW axis). Each curve corresponds to one of the dashed lines of Figure 2, with the most abrupt profiles corresponding to initial conditions near the critical point.

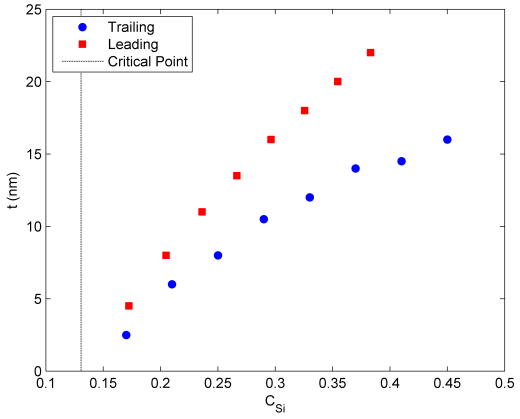

Figure 5: Widths of the trailing and leading HJs as a function of the initial Si concentration in the liquid droplet. The trailing HJ is sharper than the leading HJ for all values of C_{Si}, and they converge at the critical point, which corresponds to an ideally abrupt transition for both interfaces.

this difference results in distinct growth dynamics, therefore, distinct composition profiles across the heterointerface.

We have shown that the expected HJ widths are in both cases narrower than usually assumed. Figure 5 summarizes the data of Figures 3 and 4. It shows the leading and trailing HJ widths for $B = 0.5$ as a function of the Si concentration in the catalyst droplet, i.e. the initial position along the $x = 0.5$ curve. We see that both trailing and leading HJs become more abrupt as the initial state of the system approaches the critical point. Furthermore, close to the critical point both heterointerfaces present almost similar abruptness tending to zero, while departing away from the critical point, the heterointerfaces become more gradual. In all cases the trailing transition is more abrupt than the leading one, considering that the growth temperature and chamber pressure are kept constant, and the NW diameter does not change all along the growth run.

On the other hand, Figure 6 summarizes the dependence of both leading and trailing heterointerfaces widths with respect to the B parameter. We see that for all values of B the trailing heterointerface is sharper than the leading one, assuming the same pressure and temperature conditions for both heterointerfaces. Moreover, we know that the values of B must be smaller than unity because of the higher solubility of Ge in Au, which results in HJ mean widths narrower than 30 nm according to Figure 6.

4 Experimental Measurements

In order to check the validity of the theoretical model, energy dispersive X-ray spectroscopy (EDX) measurements were carried out on SiGe/Si/SiGe heterostructured NWs. [31] For this, a field emission scanning electron microscope (FESEM) FEI Quanta 200FEG was used. The EDX profiles of the HJs allow us to have a measurement of the HJ width. However, these measurements have a great number of error sources. First, the electron beam drift due to charge localization in the NW can induce a relative error of up to 50 % of the distance measured during the profile acquisition. Secondly, the electron beam diameter, which depends on several parameters, mainly on acceleration voltage and aperture size. For our experimental conditions, 10 kV, the expected beam diameter is $\approx$ 4 nm. Furthermore, when the beam reaches the sample it broadens, in our experiment the beam is expected to change from 4 nm in the NW surface to $\approx$ 6 nm on the opposite side of the NW, according to the material properties and NW diameter. The magnitude of the errors does not allow for a reli-

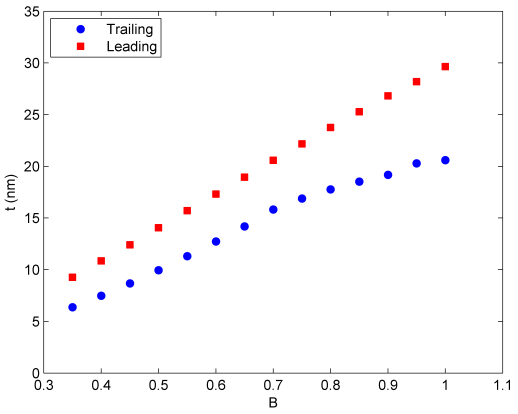

Figure 6: Trailing and leading HJ mean widths as a function of B parameter for $x = 0.5$ and $d = 100$ nm.

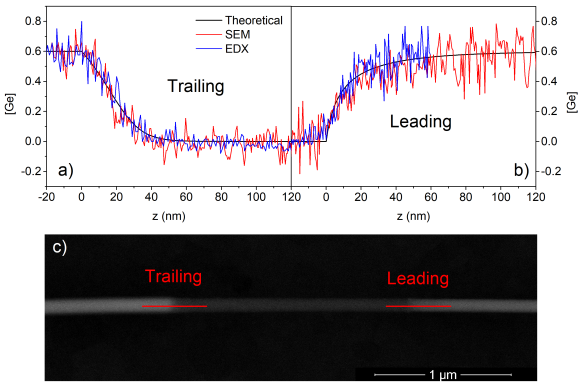

Figure 7: Rescaled backscattered SEM and EDX profiles of a trailing (a) and leading (b) HJs compared with the theoretically calculated profiles. c) Backscattering SEM image of a SiGe/Si/SiGe axially heterostructured NW ($d \approx 100$ nm) showing the trailing and leading HJs and the region of the profiles plotted in (a) and (b). It is important to note that the EDX profile is acquired in a continuous measurement for both trailing and leading HJ, this ensures that both are comparable even after the rescale process.

able measurement of the HJ width with these techniques. However, since the principal (and less controllable) source of errors is the beam drift we can still obtain qualitative information and check the validity of the modelled HJ profiles. If we rescale the distance of the EDX and backscattering scanning electron microscopy (SEM) profiles obtained from SiGe/Si/SiGe axially heterostructured NWs we can compare them with the theoretically calculated profiles, Figure 7.

We see that the experimental measurements follow the theoretical profiles in both leading and trailing HJs, and also for the two types of recorded signals, backscattered SEM and EDX. All the analysed NWs presented similar profiles with only subtle variations and all of them followed the theoretical profiles. In all cases the trailing HJ appears to be sharper than the leading one. We should also note that two behaviours predicted by the model are observed in all the experimentally analysed NWs. First, the trailing HJ does not start with an exponential decay, but initially, in an extension of a few nanometres, a slower decrease is observed, later followed by an exponential decay. Second, an opposite effect is observed in the leading HJ. Initially, the incorporation of Ge to the solid phase is faster, and near equilibrium it shows an exponential approximation to the composition target slower than initially expected. This effect appears as a result of the non-linearity of Eqs. (1) - (4). Further details about the profile shape can be found in the supporting information S2.

5 Discussion

It has been claimed that the Si/SiGe heterointerface width using Au catalyst droplets must have an extension equivalent to the NW diameter. This assertion is based on the reservoir effect, in which the Ge solved in the droplet continues to be deposited until exhaustion once the Ge flux has been switched off. Upon this mechanism, the extension of the graded heterointerface would be determined by the ratio between the droplet volume and the interface surface giving a graded interface width of around one diameter.[17] The reservoir effect must be reconsidered on the bases of the growth model developed here. In this model the Ge solved in the droplet is not exhausted, but it stops depositing once the equilibrium concentration of Ge in the droplet is reached, blue curve in Figure 2. This means that for the case represented in Figure 2 ($x = 0.5$), the deposited amount of Ge corresponds to the difference between the black and blue curves. Therefore, in the most unfavourable case a concentration fraction of ≈ 0.1 of Ge in the droplet is deposited, see the difference between the black and blue curves on the right side of Figure 2, while

the rest of the Ge is under saturation and remains stored in the droplet.

If we balance the total Ge in the droplet that is deposited during the growth of the heterointerface, and the dimensions of the droplet and the heterointerface we can establish a simple relation between the heterointerface width and the diameter of the NW. Let assume that the difference of Ge being in the droplet right before and after the compositional transition is the one deposited in the HJ region. The Ge deposited in the HJ must equal the Ge leaving the droplet, therefore, the density of Ge atoms in the droplet susceptible to be deposited (n_d) times the droplet volume should equal the mean density of Ge atoms in the HJ (n_{HJ}) times its volume. For the HJ region the mean value will be roughly half of the Ge concentration in the homogeneous segment, ≈ 0.25 in this example. If t is the HJ thickness and d the droplet diameter the Ge conservation reads as

$$n_d V_d = n_{HJ} V_{HJ} \rightarrow 0.1 \frac{1}{2} \frac{4}{3} \pi r^3 = 0.25 t \pi r^2$$
$$t = \frac{2r}{7.5} = \frac{d}{7.5} \quad (8)$$

The HJ thickness is still proportional to the NW diameter, but the proportionality factor is sensitively smaller than unity. For a 100 nm NW we can see that the estimation, $t = 13.33$ nm, is in good agreement with the model calculations, Figure 5, also in good agreement with other experimental measurements. [32]

6 Conclusions

A systematic study of the VLS growth of axially heterostructured Si/SiGe NWs has provided information about the growth dynamics of axial heterojunctions. We show that both trailing and leading Si/SiGe heterojunctions can be narrower than usually claimed. Moreover, the existence of a critical point in the Au/Si/G alloy composition map shows a path to tailor the heterojunction width by changing the growth conditions (gas flows, temperature, pressure, etc). The heterojunction becomes narrower as the growing conditions approach the critical point. In practice, lowering both Si and Ge concentrations in the liquid droplet should allow to produce sharper heterojunctions. This is in good agreement with the dynamics observed in III-V heterojunctions, where the low solubility of one of the constituents makes the abrupt heterointerfaces the natural process for those semiconductor NWs. In practice, the effect of selecting the growth conditions near the critical point, i.e. low Ge concentration, is equivalent to the natural low solubility of group V elements, a reduced amount of Ge in the droplet results in a more abrupt transition.[24] It also converges with the use of catalysts aiming to reduce the solubility of the atomic species. [14–16, 32] Finally, the model results were compared with experimental measurements, obtaining a very good agreement from both quantitative and qualitative points of view.

Achnowledgements

This work was funded by Junta de Castilla y León (Projects VA293U13, and VA081U16), and Spanish Government (CICYT MAT2010-20441-C02 (01 and 02) and ENE 2014-56069-C4-4-R). J L Pura was granted by the FPU programme (Spanish Government) (FPU14/00916).

Supporting Information

Table with all the parameters used in the model. Logarithmic plot of the calculated heterojunction profiles showing the exponential and non-exponential behaviours of the growth mechanism.

References

[1] Y. Li, F. Qian, J. Xiang, C. M. Lieber. Nanowire electronic and optoelectronic devices. *Materials Today*, **9** (10), 18–27 (2006). doi:10.1016/S1369-7021(06)71650-9

[2] C. Thelander, P. Agarwal, S. Brongersma, J. Eymery, L. F. Feiner, A. Forchel, M. Scheffler, W. Riess, B. J. Ohlsson, U. Gösele, L. Samuelson. Nanowire-based one-dimensional electronics. *Materials Today*, **9** (10), 28–35 (2006). doi:10.1016/S1369-7021(06)71651-0

[3] R. Yan, D. Gargas, P. Yang. Nanowire photonics. *Nature Photonics*, **3** (10), 569–576 (2009). doi:10.1038/nphoton.2009.184

[4] A. I. Boukai, Y. Bunimovich, J. Tahir-Kheli, J. K. Yu, W. A. Goddard, J. R. Heath. Silicon nanowires as efficient thermoelectric ma-

terials. *Nature*, **451** (7175), 168–171 (2008). doi:10.1038/nature06458

[5] S. Jebril, H. Kuhlmann, S. Müller, C. Ronning, L. Kienle, V. Duppel, Y. K. Mishra, R. Adelung. Epitactically interpenetrated high quality ZnO nanostructured junctions on microchips grown by the vapor-liquid-solid method. *Crystal Growth and Design*, **10** (7), 2842–2846 (2010). doi:10.1021/cg100538z

[6] W. Pötz, Z. Q. Li. Imperfections and resonant tunneling in quantum-well heterostructures. *Solid-State Electronics*, **32** (12), 1353–1357 (1989)

[7] S. Cosentino, a. M. Mio, E. G. Barbagiovanni, R. Raciti, R. Bahariqushchi, M. Miritello, G. Nicotra, A. Aydinli, C. Spinella, A. Terrasi, S. Mirabella. The role of the interface in germanium quantum dots: when not only size matters for quantum confinement effects. *Nanoscale*, **7** (26), 11401–11408 (2015). doi:10.1039/c5nr01480h

[8] R. Wagner, W. Ellis. Vapor-Liquid-Sold Mechanism of Single Crystal Growth. *Applied Physics Letters*, **4** (5), 89–90 (1964). doi:10.1063/1.1753975

[9] K. A. Dick, K. Deppert, M. W. Larsson, T. Mårtensson, W. Seifert, L. R. Wallenberg, L. Samuelson. Synthesis of branched 'nanotrees' by controlled seeding of multiple branching events. *Nature Materials*, **3** (6), 380–384 (2004). doi:10.1038/nmat1133

[10] L. J. Lauhon, M. S. Gudiksen, C. M. Lieber. Semiconductor nanowire heterostructures. *Philosophical transactions of the Royal Society A*, **362** (1819), 1247–1260 (2004). doi:10.1098/rsta.2004.1377

[11] M. S. Gudiksen, L. J. Lauhon, J. Wang, D. C. Smith, C. M. Lieber. Growth of nanowire superlattice structures for nanoscale photonics and electronics. *Nature*, **415**, 617–620 (2002). doi:10.1038/415617a

[12] M. T. Borgström, M. A. Verheijen, G. Immink, T. De Smet, E. P. A. M. Bakkers. Interface study on heterostructured GaP-GaAs nanowires. *Nanotechnology*, **17**, 4010–4013 (2006). doi:10.1088/0957-4484/17/16/002

[13] N. D. Zakharov, P. Werner, G. Gerth, L. Schubert, L. Sokolov, U. Gösele. Growth phenomena of Si and Si/Ge nanowires on Si (1 1 1) by molecular beam epitaxy. *Journal of Crystal Growth*, **290** (1), 6–10 (2006). doi:10.1016/j.jcrysgro.2005.12.096

[14] H. Geaney, E. Mullane, Q. M. Ramasse, K. M. Ryan. Atomically abrupt silicon-germanium axial heterostructure nanowires synthesized in a solvent vapor growth system. *Nano Letters*, **13** (4), 1675–1680 (2013). doi:10.1021/nl400146u

[15] C. Y. Wen, M. C. Reuter, J. Bruley, J. Tersoff, S. Kodambaka, E. A. Stach, F. M. Ross. Formation of compositionally abrupt axial heterojunctions in silicon-germanium nanowires. *Science*, **326** (5957), 1247–1250 (2009). doi:10.1126/science.1178606

[16] Y.-C. Chou, C.-Y. Wen, M. C. Reuter, D. Su, E. A. Stach, F. M. Ross. Controlling the Growth of Si/Ge Nanowires and Heterojunctions Using Silver-Gold Alloy Catalysts. *ACS Nano*, **6** (7), 6407–6415 (2012). doi:10.1021/nn301978x

[17] N. Li, T. Y. Tan, U. Gösele. Transition region width of nanowire hetero- and pn-junctions grown using vapor - liquid - solid processes. *Applied Physics A: Materials Science and Processing*, **90**, 591–596 (2008). doi:10.1007/s00339-007-4376-z

[18] J. L. Pura, J. Anaya, J. Souto, Á. C. Prieto, A. Rodríguez, T. Rodríguez, J. Jiménez. Local electric field enhancement at the heterojunction of Si/SiGe axially heterostructured nanowires under laser illumination. *Nanotechnology*, **27** (45), 455709 (2016). doi:10.1088/0957-4484/27/45/455709

[19] J. L. Pura, J. Anaya, J. Souto, A. C. Prieto, A. Rodríguez, T. Rodríguez, P. Periwal, T. Baron, J. Jiménez. Electromagnetic field enhancement effects in group IV semiconductor nanowires. A Raman spectroscopy approach. *Journal of Applied Physics*, **123** (11), 114302 (2018). doi:10.1063/1.5012987

[20] P. Periwal, F. Bassani, G. Patriarche, L. Latu-Romain, V. Brouzet, B. Salem, T. Baron. Interfacial abruptness in axial Si/SiGe heterostructures in nanowires probed

by scanning capacitance microscopy. *Physica Status Solidi (A) Applications and Materials Science*, **211** (2), 509–513 (2014). doi:10.1002/pssa.201300208

[21] P. Periwal, T. Baron, L. Latu-romain, B. Salem, G. Patriarche, P. Gentile. Control of the interfacial abruptness of Au-catalyzed Si-Si1-xGex heterostructured nanowires grown by vapor-liquid-solid. *Journal of Vacuum Science & Technology A: Vacuum, Surfaces, and Films*, **32** (3), 031101 (2014). doi:10.1116/1.4867264

[22] Y. C. Chou, K. Hillerich, J. Tersoff, M. C. Reuter, K. A. Dick, F. M. Ross. Atomic- Scale Variability and Control of III- V Nanowire Growth Kinetics. *Science*, **343**, 281–284 (2014). doi:10.1126/science.1244623

[23] A. D. Gamalski, C. Ducati, S. Hofmann. Cyclic supersaturation and triple phase boundary dynamics in germanium nanowire growth. *Journal of Physical Chemistry C*, **115** (11), 4413–4417 (2011). doi:10.1021/jp1095882

[24] C.-Y. Wen, J. Tersoff, M. C. Reuter, E. A. Stach, F. M. Ross. Step-flow kinetics in nanowire growth. *Physical Review Letters*, **105** (19), 195502 (2010). doi:10.1103/PhysRevLett.105.195502

[25] H. Wang, L. A. Zepeda-Ruiz, G. H. Gilmer, M. Upmanyu. Atomistics of vapour-liquid-solid nanowire growth. *Nature Communications*, **4**, 1956 (2013). doi:10.1038/ncomms2956

[26] B. A. Wacaser, K. A. Dick, J. Johansson, M. T. Borgström, K. Deppert, L. Samuelson. Preferential interface nucleation: An expansion of the VLS growth mechanism for nanowires. *Advanced Materials*, **21** (2), 153–165 (2009). doi:10.1002/adma.200800440

[27] F. Glas. Chemical potentials for Au-assisted vapor-liquid-solid growth of III-V nanowires. *Journal of Applied Physics*, **108** (7), 073506 (2010). doi:10.1063/1.3488908

[28] G. B. Stringfellow. Calculation of ternary phase diagrams of III-V systems. *Journal of Physics and Chemistry of Solids*, **33** (3), 665–677 (1972). doi:10.1016/0022-3697(72)90075-3

[29] T. B. Massalski. *Binary Alloy Phase Diagrams*. ASM International: Metals Park, Ohio, 2nd Auflage (1990). ISBN 978-0-87170-403-0

[30] T. E. Clark, P. Nimmatoori, K.-k. Lew, L. Pan, J. M. Redwing, E. C. Dickey. Diameter Dependent Growth Rate and Interfacial Abruptness in Vapor-Liquid-Solid Si/Si 1- x Ge x Heterostructure Nanowires. *Nano Letters*, **8** (4), 1246–1252 (2008). doi:10.1021/nl072849k

[31] P. Periwal, N. V. Sibirev, G. Patriarche, B. Salem, F. Bassani, V. G. Dubrovskii, T. Baron. Composition-Dependent Interfacial Abruptness in Au-Catalyzed Si 1-x Ge x /Si/Si 1-x Ge x Nanowire Heterostructures. *Nano Letters*, **14** (9), 5140–5147 (2014). doi:10.1021/nl5019707

[32] D. E. Perea, N. Li, R. M. Dickerson, A. Misra, S. T. Picraux. Controlling heterojunction abruptness in VLS-grown semiconductor nanowires via in situ catalyst alloying. *Nano Letters*, **11** (8), 3117–3122 (2011). doi:10.1021/nl201124y

Supporting Information

Magnitude	Value
ΔH^{at}_{Au}	366 kJ/mol
M_{Au}	196.97 g/mol
χ_{Au}	2.54
ρ_{Au}	17.31 g/cm^3
ΔH^{at}_{Ge}	377 kJ/mol
M_{Ge}	72.63 g/mol
χ_{Ge}	1.9
ρ_{Ge}	5.6 g/cm^3
ΔH^{at}_{Si}	456 kJ/mol
M_{Si}	28.97 g/mol
χ_{Si}	2.01
ρ_{Si}	2.57 g/cm^3

S1: List of all the parameters used in the model.

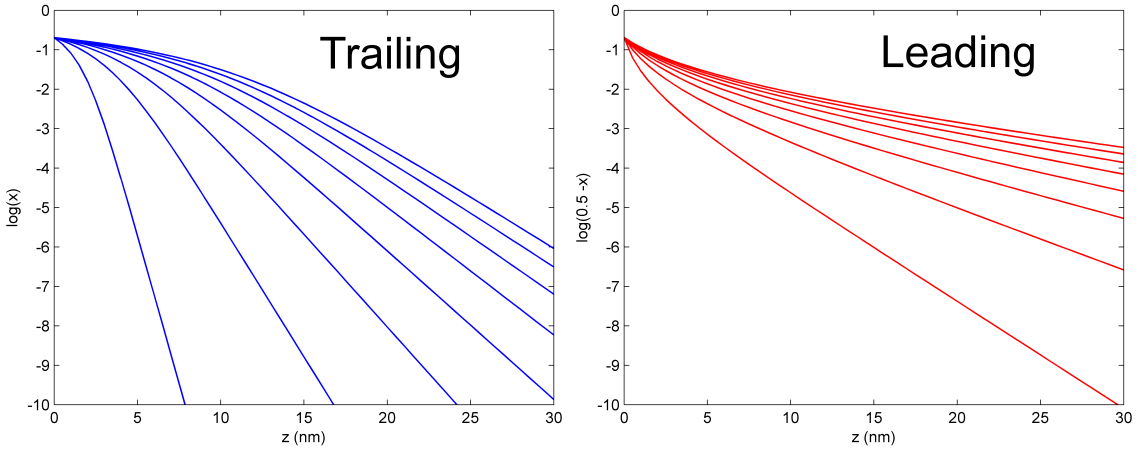

S2: Logarithmic plot of the calculated heterojunction profiles showing the exponential and non-exponential behaviours of the growth mechanism

P6

Chapter 7

Las estrellas están desordenadas
- Lírico -

Theoretical study of the light enhancement effect

This chapter is intended to delve into the underlying physics of the enhancement effect. We will focus on a deeper study of the EM field distribution, its components, and its causes, to understand why this effect emerges.

The results of this chapter are summarized in the paper *Fourier Transform Study of the Complex Electric Field Induced on Axially Heterostructured NWs* (P7). The EM field induced by a linearly polarized plane wave in different NWs was studied. First, the field distributions induced inside the NW are analysed by simple inspection of their profile and by a qualitative comparison in the case of a homogeneous NW and Si/SiGe heterostructured NWs of different lengths. The results demonstrate the enhancement of the incident field in the vicinity of the HJ region. After this, the Fourier Transform (FT) is used to obtain the main components of the field distributions. We should note that the Fourier Transform is performed with respect to the spatial coordinate (instead of the more common FT in the time component). As a result of this mathematical treatment, we will obtain the FT as a function of the wavevector (wavelength) rather than the frequency. For this analysis, plane wave excitation is preferred over the Gaussian beam in order to simplify the problem, because it presents only one Fourier component (one wavelength), while the Gaussian distribution results in another Gaussian profile in Fourier space. In the case of the Gaussian distribution, we obtain a convolution between the Gaussian profile and other components, hindering the interpretation of the results.

First, homogeneous Si NWs were investigated. The FT, in this case, shows a single Fourier component, which is symmetric in k-space. This component is associated with the fundamental mode of the incident plane wave. Then, SiGe/Si axially heterostructured NWs are studied using the same FT methodology. In this case, the FT shows a new component on its negative side, which is directly coupled with a symmetric reduction of the FT intensity at the opposite value of k on the positive axis, Figure 4 of P7. We associated this effect with a new antisymmetric component. This feature only appears on axially heterostructured NWs, which points to its origin as a contribution of the material discontinuity, the HJ.

Finally, the origin of both contributions is double checked through the study of their dependence on the incident light wavelength and the NW length. The results are displayed in Figure 5 of P7. The position of the symmetric component is independent of the NW length and only varies with the incident light wavelength. Conversely, the antisymmetric peak position changes with the NW length but it is independent of the incident wavelength. We can conclude that the presence of the HJ is adding a contribution to the EM field that modifies its distribution and is directly related to the discontinuity along the NW axis, showing a coupling with the longitudinal dimension: the NW length.

Fourier Transform Study of the Complex Electric Field Induced on Axially Heterostructured NWs

J. L. Pura[1,*] and J. Jiménez[1]

[1] *GdS Optronlab, Dpt. Física de la Materia Condensada, ed. LUCIA Universidad de Valladolid, Paseo de Belén 19, 47011 Valladolid, Spain*
[*] *jlpura@fmc.uva.es*

Keywords: nanowires, axial heterostructures, Fourier Transform, electromagnetic enhancement

Abstract

We present in this work a study of the effect of Raman enhancement on axially heterostructured nanowires (NWs). The investigation is motivated by the recent detection of a Raman signal enhancement effect at the heterojunction (HJ) of axially heterostructured NWs. Semiconductor NWs offer very interesting properties as compared to their bulk counterparts, making them the building blocks of future optoelectronic nanodevices. The use of HJs turns out to be essential for a great variety of devices. As a result, understanding the optical properties of heterostructured NWs is a fundamental step for their possible application on future technologies. In order to unveil the underlying physics of the light/NW interaction, the complex-valued electromagnetic (EM) field distribution induced inside heterostructured NWs under light exposure is studied. The use of the Fourier Transform is presented as a key tool in order to ascertain the different components of the EM field generated inside the NW. The results show the presence of two components: one associated with the incident light beam and a second one which appears as a consequence of the presence of the axial HJ. This second component explains the emergence of the Raman enhancement effect as a result of the interaction of the incident beam with the dielectric discontinuity associated with the HJ.

1 Introduction

A great amount of research is being devoted to semiconductor nanowires (NWs) aiming to the fabrication of nanoscale devices. Semiconductor NWs present advantages with respect to thin films, as the possibility of combining highly mismatched materials, which allows for the growth of structures that are not available as thin layer devices [1, 2]. Furthermore, NWs were shown to be very efficient optical emitters and colectors [3], which makes them suitable for the development of high-performance photovoltaic cells [4], sensitive light detectors [5, 6], electro-optic modulators [7, 8], and light sources [9–11], among other applications. As mentioned above, NWs present large flexibility to be assembled in complex structures; in particular, a large range of mismatched heterostructures can be grown free of defects, as compared to the limitations imposed to thin films by large lattice mismatches. As a prerequisite for the extended use of these heterostructured NWs in photonic devices one needs to understand the way in which they interact with light.

Geometrical optics applies to large objects, in this situation the absorption/scattering cross section is directly related with the geometrical cross section of the material, which results in absorption/scattering efficiencies between 0 and 1. However, when dealing with objects of subwavelength size the absorption/ scattering efficiencies can scale to values well above unity [12, 13]. As a consequence of the subwavelength dimension and the large dielectric mismatch between the NW and its environment the effective light collection area is larger than the geometrical section of the object, i.e. the NW behaves as an optical nanoantenna. Furthermore, the electromagnetic resonances reported for semiconductor NWs can enhance the electromagnetic field by orders of magnitude, which points to the great potential of semiconductor NWs for photonic applications.

Most of the research about the optical properties of NWs concerns homogeneous NWs. In this case, Mie theory applies to the light scattering by NWs under illumination perpendicular to its axis; meanwhile, vertically aligned NWs can support guided modes when illuminated parallel to its axis, even conforming Fabry-Perot cavities [14].

Complex structures based on heterojunctions (HJs) must be included in a great number of devices. Understanding the role of these HJs under light illumination is a crucial issue for their use in advanced photonic devices. In bulk materials, light/semiconductor interaction is solely governed by the refractive index; however, subwavelength diameter semiconductor NWs exhibit resonances related to other factors like their size, shape and composition [16, 17]. On the other hand, the scattering cross section of these systems strongly depends on the NW orientation with respect to the light polarization, another sign of the drastic difference between the NWs behavior and their bulk counterpart.

Luminescence emitters have been previously used to study this phenomenon. However, the spontaneous radiative emission in semiconductor NWs is sometimes suppressed by the surface recombination. Furthermore, luminescence emission, if any, is weak in the case of Si and SiGe NWs, all these factors make it difficult to quantify the changes in the spontaneous emission [18]. Unlike luminescence emission, Raman scattering is less sensitive to the surface state, moreover, it can be observed for any semiconductor and excitation wavelength, independently of their radiative recombination efficiency. Thus, Raman scattering can be used as an alternative way to study the interaction between light and complex heterostructured semiconductor NWs. For Raman scattering, the signal intensity is proportional to the electromagnetic field intensity, i.e. $|E|^2$, which allows studying the distribution of the radiation inside heterostructured systems.

The diameter dependence of the light scattering resonances can be explained in the Mie scattering framework, where the eigenfunctions of the Mie solution of Maxwell equations are coupled with the NW diameter, giving the Mie resonances [19, 20]. Usually, this approach is applied to infinite homogeneous NWs. Alternatively, finite element methods (FEM) can be used to solve the Maxwell equations of the system formed by the light and the finite NW. A significant body of research has been devoted to homogeneous infinitely long NWs, while, a detailed analysis of the interaction of light with finite length NWs and heterostructured NWs is still lacking.

Recently, we have reported a significant local enhancement of the Raman efficiency at the heterojunction of axially heterostructured Si/SiGe NWs [21, 22] and Si/InAs NWs [23]. This is an interesting issue since the enhancement of the electromagnetic field at the HJ of NWs should provide an additional degree of freedom to engineer the photon absorption and scattering by semiconductor NWs, which should permit to operate photons over dif-

ferent optical resonances. Nevertheless, further research effort is needed to understand this interaction.

We present herein an analysis of the semiconductor NW/ light interaction based in the numerical solution of the Maxwell equations by FEM of group IV NWs, in particular, homogeneous Si NWs and axially heterostructured Si/SiGe NWs. This study entails both plane wave illumination, and illumination with a focused laser beam allowing to reproduce the conditions of μ-Raman and μ-photoluminescence (PL) experiments.

2 Finite Element Method Model and Results

The FEM simulations were performed by using the Electromagnetic Waves in Frequency Domain module of COMSOL Multiphysics. The air/NW/substrate system is simulated using the same arrangement of the experimental measurements, i.e. the NWs are lying flat over an Al substrate, and the dimensions of the NWs (diameter, length, etc) were selected to match those of the typically investigated NWs. Further details about the FEM model can be found elsewhere [21, 22].

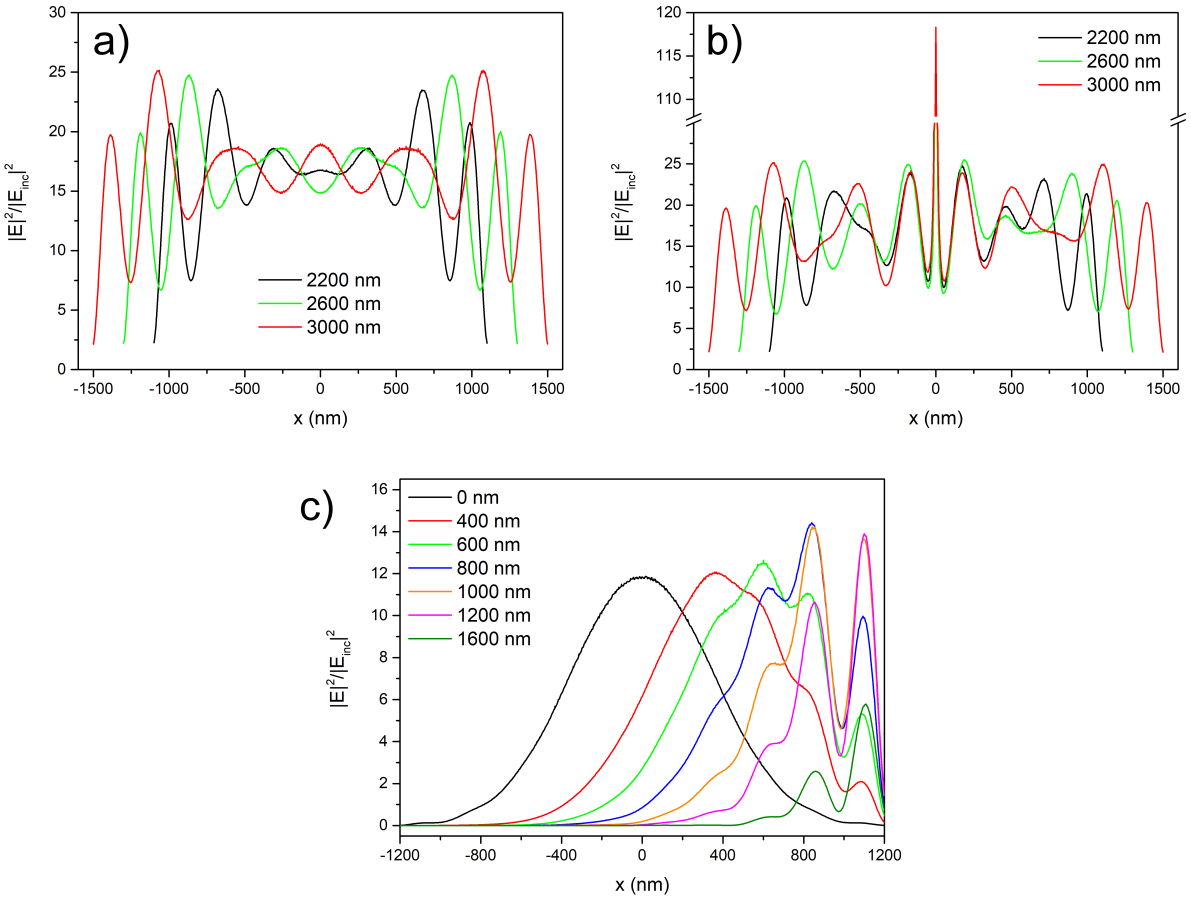

Figure 1: a) EM field distribution inside a homogeneous Si NW for different NW lengths and plane wave illumination. b) EM field distribution inside a SiGe/Si axially heterostructured NW for different NW lengths and plane wave illumination. c) EM field distribution inside a homogeneous Si NW under Gaussian beam illumination for different positions of the beam focus.

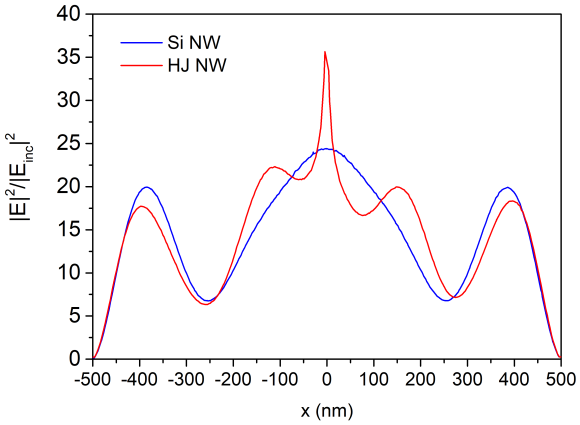

Figure 2: Distribution of the electric field modulus along the axis of a 1 μm Si NW and a 1 μm Si/SiGe heterostructured NW under 532 nm plane wave illumination.

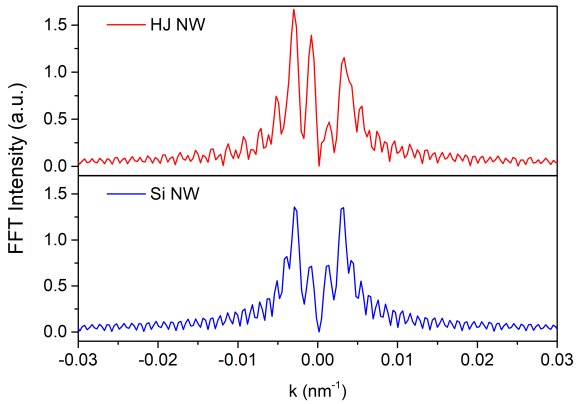

Figure 3: Fast Fourier Transform intensities obtained from the electric field profiles of Figure 2. There are 2 symmetric peaks on the Si NW that remain visible in the heterostructured NW. However the SiGe/Si NW presents a new asymmetric structure that results in a new peak on the negative side, and symmetrically lowers the FFT on the positive side. The symmetric peak can be associated with the principal component of the field, 532 nm light, while the antisymmetric one is induced by the presence of the HJ.

By using this model, a full 3D solution of the Maxwell equations was performed in order to ascertain the effect of the NW length and the presence of the axial HJs over the light/NW interaction. The first simulation concerns the study of the simplest case: a Si NW of varying length under plane wave excitation (λ = 532 nm). The calculated value of $|E|^2$ is plotted for different NW lengths in Figure 1a. In particular, for plane wave illumination of a homogeneous NW, longitudinal modes are observed, contrarily to an infinite NW that did not exhibit any longitudinal modes. After this, a SiGe/Si axially heterostructured NW was studied under plane wave illumination, Figure 1b. The pattern is very similar to the homogeneous NW, but the EM field enhancement at the HJ can be observed. Furthermore, the coupling of the incident plane wave with the material change of the HJ modifies the longitudinal mode of the EM field distribution on its vicinity.

The first simulation of a homogeneous Si NW was repeated for local illumination using a focused Gaussian beam, Figure 1c. These illumination conditions are much closer to the real experiments of μ-Raman and μ-PL. In this situation, the longitudinal modes only appear when the NW end is illuminated by the laser beam. These modes are not observed for homogeneous NWs and local illumination at the central region of the NW when the laser beam does not reach the NW ends. According to the infinite extension of a plane wave longitudinal modes always appear for plane wave illumination.

Note that these longitudinal modes cannot be associated with guided modes, since the incident wave arrives perpendicular to the NW axis (TM polarization with respect to the NW axis) which is not suitable for the transmission of light along the NW. Moreover, the SiGe absorption coefficient for 532 nm light is relatively large, especially when increasing the Ge content, which gives a very short light path inside the NW (the values range from $\approx$ 18 nm for pure Ge, to $\approx$ 890 nm for pure Si). Similar behaviour was reported in [24], where second harmonic generation (SHG) oscillations were observed when the light source illuminate the NW ends, but the SHG oscillations were absent when the light source hits the NW body without affecting the NW ends. SHG modes are sustained by the distribution of the internal optical field [25].

Upon the above observations one can say that the longitudinal modes are due to the disturbance of the electromagnetic field by the end boundaries of the NW. One cannot define an effective wavelength for the longitudinal modes for long NWs just by visual inspection of the EM field. In fact, the sep-

P7

aration between the successive maxima depends on the NW length and on the distance to the NW ends. These oscillations are determined by the boundary conditions at the NW ends and are sustained by the incident electromagnetic wave. Therefore, the electromagnetic field inside the NW is modulated by the field coupling with the NW boundaries. An analogous effect occurs when the light beam hits the HJ.

3 Fourier Transform study of the Electric Field

In order to better understand the role of the HJ and its effect on the electromagnetic field we performed a Fourier Transform study of the electromagnetic field distributions inside the NW. For that purpose, a standard Fast Fourier Transform (FFT) [26] is applied to the complex-valued electric field distribution to obtain its principal Fourier components. Figure 2 shows the electric field distribution of two different NWs used as an example. Both are 1 μm long, one is a homogeneous Si NW and the other one a heterostructured Si/SiGe NW. It can be observed that the presence of the HJ, located at the NW centre, disturbs the field distribution raising its value around this position, which explains the already mentioned enhancement effect.

FFT was applied over this EM field distributions (note that the FFT operation is performed over the complex valued original data and not the field modulus). The results are shown in Figure 3.

The Fourier Transform of the Si NW shows the main component of the field which is symmetric in k-space. However, if we look at the FFT of the HJ NW the plot is completely different.We can see that the main shape is similar to the Si NW FFT but it is no longer symmetric. If the plot is carefully analysed we could detect that the negative symmetric peak is increased, while the positive symmetric peak is decreased. Therefore, there is a new contribution which appears at symmetric values of k, but with opposite signs, i.e. an antisymmetric component, see Figure 4.

In order to ascertain the origin of these two components we performed an analysis of their dependence with the NW length and the incident light wavelength. The results are summarized in Figure 5. The position of the symmetric component turns out to be independent of the NW length and only varies with the incident light wavelength, Figure 5a.

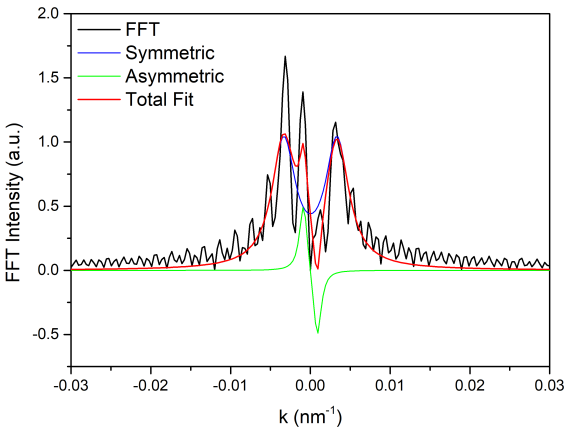

Figure 4: Example of the fit of the FFT data by using two components: symmetric (blue curve) and antisymmetric (green curve).

This direct correlation with the incident light wavelength tells us that this component is precisely the main component of the field. Conversely, the antisymmetric peak position changes with the NW length but it is independent of the incident wavelength, Figure 5b.

We can conclude from this information that the presence of the HJ is adding a contribution to the EM field that modifies its distribution and is directly related to the discontinuity along the NW axis, according to its dependence on the NW length. It is worth noting that for high values of the incident wavelength (600 nm on Figure 4a) there is a subtle dependence of the symmetric peak position with the NW length, which is followed by the predicted independence for higher values. This is an expected behaviour since a wavelength of 600 nm is comparable to the first two values of NW length that have been simulated, and for these values the interaction with the NW length modifies the fundamental mode wavelength.

According to this, the symmetric mode would correspond to the natural mode of the 532 nm light inside the NW. The even symmetry of this peak in Fourier space will result in the electric field having a large real part, as a consequence of Fourier Transform properties. On the other hand, the antisymmetric peak will represent the effect of the HJ inducing a stationary wave, and its odd symmetry results in a large imaginary part ($\pi/2$ phase shift) on the electric field. Essentially, symmetric functions result in real valued functions under inverse

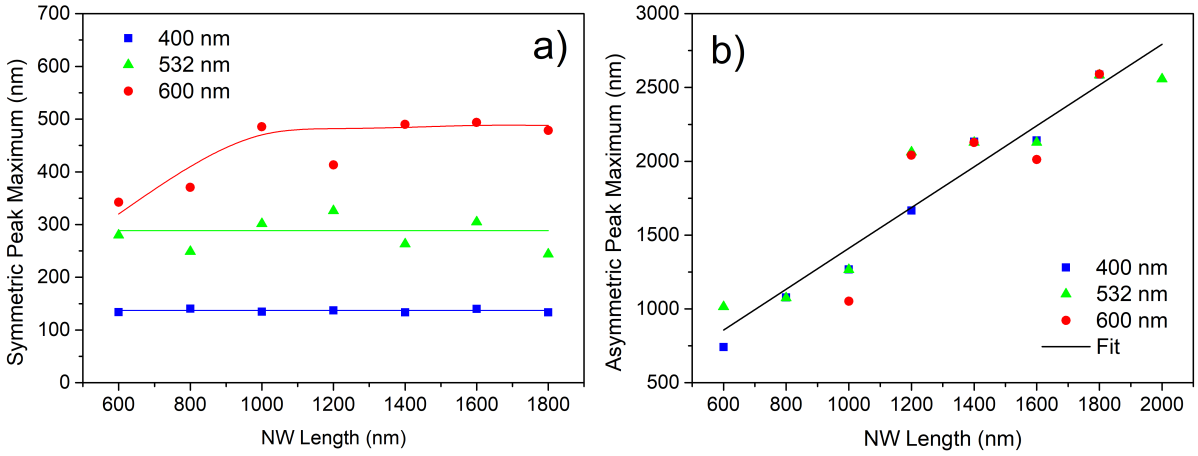

Figure 5: a) Position on k-space of the symmetric peak as a function of the NW length for different incident wavelengths, showing its dependence on the light wavelength and independence on NW length. b) The same plot for the antisymmetric peak, showing the opposite behaviour, linear dependence with NW length and independence on the incident light wavelength.

Fourier transform (e.g. cosine function), while antisymmetric functions result in pure imaginary functions (e.g. sine function). If we come back to Figure 3, the relation between the k value of the main symmetric component (propagation constant), and the corresponding value of the wave vector in vacuum, $k_0 = 2\pi/\lambda_0$, allow us to calculate the effective refractive index (or mode index)

$$n_{eff} = k/k_0 \tag{1}$$

As we have already mentioned this effective index depends exclusively on the incident wavelength, and not on the NW length. Figure 6 shows the dependence of the effective index with the incident wavelength. In Figure 6 we can observe two different physical limits:

- For $\lambda << d$ the incident wave interacts with the NW as if it was infinite (bulk), and the refractive index tends to be that of bulk Si ($\approx$ 4.13).
- For $\lambda >> d$ the NW is too small to interact with the incident wave and it behaves as if it was transparent, the index tends to be that of air.

It is important to note that this effective index is not a proper refractive index, i.e. it does not involve a travelling wave. This number just evidences the supported wavelength inside the NW. It can be understood as the degree of interaction between the NW and the incident electromagnetic field [24, 27].

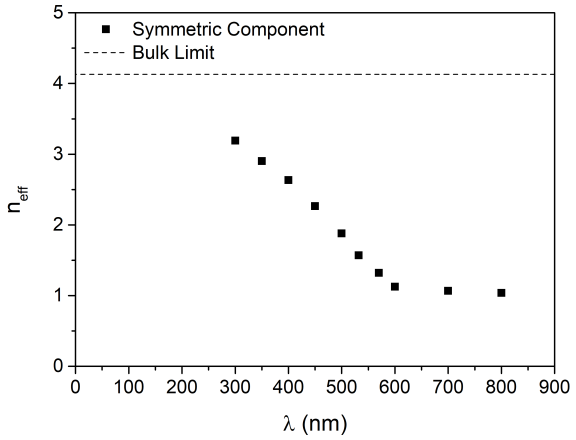

Figure 6: Dependence of the effective index with the incident wavelength for a 45 nm diameter NW. There are two limiting regions: for $\lambda << d$ the wave "sees" the NW as infinite, and the refractive index tends to be that of bulk Si ($\approx$ 4.13); for $\lambda >> d$ the NW is too small to be "seen" by the incident wave and it behaves as if it were transparent, the index tends to be that of air.

4 Conclusions

The effect of the HJ of axially heterostructured NWs on the EM field distribution under light illumination has been investigated. The results show a clear coupling between the incident EM field and dielectric discontinuity of the axially heterostructured NW, which results in the enhancement of the EM field around this region. The Fourier analysis reveals the existence of a new field component on heterostructured NWs, as compared with homogeneous NWs. This mode is antisymmetric in k-space, contrary to the principal mode of the incident light which is symmetric. The study of the dependence of these two modes with both the incident light wavelength and the NW length accounts for their respective origins. The symmetric peak varies with the incident light wavelength and it is independent on the NW length, while the antisymmetric peak has the opposite behaviour, having a direct dependence with the NW length and being clearly independent of the incident light wavelength. Finally, the effective index of the symmetric mode is studied, showing a dependence of the light/NW interaction as a function of the incident wavelength. For large values of the wavelength it can be observed that the light does not interact with the NW because it is much smaller than one wave cycle. For small values of the wavelength the NW behaves bulk-like, showing the response of an ordinary travelling wave. It is in the intermediate region (the visible range) in which the light strongly interacts with the NW, changing the effective refractive index. These results shed light on the phenomenon of light/NW interaction, particularly in the case of axially heterostructured ones, for their application on future optoelectronic nanodevices, like light sensors or solar cells, among others.

Achnowledgements

This work was funded by Junta de Castilla y León (Project VA283P18), and Spanish Government (ENE 2014-56069-C4-4-R). J L Pura was granted by the FPU programme (Spanish Government) (FPU14/00916).

References

[1] M. J. Tambe, S. K. Lim, M. J. Smith, L. F. Allard, S. Gradečak. Realization of defect-free epitaxial core-shell GaAs/AlGaAs nanowire heterostructures. *Applied Physics Letters*, **93** (15), 2013–2016 (2008). doi:10.1063/1.3002299

[2] U. Krishnamachari, M. Borgstrom, B. J. Ohlsson, N. Panev, L. Samuelson, W. Seifert, M. W. Larsson, L. R. Wallenberg. Defect-free InP nanowires grown in [001] direction on InP (001). *Applied Physics Letters*, **85** (11), 2077–2079 (2004). doi:10.1063/1.1784548

[3] S. K. Saini, R. V. Nair. Quantitative analysis of gradient effective refractive index in silicon nanowires for broadband light trapping and anti-reflective properties. *Journal of Applied Physics*, **125** (10) (2019). doi:10.1063/1.5083902

[4] J. Wallentin, N. Anttu, D. Asoli, M. Huffman, I. Åberg, M. H. Magnusson, G. Siefer, P. Fuss-Kailuweit, F. Dimroth, B. Witzigmann, H. Q. Xu, L. Samuelson, K. Deppert, M. T. Borgström. InP Nanowire Array Solar Cells Achieving 13.8% Efficiency by Exceeding the Ray Optics Limit. *Science*, **339** (6123), 1057–1060 (2013). doi:10.1126/science.1230969

[5] Y. H. Ahn, J. Park. Efficient visible light detection using individual germanium nanowire field effect transistors. *Applied Physics Letters*, **91** (16), 8–11 (2007). doi:10.1063/1.2799253

[6] C. Soci, A. Zhang, B. Xiang, S. A. Dayeh, D. P. R. Aplin, J. Park, X. Y. Bao, Y. H. Lo, D. Wang. ZnO Nanowire UV Photodetectors with High Internal Gain. *Nano Letters*, **7** (4), 1003–1009 (2007). doi:10.1021/nl070111x

[7] A. B. Greytak, C. J. Barrelet, Y. Li, C. M. Lieber. Semiconductor nanowire laser and nanowire waveguide electro-optic modulators. *Applied Physics Letters*, **87** (15), 1–3 (2005). doi:10.1063/1.2089157

[8] B. Piccione, C. H. Cho, L. K. Van Vugt, R. Agarwal. All-optical active switching in individual semiconductor nanowires. *Nature Nanotechnology*, **7** (10), 640–645 (2012). doi:10.1038/nnano.2012.144

[9] J. Bao, M. A. Zimmler, F. Capasso, X. Wang, Z. F. Ren. Broadband ZnO Single-Nanowire Light-Emitting Diode. *Nano Letters*, **6** (8), 1719–1722 (2006). doi:10.1021/nl061080t

[10] C. P. T. Svensson, T. Mårtensson, J. Trägårdh, C. Larsson, M. Rask, D. Hessman, L. Samuelson, J. Ohlsson. Monolithic GaAs/InGaP nanowire light emitting diodes on silicon. *Nanotechnology*, **19** (30), 305201 (2008). doi:10.1088/0957-4484/19/30/305201

[11] C. P. T. Svensson, W. Seifert, M. W. Larsson, L. R. Wallenberg, J. Stangl, G. Bauer, L. Samuelson. Epitaxially grown $GaP/GaAs_{1-x}P_x/GaP$ double heterostructure nanowires for optical applications. *Nanotechnology*, **16** (6), 936–939 (2005). doi:10.1088/0957-4484/16/6/052

[12] D. V. Murphy, S. R. J. Brueck. Enhanced Raman scattering from silicon microstructures. *Optics Letters*, **8** (9), 494 (1983). doi:10.1364/OL.8.000494

[13] G.-H. Ding, C. T. Chan, Z. Q. Zhang, P. Sheng. Resonance-enhanced optical annealing of silicon nanowires. *Physical Review B*, **71** (20), 205302 (2005). doi:10.1103/PhysRevB.71.205302

[14] X. Duan, Y. Huang, R. Agarwal, C. M. Lieber. Single-nanowire electrically driven lasers. *Nature*, **421** (6920), 241–245 (2003). doi:10.1038/nature01353

[15] J. Pura, P. Periwal, T. Baron, J. Jiménez. Growth dynamics of SiGe nanowires by the vapour-liquid-solid method and its impact on SiGe/Si axial heterojunction abruptness. *Nanotechnology*, **29** (35) (2018). doi:10.1088/1361-6528/aaca74

[16] M. Khorasaninejad, S. Patchett, J. Sun, N. O, S. S. Saini. Diameter dependence of polarization resolved reflectance from vertical silicon nanowire arrays: Evidence of tunable absorption. *Journal of Applied Physics*, **114** (2), 024304 (2013). doi:10.1063/1.4813081

[17] F. J. Lopez, J. K. Hyun, U. Givan, I. S. Kim, A. L. Holsteen, L. J. Lauhon. Diameter and polarization-dependent raman scattering intensities of semiconductor nanowires. *Nano Letters*, **12** (5), 2266–2271 (2012). doi:10.1021/nl204537d

[18] G. Bourdon, I. Robert, R. Adams, K. Nelep, I. Sagnes, J. M. Moison, I. Abram. Room temperature enhancement and inhibition of spontaneous emission in semiconductor microcavities. *Applied Physics Letters*, **77** (9), 1345–1347 (2000). doi:10.1063/1.1290144

[19] G. Brönstrup, C. Leiterer, N. Jahr, C. Gutsche, A. Lysov, I. Regolin, W. Prost, F. J. Tegude, W. Fritzsche, S. Christiansen. A precise optical determination of nanoscale diameters of semiconductor nanowires. *Nanotechnology*, **22**, 385201 (2011). doi:10.1088/0957-4484/22/38/385201

[20] L. Cao, P. Fan, A. P. Vasudev, J. S. White, Z. Yu, W. Cai, J. A. Schuller, S. Fan, M. L. Brongersma. Semiconductor nanowire optical antenna solar absorbers. *Nano Letters*, **10** (2), 439–445 (2010). doi:10.1021/nl9036627

[21] J. L. Pura, J. Anaya, J. Souto, Á. C. Prieto, A. Rodríguez, T. Rodríguez, J. Jiménez. Local electric field enhancement at the heterojunction of Si/SiGe axially heterostructured nanowires under laser illumination. *Nanotechnology*, **27** (45), 455709 (2016). doi:10.1088/0957-4484/27/45/455709

[22] J. L. Pura, J. Anaya, J. Souto, A. C. Prieto, A. Rodríguez, T. Rodríguez, P. Periwal, T. Baron, J. Jiménez. Electromagnetic field enhancement effects in group IV semiconductor nanowires. A Raman spectroscopy approach. *Journal of Applied Physics*, **123** (11), 114302 (2018). doi:10.1063/1.5012987

[23] J. L. Pura, A. J. Magdaleno, D. Muñoz-Segovia, M. Glaser, A. Lugstein, J. Jiménez. Electromagnetic enhancement effect on the atomically abrupt heterojunction of Si/InAs heterostructured nanowires. *Journal of Applied Physics*, **125** (6), 064303 (2019). doi:10.1063/1.5058276

[24] R. Grange, G. Brönstrup, M. Kiometzis, A. Sergeyev, J. Richter, C. Leiterer, W. Fritzsche, C. Gutsche, A. Lysov, W. Prost, F. J. Tegude, T. Pertsch, A. Tünnermann, S. Christiansen. Far-field imaging for direct visualization of light interferences in GaAs nanowires. *Nano Letters*, **12** (10), 5412–5417 (2012). doi:10.1021/nl302896n

[25] R. Cisek, V. Barzda, H. E. Ruda, A. Shik. Nonlinear Optical Properties of Semiconductor Nanowires. *IEEE Journal of Selected Topics in Quantum Electronics*, **17** (4), 915–921 (2011). doi:10.1109/JSTQE.2010.2065796

[26] R. Bracewell. *The Fourier Transform and Its Applications*. McGraw-Hill, 3rd Auflage (1963). ISBN 0-07-116043-4

[27] L. Tong, J. Lou, E. Mazur. Single-mode guiding properties of subwavelength-diameter silica and silicon wire waveguides. *Optics express*, **12** (6), 1025–1035 (2004). doi:10.1364/OPEX.12.001025

Chapter 8

This isn't right.
This isn't even wrong
- Wolfgang Pauli -

Conclusions

Semiconductor NWs have proven to be very promising systems for light/matter based applications at the nanoscale. The main characteristic of semiconductor NWs is their nanoscale diameter. The presence of a subwavelength dimension results in a complex interaction with the electromagnetic (EM) fields that are confined inside the NW. Finally, this interaction emerges as a diameter dependent enhancement of different optical processes. The unique properties regarding their interaction with light open the possibility for novel applications on electronic and optoelectronic nanodevices. Over the course of this thesis, we delved into the optical properties of axially heterostructured semiconductor NWs. These nanostructures exhibit intriguing behaviours when the light/NW interaction takes place in the vicinity of an axial heterojunction (HJ). When this situation occurs, the electromagnetic field is enhanced and localized at or close to the HJ region, thus increasing optical phenomena like Raman scattering. It is important to note that this effect appears as a superposition with the enhancement effects non-specific of the HJ, i.e., the antenna effect and the diameter resonances. The antenna effect is a consequence of the NW anisotropy as its diameter is considerably smaller than its length. This produces a dramatic dependence of the NW optical response with the polarization of the involved electromagnetic fields. Additionally, according to their subwavelength nature, the distribution of the electromagnetic fields inside the NW is highly sensitive to the NW diameter, presenting optical resonances for certain diameters that support the NW eigenmodes of the EM field. These two phenomena act together with the HJ enhancement to produce a larger concentration of the incident electromagnetic radiation on the NW HJ. The presence of this enhancement could explain recent reports on higher than expected efficiencies on devices based on axially heterostructured NWs, like NW based solar cells, and also suggests its possible application on other photonic nanodevices.

Chapter 4 is devoted to the study of SiGe/Si axially heterostructured NWs. These NWs present a Raman enhancement phenomenon when the HJ region is being illuminated with the excitation laser beam. The effect was first detected on SiGe/Si NWs with low Ge concentration ($\approx 10\%$). According to the reduced Ge content, the Raman spectra of these samples is mainly characterized by the Si-Si mode, which is very close to the crystalline Si phonon, being the Si-Ge and Ge-Ge modes very weak. This compels us to perform a deconvolution of the Raman spectrum in order to ascertain the different Raman bands. Unexpectedly, the obtained Raman spectrum cannot be reproduced with just two peaks, those of the homogeneous segments, and it is necessary to add a third band to achieve a successful fit of the experimental data, i.e., the signal of the HJ. The most interesting point is the high intensity of the HJ component, being of the same order of magnitude as the signals coming from the homogeneous segments. However, the volume of the HJ is at least ten times smaller than the homogeneous segments. Then, it can be concluded that the Raman signal is effectively being enhanced at the HJ.

As a consequence of the complexity of the analysis of the Raman spectrum, NWs with more Ge content were studied, around 60%. This results in a higher shift of the Si-Si peak, which is now clearly differentiated from the crystalline Si band so that the deconvolution is no longer necessary. The Raman measurements on these NWs lead to similar results to those from low Ge concentrations with the advantage of all the Raman bands being unambiguously separated.

As a complement to the Raman experiments, the interaction between laser light and axially heterostructured NWs has been analysed by Finite Element Methods (FEM) simulations. The axially heterostructured NW, as well as the substrate and the surrounding air, have been simulated by using the same geometrical characteristics as those of the experiments, NW length, diameter, geometrical disposition, etc. The model is then fed with the optical properties of each material conforming the heterostructured NW and its vicinity. The excitation laser beam is modelled as a focused Gaussian beam, accounting for the experimental conditions of μ-Raman spectroscopy. The solution of the model provides us with the 3D distribution of the electromagnetic field over the whole model, which allows the computation of the theoretical Raman signal. The results of the simulations show a localization and enhancement of the EM field at the HJ region. This explains the effect of Raman enhancement observed in the experiments. Moreover, the theoretical Raman signals obtained from the model as a function of the incident laser beam position are in perfect agreement with the experimental Raman profiles.

In this chapter, we also worked with double heterojunction SiGe/Si/SiGe NWs. They are especially interesting because of the two dissimilar HJs as a consequence of the growth process. The experimental measurements show the enhancement effect only on the leading (Si to SiGe) HJ. The trailing HJ (SiGe to Si) seems to be fully abrupt since no signal of any intermediate composition has been recorded. This suggests that the trailing HJ

might be unexpectedly abrupt, in contrast to what is usually claimed, while the leading one has a certain transition volume with a gradient in the Ge concentration, revealed by the Raman enhancement. The study of this feature has been complemented by analysing the dependence of the enhancement effect with the HJ thickness through the FEM model. Indeed, the model shows the demise of the enhancement effect as the HJ thickness tends to zero. This was in a flagrant contradiction with the current paradigm of vapour-liquid-solid (VLS) of this kind of NW heterostructures. The results of our experiments compelled us to work in a theoretical growth model, developed in chapter 6, that shows from a thermodynamic point of view that the expected HJ thicknesses agree with our experiments.

In order to finish this chapter, we designed an experiment to study the NW near field. A monolayer of CVD graphene was deposited between the Al substrate and the SiGe/Si/SiGe NWs. This, together with μ-Raman spectroscopy resolution allows for the detection of the NW near-field while the graphene layer guarantees the closest proximity to the NW surface. The first measurements over isolated graphene showed no Raman signal as a result of Al producing an effective quenching of the graphene Raman signal. However, when there is a NW lying over graphene, the graphene Raman signal is recovered. This manifests the potential of semiconductor NWs to control electromagnetic fields. Even in unfavourable conditions, like in the presence of a metallic surface, the NWs are able to localize the field in its interior and its surface. The full Raman measurement along the SiGe/Si/SiGe NW axis is repeated in the presence of the graphene layer. The HJ enhancement effect is detected in one of the HJs, as in preceding experiments. Conversely, the graphene Raman signal is highly reduced when the HJ enhancement takes place. A priori, this may appear counter-intuitive; however, the FEM model gave a simple explanation to this phenomenon: the EM field at the HJ is highly localized inside the NW core. This explains the reduced value of the near-field that results in a lower Raman signal of graphene near the HJ instead of the Raman signal enhancement of graphene close to the homogeneous region.

In **Chapter 5** axially heterostructured Si/III-V NWs are studied. The aim is to double-check that the observed enhancement effect is a purely structural phenomenon, and independent on the materials forming the heterostructured NWs. Si/III-V heterostructured NWs presents another advantage for the study of the enhancement effect, which is the different HJ structure as compared to that of SiGe/Si NWs. Si and Ge are both non-polar, while III-V semiconductors are polar. This results in the immiscibility of the Si and III-V compounds and the formation of an atomically abrupt HJ if they are joined in the same NW. The Raman measurements were performed over three different III-V semiconductors: GaAs, InAs, and InGaAs. The first experiments on Si/GaAs NWs did not reveal the presence of measurable GaAs segments in the NWs. The subsequent examination of these samples by SEM confirmed the absence of well-formed GaAs segments along the Si core. The Raman measurements on the next group, Si/InAs NWs, were much more

fruitful, showing now the presence of a Raman enhancement effect. However, in this case, the enhancement appears in a different way. As it has been explained there is no HJ volume on these NWs, so the enhancement appears on the Si section immediately adjacent to the HJ. The FEM model was adapted to the new NWs properties, both optical and geometrical. Its solution predicted the localization of the EM field on the Si side next to the HJ, perfectly matching the experimental Raman measurements. Finally, Si/InGaAs NWs were investigated, revealing once more the expected enhancement. It is interesting to note that the InGaAs segments were noticeably shorter than those of InAs, more numerous and scattered along the Si backbone instead of being localized on a single segment at the NW end. This, together with the spurious detection of segregated In on both Si/InAs and Si/InGaAs and the absence of fully formed segments on Si/GaAs NWs point to In atoms playing an important role on the recrystallization of the III-V segments on these systems, that might be interesting for future investigations.

As anticipated, **Chapter 6** contains the development of a new model for VLS growth of axially heterostructured SiGe/Si NWs. The motivation came from the experimental Raman measurements on SiGe/Si/SiGe axially heterostructured NWs, that suggested a flagrant contradiction with the pre-existing scheme for the HJ formation in NW systems. Moreover, an exact calculation and study of the full transition process were still lacking. The developed model is based on previous VLS growth models adapted to the SiGe alloy system. The analysis of the chemical potentials and their balance during the growth process led to the development of a composition map, that helps to keep track of the growth dynamics as a function of the concentration of Ge and Si atoms in the Au catalyst droplet. The exact state of the system on the composition map will determine the possibility of NW growth and also the Ge concentration of the solid phase. The model allows for the calculation of the growth composition and the evolution of the system during the growth process, including the formation of HJs. The complete analysis showed that the trailing HJ (SiGe to Si) is always sharper than the leading HJ (Si to SiGe). These results are in good agreement with the Raman measurements presented in this thesis, but also with other experimental evidence. It is important to note the existence of a critical point in the composition map. It is found that all the transition processes are much more abrupt when the system is closer to the critical point in the composition map. This opens a new path to control the HJ abruptness on heterostructured NWs based on Si and Ge, and also to foresee the results that should be expected previous to the actual growth process.

In **Chapter 7** we delved into the understanding of the enhancement effect studied through Chapters 4 and 5. The principal objective is to investigate the physical reasons behind the emergence of the enhancement effect. In order to do this, we performed a detailed analysis of the EM field distributions provided by the FEM model. The core of the study was focused on the use of Fourier Transform (FT) to ascertain the Fourier components of the EM field. The illumination was changed from the Gaussian beam profile

to a simpler monochromatic plane wave. This is a key point since the problem should be simplified as much as possible to clarify the subsequent analysis. We performed a systematic study of the EM field profiles by analysing two cases: a pure Si NW and a SiGe/Si axially heterostructured NW, both under plane wave illumination. This allows to directly compare the differences in both cases and extract the effect of the HJ. The FT of these two reference cases has a common part, which can be attributed to the main component of the incident field. This common component is the only one present on the pure Si NW spectrum; however, the FT of the heterostructured NW presents another feature. Two antisymmetric modifications of the Si FT can be observed: on the negative side of the k-axis, a new component appears, while in the opposite side we can observe a symmetric lowering of the FT intensity. This corresponds to an antisymmetric component that only appears on the SiGe/Si NW, so it has been attributed to the effect of the HJ. Subsequently, we analysed the behaviour of these two components with respect to the two basic parameters of the problem: the incident light wavelength and the NW length. The results show completely opposite behaviours, confirming the radically different nature of both components. The symmetric peak shows a direct dependence on the incident wavelength, while it is fully independent of the NW length. On the other hand, the antisymmetric peak does not depend on the incident wavelength and it is highly variable with the NW length. This explains the origin of the HJ contribution to the EM field distribution.

Finally, the effective index of the NW longitudinal modes, defined as the quotient between the longitudinal mode wavevector k and its value on vacuum, k_0, is studied as a function of the incident wavelength. The results show the expected behaviour: for large values of the wavelength the effective index tends to unity, which means that the incident wave is too large to interact with the reduced dimension of the NW; as the wavelength becomes smaller than the NW diameter, no size effects can be appreciated in the interaction with the material, and the effective index tends to that of bulk Si.

All in all, we have investigated the optical properties of different axially heterostructured semiconductor NWs. A Raman enhancement effect has been detected on the HJ of Si/SiGe, Si/InAs, and Si/InGaAs NWs. The detection of this effect on different NW materials reinforces its interpretation as a pure electromagnetic interaction, independently of the specific material forming the NW. The light/NW interaction has been studied by FEM simulations, showing enhancement and localization of the EM field at, or close to, the HJ of axially heterostructured NWs. This EM field increment gives rise to the detected Raman enhancement at the HJ. The Raman profiles calculated from the FEM simulations are in excellent agreement with the experimental measurements. The near-field induced in these NWs has been investigated by the use of a CVD graphene layer under the studied NWs. The results show a concentration of the EM field near the NW surface, improving the graphene Raman signal. The effect of the HJ was studied too, revealing a localization of the EM field at the NW interior lowering its value on the surface and consequently the

graphene Raman signal. This effect coincides with the Raman measurements. The Raman study of double HJ SiGe/Si/SiGe NWs showed the presence of Raman enhancement on only one of the two HJs, the leading HJ (Si to SiGe). According to the simulations, this could be expected if the trailing (SiGe to Si) is much more abrupt than the leading HJ. Then, we analysed the problem of HJ growth on NWs. For this, we studied the evolution of the chemical potentials of Si and Ge during growth, establishing a composition map that allows knowing the solid SiGe concentration during growth as a function of the catalyst droplet composition. The model permits to study the evolution of the system during HJ growth and to calculate the HJ thickness. The results were in good agreement with the experimental measurements, showing a trailing HJ more abrupt than the leading one in all cases. Finally, we performed a careful study of the EM field distributions obtained from the FEM model. The model was solved for a homogeneous Si NW and an axially heterostructured SiGe/Si NW with the same dimensions to isolate the effect of the HJ. We took advantage of the Fourier Transform to ascertain the main Fourier components of the EM field. The first results revealed a common symmetric mode in both NWs, but also the presence of an antisymmetric contribution on the SiGe/Si NW as compared with the pure Si NW. We associated the common symmetric component to the main mode of the EM field, and the antisymmetric component to the effect of the HJ. A further analysis was performed by varying the incident light wavelength and the NW length. This explained the origin of both components and shed light on the effect of the HJ on the EM field.

The study of the underlying interplay between axially heterostructured NWs and light constitutes a step forward for the understanding of the complex interaction of these systems. The comprehension and control of all the enhancement effects that appear on heterostructured NWs will allow for their application on the next generation of optoelectronic nanodevices.

Appendix

With great power comes
great responsibility
- Stan Lee -

A

Catastrophic Optical Damage of high power laser diodes

The principal object of study of this appendix is the degradation of quantum well (QW) based high power laser diodes. A scheme of this type of devices is provided in Figure A.1a. Of all the degradation modes, we have specifically studied the Catastrophic Optical Damage (COD). COD is a sudden breakup after many hours of regular operation. It can be differentiated from wear-out degradation because it takes place suddenly without previous symptoms of severe deterioration [1].

This phenomenon occurs in a very short period of time, therefore, it is very difficult to screen. COD is studied by doing post-mortem analysis of the degraded devices. Electron beam techniques, such as cathodoluminescence (CL) or electron beam induced current (EBIC), are very useful because the penetration depth of the electron beam can be controlled by changing the acceleration voltage. These measurements allow differentiating damaged regions from the non-degraded ones in the device, providing relevant information about the defects generated by the COD process.

The COD process is a local event, associated with the self-absorption of the laser radiation [2–4]. Basically, one can build up the following scenario. A local zone of the active region (the QW) is heated by a mechanism of non-radiative recombination because of a local accumulation of point defects. This temperature increment reduces the local band gap. This tiny zone of the active region starts to absorb the laser radiation generated in the ”cold” zones of the laser cavity. This mechanism contributes to the self-propagation of the defects in positive feedback, leading to the formation of typically extended defects along the laser cavity. These extended defects provide the dark contrast observed in the luminescence images, e.g., cathodoluminescence, see Figure A.1b. Elongated defects are known as dark line defects (DLDs), which are the products of catastrophic degradation.

The beginning of the COD appears as a thermal flash. Then, successive thermal flashes can be observed, resulting in a discontinuous array of DLDs propagating along the laser cavity. In the points where the damage is more severe, CL reveals that not only the QW but also the guide layers are damaged. The propagation of the DLDs is a fundamental issue because it is responsible for the destruction of the laser cavity and the end of the life of the device. Understanding these mechanisms is, therefore, a critical problem.

In previous works, the group built up a thermomechanical model accounting for COD [5–7]. This model has been further refined recently [8], by focusing on nanoscale effects [9] and different types of laser structures [10, 11]. However, the propagation of the DLDs has not received enough attention [12]. Aiming to understand this propagation, we applied the methodology developed in this thesis to study the laser radiation field inside these devices. The objective is to understand the cause of the sequential generation of defects along the laser QW. To do this, FEM simulations in 2D were performed, in order to study two different matters: the effect of high thermal gradients on the laser light distribution, and the impact of degraded regions on the cavity eigenmodes. All the scientific publications about this topic generated during the present thesis are gathered in Table 1.2.

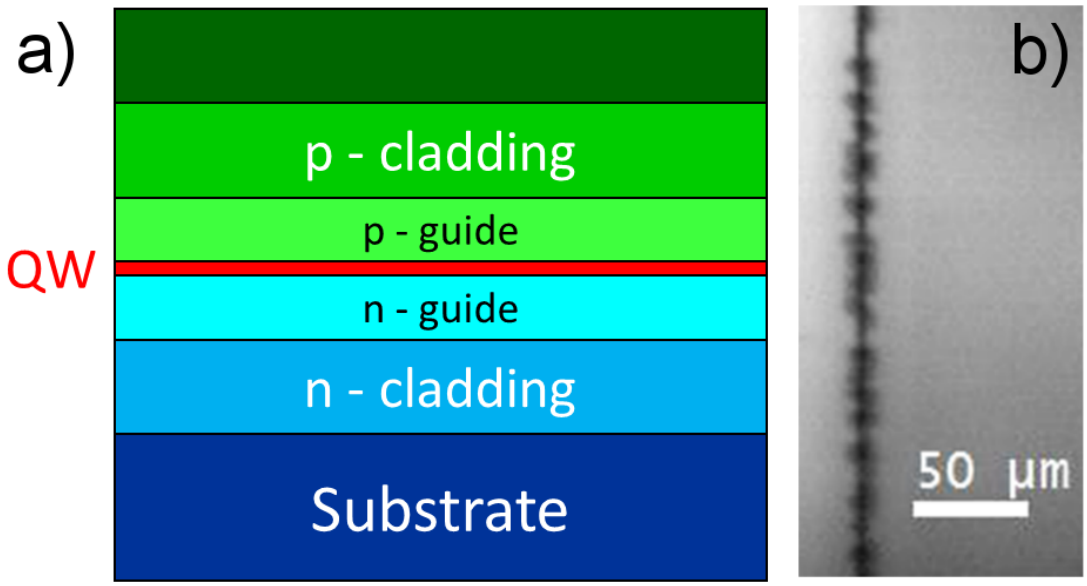

Figure A.1: a) Scheme of a typical QW laser diode arrangement. The laser beam is confined between the two guides, and the light is generated in the QW. Usually, the guides are not symmetric and a higher optical density travels through the n-guide. b) CL image of the QW region of a degraded laser diode. The dark regions are those that do not emit CL as a result of the degradation. The DLDs follow the QW (dark vertical line) and there the DLDs congregate in dark spots extending out of the QW towards the guides.

A.1 Effect of high thermal gradients: Thermal lensing effect

In this case, the simulation comprises a monochromatic 808 nm plane wave traveling through a GaAs QW and reaching a region with a highly localized heat source, simulating the beginning of a local COD event. The heated spot is modelled as a Gaussian distribution of temperature, with an FWHM of 1 μm. The maximum temperature of the distribution is varied from room temperature up to GaAs melting point (1238 °C = 1511 K). The effect of the temperature is calculated through its variation of the band gap, and consequently the refractive index, which will change the trajectory of the laser radiation according to Fermat's principle

$$\Delta n(\vec{r}) - \frac{d}{ds}\left(n(\vec{r})\frac{d\vec{r}}{ds}\right) = 0 \tag{A.1}$$

Where n represents the refractive index, $\vec{r}$ is the light trajectory and s the arclength parameter. The presence of a temperature gradient will result in a refractive index gradient, that changes the trajectory of light.

To compute the effect of the temperature on the light trajectory, the dependence of the GaAs band gap is calculated through the Varshni's equation

$$E_g(T) = E_g(0) - \frac{\alpha T^2}{T+\beta} \tag{A.2}$$

$E_g(0)$ = 1.519 eV is the GaAs band gap at 0 K and α = 5.408×10^{-4} eV K^{-1} and β = 204 K for GaAs. Once the band gap energy is known for the corresponding temperature the refractive index can be evaluated [14]. When the band gap increases by ΔE as a consequence of the temperature change, the effect on the refractive index is equivalent to considering light propagating with energy $h\nu' = h\nu - \Delta E$. Since the radiation is always produced by the GaAs QW (at room temperature) $h\nu = E_g(300\ K)$, and $\Delta E = E_g(T) - E_g(300\ K)$. Substituting these values we get the energy that should be evaluated on the expression $n(E)$ to obtain the refractive index as a function of temperature.

$$E(T) = 2E_g(300\ K) - E_g(T) \tag{A.3}$$

Finally, the values of the refractive index as a function of the incident light energy, $n(E)$, are obtained from reference [13] and interpolated from the experimental data, see Figure A.2.

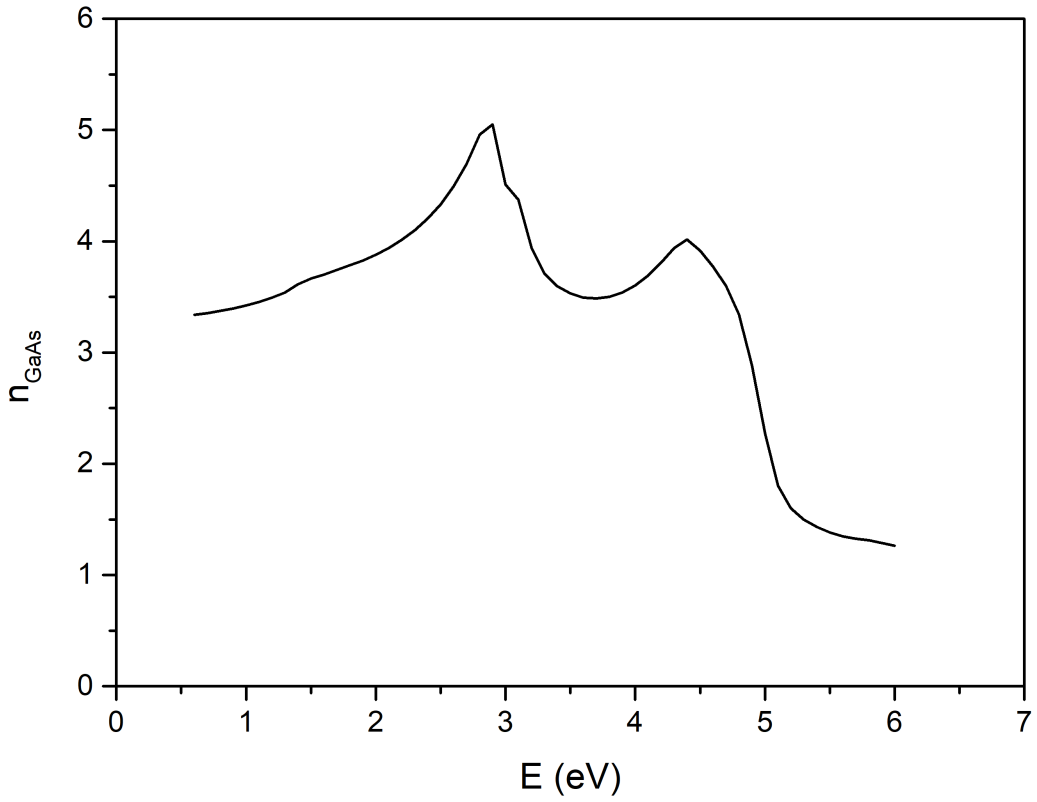

Figure A.2: Dependence of the refractive index of GaAs with the incident light energy, extracted from reference [13].

The model has been solved with two different modules of COMSOL Multiphysics: *Ray Optics* and *Electromagnetic Waves in Frequency Domain* (EWFD). The obtained results are equivalent and they are shown in Figures A.3 and A.4, respectively. In both cases, we can find a thermal lensing effect. The traveling plane wave is focused at a certain point after the heat spot. The focus progressively approaches the heat spot as the maximum temperature is increased, up to reaching a minimum distance of 3-5 μm. This is in good agreement with the experimental evidence and the magnitude of the distance between successive damaged spots, Figure A.1.

It is also interesting to note that the results of the EWFD module, Figure A.4, are much more reliable than the results of the ray optics solution, Figure A.3. This was expected a priori, since the system dimensions, especially the heat spot, are in the nanometric range, and consequently comparable to the laser wavelength. Thus, the phase differences will be very important and physical optics should be used to obtain a precise result. Furthermore, Figure A.4 shows localization of the EM field at the same point for all temperatures,

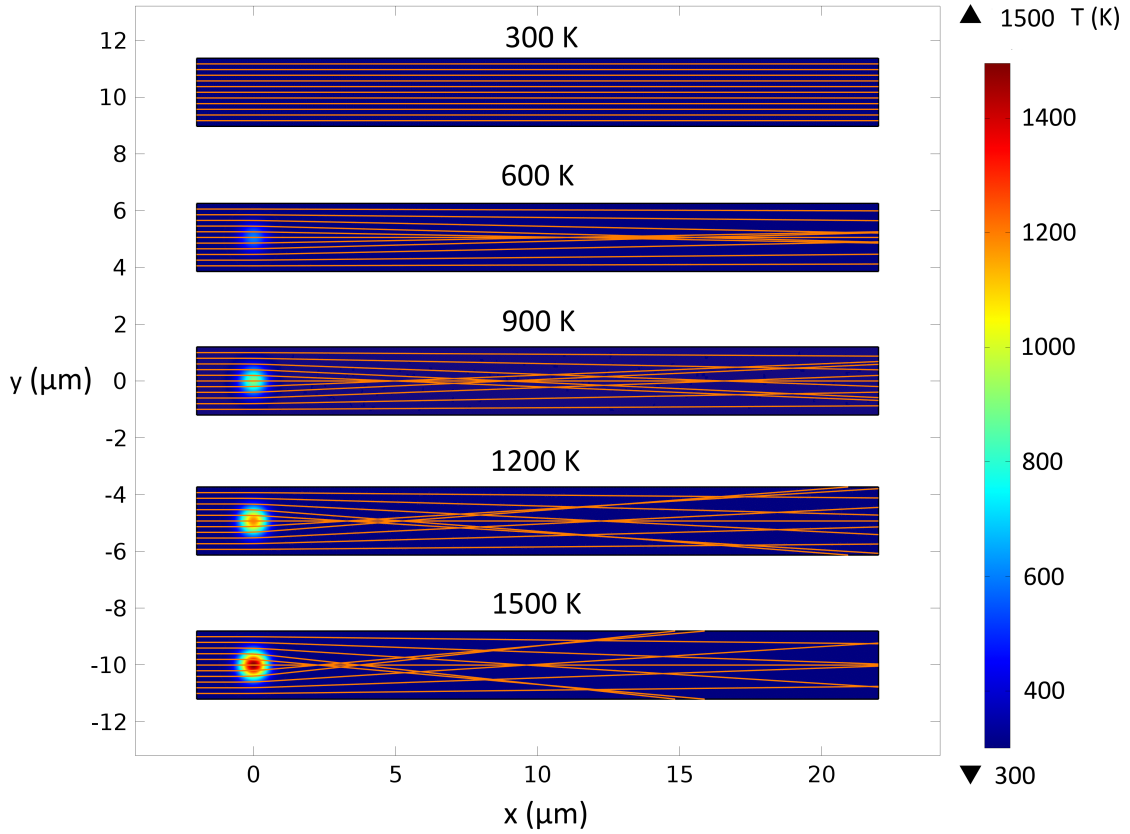

Figure A.3: Ray Optics simulation of the effect of a local heat spot over the laser beam trajectory. The laser beam is focused at a certain point after the initial defect. The distance of the focus and the defect decreases as the maximum temperature raises. Note that the presence of optical aberrations prevents a clear determination of a unique focus, resulting in a slightly wide spot, instead of a point-like focus.

increasing the localization of the EM field as the maximum temperature raises. On the other hand, in the ray optics interpretation, the focusing is not well defined because of severe optical aberrations.

Figure A.4 also shows the presence of a diffraction pattern, in the same way that it should appear if the light went through the aperture of a physical lens. The diffraction pattern, like the focus, does not change with temperature pointing to a dependence only with the heat spot dimension.

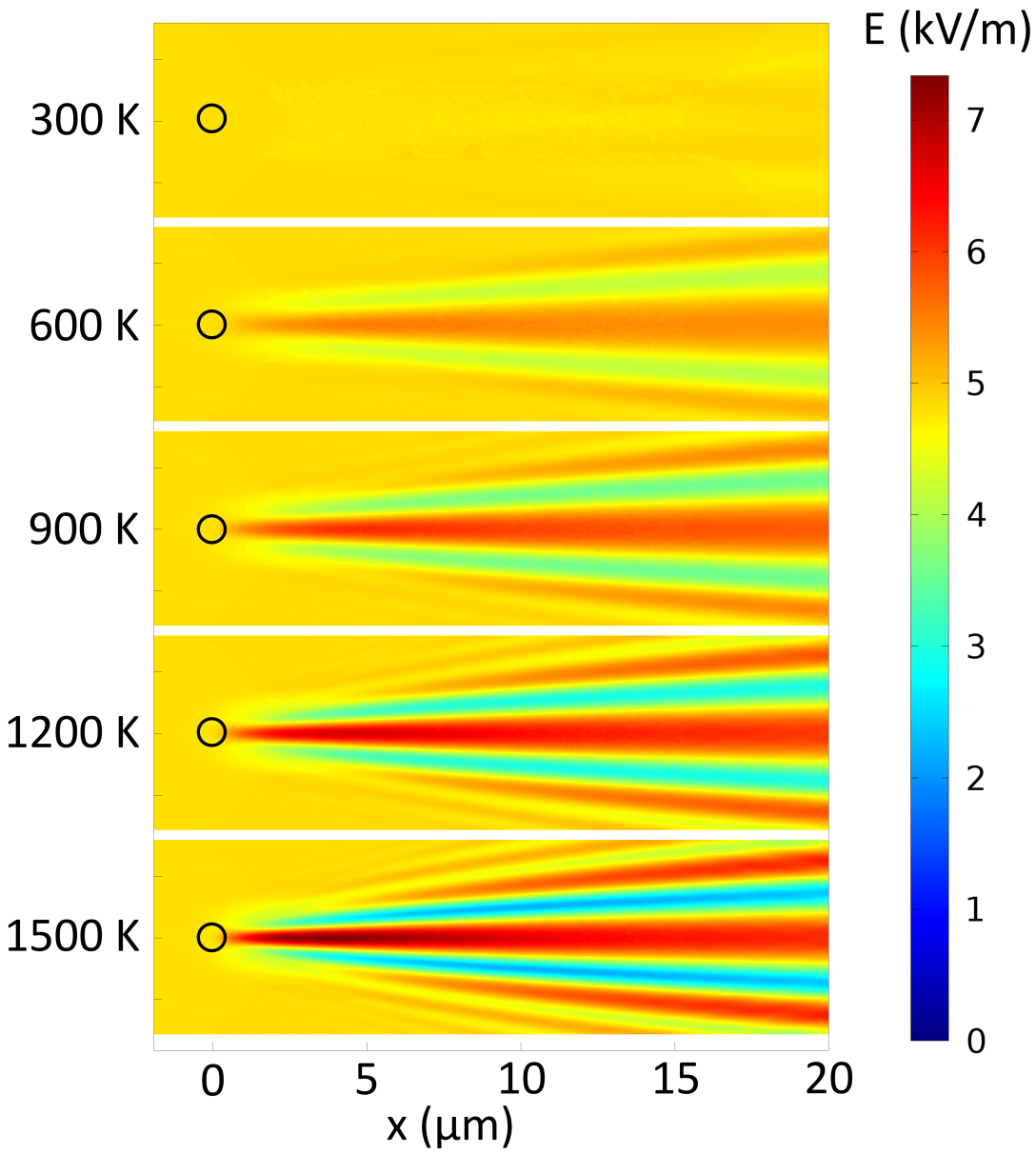

Figure A.4: Simulations with the Electromagnetic Waves in Frequency Domain module of COMSOL. The EM field is again localized in a region after the defect (black circle). In this case the location of the focus does not change with temperature, but the EM field is progressively concentrated in the focus as the defect temperature is increased.

A.2 Impact of micrometric degraded regions on the laser cavity eigenmodes

In this second section, we studied the effect of an already degraded region on the eigenmodes of the laser cavity. Once the material overcomes its mechanical limit, its properties are locally spoiled and it stops emitting light, as it has been shown in Figure A.1. According to the dimensions of the high power laser diodes under study, we performed a simulation of a 3 mm Fabry-Perot laser cavity with one $\sim$ 100 % mirror on its backside and a GaAs/air surface ($\sim$ 30 % reflectivity), which is the facet that lets the laser beam out of the device. Then, a damaged region is placed near the front surface. In order to model the defect, the refractive index of a 1 μm^2 region of GaAs has been set to 1. This region is placed in the QW and 2 μm away from the front facet into the device.

The model is solved by using the EWFD module in the "eigenfrequency" study to obtain the EM field distribution of the cavity modes. The results are plotted in Figure A.5.

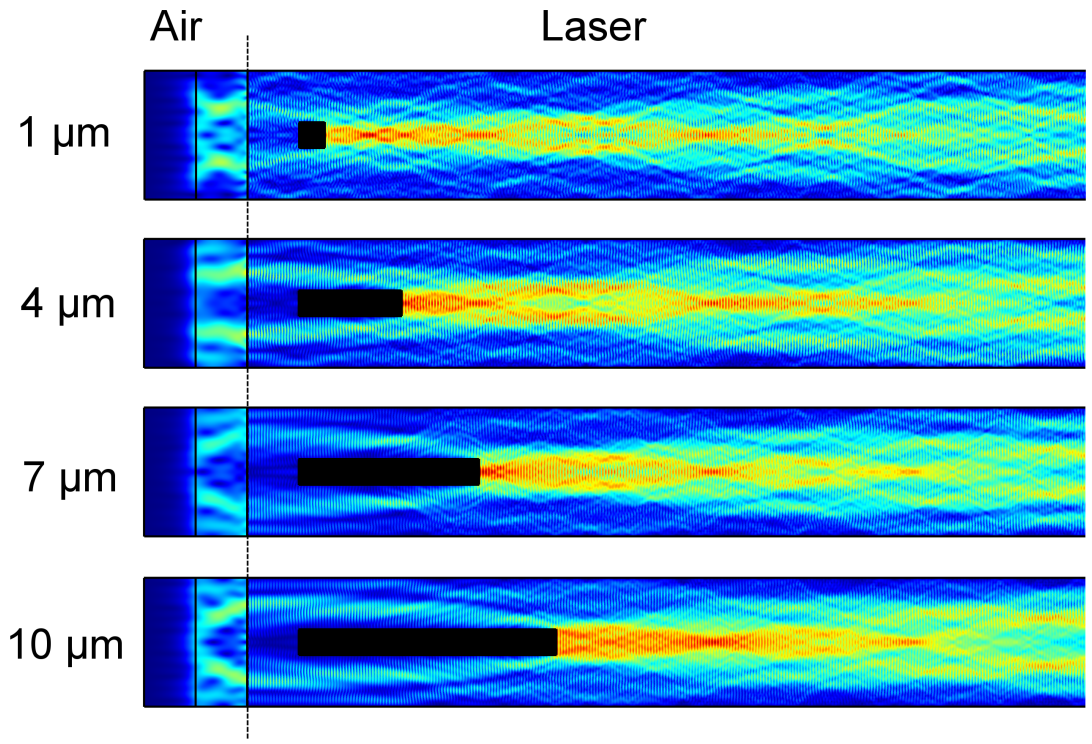

Figure A.5: Simulation of the laser cavity eigenmodes in the presence of a degraded region on the QW. The laser cavity mode is always concentrated $\sim$ 3 - 4 µm in front of the degraded region, which will eventually trigger a new local COD event, extending the damaged region.

The first simulation shows a localization of the laser mode $\sim$ 3 μm ahead of the degraded region. This is in good agreement with the experimental CL measurements and the thermal lensing results. The localization of the laser mode will trigger a new heat spot which will result in a new damaged region. We simulated this process by making the initial defect 3 μm longer on each step. Figure A.5 shows that the laser mode is always localized in front of the damaged region. This effect, together with the thermal lensing mechanism, can explain the sequential degradation process observed in the CL images, Figure A.1.

It can also be noticed that the laser mode is able to circumvent the damaged region. This is in perfect agreement with other experimental observations in which the laser device does not stop lasing when the QW is damaged, but it remains working until the degraded regions extend beyond the laser guides or until the extent of the degradation of the QW reduces the effective cavity length below the lasing threshold.

A.3 Conclusions

In this appendix, we studied the effect of QW damaged regions on the Catastrophic Optical Degradation of high power laser diodes. We did this by analyzing two different aspects of these defects.

First, we studied the effect of a QW hot spot on the laser beam trajectory. A 2D model with a 1 µm Gaussian temperature profile has been solved by using both rays and waves optics. The results are equivalent, being the wave optics solution more accurate. In both cases the defect shows a thermal lensing effect that focuses the travelling wave on a point situated 3 - 5 µm behind the hot spot.

Second, we investigated the effect of a fully degraded region of material on the QW. In this case, the simulation was focused on the laser cavity modes, that are highly sensitive to any change in the interior of the cavity. A 1 μm^2 defect located near the front facet of the laser has been simulated. The result is the localization of the cavity mode $\sim$ 3 - 5 µm in front of the degraded region. This localization, together with the thermal lensing effect, could trigger the occurrence of a new COD event at this point, similar to what is observed on CL measurements, Figure A.1. We extended the degraded region according to this and repeated the simulation. The cavity mode is again localized at a new point $\sim$ 3 - 5 µm in front of the new extended defect. This explains the sequence of dark spots observed in the CL images.

As a summary, the results of both approaches show a concentration of the laser beam on the region near a heated or degraded area inside the QW. This laser beam concentration could trigger new sequential COD events, explaining the chain of dark spots observed in high power laser diodes presenting COD breakup.

Bibliography

[1] O. Ueda. On Degradation Studies of III-V Compound Semiconductor Optical Devices over Three Decades: Focusing on Gradual Degradation. *Japanese Journal of Applied Physics*, **49** (9), 090001 (2010). doi:10.1143/JJAP.49.090001

[2] J. Tomm, M. Ziegler, M. Hempel, T. Elsaesser. Mechanisms and fast kinetics of the catastrophic optical damage (COD) in GaAs-based diode lasers. *Laser & Photonics Reviews*, **5** (3), 422–441 (2011). doi:10.1002/lpor.201000023

[3] P. W. Epperlein. *Semiconductor Laser Engineering, Reliability and Diagnostics*. John Wiley & Sons Ltd, Oxford, UK (2013). ISBN 9781118481882. doi:10.1002/9781118481882

[4] J. Souto, J. L. Pura, J. Jiménez. Thermomechanical issues of high power laser diode catastrophic optical damage. *Journal of Physics D: Applied Physics*, **52** (34), 343002 (2019). doi:10.1088/1361-6463/ab243f

[5] A. Martín-Martín, M. Avella, M. P. Iñiguez, J. Jiménez, M. Oudart, J. Nagle. A physical model for the rapid degradation of semiconductor laser diodes. *Applied Physics Letters*, **93** (17), 171106 (2008). doi:10.1063/1.3009290

[6] A. Martín-Martín, M. Avella, M. P. Iñiguez, J. Jiménez, M. Oudart, J. Nagle. Thermomechanical model for the plastic deformation in high power laser diodes during operation. *Journal of Applied Physics*, **106** (7), 073105 (2009). doi:10.1063/1.3236507

[7] A. Martín-Martín, P. Iñiguez, J. Jiménez, M. Oudart, J. Nagle. Role of the thermal boundary resistance of the quantum well interfaces on the degradation of high power laser diodes. *Journal of Applied Physics*, **110** (3), 033113 (2011). doi:10.1063/1.3622508

[8] J. Souto, J. L. Pura, J. Jiménez. About the physical meaning of the critical temperature for catastrophic optical damage in high power quantum well laser diodes. *Laser Physics Letters*, **13** (2), 025005 (2016). doi:10.1088/1612-2011/13/2/025005

[9] J. Souto, J. L. Pura, J. Jiménez. Nanoscale effects on the thermal and mechanical properties of AlGaAs/GaAs quantum well laser diodes: influence on the catastrophic optical damage. *Journal of Physics D: Applied Physics*, **50** (23), 235101 (2017). doi:10.1088/1361-6463/aa6fbd

[10] J. Souto, J. Pura, A. Torres, J. Jiménez, M. Bettiati, F. Laruelle. Catastrophic optical damage of high power InGaAs/AlGaAs laser diodes. *Microelectronics Reliability*, **64**, 627–630 (2016). doi:10.1016/J.MICROREL.2016.07.038

[11] J. Souto, J. Pura, A. Torres, J. Jiménez. Thermomechanical degradation of single and multiple quantum well AlGaAs/GaAs laser diodes. *Microelectronics Reliability*, **76-77**, 588–591 (2017). doi:10.1016/J.MICROREL.2017.07.005

[12] M. Hempel, J. Tomm, V. Hortelano, N. Michel, J. Jiménez, M. Krakowski, T. Elsaesser. Time-resolved reconstruction of defect creation sequences in diode lasers. *Laser & Photonics Reviews*, **6** (6), L15–L19 (2012). doi:10.1002/lpor.201200039

[13] S. Adachi. Optical dispersion relations for GaP, GaAs, GaSb, InP, InAs, InSb, $Al_xGa_{1-x}As$, and $In_{1-x}Ga_xAs_yP_{1-y}$. *Journal of Applied Physics*, **66** (12), 6030–6040 (1989). doi:10.1063/1.343580

[14] P. Geng, W. Li, X. Zhang, Y. Deng, H. Kou, L. Chen, X. Wu. Effects of temperature and redshift on the refractive index of semiconductors. *Journal of Applied Physics*, **124** (3), 035703 (2018). doi:10.1063/1.5027771

```
if (A440 == 6) {
    play (abcehijlopqsvsqpoljihecba);
}
```